AD-A146 148 FUNDAMENTAL ELECTRONIC PROPERTIES OF DONOR-TYPE GRAPHITE INTERCALATED COM..(U) MOORE SCHOOL OF ELECTRICAL ENGINEERING PHILADELPHIA PA S RABII ET AL. 1/1

UNCLASSIFIED 01 AUG 84 ARO-17299.18-PH DAAG29-80-K-0019 F/G 11/2 NL

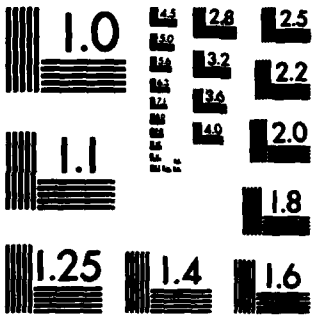

MICROCOPY RESOLUTION TEST CHART
NATIONAL BUREAU OF STANDARDS-1963-A

ARO 17299.18-PH

(2)

AD-A146 148

FUNDAMENTAL ELECTRONIC PROPERTIES OF DONOR-TYPE GRAPHITE INTERCALATED COMPOUNDS

FINAL REPORT

S. RABII AND J.E. FISCHER

8/1/84

U. S. ARMY RESEARCH OFFICE

DAAG29-80-K-0019

MOORE SCHOOL OF ELECTRICAL ENGINEERING
UNIVERSITY OF PENNSYLVANIA

DTIC
ELECTE
OCT 1 1984
S D
A

DTIC FILE COPY

APPROVED FOR PUBLIC RELEASE;
DISTRIBUTION UNLIMITED.

84 09 25 151

THE VIEW, OPINIONS, AND/OR FINDINGS CONTAINED IN THIS REPORT ARE THOSE OF THE AUTHOR(S) AND SHOULD NOT BE CONSTRUED AS AN OFFICIAL DEPARTMENT OF THE ARMY POSITION, POLICY, OR DECISION, UNLESS SO DESIGNATED BY OTHER DOCUMENTATION.

SECURITY CLASSIFICATION OF THIS PAGE (When Data Entered)

REPORT DOCUMENTATION PAGE

READ INSTRUCTIONS BEFORE COMPLETING FORM

1. REPORT NUMBER: ARO 17299.18-PH
2. GOVT ACCESSION NO.: AD-A146148
3. RECIPIENT'S CATALOG NUMBER:

4. TITLE (and Subtitle): Fundamental Electronic Properties of Donor-Type Graphite Intercalation Compounds

5. TYPE OF REPORT & PERIOD COVERED: Final 10/80 - 3/84

6. PERFORMING ORG. REPORT NUMBER:

7. AUTHOR(s): S. Rabii and John E. Fischer

8. CONTRACT OR GRANT NUMBER(s): DAAG29-80-K-0019

9. PERFORMING ORGANIZATION NAME AND ADDRESS:
Moore School of Electrical Engineering
University of Pennsylvania
Philadelphia, PA

10. PROGRAM ELEMENT, PROJECT, TASK AREA & WORK UNIT NUMBERS:

11. CONTROLLING OFFICE NAME AND ADDRESS:
U.S. Army Research Office
Post Office Box 12211
Research Triangle Park, N.C. 27709

12. REPORT DATE: August 1, 1984

13. NUMBER OF PAGES: 13

14. MONITORING AGENCY NAME & ADDRESS (if different from Controlling Office):

15. SECURITY CLASS. (of this report): UNCLASSIFIED

15a. DECLASSIFICATION/DOWNGRADING SCHEDULE:

16. DISTRIBUTION STATEMENT (of this Report):

Approved for public release; distribution unlimited.

17. DISTRIBUTION STATEMENT (of the abstract entered in Block 20, if different from Report):

N/A

18. SUPPLEMENTARY NOTES:

The view, opinions, and/or findings contained in this report are those of the author(s) and should not be construed as an official Department of the Army position, policy, or decision, unless so designated by other documentation.

19. KEY WORDS (Continue on reverse side if necessary and identify by block number):

graphite, intercalation, band structure, electronic properties

20. ABSTRACT (Continue on reverse side if necessary and identify by block number):

DD FORM 1 JAN 73 1473 EDITION OF 1 NOV 65 IS OBSOLETE

UNCLASSIFIED

SECURITY CLASSIFICATION OF THIS PAGE (When Data Entered)

INTRODUCTION

This final report covers the period October 1, 1980 to March 31, 1984. It is a follow on to a previous contract DAAG29-80-K-0019 which carried the title "Fundamental Electronic Properties of Donor-Type Graphite Intercalated Compounds".

All the significant results have been published in the open literature. We present here the highlights of those results. Attached as appendices are reprints of papers published during the second 3-year contract.

DTIC COPY INSPECTED

A1

STATEMENT OF PROBLEM

Graphite intercalation compounds are a large family of quasi-two dimensional synthetic metals. Fundamental interest centers on their unusual crystal structures and their effects on electronic properties. Practical applications are envisaged as lightweight conductors of electricity.

The goals of this program are to understand the electronic structure of donor-type compounds, with a view toward obtaining detailed correlations between chemical and physical variables. Emphasis is placed on the one-electron spectrum, transport and optical properties and charge distributions. Synthetic methods are developed to provide high-quality specimens for a variety of physical measurements. Band theoretical techniques are applied to develop models for the electronic structure. Iteration between theory and experiment leads to more sophisticated models.

HIGHLIGHTS

The experimental work conducted during this contract consisted of three projects:

i. Detailed structural studies of the Li-graphite system versus Li concentration and temperature.

ii. Preliminary experiments revealing an unusual temperature dependence of c-axis conductivity in various donor compounds.

iii. Definitive reflectivity measurements which provide sensitive tests of the theoretical band structures.

The theoretical efforts were focused on:

iv. Calaculation of the optical spectra, $\varepsilon(\omega)$, for graphite and LiC_6 providing for detailed test of the calculated band structure through comparison with measured reflectivity and electron-energy-loss spectra.

v. Determination of the charge transfer in the donor graphite intercalation compounds.

vi. Determination of the nature of c-axis screening in higher stage Li-graphite.

1. Structural Studies of Li-Graphite

The saturated stage 1 compound LiC_6 is a physical realization of the 3-component Potts model in 3 dimensions, so its melting behavior should be directly comparable to symmetry-based theories and Monte Carlo simulations. We found a weakly first-order transition at 715K as predicted by Landau-Ginzburg expansions, preceded by a large continuous precursor which occurs also in the computer experiments. Detailed comparison of the T dependence of the order parameter below T_c reveals significant discrepancies, however. These may be due to different jump rates parallel and perpendicular to the layers, or may be a manifestation of vacancies or their associated random field. Further measurements with vacancy concentration as a parameter would be clearly useful.

The staging phase diagram for Li_xC_6 versus x and T has been determined in broad outline from x-ray and neutron diffraction. The general prediction of Safran is confirmed: at high T, only stage 1 is stable independent of x, a direct consequence of the dimensionality of the configurational entropy. The corrugation potential between Li and the 2D hexagonal "substrate" is very strong due to the compact Li^+ core, thus leading to unusual regions of stability for different in-plane densities. Phonon spectra and c-axis compressibilities have been obtained as a function of in-plane density at constant stage; these data accord well with a simple electrostatic model of interlayer interactions.

2. C-axis conductivity

Much of the interest in GIC's has been motivated by the large in-plane (a-axis) conductivity and the resulting potential for applications as synthetic conductor. On the other hand, the interlayer, or c-axis transport should be fundamentally interesting as a probe of staging transitions, nonlinear screening and possible localization effects.

We measured the c-axis conductivity from 4-300K on all the usual stage 1 donors, and on K-GIC's up to stage 7. Some samples of MC_8 (M = K, Rb, Cs) show a transition from metallic to activated behavior as T is reduced below 40-100K. In one case the 4K conductivity is only half the 300K value. In all cases $\sigma \rightarrow$ constant as $T \rightarrow 0$, implying an incipient metal-insulator transition which is interrupted by another process. The overall $\sigma_c(T)$ behavior differs markedly from $\sigma_a(T)$, which leads us to believe that we're seeing intrinsic behavior rather than a-axis shorting paths. High stage samples show strongly first-order anomalies in the 220K region which correlate with similar anomalies in static susceptibility. In a separate project, structural studies show that these anomalies originate in a curious temperature-dependent disorder in the perfection of the high-stage "superlattice".

3 and 4. Dielectric Function of LiC_6 - Theory and Experiment

On the experimental side, reflectivity measurements were carried out up to 11 eV, with polarization perpendicular to the c-axis, on the first stage alkali graphite intercalation compounds LiC_6 and KC_8 as well as the ternary compound $KHgC_4$. In addition, infrared reflectivity measurements were carried out as a function of stage on a number of donor and acceptor compounds. The results for LiC_6 are in excellent agreement with our calculations as will be discussed below. The results of $KHgC_4$ support the idea that the excess K (4s) charge is transferred to mercury bands. The low energy reflectivity as a function of stage for the acceptor compounds show an absence of Burstein-Moss shift, indicating that the partially ionized intercalant layers are screened by the compensating free carriers within one layer spacing, i.e., the bounding layer. This is in agreement with our theoretical calculations described in 6. The calculated energy bands and wave functions were used to calculate the complex dielectric function up to 40 eV for polarization both parallel and perpendicular to the c-axis. This is the first such calculation for any intercalation compound, and shows excellent agreement not only with the above reflectivity measurement but with results of electron-energy-loss experiments and reflectivity measured by other workers. Our calculations show that the observed plasmon at 2.85 eV for $\varepsilon_{1\perp}$ is due to the oscillations of the free carriers screened by interband transitions.

Without this screening the plasma frequency would have been at 6.3 eV obtained from the Fermi surface calculation for the combination of both carrier surfaces.

5. Charge Transfer in the Donor Graphite Intercalation Compounds

Our original nonselfconsistent calculation of the energy band structure of LiC_6 and KC_8 using the Green's function (KKR) technique, had indicated that the charge transfer from the intercalant to graphite layers is unity. This was in contrast to the calculations for KC_8 from the group of Kamimura at Tokyo University which predicted the existence of a large s-type pocket of carriers at the Brillouin zone center. During the past three years, we have carried out selfconsistent calculations of the energy band structure for LiC_6 and KC_8 using the *ab initio* norm-conserving pseudopotentials. The results confirmed our original conclusions that any carriers that may exist at the zone center in KC_8 will be extremely few in number and due to the intersection of the Fermi level with π bands. These π bands are deformed due to hybridization with the potassium levels. The current experimental data are being interpreted in agreement with our model. In the case of BaC_6, even though there are two s electrons on Ba that could potentially be transferred to graphite, only between 0.7 and 1.0 electron per Ba atom are transferred to the graphite layers. The results show, further, that the band originating from Ba states has a mixture of s and d character and the d

component hybridizes appreciably with the π bands of graphite. These results are consistent with the available transport and optical measurements on graphite.

6. C-axis Charge Distribution in High Stage Li-graphite

One of the important questions dealing with the intercalation compounds has been whether the charge donated by the intercalant layer to the graphite layers in stages three or higher, is distributed uniformly among these layers or it is concentrated in the graphite layers adjacent to the intercalant. In order to answer this question, we undertook to calculate the energy band structure and charge distribution for 2nd and 3rd stage Li-graphite. Our results showed that, in fact, the major part of the transferred charge is concentrated in the bounding graphite layers. This is the explanation for the splitting of the graphite layer Raman lines when we go from the second to third stage Li-graphite.

PERSONNEL

Prof. J.E. Fischer	P/I
Prof. S. Rabii	P/I
Dr. J.M. Bloch	Postdoctoral Fellows
Dr. K.C. Woo	
Dr. H. Mertwoy	
N. Chen	Ph.D. 7/84
H.J. Kim	Ph.D. Student
K. Phan	M.S. 12/81
C. Shieh	Ph.D. 6/84
R.C. Tatar	Ph.D. Student
Tim Koch	(Student Assistant)

PUBLICATIONS (From Previous Contract)

1. "Alternate Synthesis and Reflectivity Spectrum of Stage 1 Lithium-Graphite Intercalation Compounds", M. Zanini, S. Basu and J. E. Fischer, Carbon 16, 211 (1978)

2. "Raman Scattering in LiC_6: Evidence for a Rigid Band Interpretation", M. Zanini, Lih-Ying Ching and J. E. Fischer, Phys. Rev. B18, 2020 (1978).

3. "Graphite Intercalation Compounds", J.E. Fischer and T.E. Thompson, Physics Today, 31, 36 (1978).

4. "Optical Anisotropy of HOPG: Effect of Surface Preparation", M. Zanini, D. Grubisic and J. E. Fischer, Phys. Stat. Sol. (b) 90, 151 (1978).

5. "Graphite Intercalation Compounds: An Overview", J. E. Fischer, Comments in Solid State Physics, 8, 155 (1978).

6. "Anisotropic Magnetic Susceptibility and Phase Transitions in Intercalated Graphite: KC_{24}", F.J. DiSalvo and J. E. Fischer, Solid State Comm. 28, 71 (1978).

7. "Anisotropy of Graphite Intercalation Compounds", J. E. Fischer, in "Molecular Metals", W. E. Hatfield, editor, Plenum Press, New York (1979) p. 281.

8. "Electronic Properties of Graphite Intercalation Compounds", chapter in Physics and Chemistry of Materials with Layered Structures, (F. Levy, editor) D. Reidel, Holland, Vol 6 p. 481 (1979).

9. "Intercalated Graphite: Some Aspects of Two-Dimensionality", J. E. Fischer, Comments on Solid State Physics, 9, 93 (1979).

10. "Preparation and Properties of Lithium-Graphite Intercalation Compounds", S. Basu, C. Zeller, P. Flanders, C.D. Fuerst, W. D. Johnson and J. E. Fischer, Mat. Sci. Eng. 38, 275 (1979).

11. "Large Anisotropy and Stage Dependence of the Magnetic Susceptibility of Alkali Graphite Compounds", F.J. DiSalvo, S.A. Safran, R. C. Haddon, J. V. Waszczak and J. E. Fischer, Phys. Rev. B20, 4883 (1979).

12. "Raman Scattering in Graphite Lithium Intercalation Compounds" P. C. Eklund, G. Dresselhaus, M. S. Dresselhaus and J. E. Fischer, Phys. Rev. B21, 4705 (1980).

13. "Interlayer Screening and Magnetic Susceptibility of Graphite Intercalation Compounds", S.A. Safran, F.J. DiSalvo, R.C. Haddon, J.V. Waszczak and J.E. Fischer, Physica B, 99, 494 (1980).

14. "Graphite Intercalation Compounds", J.E. Fischer, Physica B 99, 383 (1980).

15. "Specific Heat of LiC_6 from 4-300K", C. Ayache, E. Bonjour, R. Lagnier and J.E. Fischer, Physica B 99, 547 (1980).

16. "Elastic and Inelastic Neutron Scattering Studies of Lithium-Graphite", J. Rossat-Mignod, D. Fruchart, M.J. Moran, J.W. Milliken and J.E. Fischer, Synthetic Metals 2, 143 (1980).

17. "The Electronic Structure of KC_8", D.P. DiVincenzo, N.A.W. Holzwarth and S. Rabii, Physica 99B, 406 (1980).

18. "Energy Band Structure of Three Dimensional Graphite", R.C. Tatar, N.A.W. Holzwarth, and S. Rabii, Synthetic Metals 3, 131 (1981).

19. "A Calculation of the Electronic Band Structure of KC_8", D.P. DiVincenzo, N.A.W. Holzwarth and S. Rabii, Synthetic Metal 3, 123 (1981).

20. "Transport Properties of Alkali Metal-Graphite Intercalation Compounds", M.E. Potter, W.D. Johnson and J.E. Fischer, Solid State Communications 37, 713 (1981).

PUBLICATIONS - Current Contract

1. "First-Order Phase Transition in the Graphite Compound LiC_6", J. Rossat-Mignod, A. Wiedenmann, K.C. Woo, J.W. Milliken and J.E. Fischer, Solid State Comm. 44, 1339 (1982).

2. "C-axis Resistivity of Stages 1-7 Potassium-Intercalated Graphite", K. Phan, C.D. Fuerst and J.E. Fischer, Sol. St. Comm. 44, 1351 (1982).

3. "Theoretical Investigation of the Electronic Properties of Potassium Graphite", D.P. DiVincenzo and S. Rabii, Phys. Rev. B25, 4110 (1982).

4. "Electronic Properties of Graphite: A Unified Theoretical Study", R.C. Tatar and S. Rabii, Phys. Rev. B25, 4126 (1982).

5. "Electronic Structure of Third-Stage Lithium Intercalated Graphite", N.A.W. Holzwarth, S.G. Louie and S. Rabii, Phys. Rev. Lett. 47, 1318 (1982).

6. "X-Ray Form Factors and the Electronic Structure of Graphite", N.A.W. Holzwarth, S.G. Louie and S. Rabii, Phys. Rev. B26, 5382 (1982).

7. "The Effect of In-plane Density on the Structural and Elastic Properties of Graphite Intercalation Compounds", K.C. Woo, W.A. Kamitakahara, D.P. DiVincenzo, D.S. Robinson, H. Mertwoy, J.W. Milliken and J.E. Fischer, Phys. Rev. Letters, 50, 182 (1983).

8. "Experimental Phase Diagram of Lithium Intercalated Graphite", K.C. Woo, H. Mertwoy, J.E. Fischer, W.A. Kamitakahara and D.S. Robinson, Phys. Rev. B27, 7831 (1983).

9. "C-Axis Resistivity of Some Stage 1 Donor Compounds", J.E. Fischer, C.D. Fuerst and H.J. Kim, Proc. MRS Symposium on Intercalated Graphite (North Holland, 1983) p. 169.

10. "Staging Transitions in Li-Graphite: Phonon Spectra of Dilute Stage 1", K.C. Woo, H. Mertwoy, J.E. Fischer, W.A. Kamitakahara and D.S. Robinson, Proc. MRS Symposium on Intercalated Graphite (North Holland, 1983), p. 265.

11. "Staging Transitions in Intercalated Graphite", J.E. Fischer, C.D. Fuerst and K.C. Woo, Synthetic Metals 7, 1 (1983).

12. "Energy-band Structure and Charge Distribution for BaC_6", N.A.W. Holzwarth, D.P. DiVincenzo, R.C. Tatar and S. Rabii, Int. Jr. of Quantum Chem. XXIII, 1223 (1983).

13. "Calculation of the Optical Spectra for Graphite", N.X. Chen, S. Rabii and N.A.W. Holzwarth, Synthetic Metals, 8, 197 (1983).

14. "Electronic Structure of Graphite Intercalation Compounds", N.A.W. Holzwarth, S.G. Louie and S. Rabii, Proc. MRS Symposium on Intercalated Graphite (North Holland, 1983), p. 107.

15. "Lithium-Intercalated Graphite: Selfconsistent Electronic Structure for Stages One, Two and Three", N.A.W. Holzwarth, S.G. Louie and S. Rabii, Phys. Rev. B28, 1013 (1983).

16. "Ab Initio Calaculation of the Optical Spectra of LiC_6 and the Origins of its Plasmons", N.X. Chen and S. Rabii, Phys. Rev. Lett. 52, 2386 (1984).

17. "Interlayer States in Graphite and in Alkali-Metal-Graphite Intercalation Compounds", Phys. Rev. B30 (1984).

18. "Theoretical Valence Charge Densities for Graphite, Diamond and LiC_6", N.A.W. Holzwarth, S.G. Louie and S. Rabii, To appear in Local Density Approximation in Quantum Chemistry and Solid State Theory, Editors, J. Avery and J.P. Dahl, Plenum Press.

Solid State Communications, Vol. 44, No. 8, pp. 1339–1342, 1982.
Printed in Great Britain.

0038–1098/82/441339–04$03.00/0
Pergamon Press Ltd.

FIRST-ORDER PHASE TRANSITION IN THE GRAPHITE COMPOUND LiC_6

J. Rossat-Mignod and A. Wiedenmann

Laboratoire de Diffraction Neutronique, Department de Recherche Fondamentale, Centre d'Etudes Nucleaires, 85X, F-38 041 Grenoble, France

and

K.C. Woo, J.W. Milliken* and J.E. Fischer

Moore School of Electrical Engineering and
Laboratory for Research on the Structure of Matter, University of Pennsylvania, Philadelphia, PA 19104, U.S.A.

(*Received* 12 *July* 1982 *by E.F. Bertaut*)

Elastic neutron scattering and scanning calorimetry reveal a weakly first-order "melting" of the Li layers in the graphite intercalation compound LiC_6 at $T_0 = 715.4$ K, in excellent agreement with recent experiments by Robinson and Salamon. The first-order nature of the transition also agrees with a prediction by Bak and Domany derived from Landau expansions, but the detailed behavior of the fluctuation-induced power-law precursor differs from recent Monte Carlo simulations of the $3D$–$3q$ Potts model.

LiC_6 HAS THE SIMPLEST ground state structure of all the graphite intercalation compounds (GIC). The hexagonal unit cell contains one Li and six C atoms, with alternate stacking of commensurate C and Li layers in which the Li's occupy only one of three sets of equivalent interstitial sites on a $\sqrt{3} \times \sqrt{3}$ in-plane superlattice [1]. This structure, characterized by a stacking sequence $A\alpha A\alpha$ (A = carbon, α = Li), is stable at least over the interval $10\,K < T < 300\,K$ [2], and is isomorphous to the ordered phase of the three dimensional three-state Potts model, the critical behavior of which has been explored theoretically [3] and by Monte Carlo simulations [4–6]. We set out to characterize the order–disorder transition by neutron diffraction. What we observed was a weakly first order reversible "melting" of the Li sublattice at $T_0 = 715.4 \pm 0.2$ K, in agreement with Bak and Domany's prediction [3]. However, over a 200 K range extending to within 1 K of T_0 the melting is characterized by a continuous power-law decrease of the order parameter. Our results agree in detail with the data of Robinson and Salamon [7] (RS), but our interpretation is different. Whereas experiments and simulations agree that the transition is first order, differences in detail regarding the continuous precursor suggest that the $3D$–$3q$ Potts model may only be applicable to the universal aspects of the transition in LiC_6, and that conclusions regarding the significance of the precursor are premature. The simulations all assume a s.c. lattice with lattice-gas disorder above T_0; the Li sublattice in LiC_6 is hexagonal with two out-of-plane neighbors at 3.7 Å (shielded by graphite monolayers) and six in-plane neighbors at 4.3 Å, and the nature of the disordered phase above T_0 is unknown. We therefore suggest that subtle features of the Monte Carlo simulations regarding critical fluctuations which precede the first-order transition may not be applicable to the diffraction results on LiC_6.

Neutron scattering experiments were performed on a triple-axis spectrometer at the Siloe reactor (CEN-Grenoble), using monochromatized neutrons with $\lambda = 2.4$ Å. LiC_6 samples $10 \times 20 \times 1$–2 mm were prepared from highly-oriented pyrolytic graphite by immersion in molten Li and were sealed in thin-wall stainless tubes containing a small amount of Li to maintain equilibrium vapor pressure. Details are given elsewhere [2]. In Fig. 1 we plot the T-dependence of the peak intensity of the (100) reflection from the $\sqrt{3} \times \sqrt{3}$ Li commensurate superlattice, scanned along h. We observe a continuous loss of intensity up to 714 K upon heating, but the transition is actually weakly first order, as is apparent from the expanded scale insert. The intensity drops discontinuously at T_0 (factor of ~ 10 within 1 K), and there is ~ 5 K hysteresis between heating and cooling. The discontinuous drop accounts for 30% of the intensity, or 55% of the order parameter, of the completely ordered phase. The diffraction results are completely reversible. Differential scanning calorimetry (lower insert) indicates a lambda-like anomaly, which in light of the diffraction data may be attributed to fluctuation effects rather than to a second-order process [7]. Above 750 K the sample transforms rapidly

*Current address: Naval Research Laboratory, Washington, D.C., U.S.A.

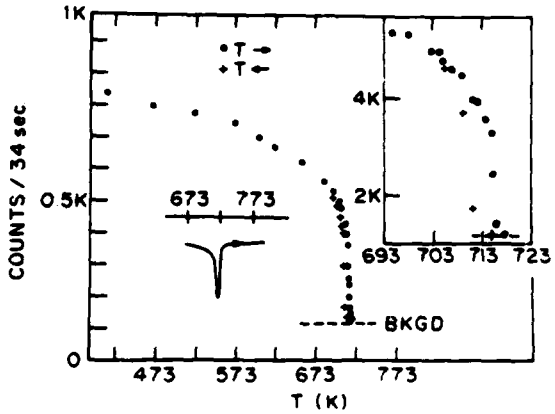

Fig. 1. Temperature dependence of the peak intensity of the (100) Li superlattice reflection in LiC_6 scanned in the plane (powder average of h and k). Inset upper right: expanded scale showing hysterisis and discontinuous drop at $T_0 = 715.4 \pm 0.2$ K upon warming. Inset lower left: differential scanning calorimetry trace of the transition.

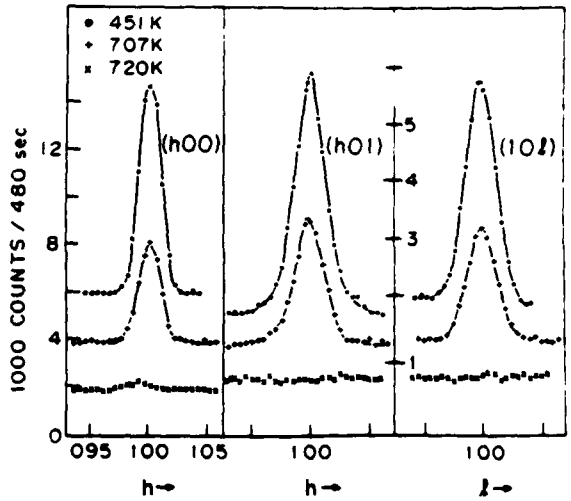

Fig. 2. Elastic scans at 451 K (...), 707 K (+++): (a) (100) scanned along h, (b) (101) along h, (c) (101) along l. Scattering wave vectors q_a and q_c in units of $2\pi/a$ and $2\pi/c$ where $a = 4.304$ A, c varies from 3.691 to 3.770 A respectively. Upper two curves shifted vertically for clarity; solid lines are guides to the eye.

and irreversibly into Li_2C_2 so we did not explore the disordered region in detail. The observed width in h of the (100) reflection is independent of T within our resolution $\Delta q/q = 0.02$ (FWHM), as shown in the first panel of Fig. 2. Thus the in-plane correlation length is constant up to T_0. One possible explanation for the continuous decrease of (100) intensity followed by a first-order "melting" would be a continuous loss of c-axis correlations, which would broaden the (100) reflection along l and thus reduce the peak intensity scanned along h. This in turn would indicate a $3D \rightarrow 2D$ crossover [8] below the first-order transition at T_0, in which case the latter would be a $2D$ rather than $3D$ process. The second and third panels of Fig. 2 allow us to rule out this possibility, since the (101) reflection has essentially the same T dependence when scanned along h or l. The broad region of continuous behavior in Fig. 1 therefore indicates a precursor effect to the first-order transition, both phenomena being $3D$.

In addition to the above observations, we find that within experimental error the Li and graphite sublattices remain commensurate up to T_0 and that the in-plane parameter $a = 4.304$ A exhibits no measurable T-dependence. The small peak at $q = 0.99$ in the (h00) scan at 720 K ($T > T_0$, first panel of Fig. 2) occurs at constant Bragg angle (independent of sample orientation) and therefore may be an "impurity" powder peak or a multiple-scattering effect. The (10l) scans indicate a large thermal dilation in the stacking direction [9].

Figure 3 is a plot of $\log(I/I_0)$ vs. $\log(1 - T/T_0)$ where I is the background-corrected (100) peak intensity (+++) or the square of the Monte Carlo order parameter [5] (ooo). We emphasize that a power law analysis is motivated only to facilitate comparison of various results. We view the exponents as empirical parameters characterizing the continuous precursor to a first-order transition, not as critical exponents in the usual sense. The latter are defined in the limit $T/T_0 \rightarrow 1$, so the fact that the same exponent fits the data in the range $0.0017 < (1 - T/T_0) < 0.34$ militates against interpreting it as a second-order critical exponent. From Fig. 3, the best fit exponent to our intensity data is 0.20 ± 0.02 which would correspond to a pseudo critical exponent "β" $= 0.10 \pm 0.01$. The data point closest to T_0 lies below the power law line, indicating the onset of the discontinuous transition. The integrated intensity data of RS shows the same temperature dependence within experimental errors; since the line width and line shape are independent of T, peak and integrated intensities should give the same exponents. However, RS derived from their data a value of the critical exponent $\beta = 0.22 \pm 0.03$ by fitting

$$I(T) = A(T - T_0)^{2\beta} + B\delta(T - T_0),$$

thus allowing an infinite slope at T_0. In our opinion, there is no physical justification of such a fitting procedure.

Both diffraction experiments agree with the prediction [3] based on universality of a first-order transition in LiC_6. The Monte Carlo simulations provide more information, at the expense of specifying a detailed model (e.g., s.c. lattice, nearest-neighbor interactions only in [4–6]). The simulation by Knak Jensen and Mouritsen [5] gives an exponent 0.27 for the square of the order

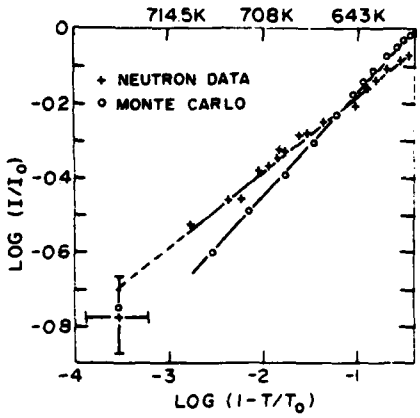

Fig. 3. Log–log plot of reduced intensity vs reduced temperature. Comparison of our data (+++) with the square of the order parameter [5] (ooo).

parameter (Fig. 3), while Herrmann [6] finds $\beta = 0.17$ for the magnetization, hence an exponent $2\beta = 0.34$ to be compared with the numbers cited above. Thus the experiments and simulations disagree in all cases. The closest approach to agreement is between the RS data and the simulation of [5], whereas Fig. 3 clearly shows that our experimental exponent is significantly less than the Monte Carlo value. Reference [5] gives a clear indication of a first-order transition with a coexistence region $\Delta T/T_0 \sim 10^{-3}$ in the order parameter, whereas Herrmann's evidence for a discontinuous transition is based principally on the behavior of thermodynamic properties away from T_0. The experimental hysterisis $\Delta T/T_0 = 0.007$ (Fig. 1) is significantly larger than the Monte Carlo result [5], although a previous simulation [4] gave $\Delta T/T_0 \sim 0.01$. Finally, the 10% discontinuity in magnetization found by Harrmann [6] is inconsistent with the magnitude of the discontinuous drop in intensity (Fig. 1), whereas the agreement with Fig. 4 of [5] is satisfactory in this aspect. While conclusions based on universality are probably on solid ground, caution is suggested in applying the details of model-dependent computer simulations to "real" experimental results.

The discrepancies noted above may be due to differences between the actual Li lattice and the idealized models on which the simulations are based, as noted above. Another possibility is that the Li sublattice melting does not terminate in a lattice gas. In the only comparable case studied to date, Clarke *et al.* [10] find lattice-gas behavior in the disordered phase of CsC_8 only if some Cs is allowed to permanently deintercalate in the course of the experiment. After the first heating above T_0, the ordered phase becomes a mixture of stages 1 and 2, thus providing the necessary vacancies for lattice-gas disorder upon subsequent heating above T_0. Despite the relatively low vapor pressure of Li and the presence of excess Li in the container, a similar justification for lattice-gas behavior can be made in our case. The samples originally contain a very small admixture of stage 2 at 300 K, which disappears upon heating above 430 K [2]. This admixture grows with each heating cycle, a phenomenon which was also noted by RS. The relative sizes of Li and Cs would suggest that lattice-gas disorder is more readily accommodated, even without vacancies, beginning from a Li $\sqrt{3} \times \sqrt{3}$ structure than from a Cs 2×2. A search for energy broadening of the Li (100) reflection just below T_0 showed nothing within our energy resolution of 2×10^{-4} eV, thus ruling out structural fluctuations (e.g., hopping among α, β and γ sites) faster than 10^{11} sec^{-1}. Lattice-gas disorder would therefore appear static on this time scale. Direct measurement of the diffuse scattering above T_0 is frustrated by the container background [7]; such experiments, if feasible, would confirm or deny whether the Potts model applies to both the ordered and disordered phases of LiC_6.

Another possible complication in LiC_6 might be the existence of strong 2*D* fluctuations, associated with the fact that the Li sublattice is not entirely decoupled from the graphite network at any temperature. Given the small diameter of either Li^+ or Li^0 relative to the 4.3 Å circle available to it in the $\sqrt{3} \times \sqrt{3}$ superlattice, and given the evidence for partial covalent (i.e., strong) interlayer C–Li bonding [2], any fluctuations in Li positions would be largely confined to a Li layer. While the amplitude of such 2*D* fluctuations might be too small to produce differences between *h* and *l* scans with moderate resolution, they might affect the exponent of a basically 3*D* continous precursor.

It is significant that LiC_6 exhibits a discontinuous transition. The simple $A\alpha A\alpha$ stacking is less susceptible to stacking faults than the more complex arrangements which occur in all ordered stage ≥ 2 compounds. Random fields associated with faults may be expected to broaden a first-order transition enough to yield data which fit continuous models [8, 11]. Similar arguments have been advanced to explain the absence of disorder-induced Raman scattering in compounds with relatively simple stacking sequences, in particular LiC_6 [12].

Another unusual aspect of LiC_6 is the stability of the $A\alpha A\alpha$ stacking sequence over the entire *T* range within which the Li is ordered [2, 7]. essentially $0 < T < T_0$. This implies that relative to other stage 1 compounds (and certainly stage $n \geq 2$) the interlayer C–Li interaction is stronger than the interlayer Li–Li interaction. This could simply be a matter of relative distances (2.3 Å vs 3.7 Å for C–Li and Li–Li nearest neighbors respectively), but that would not explain why MC_8 compounds do exhibit stacking transtions [13] and/or metastable "polytypes" [14] below T_0. In this context the detailed study of phase transitions in stage 2 Li compounds [2] may be profitable.

In conclusion, we find a weakly first-order $3D$ melting of the Li sublattice in LiC_6, preceded by a continuous power-law precursor characterized by a pseudo exponent 010. It is unlikely that the precursor is due to random field smearing [7], but neither is it accurately represented by Monte Carlo calculations of the $3D$–$3q$ Potts model. This might be due to a disordered phase in which Li atoms do not randomly occupy well-defined sites, although a more likely reason is that LiC_6 is not well-represented in detail by the Monte Carlo models. Symmetry-based predictions are borne out; the transition is indeed first order [3].

Acknowledgements – We acknowledge helpful discussions with P. Bak, J.B. Hastings, A.R. McGhie and J. Villain, and the generosity of A.W. Moore (Union Carbide) in donating substantial quantities of HOPG. This research was supported in part by ARO Contract DAAG-29-80-K0019 (K.C.W., J.E.F.) and BMFT Project 03-41E-21P of the Federal Republic of Germany (A.W.). Materials preparation and characterization were supported by the NSF MRL Porgram, DMR 79-23647 (J.W.M.).

REFERENCES

1. D. Guerard & A. Herold, *Carbon* **13**, 337 (1975).
2. J. Rossat-Mignod, D. Fruchart, M.J. Moran, J.W. Milliken & J.E. Fischer, *Syn. Met.* **2**, 143 (1980).
3. Per Bak & Eytan Domany, *Phys. Rev.* **B20**, 2818 (1979).
4. H.W.J. Blote & R.H. Swendson, *Phys. Rev. Lett.* **43**, 799 (1979).
5. S.J. Knak Jensen & O.G. Mouritsen, *Phys. Rev. Lett.* **43**, 1736 (1979).
6. H.J. Herrmann, *Z. Physik* **B35**, 171 (1979).
7. D.S. Robinson & M.B. Salamon, *Phys. Rev. Lett.* **48**, 156 (1982).
8. S.A. Solin, *Adv. Chem. Phys.* (in press).
9. As a result of improved thermomentry and control, we found that Fig. 2 of [2] is incorrect. The c-axis expansion coefficient is constant, $\Delta c/c = 6.5 \times 10^{-5} K^{-1}$ from 300 to 714 K, and $\Delta a/a$ is less than $10^{-6} K^{-1}$ over the same interval.
10. R. Clarke, N. Caswell & S.A. Solin, *Phys. Rev. Lett.* **40**, 61 (1979).
11. J.B. Hastings, W.D. Ellenson & J.E. Fischer, *Phys. Rev. Lett.* **42**, 1552 (1979).
12. D.M. Hwang, S.A. Solin & D. Guerard, *Physics of Intercalation Compounds* (Edited by L. Pietronero and E. Tosatti), p. 187. Springer-Verlag, Berlin (1981).
13. W.D. Ellenson, D. Semmingson, D. Guerard, D.G. Onn & J.E. Fischer, *Mat. Sci. Eng.* **31**, 137 (1977).
14. N. Caswell, *Phys. Rev.* **B22**, 6308 (1980).

Solid State Communications, Vol.44,No.9, pp.1351-1355. 1982.
Printed in Great Britain.

0038-1098/82/451351-05$03.00/0
Pergamon Press Ltd.

C - AXIS RESISTIVITY OF STAGES 1-7 POTASSIUM-INTERCALATED GRAPHITE

K. Phan*, C.D. Puerst+ and J.E. Fischer*

Laboratory for Research on the Structure of Matter
University of Pennsylvania
Philadelphia, Pennsylvania 19104

(Received July 26, 1982, in revised form September 27, 1982 by R.H. Silsbee)

Temperature-dependent c-axis resistivity measurements on stages 1-7 potassium-graphite compounds show a crossover from metallic to activated behaviour between stages 4 and 5, as well as the onset of a new type of anomaly for stage ≥ 4. KC_8 shows in addition a tendency toward a metal-insulator transition below 40K. The high-stage transport process is discussed in terms of weak depletion of the interior layers by interlayer screening. We suggest that the high stage anomalies reflect an instability in the c-axis charge distribution.

Intercalation of donors or acceptors into graphite produces large changes in ρ_a and ρ_c, the a-axis and c-axis resistivities. The former has been extensively studied in graphite intercalation compounds[1,2](GIC), whereas ρ_c should be maximally sensitive to guest-host interactions[3], staging transitions[4] and the c-axis charge distribution in high-stage compounds (e.g. interlayer screening[5,6]). We report here a systematic survey of the temperature dependence of ρ_c for stages 1-7 potassium GIC's. We observe a crossover in the dominant transport mechanism between stages 4 and 5, as evidenced by a change from positive to negative $d\rho_c/dT$, which we attribute to interlayer screening coupled with the establishment of weak depletion regions midway between intercalant layers. We also find dramatic and systematic stage dependent anomalies in $\rho_c(T)$, from which we suggest the possibility of a new type of instability in high-stage compounds which is not simply the consequence of an order-disorder transition.[7,8]

Measurements were made with four large area gold pressure contacts to 5x5x0.6-0.8 mm^3 HOPG-based specimens, using dc or low frequency ac detection and 10 mA sample current. Data were taken for cooling and warming at rates 1-3 K/min. (00ℓ) diffractograms were checked before and after each measurement. Particular attention was paid to the low-index reflections of high stage compounds; only samples with <3% contamination from unwanted stages were retained for measurement.

Figure 1 gives an overview of all the data for stages 1-5, 7 and ∞ (i.e. HOPG); details are shown in Figs. 2 and 3. The overall dependence is metallic ($d\rho_c/dT>0$) for stages 1-4, whereas stages 5 and 7 exhibit decreasing ρ_c with increasing T, as does HOPG.[9] For stage 1 $d\rho_c/dT$ changes sign at ∿ 40K; ρ_c increases rapidly as

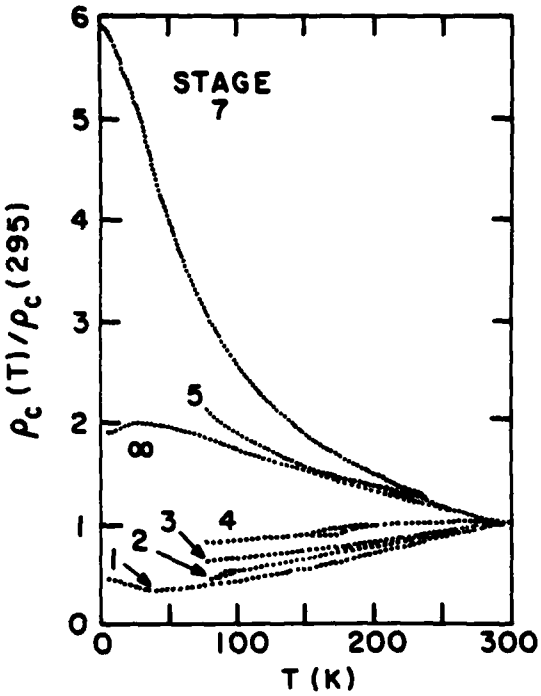

Figure 1. Normalized c-axis resistivity versus temperatures for stages 1-5 and 7 potassium GIC; data for HOPG (stage ∞) is included for comparison. Absolute values at 295K are given in Table I.

T→0 (Fig. 2), but the increase is truncated by a limiting $\rho_c(0)$ about half the 295K value. Stage 7 and HOPG also exhibit (much larger) limiting $\rho_c(0)$ values (Fig. 1); stages 2-5 were only measured down to 77K. In contrast to the $\rho_c(T)$ behavior reported here, $\rho_a(T)$ is metallic for

*Also Moore School of Electrical Engineering
+Also Physics Department

stages 1-8 and Matheissen's rule holds approximately.[10,11]

A most surprising feature of the stage 5 and 7 curves is that at low T ρ_c exceeds the HOPG value. This deduction can be made from the relative ρ_c plots of Fig. 1 because ρ_c(295K) is about the same for n=5,7 and ∞, as shown in Table I. This is inconsistent with a series resistor model for c-axis conduction[6] in which the K layer plus the highly charged bounding graphite layers have negligible resistance due to s-π overlap while the interior layers, essentially devoid of excess charge due to screening, contribute the resistance of an equal length of graphite. Note further that the enhancement of the low-T ρ_c over the HOPG value is greater for stage 7 than for stage 5, whereas in a simple view stage 7 would be the more graphite-like of the two.

All stages ≥ 2 exhibit hysteretic anomalies characteristic of first order transitions (Figs. 2 and 3). For stages 2-4, the anomalies are consistent with order-disorder processes; the resistivity increases discontinuously with increasing T as would be expected from excess scattering associated with disorder in the high-T phase.[12] In contrast, stages 5 and 7 have discontinuously lower ρ_c above the anomaly temperatures. Stages 2 (Fig. 2) and 3 (Fig. 3) show two anomalies in the range 77-300K while stages ≥ 4 show only one. Column 2 of Table I summarizes the locations in T and the amplitudes of the ρ_c anomalies, and columns 3 and 4 indicate the correlation or lack thereof with anomalies in ρ_a[11,12] and static susceptibility[13,14] (χ).

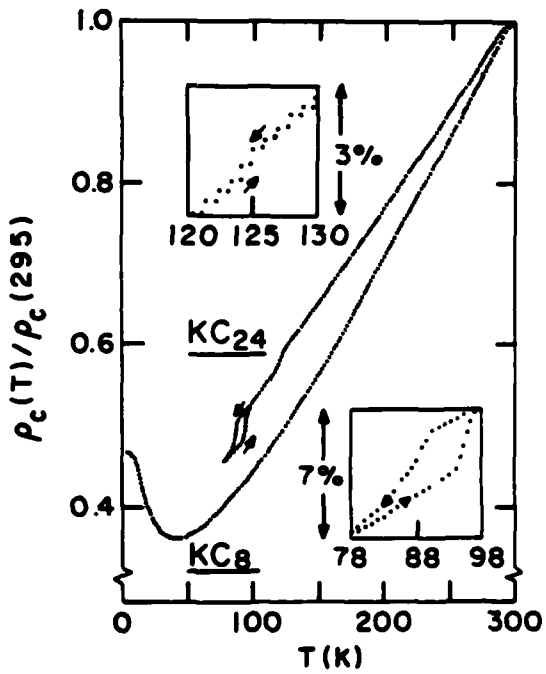

Figure 2. Expanded view of normalized ρ_c(T) for stages 1 (KC_8) and 2 (KC_{24}). The insets show details of the upper and lower KC_{24} anomalies.

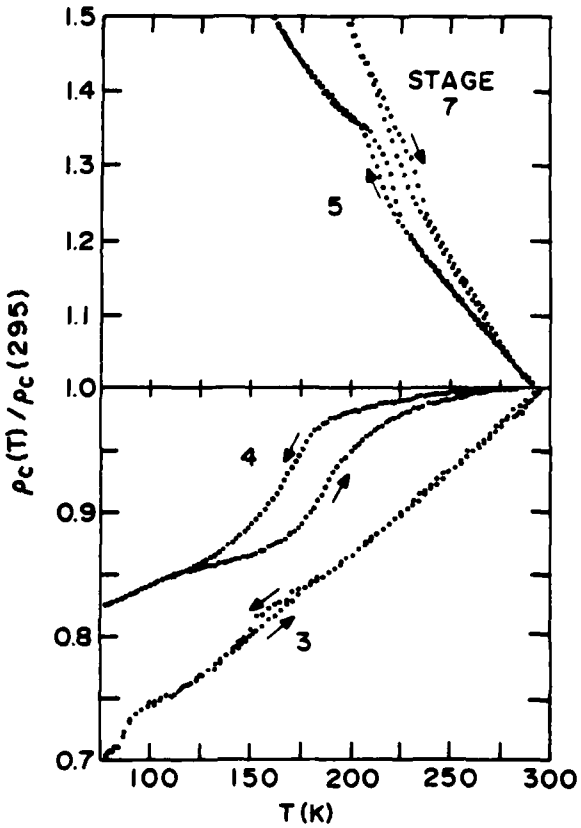

Figure 3. Expanded view of normalized ρ_c(T) for stages 3 and 4 (lower half), 5 and 7 (upper half). The two vertical scales are different.

The temperature dependence of ρ_c for KC_8 suggests the same scattering processes as in ρ_a from 50-300K: a linear -T component from electron-phonon scattering and a small T^2 component attributable to interpocket scattering (Fig. 2). The linear term dominates ρ_c to a much greater extent than ρ_a, consistent with the attribution of the quadratic term to interpocket scattering between cylindrical surfaces aligned along the c-direction.[10] The linear coefficient also appears to be smaller in ρ_c than in ρ_a, no doubt due to anisotropic electron-phonon interaction. The surprising change to activated behavior below 50K suggests localization but the magnitude of $\rho_c(0)$, 4×10^{-4} Ωcm, is still well above the minimum metallic conductivity. The upturn in ρ_c at low T is suggestive of magnetic impurity scattering via the Kondo effect, but we do not observe similar behavior in $\rho_a(T)$[10]. The upturn appears to be an intrinsic feature of the binary compound MC_8 structure since we also see it in RbC_8 but not in LiC_6 nor in $KHgC_4$. Defects introduced during intercalation are also an unlikely origin since the c-axis expansion of $KHgC_4$ relative to graphite is by far the largest of any of the materials studied. Furthermore, since $\rho_a(T)$ is metallic down to 10K, a parasitic ρ_a contribution to an

TABLE I

	ρ_c(295K) Ωcm	ρ_c anomalies	ρ_a anomaly at same T? (Refs. 11, 12)	χ anomaly at same T? (Refs. 13, 14)
KC_8 (stage 1)	0.0008	none	none	none
KC_{24} (stage 2)	0.008	92K midpoint, 6%, first order	yes, 7%	no
		125K, 1%	yes, 8%	no
KC_{36} (stage 3)	0.015	90K, 6%	yes, 10%	no
		150K, 4%	no(250K)	no
KC_{48} (stage 4)	0.05	175K midpoint, 15%, first order	no(250K)	weak
KC_{60} (stage 5)	0.15	215K midpoint, 14%, first order	?(235K)	yes
KC_{84} (stage 7)	0.17	225K midpoint, 17%, first order	yes	yes
HOPG (stage ∞)	0.14	none	none	none

otherwise metallic ρ_c could not produce a negative $d\rho_c/dT$ in the range 10-50K. One possibility is a true metal-insulator transition which is cut off by a tiny ρ_a contribution, limiting $\rho_c(0)$ to a finite value.

The gradual reduction in metallic behavior from stage 1 to 4 (Figs. 2 and 3) must be associated directly or indirectly with the increased spacing between intercalant layers. From the viewpoint of intercalant wave function overlap in the c-direction, the s-bandwidth would decrease rapidly with increasing stage, leading eventually to a diffusive or hopping process from layer to layer. The decrease in slope from stage 1 to stage 4 could be due either to a reduction in the strength of the linear-T mechanism or to the gradual emergence of a new contribution with a negative temperature coefficient. The stage 3,4 and 5 data (Fig. 1) could well represent a competition between two processes, so we focus on stage 7 for which the new effect dominates.

It is known that the free charge donated by the intercalant strongly screens the sheet of ions, leading to highly nonuniform conduction charge distribution in the c-direction[5]. This screening is qualitatively different from the Debye screening of dilute impurities in semiconductors because graphite is a semimetal and because the coulomb and band energies are nonlinear in the density of intercalant ions per unit area[5]. Thus, whereas the usual Debye length $L_D = (\varepsilon kT/2\, n_i\, q^2)^{1/2}$ would be of order 100 A (ε along $\vec{c}$ ~ 2, n_i ~ $10^{18}/cm^3$)[16], the nonlinear Thomas-Fermi calculation gives an effective decay length comparable to the carbon interlayer spacing for reasonable ion densities.[5] Since the calculation is based on the 2D graphite energy band dispersion for which $N(E_F)=0$, the free electrons and holes initially present in real 3D graphite are ignored. If this intrinsic charge participates in the screening, along with the charge transferred from the intercalant, the innermost carbon layers could become partially depleted of mobile charge. This would increase ρ_c relative to HOPG either by reducing the density of carriers available for diffusion or hopping, or by shutting off communication between adjacent screening charge tails and leaving a very small effective length with graphite charge density. Since the effective screening length is actually quite small,[5] very little thermal energy would be required to overcome the weak static electric field, leading to a less nonuniform charge distribution at high T. This in turn would improve the c-axis conduction such that ρ_c would approach the graphite value, as observed. Strictly speaking, depletion effects are impossible in either the 2D or 3D model of graphite since E_F lies at an absolute minimum in N(E) for space charge neutral material. A more appropriate model for the n contiguous carbon layers in stage n might be a 1D "cluster" of n weakly interacting monolayers[17] for which N(E) exhibits local maxima and minima versus E; with this model, a shift of E_F in either direction could reduce $N(E_F)$ below its neutral value, yielding small but observable depletion effects due to the very small initial value of $N(E_F)$.

The $\rho_c(T)$ data for stage 7 qualitatively suggest a thermally activated process but the results are not well represented by the conventional ρ_c ~ exp (a/T) activated semiconductor result nor by a power law. A reasonable fit is obtained with the strictly empirical relation $\rho_c = A \exp(-aT) + B$ yielding a characteristic temperature 1/a = 100K. Since ρ_c is not activated in the usual sense, one

should not think in terms of localized trapping levels with well-defined energies. Intuition almost demands that at some stage $\rho_c(T)$ should decrease toward the HOPG curve. The stage at which this occurs would help to define the characteristic length relevant to the c-axis transport mechanism.

Stage-by-stage comparison of ρ_c anomalies with ρ_a and χ anomalies and with structural information also suggests different phenomena in low- and high-stage compounds. All the data on KC_{24} can be interpreted rather simply (Table I). The upper anomaly at 125K is associated with the order-disorder transition of the intercalant sublattice.[18] From the standpoint of carrier scattering, the most important consequence of this transition is the liquid-like in-plane structure of the K layers above 125K. Carrier motion is expected to be sensitive to intercalant layer disorder, since epr results show that the conduction electrons interact via spin-orbit coupling with the intercalant ions.[19] This produces a substantial ρ_a anomaly at the order-disorder transition which Onn et. al. identify as a mobility effect.[12] ρ_c should be less sensitive to this transition since the I layers are uncorrelated above 125K and poorly correlated below.[18] Thus we expect, and observe, a small ρ_c anomaly. X-ray diffraction indicates that below 92K the complex stacking order of the 3D structure is rather perfect while above 95K the K-layer stacking (but not the staging) is highly faulted.[18] The ρ_a and ρ_c anomalies associated with this lower transition are comparable in magnitude, suggesting that the conduction electron wave function has sufficient extent in the $\bar{c}$-direction to sample the stacking disorder for both directions of net carrier motion. Neither transition shows up in χ.[13] These observations are all consistent with disorder-induced excess scattering as the origin of both anomalies. For stages 3 and 4 the ρ_a and ρ_c anomalies occur at different temperatures (except the lower stage 3 anomaly). Low temperature structural data is fragmentary for stage 3 and nonexistent for stages ≥ 4. Mori et. al.[20] recently observed the gradual development of 3D order upon cooling stage 3; nothing in their data suggests discontinuous behavior at the upper ρ_a and ρ_c anomalies, and they did not study the lower anomaly region, $\sim$ 90K. Stage 4 begins to show weak effects in χ, suggesting that the confusing stage 3 behavior again indicates a crossover between low- and high-stage processes.

The χ data[14] strongly suggest a new origin for the ρ_c anomalies in stages 4 and above. Some stage 4 and all stage 5 samples exhibit weak χ anomalies, while stages 6-8 show strong hysteretic anomalies which agree closely in T and width to the corresponding ρ_c anomalies (Table I). The χ anomalies consist of discontinuous increases with decreasing T, and clearly originate in the orbital contribution rather than the Pauli or core terms because they vanish with $H \perp c$ and because the orbital term dominates in high stage compounds.[21] We have previously shown that the combination of unusual band dispersion and interlayer screening produces a large paramagnetic orbital susceptibility, and that χ is extremely sensitive to the c-axis charge distribution.[21] Our earlier discussion of c-axis transport mechanisms shows that ρ_c in high-stage compounds also depends directly on the charge distribution resulting from the strongly nonlinear interlayer screening. We therefore tentatively suggest that the ρ_c and χ anomalies are associated with small but discontinuous rearrangements in the c-axis charge distributions at temperatures corresponding to the anomalies at a given stage. For stages 5 and 7 the fact that both ρ_c and χ are higher in the low-T phase is consistent with the screening argument. A small decrease in the charge density on the interior layers would simultaneously increase the contribution of those layers to χ(orbital)[21] and decrease the overlap of the tails from neighboring charge distributions. The behavior of stage 4 is borderline in this regard since the magnitude of ρ_c is still (barely) compatible with a band mechanism, its overall temperature dependence is metallic, and the χ anomaly is weak.

Our proposed c-axis charge instability could in fact be a consequence of changes in in-plane structure. Miniscule changes in the Fermi level state density associated with subtle in-plane rearrangements (even if not true 2D melting) could affect the nonlinear screening enough to produce measurable effects in χ and ρ_c. The feedback between interlayer screening and essentially 2D in-plane structural effects could be sufficient to explain the observed weak stage dependence of the transition temperature. At sufficiently high stage, a given intercalant layer plus its screening charge could undergo a coupled in-plane/interlayer transition independent of all other such assemblies; alternatively, random thermal effects could wipe out the relevant structural and/or coulomb energy differences. In any event, it will be interesting to look for other consequences of this proposal, to identify the driving force for the proposed transition, and/or to search for alternative explanations for the dramatic ρ_c and χ anomalies.

Acknowledgements: We are grateful to A.W. Moore (Union Carbide) for furnishing the HOPG, and to S.C. Moss for a preprint of Ref. 20. This work was supported by U.S. Army Contract DAAG-29-80-K0019; the LRSM Central Facilities are supported by the NSF MRL Program, DMR 79-23647.

REFERENCES

1. J.E. Fischer and T.E. Thompson, Physics Today 34, 36 (1978).
2. M.S. Dresselhaus and G. Dresselhaus, Adv. Phys. 30, 139 (1981).
3. J.E. Fischer, Mat. Sci. Eng. 31, 211 (1977).
4. C.D. Fuerst, D. Moses and J.E. Fischer, Phys. Rev. B24, 7471 (1981).
5. L. Pietronero, S. Strassler, H.R. Zeller and M.J. Rice, Phys. Rev. Lett. 41, 763 (1978).
6. J.E. Fischer, Physica 99B, 383 (1980).
7. J.E. Fischer, Comments on Sol. St. Phys. 9, 93 (1979).
8. S.A. Solin, Adv. Chem. Phys. 49, 455 (1982).
9. G.J. Morgan and C. Uher, Phil. Mag. B44, 427 (1981).
10. M.E. Potter, W.D. Johnson and J.E. Fischer, Sol. St. Comm. 37, 713 (1981).
11. D. Billaud, J.F. Mareche, E. McRae and A. Herold, Synth. Met. 2, 37 (1980).
12. D.G. Onn, G.M.T. Foley and J.E. Fischer, Phys. Rev. B19, 6474 (1979).
13. F.J. DiSalvo and J.E. Fischer, Sol. St. Comm. 28, 71 (1978).
14. F.J. DiSalvo, J.V. Waszczak and J.E. Fischer, 15th Biennial Conference on Carbon, Extended Abstracts p. 38 (Philadelphia 1981).
15. I.L. Spain, Chemistry and Physics of Carbon 8, 1 (Dekker NY 1973).
16. M. Zanini, D. Grubisic and J.E. Fischer, Phys. Stat. Sol. B90, 151 (1978).
17. N.A.W. Holzwarth, Phys. Rev. B21, 3665 (1980).
18. J.B. Hastings, W.D. Ellenson and J.E. Fischer, Phys. Rev. Lett. 42, 1552 (1979).
19. K.A. Muller and R. Kleiner, Phys. Lett. 1, 98 (1962).
20. M. Mori, S.C. Moss and Y.M. Jan, preprint.
21. F.J. DiSalvo, S.A. Safran, R.C. Haddon, J.V. Waszczak and J.E. Fischer, Phys. Rev. B20, 4883 (1979); S.A. Safran and F.J. DiSalvo, ibid B20, 4889 (1979).

PHYSICAL REVIEW B VOLUME 25, NUMBER 6 15 MARCH 1982

Theoretical investigation of the electronic properties of potassium graphite

D. P. DiVincenzo and S. Rabii
Department of Electrical Engineering and Science, Moore School of Electrical Engineering, University of Pennsylvania, Philadelphia, Pennsylvania 19104
(Received 31 August 1981)

We present the results of a band-structure calculation for the first-stage graphite-intercalation compound of potassium, KC_8. A modified Korringa-Kohn-Rostoker formalism which was applied successfully to LiC_6 has been used. To good approximation, the KC_8 bands are given by those of two-dimensional graphite folded into the smaller Brillouin zone of KC_8, with $\frac{1}{8}$ of an extra electron per C atom. The K $3p$ states lead to a dispersionless set of bands 14 eV below the Fermi level, and the K $4s$ states create an isotropic, parabolic band with a minimum 1.8 eV above E_F. Hybridization of K states with the filled C bands is fairly weak but has a noticeable effect on the band dispersion at the Fermi level. From our band calculation we extract the KC_8 density of states, the Fermi surface, de Haas–van Alphen frequencies and masses, and plasma frequencies. We find fairly good agreement with the experimental de Haas–van Alphen frequencies, but our calculated density of states at the Fermi level is smaller than that obtained from low-temperature specific heat. We compare our work with other experimental and theoretical studies of KC_8.

I. INTRODUCTION

The intercalation compounds of graphite are highly anisotropic metals which consist of a regular array of n carbon planes separating planes of some foreign species (e.g., Li, K, AsF_5, $SbCl_5$, Br_2), n denoting the stage of the compound. These compounds have been the object of great experimental and theoretical interest in recent years[1–4] because of the tremendous chemical variety they offer, because of the different ordered phases which they display, and because of the unique competition in their binding properties between covalent, metallic, and electrostatic.

This paper presents the results of a band-structure calculation for the saturated intercalation compound of potassium, first-stage potassium graphite, KC_8. We have been motivated by the successful earlier calculation for first-stage lithium graphite, LiC_6,[5] by the availability of other theoretical studies[6,7] of KC_8, and by the question of the degree of occupancy of the K s band. By applying the identical modified Korringa-Kohn-Rostoker (KKR) formalism to KC_8 as was used for LiC_6, we hope to follow the chemical and structural trends for different members of the alkali metals and to provide a further test of the formalism. KC_8 has the additional advantage that, besides LiC_6, it is structurally one of the simplest and best characterized intercalation compounds. Also, KC_8 has been particularly well studied by a variety of experimental techniques. Many of these experiments have been interpreted in terms of the previous theoretical band-structure calculations[6,7] on KC_8. We will provide a thorough reexamination of these measurements in light of the present work.

The remainder of our paper is organized as follows. Section II discusses the crystal structure and symmetry of KC_8 and the model one-electron potential which we use. Section III presents the non-muffin-tin KKR formalism for the band-structure calculation. The energy bands of KC_8 are shown in Sec. IV, and Sec. V gives the KC_8 density of states, Fermi surface, plasma frequencies, and de Haas–van Alphen frequencies and masses. Section VI discusses our results in terms of a number of the experiments on KC_8.

II. CRYSTAL STRUCTURE AND POTENTIAL

The crystal structure of KC_8, shown in Fig. 1, has been firmly established by experiment.[8,9] It consists of alternate layers of potassium and car-

 ©1982 The American Physical Society

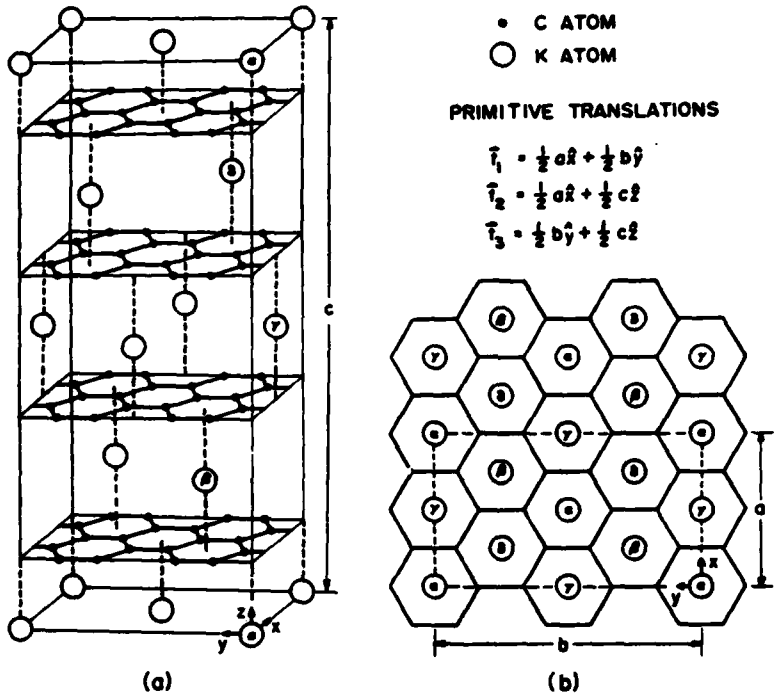

FIG. 1 (a) Conventional face-centered orthorhombic unit cell for KC_8. (b) Top view of the KC_8 structure.

bon. The carbon layers form an open hexagonal net as in pure graphite; the nearest-neighbor carbon-carbon separation is 1.42 Å. Adjacent carbon layers are in registry (*A-A* stacking) and are separated by 5.35 Å. K layers order in a triangular lattice such that a potassium atom lies above the center of every fourth carbon hexagon; that is, the potassium atoms form a 2×2 superlattice. Adjacent K layers are staggered, and begin successively at each of four possible origins denoted α, β, γ, and δ. Thus the intercalant layer sequence follows the pattern $\alpha\beta\gamma\delta\alpha\beta\gamma\delta\alpha\ldots$.

The space-group symmetry of KC_8 is *Fddd* (C_{2h}^{24}).[10,11] The Bravais-lattice type is face-centered orthorhombic. Figure 1 outlines the conventional orthorhombic unit cell, which contains four primitive unit cells. Besides translational symmetry operations, there are eight operations which leave the crystal invariant: identity, three orthogonal twofold rotations through a potassium atom, inversion, and three distinct diamond-type glide planes. The point group about each K site is 222 (D_2), and about each C site it is 1 (E), the trivial group. Each primitive unit cell contains two K atoms and 16 C atoms. The two K atoms are equivalent by symmetry. However, there are two crystallographically distinct C atoms; half of the carbons have two potassium nearest neighbors, the other half only one. All of this symmetry information is indispensable for the accurate calculation of wave functions and matrix elements (Appendix C).

The one-electron model potential is constructed by the superposition of spherically averaged atomic-charge densities for K and C. Slater's $X\alpha$ approximation to the exchange and correlation[12] is used, with Schwarz's[13] values of $\alpha=0.721\,17$ for K and $\alpha=0.759\,28$ for C. Atomic calculations are carried out using the Hartree-Fock-Slater self-consistent-field technique as developed by Herman and Skillman.[14] We use the following atomic configurations:

$$C(-\tfrac{1}{8}):\ 1s^2 2s^1 2p^{3+1/8}\,,$$

$$K(+1):\ 1s^2 2s^2 2p^6 3s^2 3p^6\,.$$

These reflect the known sp^2 hybridization of the σ bonding states of carbon and the presumed ionization of the potassium intercalant in the crystal.

III. FORMALISM

The large anisotropy of KC_8 dictates the technique which we use to solve Schrödinger's equation

for our model potential. Figure 2 shows the crystal potential at carbon and potassium sites along several directions. Even within the C and K atomic spheres this potential is highly nonspherical, and it is far from flat in the interstitial region. This discourages the use of a conventional muffin-tin (MT) approximation. We have modified the standard muffin-tin formulation of the KKR technique[15,16] to accurately calculate the eigenstates and eigenvalues of such a system. Our method, applied recently to LiC_6 (Ref. 5) and developed originally by Painter,[17] still relies on the separation of the crystal volume into muffin-tin and interstitial regions. In KC_6 the carbon muffin-tin (CMT) spheres are chosen to touch ($r_{CMT}=0.71$ Å), then the potassium muffin-tin (KMT) spheres are required to touch to carbon muffin tins ($r_{KMT}=2.34$ Å). The muffin tins contain 58% of the crystal volume. The crystal potential is then divided into two parts: $V_{cryst}(\vec{r})=V_{MT}(\vec{r})+\Delta V(\vec{r})$. $V_{MT}(\vec{r})$ is the full potential inside the muffin tins, a constant ($V_I=-0.984$ Ry) in the interstitial volume. The eigenvalues and eigenvectors for the muffin-tin part of the potential $V_{MT}(r)$ are obtained from a KKR secular equation:

$$\sum_{\vec{\tau},\vec{\tau}',m'}[\mathcal{A}^{-1}(E)^{\vec{\tau}}_{lml'm'}\delta_{\vec{\tau}\vec{\tau}'}+M(\vec{k},E)^{\vec{\tau}\vec{\tau}'}_{lml'm'}]\times w(\vec{k},E)^{\vec{\tau}}_{l'm'}=0\ . \quad (1)$$

$\mathcal{A}^{-1\vec{\tau}}_{lml'm'}$ is the inverse scattering matrix, $M^{\vec{\tau}\vec{\tau}'}_{lml'm'}$ is the structure factor matrix, $\vec{\tau}$ and $\vec{\tau}'$ index atoms in the unit cell, l,m,l',m' are angular momentum indices, and the $w^{\vec{\tau}}_{lm}$'s are the components of the KKR eigenfunction. Appendix A describes the details of this calculation. The energies and wave functions obtained from Eq. (1), E_{KKR} and $\Psi^{KKR}_n(\vec{k},\vec{r})$, are then used in a second secular equation, which takes the remainder of the crystal potential $\Delta V(\vec{r})$ into account:

$$\sum_m[(E_{KKR}-E_{final})\delta_{mn}+\Delta_{mn}(\vec{k})]C_m(\vec{k})=0\ , \quad (2)$$

where $\Delta_{mn}(\vec{k})$ is the matrix element of $\Delta V(\vec{r})$ between the KKR wave functions:

$$\Delta_{mn}(\vec{k})=\int_{\substack{\text{unit}\\\text{cell}}}\Psi^{*KKR}_m(\vec{k},\vec{r})\Delta V(\vec{r})\Psi^{KKR}_n(\vec{k},\vec{r})d\vec{r}\ . \quad (3)$$

Appendix B explains in detail the calculation of the KKR wave functions and the numerical methods used for the integral in Eq. (3). Diagonal-

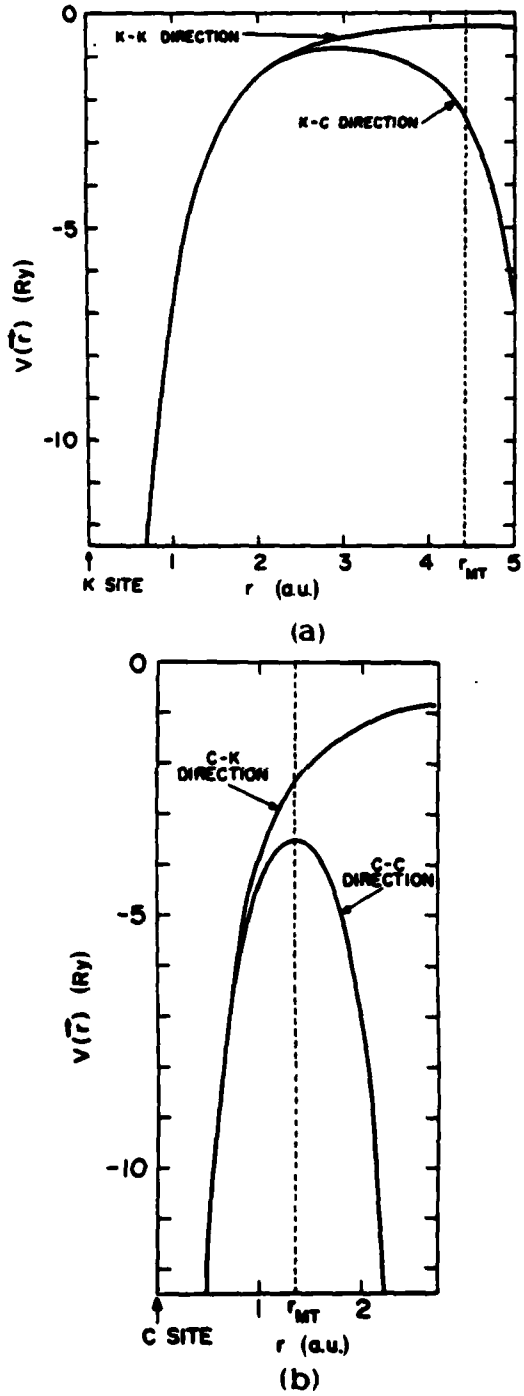

FIG. 2. Model one-electron crystal potential for KC_6 (a) around the K atom in different nearest-neighbor directions, and (b) around the C atom in different nearest-neighbor directions. The muffin-tin radii are indicated.

ization of Eq. (2) gives the final energy bands and eigenfunctions for this calculation.

IV. CALCULATED ENERGY BANDS

Equations (1)–(3) of Sec. III allow us to find the energy eigenvalues $E(\vec{k})$ for any wave vector in the Brillouin zone. In the present calculation we have determined the bands in a 40-eV energy range at the high-symmetry $\vec{k}$ points Γ, X, Y, and Z, and along the high-symmetry directions Σ, Δ, A, and B—14 points in all, as shown in Fig. 3.

Figure 4 shows the resulting band structure for KC_8. The bands are labeled according to the irreducible representation of the group of $\vec{k}$.[18] Except for the set of dispersionless K $3p$ bands at -18.9 eV, the bands drawn as solid lines up to an energy of about -10.5 eV come from the $\sigma(sp^2)$ states of graphite. Up to an energy of about -5 eV, bands derived from the π bands of graphite are dashed; above this energy, the π bands mix too much with other states to be distinguished clearly. On this band structure, the Fermi energy of graphite lies at approximately -6.8 eV.

Many of the KC_8 energy bands at and below the Fermi level can be identified with the π and σ bands of two-dimensional graphite. This identification is made clear by comparing our calculation with the KC_8 bands in the "folded-band" approximation, in which we assume that there is no interaction between the carbon layers and that the K potential is vanishingly small at the graphite planes. Under these conditions the KC_8 bands have no k_z dispersion and are simply given by the bands of two-dimensional graphite folded into the KC_8 Brillouin zone; Fig. 5 shows the result of such folding applied to Nagayoshi's[19] graphite bands. (The zeros of energy in Figs. 4 and 5 are not related.) Comparing this with our calculated KC_8 bands shows the σ band shapes to be quite similar to those of the folded bands. The 16-eV width of the σ bands is correctly predicted by Fig. 5, and the band degeneracies indicated on the folded bands correspond in each case to the same number of nearly degenerate bands in Fig. 4.

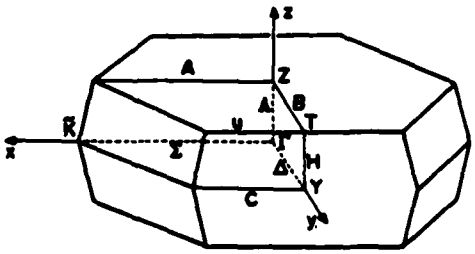

FIG. 3. Brillouin zone of KC_8. Special points and lines are labeled according to Ref. 18.

A closer comparison of the KC_8 bands with the folded two-dimensional graphite levels also reveals important differences. While the lowest-energy π bands of KC_8 have the same shape as those of graphite, the position of the π bands relative to the σ bands is about 2 eV lower than in graphite. This is consistent with the expectation that the energy of the π states, which extend away from the carbon layer, will be lowered by the attractive potassium potential. Around the Fermi level, the presence of potassium also has a significant effect on the π band shapes, and the splittings of degenerate graphite levels are greater than 1 eV. The effective masses of the π bands starting as Γ_1^+ and Γ_2^+ states at about -5.1 eV are reversed from negative to positive by the interaction with potassium states. For energies higher than -4 eV, the picture of the KC_8 bands as slightly perturbed graphite states breaks down completely.

Besides disturbing the carbon eigenstates, potassium introduces entirely new bands which originate from K atomic levels. The core $3p$ states of potassium manifest themselves as a set of six almost flat bands at -19 eV. Although they lie within the σ bands, they interact very little with the carbon planes and remain corelike. The valence $4s$ level of potassium appears as a parabolic band with its minimum, Γ_1^+ at -3.5 eV, about 1.8 eV above the Fermi level. The band starting at the Γ_1^- level at -2.9 eV is another piece of the K $4s$ band arising from folding in the k_z direction. Although these bands interact significantly with graphite levels, particularly along the Σ direction, they largely retain their K s identity throughout the Brillouin zone. In contrast to the graphite state, the K $4s$ bands have significant dispersion in the k_z direction, which is consistent with their metallic, isotropic, plane-wave character.

V. FERMI-LEVEL PROPERTIES

In order to obtain the shape of the Fermi surface and calculate the optical properties of KC_8, we need to know the energy bands on a fine mesh in the Brillouin zone. It is, however, not feasible to use an *ab initio* approach for this purpose. Therefore, we have fitted a tight-binding model to our

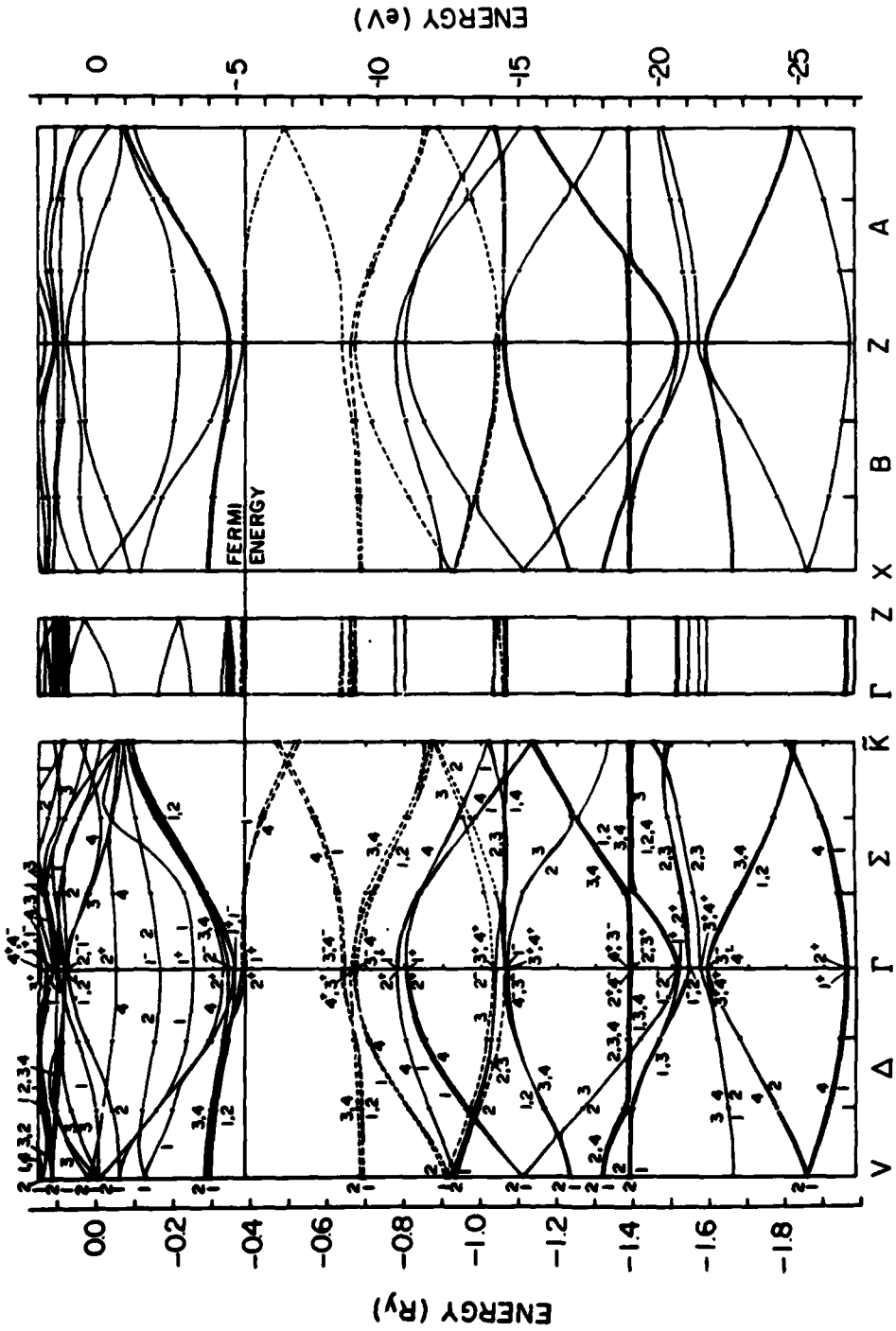

FIG. 4. Energy-band structure for KC_8 along several high-symmetry directions in the Brillouin zone. Bands drawn solid correspond to predominantly σ graphite states, except for the K $3p$ levels at -18.9 eV. Bands derived from the π states of graphite are shown dashed up to -5 eV. The minimum of the K $4s$ band is the Γ_1^+ state at -3 eV.

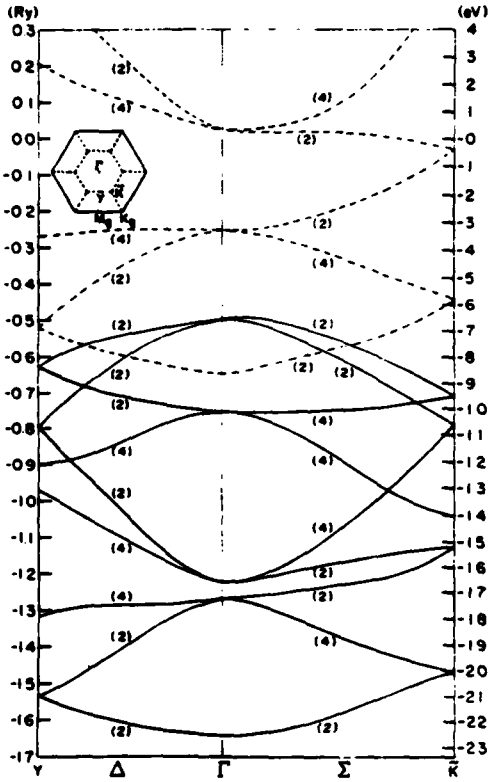

FIG. 5. Energy bands of two-dimensional graphite (Ref. 19) folded into the smaller Brillouin zone of two-dimensional KC_8. σ bands are solid lines, π band dashed. The inset shows the relationship between the graphite and KC_8 zones.

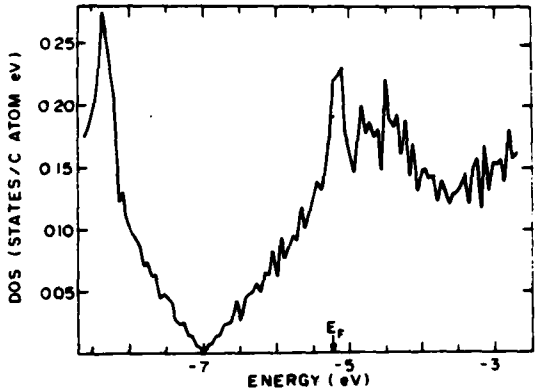

FIG. 6. Density of states of KC_8 as determined by an LCAO fit to the first-principles energy bands (Fig. 4).

KKR results. This model uses C π and K s orbitals and includes first-, second-, and third-neighbor interactions between in-plane carbons, one carbon-carbon interplane interaction, nearest-neighbor C-K interactions, and first- and second-neighbor K-K interactions. The two-center approximation is used in this calculation.[20] These matrix elements (13 in all) were adjusted to minimize the disagreement with the *ab initio* KKR calculation near the Fermi level. The resulting fit matched all the C π bands and K s bands to within 0.3 eV, and agreed with the KKR bands in the vicinity of the Fermi energy to within 0.005 eV.

The simplicity of this linear combination of atomic orbitals (LCAO) model allows us to accurately determine the KC_8 density of states, Fig. 6. This calculation uses the histogram method to do the density sum on 31 004 points in the Brillouin zone, with an energy resolution of 0.06 eV. This density of states is very similar to that of pure graphite[21] with the band minimum at -6.9 eV and the peaks due to the saddle points at M at -8.6 and -5.0 eV. The K 4s band shows a sharp onset in the density of states at about -3.0 eV. By integrating this density of states, we determine the Fermi level shown, $E_F = -5.23$ eV. This lies about 1.4 eV above the graphite Fermi level, near the upper M point peak in the density of states. The 4s metal band lies about 1.8 eV above E_F. According to this calculation, the density of states at the Fermi energy is 0.2 states/C atom eV; the value observed from specific-heat measurements[22] is 0.33 states/C atom eV. We will examine this discrepancy in Sec. IV. We have also used the LCAO fit to the KC_8 bands to calculate the Fermi surface, shown in Fig. 7. The surface consists of two electron sheets centered at each of the six corners of the Brillouin zone. The sheets are roughly triangular and show rather small dispersion in the k_z direction, in reasonable agreement with the Fermi surface in the two-dimensional rigid-band model.[5] Even though the metal band is completely empty in our calculation, there is the possibility of a third pocket of the Fermi surface centered at the Γ point in the Brillouin zone resulting from the distortion of the π bands caused by interaction with K s band. To within the accuracy of our calculation, the Γ_2^+ level is degenerate with the Fermi level; therefore, our calculation is unable to determine whether that portion of the C π band will contribute a Fermi-surface pocket, or how large it will be. We can establish bounds on the size of the sheet: Taking the overall accuracy of our calculation to be 0.1 eV, this portion of the

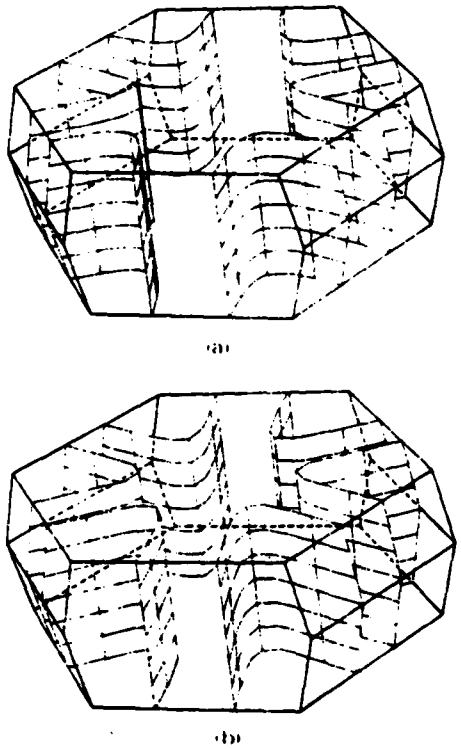

FIG. 7. (a) Lower and (b) upper band Fermi surfaces of KC_8 as derived from our LCAO interpolation of the KC_8 bands.

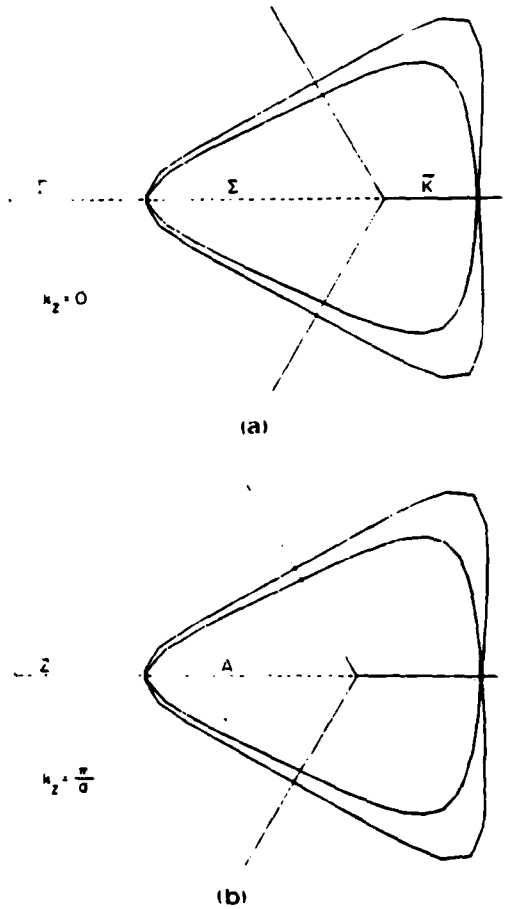

FIG. 8. Extremal cross sections of the Fermi surfaces in the (a) $k_z=0$ plane and (b) in the $k_z=\pi/c$ plane.

Fermi surface will be spheroidal and will contain no more than 0.06 electrons. In the present calculation, it is unlikely that this pocket of the Fermi surface will connect to the other sheets centered at the corners of the Brillouin zone. The presence or absence of this portion of the Fermi surface could have observable effects, as we shall discuss later.

Figure 8 shows the extremal cross sections of the Fermi surface normal to the k_z direction. There are two orbits in the $k_z=0$ plane and two in the $k_z=\pi/c$ plane. These orbits do not have trigonal symmetry as predicted by the rigid-band model because of the details of the three-dimensional stacking of the K layers (i.e., the fact that the crystal structure is orthorhombic rather than hexagonal). For each of these orbits, we can calculate the de Haas–van Alphen frequencies and masses.[5,23] As shown in Table I, these frequencies are very close together, reflecting the two dimensionality of the Fermi surface. These frequencies compare fairly well with the single observed de Haas–van Alphen frequency in KC_8, 2.9×10^7 G.[24]

The partly filled Cπ band makes an intraband contribution to the dielectric tensor, which for infinite lifetime carriers is of the form

$$\epsilon_{ij}(\omega)=1+\frac{(\omega_{ij})^2}{\omega^2}\ . \tag{4}$$

The plasma-frequency tensor is given by an integral over the Fermi surface.[25] Because of the orthorhombic symmetry of KC_8, the plasma frequency has three independent components ω_{xx}, ω_{yy}, and ω_{zz}. Measurements on highly oriented pyrolitic graphite (HOPG) intercalation compounds are only capable of measuring two components: $\omega_c=\omega_{zz}$ and $\omega_a^2=\frac{1}{2}(\omega_{xx}^2+\omega_{yy}^2)$. We have calculated all of these and show them in Table I. The anisotropy of the plasma frequency is very large, $\omega_a/\omega_c\simeq10^4$. Although the exact value of this ra-

TABLE I. Calculated Fermi-level density of states, plasma frequencies, and de Haas–van Alphen frequencies and masses for KC_8.

	Lower band	Upper band	Total
$N(E_F)$ (states/C atom eV)			0.2
ω_{xx} (eV)	3.0	3.0	4.3
ω_{yy} (eV)	3.2	3.5	4.7
$\omega_{zz}=\omega_c$ (meV)	0.27	0.10	0.29
ω_e (eV)	3.1	3.3	4.5
dHvA frequencies (G)			
$k_z=0$ plane	3.7×10^7	4.7×10^7	
$k_z=\pi/c$ plane	3.7×10^7	4.7×10^7	
dHvA masses (me)			
$k_z=0$ plane	0.58	0.70	
$k_z=\pi/c$ plane	0.58	0.70	

tio cannot be determined with great precision by our LCAO fit, it is certainly much greater than the value $\omega_d/\omega_c\simeq8$ which Zanini and Fischer[26] have derived from polarized reflectance measurements.

VI. DISCUSSION AND CONCLUSIONS

Many recent experiments on KC_8 have been interpreted using the calculated band structure of Inoshita *et al.*[6] and Ohno *et al.*[7] A comparison of the results of the present study with their results shows that although the positions of the bands near the Fermi level generally agree to within about 0.5 eV, nevertheless the Fermi surfaces are topologically quite different. In particular, the earlier work has a Fermi surface containing both cylindrical pieces at the zone corners and spherical pieces at the zone center, and these pieces are partially connected. The present studying contains cylindrical parts with at most a very small, isolated pocket at Γ.

Several of the experiments on KC_8 suggest that states at the Fermi energy have Ks character. We caution, however, that having Ks states at the Fermi level could result either from a partially filled metal band or hybridization of metal s states with the Cπ bands near E_F. Many experiments which are capable of detecting deviations from rigid-band behavior cannot distinguish between these possibilities. With this in mind, we now review the experimental data and their interpretation in light of the present calculation.

The density of states at the Fermi energy as determined by low-temperature specific-heat measurements[22] is, as mentioned earlier, substantially higher that what we predict. Inoshita *et al.*'s calculated result, $N(E_F)=0.27$ states/C atom eV is significantly closer to the measured value, although the discrepancy is still substantial. An attempt to account for this discrepancy by a specific-heat enhancement from the electron-phonon interaction was unsuccessful.[6] An estimate of $N(E_F)$ may also be made from magnetic susceptibility measurements on KC_8.[26] The total susceptibility was found to be $\chi^c=138\times10^{-6}$ cm^3/mole. An estimate of the core diagmagnetic contribution to χ^c was given as $\chi^0=-52\times10^{-6}$ cm^3/mole, and the orbital susceptibility as obtained from a tight-binding-model calculation[27] was $\chi^{or}=73\times10^{-6}$ cm^3/mole for unit charge transfer. Using these estimates, the Pauli susceptibility may be extracted: $\chi_p=\chi^c-\chi^0-\chi^{or}=117\times10^{-6}$ cm^3/mole. This corresponds to $N(E_F)=0.45$ states/C atom eV, well above the value obtained from specific-heat measurements or from electronic structure calculations. Recent spin-susceptibility measurements on LiC_6 suggest[28] that the problem is that the calculated χ^{or} is too small by a factor of 2. Although this leads to a more reasonable prediction for $N(E_F)$, it is clear that susceptibility cannot presently provide a reliable prediction for the density of states in KC_8.

Measurements of the de Haas–van Alphen effect in KC_8 are quite difficult because of sample quality and the high frequency of the predicted extremal orbits. The one successful experiment[24] has observed a single frequency at 2.9×10^7 G. This is in reasonable agreement with either the extremal orbit frequencies reported here or the extremal orbit of the zone-edge piece of the Fermi surface of Inoshita *et al.*[6] Their calculation, unlike ours, predicts a number of lower frequencies which have

not been reported.

Several measurements of the visible and near-infrared reflectivity of KC_8 have been reported.[29,30] For $\vec{E} \perp c$, a high ($\simeq 95\%$) reflectivity is observed up to about 2.2 eV, then a sharp drop with a minimum at 2.5 eV. This, of course, supports the accepted view of KC_8 as a metal, and the plasma frequency obtained from a Drude fit to this reflectivity, $\omega_p = 3.5$ eV, is in rough agreement with the $\vec{E} \perp c$ plasma frequency calculated here, $\omega_e = 4.5$ eV. However, it was also found that a much better fit was obtained by including two Drude terms, suggesting that there are two different types of carriers in the KC_8 conduction bands. Similar Drude fits to reflectance measurements with $\vec{E} \| c$ suggest that one of these two types of carriers is rather isotropic. These conclusions, although model dependent, lead to a reasonable prediction of the small anisotropy of the electrical conductivity in KC_8 ($\sigma_a/\sigma_c \simeq 34$).[31] Therefore, reflectivity data lend strong support to a partially filled K s band as suggested by Inoshita and Ohno and co-workers. We believe that much more detailed and definitive information could be extracted from reflectivity measurements if the dielectric function could be obtained from Kramers-Kronig analysis.

The Hall coefficient is very small in KC_8 ($n_H = -1/R_H e = 7.8 \times 10^{22}$ cm^{-3} at room temperature[30]), and it changes sign from n type to p type between room temperature and 4 K.[32] Since the Fermi surface of Inoshita *et al.* contains both hole and electron orbits from a free-electron model, it has been inferred that it is capable of explaining the Hall data, and that the rigid-band Fermi surface (or that of the present study), which contains only electron orbits, is not. However, taking into account the curvature of the Fermi surface, as is important at low fields, within a simple model,[33] the small value of R_H at low temperatures can be explained. In fact, a much more sophisticated analysis would be required to predict the T dependence of the Hall data.

Several independent electron energy-loss measurements have been performed on KC_8. Hwang and co-workers[34] have measured the electron energy-loss (EEL) spectrum up to 40 eV, and have extracted the loss function and dielectric function. The resulting $\epsilon_2(\omega)$ shows that the strong interband transition at 4.5 eV at the M point still appears in KC_8, but is shifted down to about 3.8 eV and broadened. As we have remarked previously,[35] and as shown in Table II, this structure at 3.8 eV can be identified successfully with a set of interband critical transitions at Γ in our KC_8 band structure. Recent EEL measurements by Ritsko[36] have also provided loss function and dielectric constant data for 0.2–300 eV. In these experiments the core excitation spectrum of C 1s electrons has been used to probe the nature of states near the Fermi level. These spectra are found to be much more complex for KC_8 than for LiC_6. Since LiC_6 is agreed to have only C π states at the Fermi level, it has been argued that KC_8 must therefore have metal s states at the Fermi level resulting either from a partially occupied K band or π-s hybridization. This conclusion cannot be considered firm, however, until the effect of the core exciton[37] is accounted for. In any case, the interpretation of both EEL experiments would be greatly aided by a theoretical calculation of the dielectric function from the band structure.

TABLE II. Optical selection rules and principle low-energy critical-point transitions at the Γ point in KC_8.

Optical selection rules at Γ	
$1+ \parallel 3-$	$2+ \perp 1-$
$1+ \parallel 4-$	$4+ \parallel 2-$
$1+ \perp 2-$	$4+ \parallel 1-$
$3+ \parallel 1-$	$4+ \perp 3-$
$3+ \parallel 2-$	$2+ \parallel 4-$
$3+ \perp 4-$	$2+ \parallel 3-$
Transition at Γ	**ΔE (eV)**
$4- \rightarrow 2+$	3.4
$4- \rightarrow 1+$	3.5
$3- \rightarrow 2+$	3.5
$4+ \rightarrow 1-$	3.8
$3+ \rightarrow 1+$	3.9
$3+ \rightarrow 1-$	4.1
$4+ \rightarrow 1-$	4.2
$3+ \rightarrow 2-$	4.3
$4+ \rightarrow 2-$	4.5
$3- \rightarrow 2+$	4.7
$4- \rightarrow 2+$	4.8

Oelhafen and co-workers have performed a careful systematic study of ultraviolet photoemission spectroscopy (UPS) spectra for the alkali-metal–intercalation compounds.[38] The shape of their photoemission spectrum near the Fermi energy for KC_8 is similar to the density of states presented here. However, their analysis of the shape of the spectra as a function of the exciting photon energy provides a strong indication that K s states lie below E_F. They have also supported this

view with positron annihilation studies.[39] Still, a similar UPS analysis, which they have performed on second-stage potassium graphite KC_{24}, also indicates that only partial charge transfer has occurred. This is in disagreement with the interpretation of a polarized reflectance measurement on KC_{24} by Zanini and Fischer,[29] which implies that there has been full charge transfer from the K layer.

So, it appears that, while the evidence provided by experiments on KC_8 is not conclusive, it is necessary to consider the possibility that charge transfer from the potassium layers is not complete, and that states with K s character exist close to the Fermi level. Since the present calculation does not predict partial charge transfer we must understand why it does not and whether our conclusions could be affected by any of the approximations of our calculation. In fact, there is evidence that if the approximations made for the crystal potential in the present calculation could be lifted, then the topology of the Fermi surface and the nature of the Fermi-level states could be modified. This evidence is provided by a new calculation[40] for LiC_6 using a self-consistent potential and with the Hedin-Lundqvist local approximation to the exchange and correlation potential. Previous theoretical work[5,41] on LiC_6 used a non-self-consistent potential with $X\alpha$ exchange and correlation as in the present paper. Comparing the two different calculations on lithium graphite shows that the minimum of the metal s band is about 1 eV lower in the new work than in the original KKR calculation. Although a similar self-consistent-field calculation for KC_8 has not been completed, presumably the K 4s band will also be lower when self-consistency and different exchange and correlation are used. If the metal band lies closer to the Fermi level, it may be expected to hybridize more with states at the Fermi energy. Moreover, since the π bands are very flat at E_F, any distortions of the bands due to hybridization could have large effects on the shape of the Fermi surface. A further lowering of the Γ_2^+ level lying at the Fermi level, for example, could introduce a new portion of the Fermi surface at Γ, changing the topology of the Fermi surface.

Despite these possible difficulties, our calculation should be judged successful on several points. The validity of the rigid-band model as a global description of the filled valence bands of first-stage potassium graphite has been established. At the same time, it has been demonstrated that small deviations from the rigid-band model near the Fermi level can lead to both qualitative and quantitative deviation from the rigid-band predictions. The present calculation predicts for the first time the position of the K 3p core states with respect to the Fermi level, and confirms the picture of the K 4s band as isotropic and free-electron-like. For the theoretician, our calculation provides another demonstration that modified muffin-tin techniques of band calculation can be used successfully for highly anisotropic materials.

Note added in proof. Recent work on KC_8 by Ritsko and Brucker[48] combining EEL and UPS measurements suggest a peak in the K s density of states of 2.0–2.5 eV above E_F, in good agreement with the present calculation.

ACKNOWLEDGMENTS

We thank Robert C. Tatar and Natalie Holzwarth for their constant interest in this work, for their help in performing the calculations, and for their critical reading of this manuscript. Thanks also to John E. Fischer and the graphite group at Penn for many stimulating discussions. We are grateful to the Moore School Computing Facility for the use of their Univac 90/70 computer. This work was supported by the NSF, MRL program under Grant No. DRM-7923647, by ARO Contract No. DAAG/29/80/K/0019, and by the IBM predoctoral fellowship program.

APPENDIX A: MODIFIED KKR FORMALISM

In this appendix we present the expressions used to evaluate the KKR secular matrix, Eq. (1). The Hamiltonian matrix elements $\mathcal{A}^{-1}$ and M are straightforward extensions of what has appeared in the literature,[16,42] generalized for many atoms per unit cell and for nonspherical muffin-tin potentials.

$\mathcal{A}^{-1}(E)$, the KKR scattering or reaction matrix, measures the strength of scattering of partial waves of energy E at the muffin-tin boundary. It is given by the expression

$$\mathcal{A}^{-1}(E)^{\vec{\tau}}_{lmr'm'} = \sum_{LM} [\mathcal{N}^{-1}]^{\vec{\tau}}_{LM,lm} \mathcal{S}^{\vec{\tau}}_{\tau'm',LM} , \tag{A1}$$

where

$$\mathcal{N}^{\vec{\tau}}_{LM,lm} = \left[R^{\vec{\tau}}_{LM,lm}(E,\vec{r}) \frac{dn_l(\kappa r)}{dr} - \frac{dR^{\vec{\tau}}_{LMlm}(E,\vec{r})}{dr} n_L(\kappa r) \right] \kappa r^2 \Big|_{r=r^{\vec{\tau}}_{MT}} , \tag{A2}$$

and

$$\mathcal{J}^{\vec{\tau}}_{l'm'LM} = \left[R^{\vec{\tau}}_{l'm'LM}(E,\vec{r}) \frac{dj_L(\kappa r)}{dr} - \frac{dR^{\vec{\tau}}_{l'm'LM}(E,\vec{r})}{dr} j_{l'}(\kappa r) \right] \kappa r^2 \Big|_{r=r^{\vec{\tau}}_{MT}} . \tag{A3}$$

$n_l(\kappa r)$ is the Neuman function, $j_l(\kappa r)$ is the spherical Bessel function, and $R^{\vec{\tau}}_{lmLM}(E,\vec{r})$ is the solution to the radial Schrödinger equation at site $\vec{\tau}$:

$$\sum_{Lm} \left\{ \delta_{ll'}\delta_{mm'} \left[-\frac{\hbar^2}{2m}\frac{d^2}{dr^2}[rR^{\vec{\tau}}_{lml'm'}(E,\vec{r})] + \left[\frac{\hbar^2 l(l+1)}{r^2} - E \right] rR^{\vec{\tau}}_{lml'm'}(E,\vec{r}) \right] \right.$$
$$\left. + rR^{\vec{\tau}}_{lml'm'}(E,\vec{r}) \int Y^*_{l'm'}(\hat{r}) V_{cryst}(\vec{r}) Y_{lm}(\hat{r}) \hat{dr} \right\} = 0 . \tag{A4}$$

$\hat{dr}$ indicates an angular integral about site $\vec{\tau}$. We solve (A4) for $l \leq 2$ by the Noumerov technique.[43,44] Full use of group theory is made, so that (A4) is evaluated for the minimum number of different sites $\vec{\tau}$, and for the minimal set l,m,l',m' (see Appendix C).

The structure matrix $M(\vec{k},E)$ is a purely geometrical quantity which describes the projection of a partial wave at site $\vec{\tau}$ onto another partial wave at another site $\vec{\tau}'$. It is given by

$$M^{\vec{\tau}\vec{\tau}'}_{lml'm'}(\vec{k},E) = \sum_{\vec{T}}{}' e^{i\vec{k}\cdot(\vec{\tau}'-\vec{\tau}+\vec{T})} N_{lml'm'}(\vec{\tau}-\vec{\tau}'-\vec{T}) , \tag{A5}$$

where $\vec{T}$ is a real lattice vector, and the prime indicates the exclusion of the $T=0$ term. $N_{lml'm'}$ is given by

$$N_{lml'm'}(\vec{r}) = 4\pi i^{(l-l')} \sum_{LM} i^{-L} n_L(\kappa r) Y^*_{LM}(\hat{r}) \int Y^*_{lm}(\hat{r}') Y_{LM}(\hat{r}') Y_{l'm'}(\hat{r}') \hat{dr}' . \tag{A6}$$

κ is the scalar wave vector $(2m|E|/\hbar^2)^{1/2}$ and n_L is again the Neumann function. In practice, the real space sum in (A5) converges too slowly for practical calculations. We therefore apply the Ewald procedure[16] to (A5), transferring part of the sum into reciprocal space. The result is

$$M^{\vec{\tau}\vec{\tau}'}_{lml'm'} = -4\pi i^{(l-l')} \sum_{L,M} i^{-L} (\mathcal{A}^{\vec{\tau}\vec{\tau}'(1)}_{LM} + \mathcal{A}^{\vec{\tau}\vec{\tau}'(2)}_{LM} + \mathcal{A}^{\vec{\tau}\vec{\tau}'(3)}_{LM}) C^{LM}_{lml'm'} , \tag{A7}$$

where

$$\mathcal{A}^{\vec{\tau}\vec{\tau}'(1)}_{LM} = \frac{4\pi i^L}{V_{UC}\kappa^{L+1}} \sum_{\vec{G}} e^{i(\vec{k}+\vec{G})\cdot(\vec{\tau}-\vec{\tau}')} Y^*_{LM}\left[\frac{\vec{k}+\vec{G}}{|\vec{k}+\vec{G}|} \right] \frac{(\vec{k}+\vec{G})^2 e^{[E-(\vec{k}+\vec{G})^2]/\eta}}{(\vec{k}+\vec{G})^2 - E} , \tag{A8}$$

$$\mathcal{A}^{\vec{\tau}\vec{\tau}'(2)}_{LM} = \frac{1}{\sqrt{4\pi}} \left[\frac{\kappa}{2} \right]^L \sum_{\vec{T}}{}' |\vec{\tau}-\vec{\tau}'+\vec{T}| Y^*_{LM}\left[\frac{\vec{\tau}-\vec{\tau}'+\vec{T}}{|\vec{\tau}-\vec{\tau}'+\vec{T}|} \right] e^{i\vec{k}\cdot\vec{T}}$$
$$\times \frac{1}{\sqrt{\pi}} \left[\frac{E}{4} \right]^{L+\frac{1}{2}} \int_0^{E/\eta} u^{-3/2-L} e^{u-E(\vec{\tau}'-\vec{\tau}+\vec{T})^2/4u} du , \tag{A9}$$

$$\mathcal{A}^{\vec{\tau}\vec{\tau}'(3)}_{LM} = \frac{\sqrt{\eta}}{2\pi\kappa} \sum_{n=0}^{\infty} \frac{1}{n!(2n-1)} \delta_{\vec{\tau}\vec{\tau}'} \delta_{L0} \delta_{M0} , \tag{A10}$$

and

$$C^{LM}_{lml'm'} = \int \hat{dr}' Y^*_{lm}(\hat{r}') Y_{LM}(\hat{r}') Y_{l'm'}(\hat{r}') . \tag{A11}$$

V_{UC} is the volume of the real-space unit cell. For $\eta = 0.22$, the sums converge in a few hundred terms, which is quite practical for actual calculations. The KKR eigenvalues are given by the roots of the equation

$$\det\,[\mathcal{A}^{-1}(E_{\rm eig})+M(\vec{k},E_{\rm eig})]=0\,. \tag{A12}$$

We show the resulting $E_{\rm eig}(\vec{k})$ in Fig. 9. This 82×82 determinant can often be blocked diagonalized by using symmetry (see Appendix C).

The eigenvectors of the secular matrix at the energies $E_{\rm eig}$, $w_{lm}^{\vec{\tau}}$, give the KKR wave functions within the interstitial region:

$$\Psi_n^{\rm KKR}(\vec{k},\vec{r})=\sum_{\vec{\tau},l,m} w_{nlm}^{\vec{\tau}} \sum_{\vec{T}} e^{i\vec{k}\cdot(\vec{\tau}+\vec{T})}\left[-n(\kappa|\vec{r}-\vec{\tau}-\vec{T}|)Y_{lm}\left[\frac{\vec{r}-\vec{\tau}-\vec{T}}{|\vec{r}-\vec{\tau}-\vec{T}|}\right]\right]. \tag{A13}$$

Again, a more rapidly convergent expression is obtained using a Ewald decomposition:

$$\begin{aligned}\Psi_n^{\rm KKR}(\vec{k},\vec{r})=&\frac{4\pi}{V_{\rm UC}\kappa}\sum_{\vec{G}} e^{i(\vec{k}+\vec{G})\cdot\vec{r}}\frac{\exp\{[\kappa^2-(\vec{k}+\vec{G})^2]/\eta\}}{(\vec{k}+\vec{G})^2-\kappa^2}\sum_{\vec{\tau},l,m} i^{-l}e^{-i\vec{G}\cdot\vec{\tau}}\left[\frac{|\vec{k}+\vec{G}|}{\kappa}\right]^l Y_{lm}\left[\frac{\vec{k}+\vec{G}}{|\vec{k}+\vec{G}|}\right]w_{nlm}^{\vec{\tau}}\\ &+\frac{1}{4\pi}\sum_{\vec{T},\vec{\tau},l,m} e^{i\vec{k}\cdot(\vec{\tau}+\vec{T})}\int_0^{\kappa^2/\eta}\exp\left[u-\frac{u^2|\vec{r}-\vec{\tau}-\vec{T}|^2}{4u}\right]u^{-3/2-l}du\\ &\times\left[\frac{\kappa|\vec{r}-\vec{\tau}-\vec{T})}{2}\right]^l Y_{lm}\left[\frac{\vec{r}-\vec{\tau}-\vec{T}}{|\vec{r}-\vec{\tau}-\vec{T}|}\right]w_{nlm}^{\vec{\tau}}\,.\end{aligned} \tag{A14}$$

An Ewald parameter of $\eta=0.8$ was found to give the best results. Equation (A14) provides a starting point for the calculation of the matrix elements of ΔV (Appendix B).

APPENDIX B: CALCULATION OF NON-MUFFIN-TIN CORRECTIONS

In this appendix we give the details of the evaluation of the matrix element of the residual crystal potential $\Delta V(r)$ between KKR wave functions $\Psi_n^{\rm KKR}(\vec{k},\vec{r})$. The calculation of the KKR wave functions is outlined in Appendix A, and $\Delta V(\vec{r})$ is determined by subtracting the constant muffin-tin potential $V_{\rm MT}$ from the model crystal potential $V_{\rm cryst}(\vec{r})$ in the interstitial region. Because of the symmetry of the wave vectors,[18] we were able to do the integral of Eq. (3) in $\frac{1}{8}$ or at most $\frac{1}{4}$ of the unit cell (see Appendix C). Also, since $\Delta V(\vec{r})$ is zero within the muffin tins, the integral is restricted to the interstitial region. This is not much of an advantage, because, as Fig. 10 shows, this integration region is highly irregular.

We adopted a very straightforward procedure for evaluating $\Delta_{nn'}$; we approximated Eq. (3) by

$$\Delta_{nn'}(\vec{k})=\sum_i w_i\Psi_n^{\rm KKR*}(\vec{k},\vec{r}_i)\Delta V(\vec{r})\Psi_{n'}^{\rm KKR}(\vec{k},\vec{r}_i)\,, \tag{B1}$$

where w_i are the weights of the integration points r_i. These points are chosen using a one-dimensional Gaussian quadrature algorithm[45] applied successively in the three coordinate directions; that is,

$$\int f(\vec{r})d\vec{r}\simeq\sum_i w_i^x\left[\sum_j w_j^y\left[\sum_k w_k^z f(x_i,y_j,z_k)\right]\right]. \tag{B2}$$

$w_i^{x,y,z}$ is the one-dimensional Gaussian weight. The one-dimensional integration regions of (B2) were chosen carefully so as to avoid discontinuities resulting from the irregular geometry of the integration region. The interested reader should see Ref. 43 for details. Grids containing up to 6000 points were tested, and from these tests it was determined that a grid of 1675 points provides adequate convergence for all the relevant matrix elements $\Delta_{nn'}(\vec{k})$.

APPENDIX C: SYMMETRIZATION

In this appendix we discuss the uses of symmetry in our calculation. Symmetry naturally is indispensible in sorting out our results and in revealing their physical significance. On a more practical level, it helps to reduce the extremely lengthy

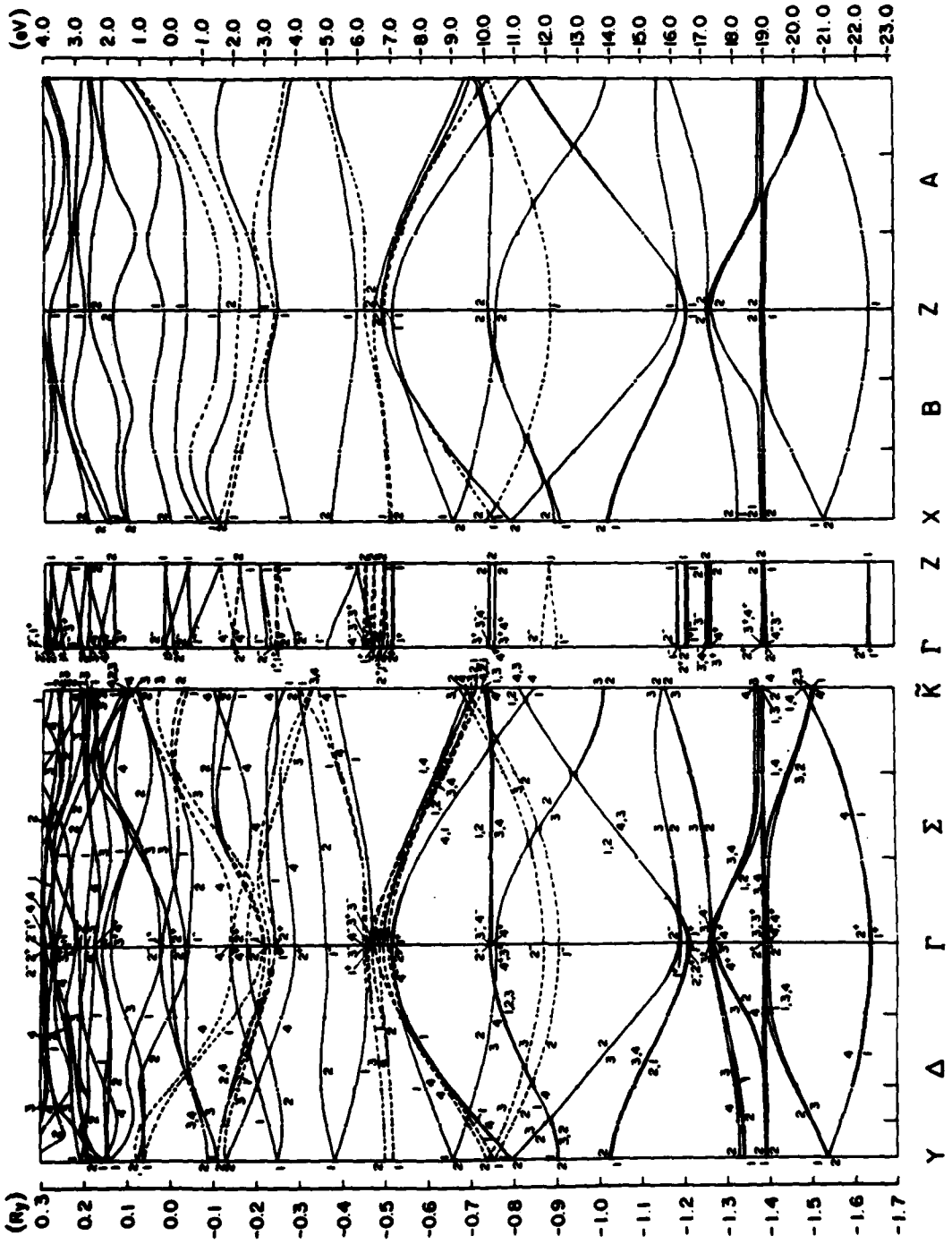

FIG. 9. KKR energy bands of KC_8 in the muffin-tin approximation. The π bands are shown as dashed lines, σ bands are solid lines. Note the inaccurate position of the K 4s band (Γ_1^+ at -6.5 eV) within this approximation.

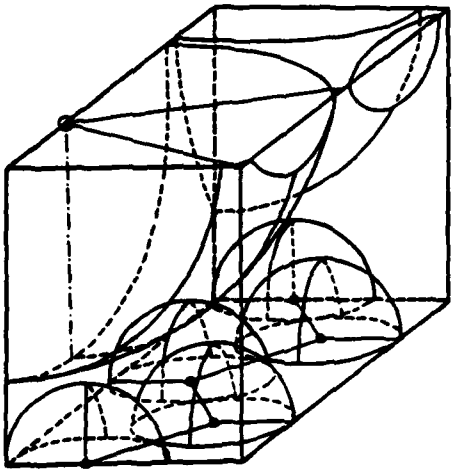

FIG. 10. The irreducible sector ($\frac{1}{8}$) of the KC_8 unit cell. The carbon and potassium muffin tins are shown. Note the irregularity of the interstitial volume, in which the integral for $\Delta_{mm}(\vec{k})$ must be performed.

numerical calculations required for our work. Most of the computer time is spent in the evaluation of matrix elements. Group theory tells us the smallest possible set of matrix elements which must be evaluated. When the matrix element is given by a sum or integral, group theory also gives us the smallest possible domain over which that sum or integral must be performed. These two applications of group theory make the KC_8 band-structure calculation tractible.

We now give several specific uses of symmetry properties in our work. The determination of the KKR scattering matrix (see Appendix A) requires the evaluation of the integral [see Eq. (A4)]

$$\int Y^*_{l'm'}(\hat{r}_{\vec{\tau}})V_{cryst}(\hat{r}_{\vec{\tau}})Y_{lm}(\hat{r}_{\vec{\tau}})d\hat{r}_{\vec{\tau}} \qquad \text{(C1)}$$

on a sphere of radius $|\vec{r}_{\vec{\tau}}|$ for every site $\vec{\tau}$. First, the symmetry of the crystal is such that there are only three inequivalent sites in the crystal, two C sites and one K site; therefore, (C1) needs to be evaluated for just three values of $\vec{\tau}$. Further simplifications result from the point-group symmetry about each site $\vec{\tau}$. In KC_8, C sites are not at centers of symmetry, so no further reduction is possible. The point-group symmetry at K is D_2, which is of considerable value in doing the integral. Since D_2 has four group elements, the spherical integral needs to be evaluated only on $\frac{1}{4}$ of the surface of the sphere. Other properties of D_2 permit us to reduce the number of integrals calculated. Since we consider partial wave scattering up to $l=2$, Eq. (C1) represents

$$81=\left[\sum_{l=0}^{2}(2l+1)\right]^2$$

integrals. Because of symmetry, many of these 81 are zero, and many are related to others. We proceed by replacing the spherical harmonics by spherical polynomials which transform according to the irreducible representations of D_2.[46] These polynomials are exhaustively catalogued by Bell.[47] Using this procedure, we reduce the number of integrals required from 81 to 9, and we block diagonalize the 9×9 matrix into four blocks of dimensions 2, 2, 2, and 3. These simplifications improve the accuracy and speed of the calculation of the KKR scattering matrix considerably.

An application of the space-group symmetry leads to a block diagonalization of the KKR secular matrix. The terms of Eq. (1) may be looked upon as matrix elements of the KKR Hamiltonian between KKR basis functions:

$$\mathcal{A}^{-1}(E)^{\vec{\tau}}_{lml'm'}\delta_{\vec{\tau}\vec{\tau}'}+M(\vec{k},E)^{\vec{\tau}\vec{\tau}'}_{lml'm'}=\langle\phi^{\mathrm{KKR}\,\vec{\tau}}_{l'm'}\,|\,H_{\mathrm{KKR}}\,|\,\phi^{\mathrm{KKR}\,\vec{\tau}'}_{lm}\rangle\,, \qquad \text{(C2)}$$

where the KKR basis functions are those implicit in Eqs. (A13):

$$\phi^{\mathrm{KKR}\,\vec{\tau}}_{lm}(\vec{k},\vec{r})=\sum_{\vec{T}}e^{i\vec{k}\cdot(\vec{\tau}+\vec{T})}\left[-n_l(\kappa\,|\,\vec{r}-\vec{\tau}-\vec{T}\,|\,)Y_{lm}\left[\frac{\vec{r}-\vec{\tau}-\vec{T}}{|\,\vec{r}-\vec{\tau}-\vec{T}\,|}\right]\right]. \qquad \text{(C3)}$$

This treatment is somewhat schematic; although (C3) is not actually the basis function used for the KKR matrix elements, it displays all the symmetry properties necessary for this discussion.

For high-symmetry points, we can block diagonalize (C2) by applying to the wave functions $\phi^{\mathrm{KKR}\,\vec{\tau}}_{lm}$ a projection operator for an irreducible representation of the group of $\vec{k}$ (Ref. 43):

$$\phi_{\text{sym}}^{\Gamma_i(\vec{k})}(\vec{r}) = \sum_{(\beta|\vec{b})\in G(\vec{k})} D_{mm}^{\Gamma_i(\vec{k})}[(\beta|\vec{b})] \times [(\beta|\vec{b})\phi_{lm}^{\text{KKR}\,\vec{r}}(\vec{k},\vec{r})] , \tag{C4}$$

where $D_{mm}^{\Gamma_i(\vec{k})}(\beta|\vec{b})$ is the mm element of the matrix representing crystal symmetry operation $(\beta|\vec{b})$ in irreducible representation $\Gamma_i(\vec{k})$; these are all given in Ref. 18. Details of the actual projection on the functions (C3) are given in Ref. 43. When the KKR Hamiltonian is expressed in the symmetrized basis (C3), the matrix is block diagonalized, making the diagonalization more rapid, and eigenvalues and eigenvectors more reliable.

As a final example of the application of symmetry to our calculation, we mention the simplifications which can be made in the matrix elements of ΔV, the non-muffin-tin part of the potential [see Eq. (3)]. First, because $\Delta V(r)$ transforms according to the identity representation of the crystal group, there are nonzero matrix elements only between those KKR wave functions n and n', which transform according to the same irreducible representations. This property of ΔV also tells us that degenerate KKR eigenvalues are not split by the perturbation.

In addition to these selection rules, symmetry allows us to reduce the region of integration in (B1). The integrand is invariant under every symmetry operation of the group of $\vec{k}$. Consequently, if the order of the group is g_k, then the integral need only be done over $1/g_k$ of the unit cell. For KC_8, this means $\frac{1}{8}$ of the unit cell for wave vectors Γ, X, Y, Z, Σ, Δ, and Λ, and $\frac{1}{4}$ of the unit cell for wave vectors A and B (see Fig. 3).

[1]J. E. Fischer and T. E. Thompson, Phys. Today 31, (7), 36 (1978).

[2]Proceedings of the Franco-American Conference on Intercalated Compounds of Graphite, edited by F. L. Vogel and A. Herold [Mater. Sci. Eng. 31, (1977)].

[3]Proceedings of the International Conference on Layered Materials and Intercalates, edited by C. F. van Bruggen, C. Haas, and H. W. Myron [Physica B 99, (1980)].

[4]Second Conference on Intercalation Compounds of Graphite, edited by F. L. Vogel [Synth. Metals 2, (1980)].

[5]N. A. W. Holzwarth, S. Rabii, and L. A. Girifalco, Phys. Rev. B 18, 5190 (1978).

[6]T. Inoshita, K. Nakao, and H. Kamimura, J. Phys. Soc. Jpn. 43, 1237 (1977); 45, 689 (1978).

[7]T. Ohno, K. Nakao, and H. Kamimura, J. Phys. Soc. Jpn. 47, 1125 (1979).

[8]W. Rudorff, and E. Schultze, Z. Anorg. Chem. 277, 156 (1954).

[9]P. LaGrange, D. Guerard, and A. Herold, Ann. Chim. (Paris) 3, 143 (1978).

[10]C. Horie, M. Maeda, and Y. Kuramoto, Physica B 99, 430 (1980).

[11]*International Tables of X-Ray Crytallography* (Kynoch, Birmingham, 1952), p. 161.

[12]J. C. Slater, *The Self-Consistent Field for Molecules and Solids* (McGraw-Hill, New York, 1974).

[13]K. Schwartz, Phys. Rev. B 5, 2466 (1972).

[14]F. Herman and S. Skillman, *Atomic Structure Calculations* (Prentice-Hall, Englewood Cliffs, N.J., 1963).

[15]J. Korringa, Physica (Utrecht) 13, 392 (1947); W. Kohn and N. Rostoker, Phys. Rev. 94, 1111 (1954).

[16]F. S. Ham and B. Segall, Phys. Rev. 124, 1786 (1961).

[17]G. S. Painter, Phys. Rev. B 7, 3520 (1973).

[18]S. C. Miller and W. F. Love, *Tables of Irreducible Representations of Magnetic Space Groups and Co-Representations of Magnetic Space Groups* (Pruett, Boulder, Colo., 1967).

[19]H. Nagayoshi, K. Nakao, and Y. Uemura, J. Phys. Soc. Jpn. 41, 2480 (1976).

[20]J. C. Slater and G. F. Koster, Phys. Rev. 94, 1498 (1954).

[21]R. C. Tatar, following paper, Phys. Rev. B 25, 4126 (1982).

[22]T. Kondow, U. Mizutani, and T. B. Massalski, Mater. Sci. Eng. 31, 267 (1977).

[23]A. V. Gold, in *Solid State Physics, Electrons in Metals*, edited by J. F. Cochran and R. R. Haering (Gordon and Breach, New York, 1968), p. 39.

[24]H. Suematsu, S. Tanuma, and K. Higuchi, Physica B 99, 420 (1980).

[25]N. F. Mott and H. Jones, *The Theory of the Properties of Metals and Alloys* (Dover, New York, 1958), p. 96.

[26]F. J. DiSalvo, S. A. Safran, R. C. Haddon, J. V. Waszczak, and J. E. Fischer, Phys. Rev. B 20, 4883 (1979).

[27]S. A. Safran and F. J. DiSalvo, Phys. Rev. B 20, 4889 (1979).

[28]J. E. Fischer, private communication.

[29]M. Zanini and J. E. Fischer, Mater. Sci. Eng. 31, 169 (1977).

[30]D. Guerarad, G. M. T. Foley, M. Zanini, and J. E. Fischer, Nuovo Cimento 38, 410 (1977).

[31]A. R. Ubbelohde, Nature 232, 43 (1971); C. D. Fuerst, W. D. Johnson, and J. E. Fischer, Extended Abstracts and Program of the 14th Biennial Conference on Carbon, 1979 (unpublished), p. 296.

[32]W. D. Johnson, M. E. Potter, and J. E. Fischer, Bull. Am. Phys. Soc. 24, 410 (1979).
[33]N. A. W. Holzwarth, Phys. Rev. B 21, 3665 (1980).
[34]D. M. Hwang, M. Utlaut, M. S. Isaacson, and S. A. Solin, Physica B 99, 435 (1980).
[35]D. P. DiVincenzo, N. A. W. Holzwarth, and S. Rabii, Synth. Metals 3, 125 (1981).
[36]J. J. Ritsko, Bull. Am. Phys. Soc. 26, 264 (1981).
[37]E. Mele (private communication).
[38]P. Oelhafen, P. Pfluger, E. Hanser, and H. J. Güntherodt, Phys. Rev. Lett. 44, 197 (1980); J. Krieg, P. Oelhafen, P. Pfluger, and H. J. Güntherodt, in Extended Abstracts and Program, 15th Biennial Conference on Carbon, 1981 (unpublished), p. 84.
[39]E. Cartier, F. Heinrich, P. Pfluger, and H. J. Güntherodt, Phys. Rev. Lett, 46, 272 (1981); Extended Abstracts and Program, 15th Biennial Conference on Carbon, 1981 (unpublished), p. 86.
[40]N. A. W. Holzwarth, Bull. Am. Phys. Soc. 26, 450 (1981), and unpublished.
[41]N. A. W. Holzwarth, L. A. Girifalco, and S. Rabii, Phys. Rev. B 18, 5206 (1978).
[42]W. John, G. Lehmann, and P. Ziesche, Phys. Status Solidi B 53, 287 (1972); B. Segall, J. Phys. Chem. Solids 8, 371 (1959).
[43]D. P. DiVincenzo, Master's thesis, University of Pennsylvania, 1980 (unpublished).
[44]D. R. Hartree, *Numerical Analysis* (Oxford University Press, London, 1958), p. 142.
[45]F. B. Hildebrand, *Introduction to Numerical Analysis* (McGraw-Hill, New York, 1974), p. 379.
[46]M. Tinkham, *Group Theory and Quantum Mechanics* (McGraw-Hill, New York, 1964).
[47]D. G. Bell, Rev. Mod. Phys. 26, 311 (1954).
[48]J. J. Ritsko and C. F. Brucker, Bull. Am. Phys. Soc. 27, 405 (1982), and unpublished.

PHYSICAL REVIEW B VOLUME 25, NUMBER 6 15 MARCH 1982

Electronic properties of graphite: A unified theoretical study

R. C. Tatar and S. Rabii
Moore School of Electrical Engineering and Laboratory for Research on the Structure of Matter, University of Pennsylvania, Philadelphia, Pennsylvania 19104
(Received 31 August 1981)

We have calculated the electronic structure of three-dimensional graphite using the modified first-principles Korringa-Kohn-Rostoker technique developed for and applied to the intercalation compound LiC_6. Whereas previous calculations of the electronic band structure of graphite provide explanations either for moderate- to high-energy excitations or for low-energy and Fermi-surface properties, we find excellent agreement between our results and experiments in both regimes. Our analysis of the band structure is based on a comparison with experiments of predicted optical transitions, values for the Slonczewski-Weiss-McClure parameters which we obtain from a fit to our bands, and Fermi-surface properties. We also present a density of states for our band structure and several constant-energy surfaces. Our discussion includes a comparison with other theoretical work.

I. INTRODUCTION

Crystalline carbon in the form of graphite is one of the most extensively studied materials both experimentally and theoretically. Because of its layered structure with a relatively large separation between layers, graphite is often modeled as a two-dimensional solid. This is very convenient for calculations and has been studied with tight-binding (TB),[1–6] linear combination of atomic orbitals (LCAO),[7] orthogonalized-plane-wave–tight-binding (OPW-TB),[8,9] generalized OPW,[10,11] self-consistent extended Hückel,[12] exact exchange Hartree-Fock,[13] and other techniques.[14] The single-layer model necessarily ignores interlayer interactions which introduce band splittings of roughly 1 eV and introduce important structure near the Fermi level. Thus low-energy optical properties, transport, and other fine-structure-dependent electronic properties are not adequately covered by these calculations.

The previous calculations of the three-dimensional graphite band structure can be divided into two categories. First there are the band structures which are fitted in detail to experimental results over a small energy range. These provide accurate information about the Fermi surface and are useful for correlating transport related measurements[1,15] and explaining optical structure at moderate energies.[16] This type of calculation is often used to supplement the single-layer calculations.[1,5,7,9,11] Zunger[12] has provided a comparison of many of the above calculations. In the second category of three-dimensional calculations, a much wider energy range and a much larger portion of the Brillouin zone is covered. The methods used range from TB,[17] LCAO,[18] pseudopotentials,[19,20] to cellular.[21] While higher-energy optical properties are potentially better predicted, in general, these calculations are not sufficiently accurate to provide an adequate representation of the Fermi surface.

The above classification also applies to experimental techniques. The Fermi surface and Fermi-surface parameters have been studied by de Haas–van Alphen effect[15,22–25] magnetoreflection,[26] cyclotron resonance,[27–29] magnetic susceptibility,[22] and various other techniques,[30–32] while higher-energy properties have been measured using photoemission,[33–35] secondary electron emission,[36] electron spectroscopy for chemical analysis,[37–39] soft x rays,[40] electron-energy loss,[41] reflectivity,[42–44] thermoreflectivity,[45] optical absorption.[46] The review articles by Spain[30,31] and McClure[32] provide a detailed study of the low-energy properties.

In the present study we produce an accurate *ab initio* energy-band structure for three-dimensional graphite that combines the features of both types of calculation. In other words, it not only provides the energy bands over a large energy range, it also leads to a very reasonable model for Fermi-surface properties of this material.

Due to the structural similarity of graphite and the graphite-intercalation compounds, we chose for

 ©1982 The American Physical Society

this study the modified Korringa-Kohn-Rostoker (KKR) approach of Holzwarth *et al.* that was developed and successfully applied to LiC_6,[47] and subsequently to KC_8.[48] Since graphite has been extensively studied in the past, a detailed evaluation of our results, and thus the formalism, is possible and this has important implications for our studies of the graphite-intercalation compounds.

II. GRAPHITE STRUCTURE AND POTENTIAL

The structure of graphite chosen for this study is the *AB* or Bernal structure[49] (Fig. 1). It consists of planes of carbon atoms, each forming a hexagonal net, stacked in a manner such that half of the carbons (*A* atoms) are located directly above each other in adjacent planes, while the other half (*B* atoms) are located above the center of the hexagon in the adjacent plane.[50] There are four atoms per unit cell, two of the inequivalent *A* and *B* carbons (Fig. 2).

The space group G_s of graphite is $P6_3/mmc$.[51] The corresponding point (factor) group, $P=G_s/T$, has 24 elements and is isomorphic to D_{6h}. T denotes the lattice (translation) group. This structure contains two inequivalent inversion centers, one located halfway between adjacent layers on a c-axis line through *A* carbons, while the other is obtained from the former by half a primitive translation perpendicular to the c axis.

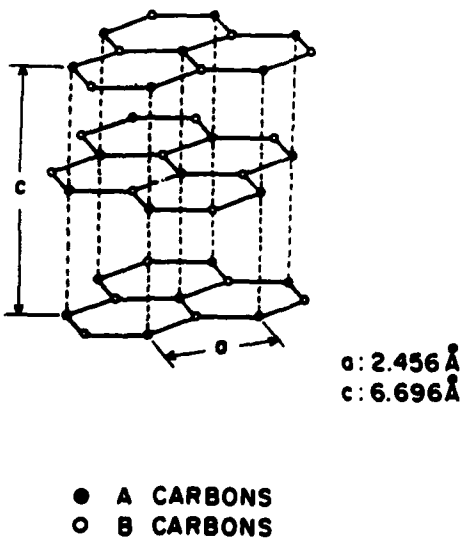

FIG. 1. Graphite structure. Lattice constants from Ref. 50.

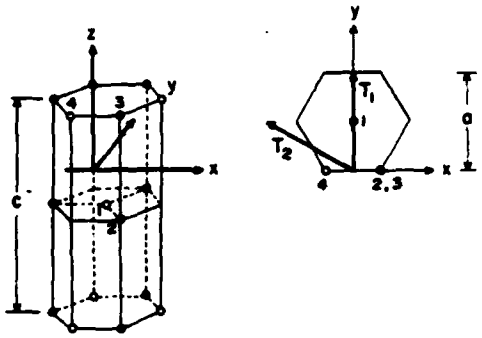

FIG. 2. Graphite unit cell and coordinate system for present work.

The local symmetry about the atoms in the unit cell enters certain aspects of the calculation such as the computation of wave functions near a site using a symmetry eigenfunction expansion. While the potentials for the *A* and *B* atoms are not identical, the local symmetry for both is described by the group D_{3h}.

The Brillouin zone of the reciprocal lattice is shown in Fig. 3 with the high-symmetry point and directions labeled. The groups of k vectors at the top and bottom surfaces of the zone have only even-dimensional representations.[52] Likewise, for points in the interior of the zone (except at Γ) the representations are all one dimensional.

The crystal potential was constructed by linear superposition of carbon self-consistent field, Hartree-Fock-Slater charge densities.[53] Since the band-structure calculation was not self-consistent, it was important to obtain as realistic a crystal potential as possible. Thus in order to reflect the in-plane bonding of carbon atoms, the atomic charge

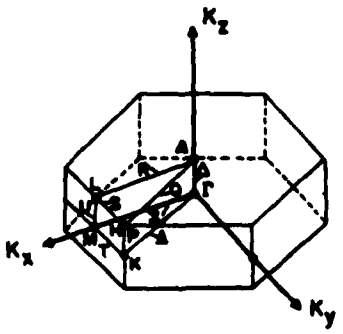

BRILLOUIN ZONE

FIG. 3. Brillouin zone of graphite.

density of carbon was calculated using a $2s^2 2p^2$ configuration. Previous experience, however, indicated that the crystal potential would be only slightly affected by changes in the neutral atomic configuration and the exchange-correlation approximation. The exchange-correlation potentials both in atomic and crystal calculations are obtained using the local $X\alpha$ statistical prescription of Slater[54] with the value of 0.759 for α as obtained by Schwartz.[55]

The results of the above procedure are displayed in Fig. 4 where the potential is shown along three directions. While the potential is nearly spherically symmetric close to the atomic sites, its angular variation is greater than 1 Ry at a distance of one-half the nearest-neighbor spacing (muffin-tin radius). Such a large potential anisotropy is typical also of graphite-intercalation compounds where we have applied our present approach to calculate their electronic properties.[47,48] How well our band-structure formalism performs under such conditions is one of the objectives of this work.

III. BAND-STRUCTURE CALCULATION

The technique used for the calculation of energy bands was a modified version of Painter's discrete

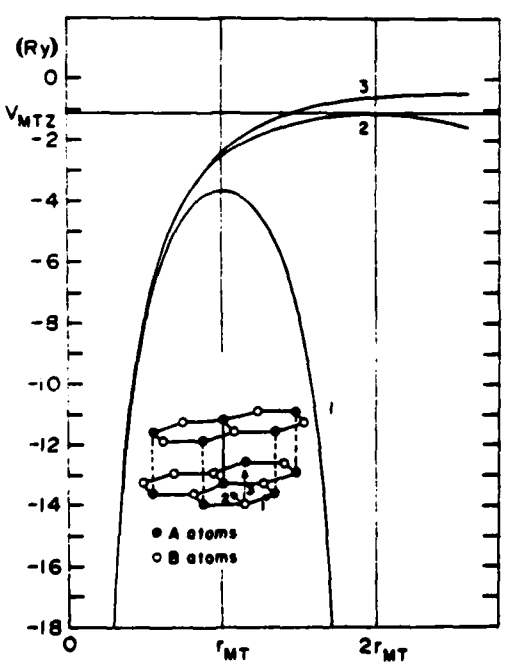

FIG. 4. Crystal potential.

variational KKR method procedure.[56–58] This method was developed by Holzwarth *et al.* (HRG) and applied to LiC_6 (Ref. 47) and later to KC_8.[48] In the first step of the HRG approach a modified KKR calculation is performed on a muffin-tin form of the crystal potential, V_{MT}. This is followed in the second step by diagonalizing the non-muffin-tin Hamiltonian in the muffin-tin basis. The reader is referred to Refs. 47 and 48 for the details of the formalism.

In the interstitial region the constant potential value or muffin-tin zero (V_{MTZ}) is taken to be the volume-averaged potential of that region and in the present work is 1.119 Ry below the atomic (carbon) zero level. The band structure for the full crystal potential, i.e., our final band structure, does not depend on V_{MTZ}. The radius of the MT spheres, r_{MT}, is chosen so that the atomic spheres touch but do not overlap. In graphite $r_{MT} = 1.34$ a.u. and the interstitial region occupies 83% of the unit cell. This is a much larger fraction than for the intercalation compounds LiC_6 and KC_8 where the corresponding numbers are 54% and 43%. Because the interstitial region is so large, with a corresponding large potential fluctuation, it is clear that a muffin-tin calculation by itself is inappropriate for graphite energy bands.

The reaction operator $\mathcal{K}_{ij}^{\sigma-1}$ [Eq. (1), Ref. 48] at the σth sphere gives the relative scattering of the ith (incident wave) component of the jth eigenfunction. In general the reaction operator $\mathcal{K}_{lm,l'm'}^{\sigma-1}$ is a complicated function of energy which is evaluated on a coarse energy grid in the angular-momentum representation. For graphite, however, it was found that the reaction matrix components are very smooth functions of energy over the range considered. This is in contrast to previous calculations[47,48] where many singularities were present. This smoothness permitted rapid and very accurate numerical interpolation and extrapolation.

The results of the first step of the calculation (modified KKR procedure) are displayed in Fig. 5. Many symmetry-dependent features are visible such as the degeneracies of the bands at K and H and the nearly free-electron-like shapes of the lower σ and π bands. The muffin-tin potential, however, exaggerates many level separations and causes level crossings that do not occur in the final bands. From the position of V_{MTZ} it is expected that the dominant distortion is a larger band dispersion along the $\vec{k}_z$ directions but the band shapes perpendicular to $\vec{k}_z$ will be very similar in the non-muffin-tin bands. This is because the

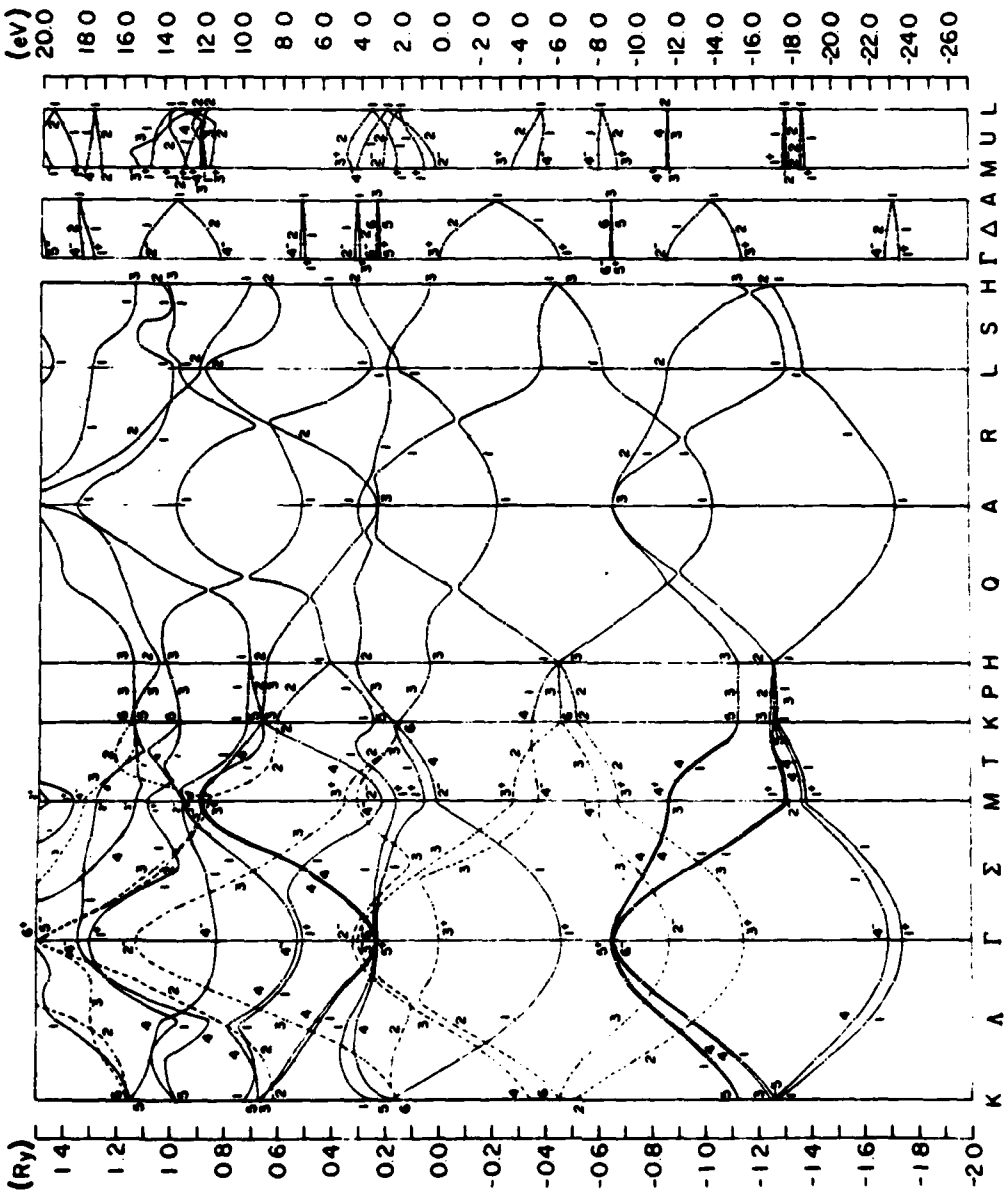

FIG. 5. Muffin-tin band structure (KKR).

muffin-tin zero lies between the potential extrema of the directions parallel and perpendicular to the layers. Thus, on the average the c-axis muffin-tin potential is more attractive than the exact potential and conversely the in-plane muffin-tin potential is more repulsive. This means that interlayer interactions between the p_z orbitals that are responsible for the splittings are overestimated by the muffin-tin potential, increasing the $\vec{k}_z$ dispersion.

In practice the secular equation [Eq. (1), Ref. 48] includes all l,m for which scattering is large. Previous work[47] showed than an s-p expansion is quite accurate and in almost all situations an expansion including d waves is extremely good. For this study components up to $l=2$ have been included. This is sufficient to obtain bands of all symmetries since all irreducible representations of groups of k have explicit representations in terms of atomic centered spherical harmonics of $l=0$, 1, or 2. In order to estimate the effect of the d-wave components, the reaction matrix and KKR eigenenergies were recomputed at Γ and M excluding $l=2$ terms. As anticipated there was no change in the π levels. Except for the Γ_5^+,Γ_6^- levels which moved by about 1.5 eV, most of the σ levels differed from the s-p-d KKR levels by less than 0.9 eV. However, we expect these shifts to be much reduced in the final non-muffin-tin bands since, in general, the d-wave scattering is exaggerated by the muffin-tin potential due to the orientation of these orbitals and their larger spatial extension into the interstitial region.

The results of the HRG procedure for the potential and structure described in Sec. II are shown in Fig. 6. The symmetry labels are those of Slater.[59]

The bands were obtained at 33 wave vectors along the edges of an irreducible sector of the Brillouin zone including all the high-symmetry points and direction. The bands on the hexagonal face of the zone (H-A-L-H) are all doubly degenerate and look much like the bands from single-layer calculations.

Most of the KKR levels were found within 0.01 mRy tolerance so the accuracy of the non-muffin-tin bands was limited by the accuracy of the potential matrix elements Δ_{NM} [Eq. (3), Ref. 48]. The position of the upper non-muffin-tin bands, i.e., those with energies about 1.3 Ry, however, should be considered as very approximate due to the necessity of truncating the non-muffin-tin secular matrix [Eq. (2), Ref. 48]. The KKR searches were taken up to at least 2 Ry above V_{MTZ} at each of the 33 wave vectors.

IV. DENSITY OF STATES AND FERMI-SURFACE PROPERTIES

A. Interpolation models

In order to analyze the implications of a given band-structure calculation for experimentally measurable phenomena, it is often necessary to perform integrations over the Brillouin zone that require knowledge of the energy bands at each k point.[60] It is extremely expensive to evaluate the eigenspectrum for a large number of wave vectors using the method outlined in Sec. III, so a physically sensible and accurate intepolation scheme is highly desirable.

In graphite it is known from experimental and theoretical studies that the bands near the Fermi level play a dominant role in transport and low-energy optical properties. A parametrized model for these bands would provide a useful interpolation scheme.

There are two currently well-known models for graphite: (1) the Slonzcewski-Weiss-McClure (SWMc) model[15] for Fermi-level bands near the H-K axis and (2) the full zone π-band Johnson-Dresselhaus (JD) model.[16] Both models are described below with additional details given in Appendices A and B.

The Slonzcewski-Weiss-McClure (SWMc) model originated about 25 years ago[5] as a tight-binding $k\cdot p$ analysis specifically for the Fermi-level bands of graphite, near the H-K axis of the Brillouin zone. This work was reexamined by McClure,[15] who demonstrated that seven parameters (SWMc parameters) adequately described the shape of the bands and the Fermi surface. This very useful analytical tool immediately became popular among experimentalists and many experimental results are still expressed in terms of these parameters.

A least-square fitting procedure with a modified gradient search[61] was used to determine the values of the SWMc parameters from the bands shown in Fig. 6. The energy levels at 6 $\vec{k}$ points including H, K, and a Λ point were used in the fit. Several types of weighting schemes were tried and all gave roughly the same results. The numbers are shown in Table I. The parameters of column a were computed with approximately equal percentage error and most accurately reflect the shapes and position of the *ab initio* bands. Column b parameters were found with equal absolute error and are not as good for parameters with small magnitude. There is a change of sign of the Δ parameter and γ_2

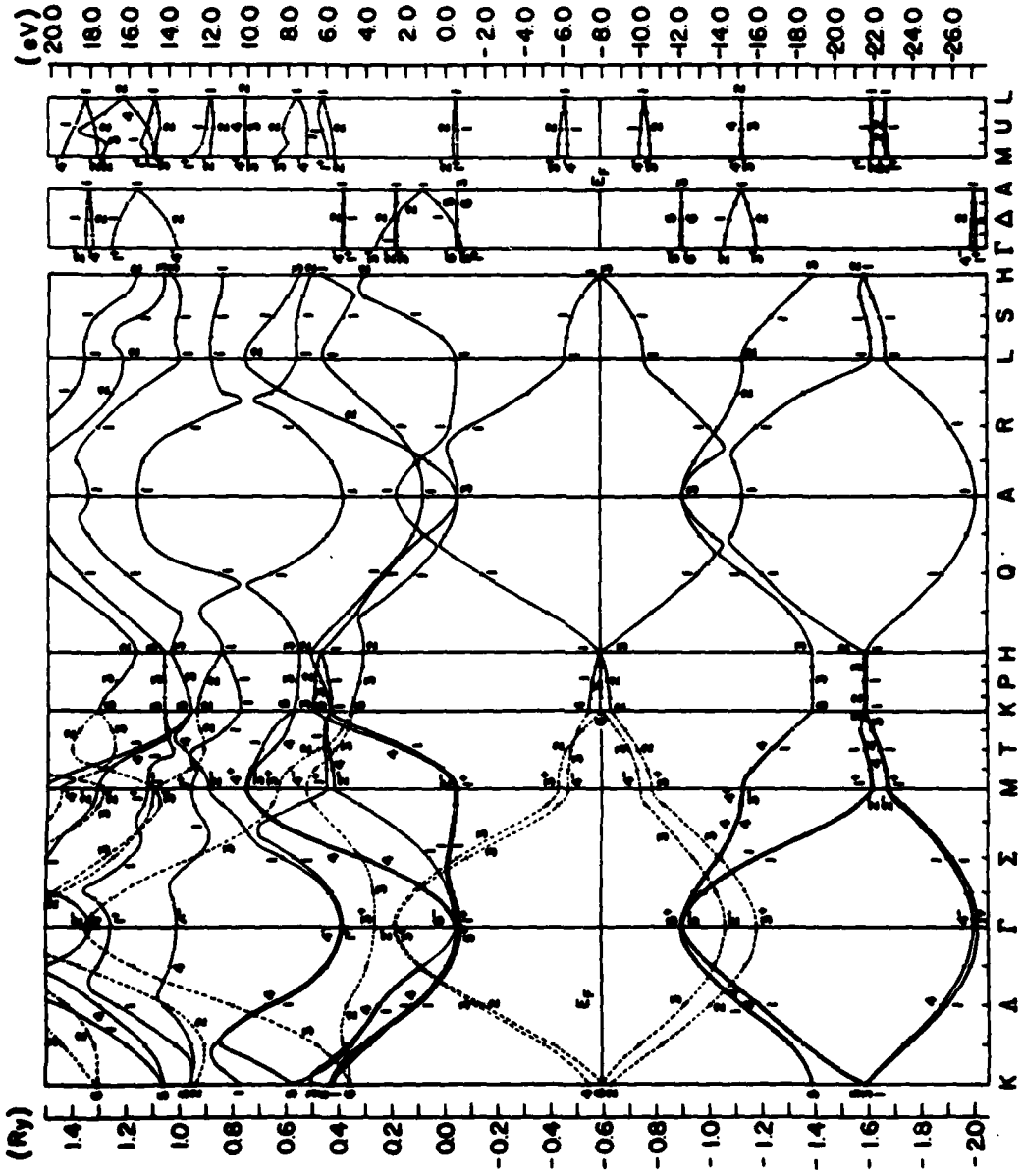

FIG. 6. Band structure of three-dimensional graphite (full crystal potential). π bands are dashed.

TABLE I. SWMc parameters for graphite (eV).

	a	b	c	d
γ_0	2.92	2.92	2.41	3.16
γ_1	0.27	0.27	0.27	0.39
γ_2	−0.022	−0.009	−0.022	−0.019
γ_3	0.14	0.15	0.14	0.28
γ_4	0.10	0.10	0.074	0.044
γ_5	0.0063	0.029	0.0065	0.038
Δ	−0.0079	−0.0085	0.0074	−0.008
E_F	−0.025			−0.024

[a]Weighted least-squares fit to *ab initio* bands (preferred); SWMc model.
[b]Equal weight least-squares fit; SWMc model.
[c]Estimated from full-zone fit to *ab initio* bands using Johnson-Dresselhaus model Hamiltonian.
[d]Experiments, Ref. 70.

grows at the expense of γ_5. Finally the column c parameters were estimated from the parameters of the full-zone JD model using the formulas as given in Appendix B (see Table VII).

The differences in the parameters reflect different emphasis of the bands. For example, the column c parameters arise from a fit that should be suitable for analysis of optical properties between 2−12 eV, while the a column parameters should accurately reflect transport properties. We feel the SWMc model is unable to consistently account for both transport and optical properties with the same parameters and there is some experimental evidence to suggest this. It is not clear, however, that simply adding higher-order terms will be useful.

Figure 7 demonstrates the accuracy of the SWMc fit along the H-K axis. The H and K point levels were fit exactly and the differences between the *ab initio* bands and SWMc arise from slightly different dispersion along P. In this sense we have an *ab initio* verification of SWMc. We expect an even greater difference off the H-K axis but can make no accurate comparison because the nearest *ab initio* off-axis $\vec{k}$ point is near the limit of validity of the SWMc model.

The JD model Hamiltonian[16] is based on a full-zone symmetrized Fourier (tight-binding) expansion of the π bands and was shown to be equivalent to the SWMc model along the H-K axis. In fact, in the original study where an analysis of optical properties was performed, this equivalence was used to determine the full-zone expansion parameters (JD parameters) from a set of experimentally determined SWMc parameters.

By performing a unitary transformation $H_M = SH_{JD}S^{-1}$ on the JD Hamiltonian with

$$S = \begin{bmatrix} \frac{1}{\sqrt{2}} & \frac{-1}{\sqrt{2}} & 0 & 0 \\ \frac{-1}{\sqrt{2}} & \frac{1}{\sqrt{2}} & 0 & 0 \\ 0 & 0 & 1 & 0 \\ 0 & 0 & 0 & 1 \end{bmatrix},$$

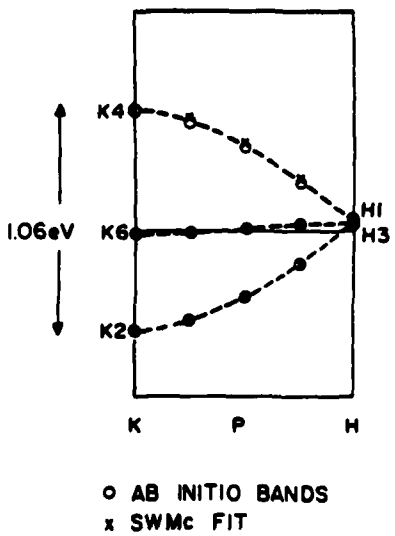

FIG. 7. Comparison of first-principles bands with SWMc fit, × SWMc fit, ○ *ab initio* bands. Most of the points overlap completely on scale shown.

one arrives at a form that can be compared with McClure's Hamiltonian and the SWMc parameters can be extracted from the JD parameters. Performing this algebra we find the relationships given in Appendix C.

It is well known that the eigenvalues of the SWMc Hamiltonian are invariant under simultaneous change of sign of γ_0 and γ_4. The JD Hamiltonian also has this property and is invariant under simultaneous change of sign of the "off-diagonal parameters": a_{AB}^{010}, a_{AB}^{020}, a_{AB}^{120}, a_{AB}^{011}. Such changes in sign might be brought about indirectly by coordinate system changes. Thus the sign of γ_0 and γ_4 are not given uniquely by this theory.

A least-squares fit (modified gradient search)[61] to the band structure along K-H, K-M, and towards Γ gave the parameters in Table II. Our parameters differ a great deal from those given by Johnson and Dresselhaus[16] and equivalent parameters given by Holzwarth[62] based on the two-dimensional band structure of Painter and Ellis. Part of this difference between our parameters and those from previous works is due to the difference in our energy scale zero (diagonal constants). Another factor contributing to this difference is that the previous fits were to bands near the rectangular faces of the Brillouin zone—unconstrained in the zone center—and the best fits to these bands caused an excessive bandwidth at Γ, between the top of the conduction band and the bottom of the valence band.

B. Density of states

The JD model has been used to give a satisfactory account of the infrared optical properties of graphite.[16] Recently Holzwarth[62] used an extension of the JD model for a layer analysis of intercalation compounds of graphite. It was because of these successes that the JD model was chosen as a full-zone interpolation of the *ab initio* bands of Sec. III. This fit was expected to provide a reasonably accurate density of states from the band structure because of the large number (11) of adjustable parameters.

The density of states was obtained from the histogram method, which uses the approximate expression:

$$g_{\Delta E}(E)=\frac{2}{(2\pi)^3}\times\sum_{\alpha}\frac{1}{\Delta E}\int_{E}^{E+\Delta E}\left[\int\delta(E_\alpha(\vec{k})-E)d\vec{k}\right]dE\ , \tag{1}$$

where the α sum is over the valence and conduction π bands.

Roughly 20 000 points in an irreducible sector of the Brillouin zone were used with a higher density of points concentrated in a wedge near the H-K axis than in the rest of the zone. This provided a

TABLE II. JD parameters (eV).

	Parameter	Used for Fig. 9 H-K fit	Full-zone fit
1	a_{AA}^{000}	−3.38	−3.29
2	a_{AA}^{100}	−1.43	−1.18
3	a_{BB}^{000}	−1.83	−1.79
4	a_{BB}^{100}	1.68	1.85
5	a_{AB}^{000}	−2.14	−2.20
6	a_{AB}^{010}	0.0450	0.0442
7	a_{AB}^{120}	0.364	0.362
8	a_{AK}^{001}	0.181	0.143
9	a_{BK}^{011}	0.272	0.279
10	a_{AB}^{011}	0.148	0.157
11	a_{AA}^{002}	0.0022	0.0104
12	a_{BB}^{002}	−0.0072	0.0110

smooth curve near the valence-conduction junction where in addition the interval ΔE was decreased.

The π density of states calculated from (1) is shown in Fig. 8. The overall shape is as expected. The width of 19 eV is a bit larger than the width of the actual π bands because of the slight inaccuracy of the fit which was weighted to more accurately fit the bands along the *L-M-K-H* face of the zone. As a self-consistent check the area under the curve was computed and found to be exactly two electrons per carbon. The peaks correspond to the *M* point dispersion and would be singular in a single-layer calculation. The peak separation is 4.3 eV on average but varies between 3.8 and 4.7 and corresponds to the 4.6 eV critical transition observed experimentally. The density of states is in qualitative agreement with that of Painter and Ellis,[7] Samuelson and Batra,[17] and Zunger.[12]

Also included in Fig. 8 for comparison is the density of states obtained from a fit to SWMc. SWMc is expected to be more accurate in a region near the minimum of roughly 200 meV in width but can be seen to rapidly diverge from the more accurate overall calculation thereafter. Although a more extensive fit to the *ab initio* bands might reduce this discrepancy somewhat, this difference was expected from the nature of the SWMc model which is limited to a small region of reciprocal space.

The conventional approach for obtaining the Fermi energy is to integrate the density of states up to the required number of carriers. The JD model, however, is inaccurate in the region of the Fermi level and the SWMc model is very inaccurate near the π-band edges. For this reason we proceeded by requiring the number of electrons and holes to be equal, leading to a Fermi level of -0.025 eV. As a check we also integrated the JD density of states up to 1 electron and found a value of -0.09 eV. This is close but too low to give a realistic Fermi surface.

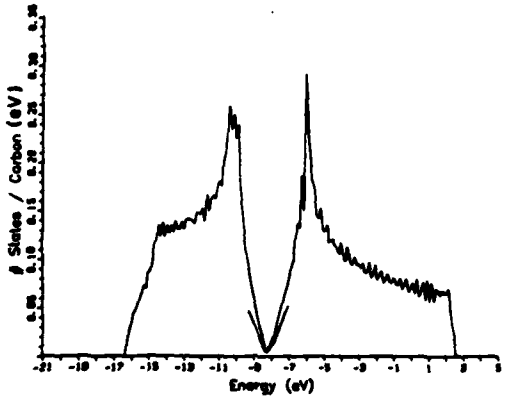

FIG. 8. Density of states obtained from JD model fit to first-principles bands (upper curve). Also shown for limited energy range is dos obtained from SWMc fit (lower curve).

C. Fermi surface and Fermi-surface properties

The Fermi surface corresponding to the energy $E_F = -0.025$ eV is shown in Fig. 9. For comparison, we performed the same procedure for the JD model and obtained a slightly different surface also shown in Fig. 9. In addition to what is shown in the figure, the SWMc and JD models include three additional legs that provide a thicker overall cross section between the electron-hole junction. These details are omitted from the figure since they are not resolvable to the precision with which the figure is drawn. Also hidden from view are the hole pockets near the *H* point.

Several measurable quantities that depend on the Fermi surface were computed numerically and are summarized in Table III. The de Haas–van Alphen frequencies are related to extremal cross sections of the Fermi surface (A_{ex}) and were comput-

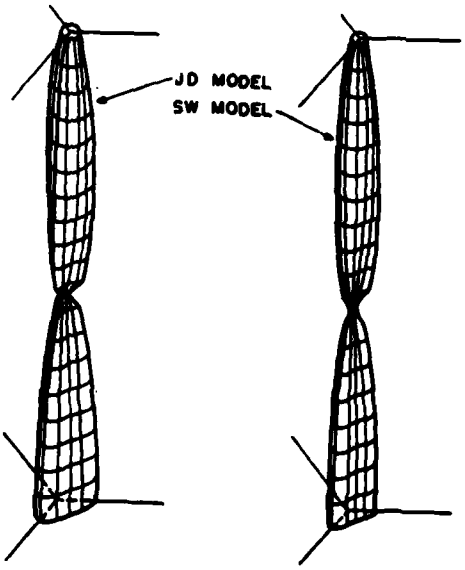

FIG. 9. Fermi surfaces of graphite from two different parametrized fits of bands. *H* (*K*) point is at intersection of upper (lower) three axes [see Fig. 10(b).]

TABLE III. Graphite Fermi-surface characteristics, de Haas–van Alphen periods (10^{-5} G^{-1}) and cyclotron masses.

	Majority electrons (K)	Majority holes	Minority holes (H)
$F(H)$			
calculated	1.68	2.37	13.7
Experiment			
Refs. 23 and 73	1.61	2.20	13.5
$M(H)$			
calculated	$0.045m_0$	$0.033m_0$	$0.006m_0$
Experiment	$0.06m_0$	$0.04m_0$	$0.002m_0$

	Plasma frequencies (eV)			
	Present	Typical[a] SWMc params.	Nakao[b]	McClure[c]
$\hbar\omega_a$	0.46	0.44	0.83	0.17
$\hbar\omega_c$	0.04	0.04	0.07	0.01

[a]See Table I, first column.
[b]From Ref. 64.
[c]From Ref. 63.

ed for field parallel to the k_z axis, as follows:

$$F(\hat{H})=\frac{c\hbar}{2\pi e}A_{ex}(\hat{H}) .$$

The cyclotron effective masses were computed from the relation

$$m^*=m_e\frac{\hbar^2}{2\pi}\int_0^{2\pi}\frac{K_\perp d\phi}{|\hat{K}_\perp\cdot\vec{\nabla}_K E|} ,$$

and are experimentally determined by magnetoreflection experiments[24] that give the Landau-level separations. $\vec{K}_\perp$ is the wave vector perpendicular to the layer planes. The agreement with experiment is good.

In some materials low-frequency optical properties can be described by the dielectric tensor:

$$\epsilon^{ij}=\delta_{ij}+\epsilon^{ij}_{\text{inter}}+\epsilon^{ij}_{\text{intra}} .$$

$\epsilon^{ij}_{\text{intra}}$ has the form

$$\epsilon^{ij}_{\text{intra}}=\sum_\alpha\frac{[(\omega_p^\alpha)^{ij}]^2}{\omega(\omega+i/\tau^\alpha)} ,$$

where the sum is over different carriers. τ^α and ω_p^α are scattering time and the plasma frequency, respectively, associated with carrier α. The plasma frequency is given by the Fermi-surface integral:

$$[(\omega_p^\alpha)^{ij}]^2=\frac{4\pi e^2}{\hbar^2}\frac{2}{(2\pi)^3}\int_{FS}\frac{d\vec{s}}{|\nabla_K E|}\left[\frac{\partial E}{\partial K_i}\frac{\partial E}{\partial K_j}\right] .$$

For graphite there are only two independent components of ω^{ij} associated with the π-band carriers, in-plane and c-axis frequencies ω_a,ω_c.

$$\omega_a^2=\frac{(\omega^{xx})^2+(\omega^{yy})^2}{2} ,$$

$$\omega_c^2=(\omega^{zz})^2 .$$

Table III shows the values of plasma frequency obtained from our calculations as well as those based on a generally accepted set of SWMc parameters. We have also included plasma frequencies obtained by McClure[63] from estimates of electron density and effective mass as well as those calculated by Nakao.[64] Our values fall between the results of McClure and Nakao. For graphite, experimental determination of plasma frequencies is very difficult if not impossible because of the screening due to interband transition.

D. Constant-energy surfaces

Several constant-energy surfaces above and below the Fermi level were computed from the JD fit. These are shown in Fig. 10. While graphite rigid-band analyses are generally applicable only in the dilute limit, these surfaces would correspond to Fermi surfaces of low-stage graphite-intercalation compounds if the only effect of intercalation was to introduce additional carriers and if structural changes leading to zone folding could be neglected.

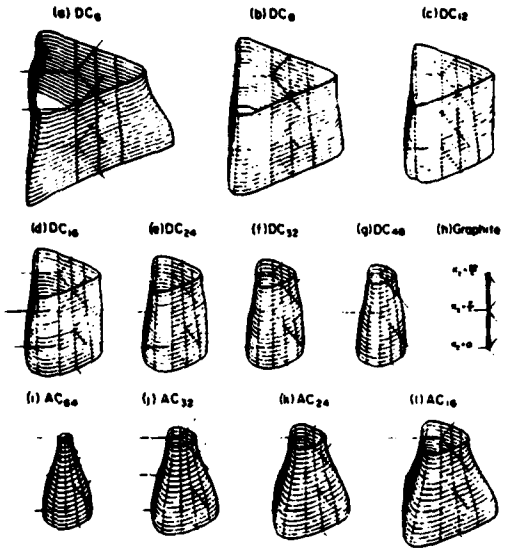

FIG. 10. Constant-energy surfaces of graphite for selected energy levels (see text, Table IV).

For this reason the figures are labeled by the stoichiometries of compounds with 100% charge transfer and the corresponding energy level is derived from the graphite density of states. For example, DC_8 has $\frac{1}{8}$ extra electron per carbon and AC_{24} has $\frac{1}{24}$ extra hole per carbon. Further, AC_{24} could correspond to a stage-two acceptor with 50% charge transfer or a stage-one acceptor with 25% charge transfer. The energy levels corresponding to the figures are given in Table IV along with additional "Fermi"-surface data that in some instances could be used as a guide to bracket the range of values for actual compounds. The double-sheeted surfaces are shown in an extended-zone scheme for clarity.

The constant-energy surfaces show more clearly than the band structure the asymmetry of the bands above and below the Fermi level of graphite. The (d) and (l) figures are approximately the same distance above and below the Fermi level, respectively. The dimples in surface (c) and (d) are caused by the crossover of the upper π bands, which can be seen between M and K. The sharpness of the corners in the larger figures is due to the limited resolution.

V. DISCUSSION

We will now compare our band-structure calculation with other theoretical studies and experimental investigations by focusing on certain key band separations as listed in Table V. The three-dimensional LCAO calculation of Willis *et al.*,[18] is closest to ours for the levels up to and including

TABLE IV. Constant-energy surface properties.

Label (see Fig. 10)		Extra charge per carbon	$E_{const.}$ (eV)	DOS (states per carbon per eV) $N(E_F)$	Lower band ($k_z=0$) dHvA (G)	Lower band ($k_z=0$) Cyclotron mass (m_e)	Upper band ($k_z=0$) dHvA (G)	Upper band ($k_z=0$) Cyclotron mass (m_e)
(a)	DC_6	−0.166 67	−6.010	0.23	4.9×10^7	0.74	7.5×10^7	1.5
(b)	DC_8	−0.125	−6.264	0.19	3.9×10^7	0.62	5.9×10^7	1.05
(c)	DC_{12}	−0.083 33	−6.532	0.11	1.5×10^7	0.49	4.0×10^7	0.67
(d)	DC_{16}	−0.0625	−6.709	0.10	1.8×10^7	0.44	3.1×10^7	0.51
(e)	DC_{24}	−0.041 67	−6.936	0.080	1.1×10^7	0.33	2.2×10^7	0.40
(f)	DC_{32}	−0.031 25	−7.074	0.070	7.0×10^6	0.27	1.7×10^7	0.35
(g)	DC_{48}	−0.020 83	−7.220	0.061	3.5×10^6	0.21	1.3×10^7	0.29
(h)	Graphite	0.0	−8.06	1.2×10^{-4} [a]	5.9×10^4	0.045		
(i)	AC_{64}	+0.015 03	−8.702	0.036	8.8×10^5	−0.093 [b]	1.3×10^7	−0.37
(not shown)	AC_{48}	+0.020 83	−8.758	0.044	1.7×10^6	−0.12	1.6×10^7	−0.43
(j)	AC_{32}	+0.031 25	−8.986	0.055	3.8×10^6	−0.16	2.3×10^7	−0.53
(k)	AC_{24}	+0.041 67	−9.117	0.073	5.9×10^6	−0.20	2.9×10^7	−0.63
(l)	AC_{16}	+0.0625	−9.345	0.098	1.0×10^7	−0.27	4.2×10^7	−0.84

[a] Calculated from the four-parameter model $N(E_f)=(2/\pi^2\sqrt{3})\gamma_1/\gamma_0^2$.
[b] Negative mass indicates hole carriers.

TABLE V. Comparison of band-structure calculations and measurements[a] (eV).

	HRG (KKR) Present results	Cellular sph. sym. Mallet (Ref. 21)	ext. LCAO Batra (Ref. 17)	LCAO Willis *et al.* (Ref. 18)	Sph. symm. Pseudopot. HJ (Ref. 19)	Ext. Hückel Zunger (Ref. 12)	LCAO PE (Ref. 7)	Experiment (Ref.)
$\Gamma_1^+-\Gamma_5^+$ σBW	14.8(16)	17	20.7	16	NA[b]	16.5	14.3	
$\Gamma_5^+-\Gamma_1^+$ occ-unocc	11.76(2.44)	5.4	12.5	12	9	12.5	12.2	11.5±1 (18)
$\Gamma_3^+-\Gamma_3^+$ πBW	18.63(28)	19	15	19	NA	17.5	17.7	
$\Gamma_3^+-\Gamma_2^-$ πsep	1.65(3.8)	2.0	1.3	1.8	NA			0.9±0.3 (35)
$\Gamma_3^+-\Gamma_1^+$	11.3(8.0)	10	16	12.5	NA	16	11.6	11 ±0.3 (35)
$E_f-\Gamma_1^+$ Val. BW	19.5(17.5)	18.6	21.7	20.7	NA	20	19.3	20.6±0.3 (35)
$M_3^+-M_4^-$	4.3(4.4)	4.1	4.5	4.3	4.0	4.8	4.6	4.6 (44)
$M_4^--M_3^+$ K_4-K_2	1.04(3.2)	1.4	0.8	1.3	1.8			1.6 (33)

[a]For optical selection rules see Ref. 71.

[b]NA—not available.

the conduction σ bands. In fact their conduction bands and those of Nagayoshi *et al.*[10] are in the best qualitative agreement with the present work, specifically the crossing of the Σ_1,Σ_4 levels between Γ and M, a feature which is absent from all other studies.

There is also much agreement with the single-layer calculation of Painter and Ellis.[7] This can probably be accounted for by the similarity in the crystal potentials. In all these calculations the same approximation to the exchange potential was used with the same α parameter of 0.76. Samuelson *et al.*[17] used the same prescription but with $\alpha=0.667$ and, while their overall results are similar, the Fermi-level bands have too little dispersion to obtain reasonable estimates of the SWMc parameters. Mallett[21] used a spherically symmetric potential with the cellular method and Haeringen and Junginger[19] used a spherically symmetric pseudopotential. Even though the use of a spherically symmetric potential is not appropriate for graphite these calculations were *ab initio* and could provide a starting point for a more accurate calculation. This conjecture is strengthened by the fact that they are similar in some ways to our muffin-tin band structure. In particular a Γ_1^+ level in Mallett's calculation, just above the σ valence bands, differs by 0.1 eV from a corresponding level in our muffin-tin band structure. This level is strongly affected by the potential away from the atomic cores and moves upward by 9.5 eV when the exact interstitial potential is included.

The SWMc parameters estimated from our band structure are in very good agreement with those obtained experimentally. This is shown in Table VI where parameter values from other calculations are also included. Although the values for γ_3 and γ_5 are slightly smaller than those suggested by experiments, we feel the agreement is remarkable given that the calculation was completely *ab initio*. The results of Nagayoshi *et al.*[11] are also very good, although their potential had an adjustable parameter that was chosen to fit optical data.

Recently, magnetoreflection experiments[65] suggest a negative sign for Δ, in disagreement with our results. Furthermore, our K_4-K_2 separation is somewhat smaller than that suggested by optical studies leading to a smaller value of γ_0. These and other discrepancies might be improved somewhat if the KKR basis was extended to much higher energies. Self-consistency might also improve the agreement with experimental results although we do not expect self-consistency to be as crucial here as for the intercalation compounds. The complexity of our *ab initio* appproach renders the inclusion of self-consistency computationally intractable at the present time. Nevertheless, this calculation is successful, on the one hand, by virtue of the good

TABLE VI. Comparison: experiment and theory SWMc parameters (eV).

	Experiments	Present results	Mallet (Ref. 21)	Batra (Ref. 17)	HJ (Ref. 19)	S. C. LCAO Zunger (Ref. 12)	PE (Ref. 7)	Nagayoshi *et al.* (Ref. 11)
γ_0	3.16	2.92				2.53		2.73
γ_1	0.39	0.27	0.36	0.2	0.41	0.32	0.25	0.32
γ_2	−0.19	−0.022	−0.045	−0.003	−0.043		0.022	
γ_3	0.28	0.15						0.29
γ_4	0.044	0.10						0.15
γ_5	0.038	0.0063	0.0004		0.033		0.003	0.021
Δ	−0.008	0.0079	−0.0009	−0.004	0.42		0.09	−0.017
E_F	−0.024	−0.025						−0.021

agreement with experiments that measure moderately large level separations and, on the other hand, by supplying reasonable SWMc parameters and a Fermi surface that is in quantitative agreement with experimental results.

We conclude that this method should work well for other highly anisotropic materials such as the intercalation compounds of graphite, although extension to self-consistency may be necessary in such cases. Nevertheless, a carefully conceived model for the potential should give reasonable results.

ACKNOWLEDGMENTS

We would like to thank David DiVincenzo and Natalie Holzwarth for their assistance and discussion during the course of this work. We would also like to thank John Fischer and other members of the graphite group for their encouragement and support. Finally, without the patience and good nature of the staff of the Moore School Computing Facility, this work would not have been possible. This work was supported by the National Science Foundation, Materials Research Laboratory program under Grant No. DMR-7923647 and also by ARO Contract No. DAAG-29-80-k-0019.

APPENDIX A: SWMc MODEL

The SWMc Hamiltonian has the form:

$$H=\begin{bmatrix} \epsilon_1^0 & 0 & H_{13} & H_{13}^* \\ 0 & \epsilon_2^0 & H_{23} & -H_{23}^* \\ H_{13}^* & H_{23}^* & \epsilon_3^0 & H_{33} \\ H_{13} & -H_{23} & H_{33}^* & \epsilon_3^0 \end{bmatrix},$$

where

$$\epsilon_1^0=\Delta+2\gamma_1\cos\beta+2\gamma_5\cos^2\beta\,,$$

$$\epsilon_2^0=\Delta-2\gamma_1\cos\beta+2\gamma_5\cos^2\beta\,,$$

$$\epsilon_3^0=2\gamma_2\cos^2\beta\,,$$

$$H_{13}=\frac{\sqrt{3}}{2\sqrt{2}}(2\gamma_4\cos\beta-\gamma_0)a\kappa e^{i\alpha}\,,$$

$$H_{23}=\frac{\sqrt{3}}{2\sqrt{2}}(2\gamma_4\cos\beta+\gamma_0)a\kappa e^{i\alpha}\,,$$

$$H_{33}=\sqrt{3}(\gamma_3\cos\beta)a\kappa e^{i\alpha}\,,$$

$\beta=k_z c/2$, α is polar angle about zone edge ($\alpha=0°$ toward Γ). $\kappa=(k_x^2+k_y^2)^{1/2}$ (origin at K point) and a,c are graphite lattice constants.

This Hamiltonian is based on a perturbation expansion and is valid only for small κ. A good discussion of this and related models can be found in the review article by Spain.[31]

APPENDIX B: JD MODEL

The full-zone π-band expansion for graphite was first introduced by Johnson and Dresselhaus.[16] Since then many variants of this model have been developed and applied to similar systems. Our reference to the JD model stands for the entire class of such expansions. Blinowski *et al.*[66] and Holzwarth[62] used versions of this model appropriate for optical and transport properties of graphite-intercalation compounds (GIC's). Saffran and DiSalvo[67] used essentially a very primitive version of this model to compute magnetic susceptibilities of GIC's.

The particular form used in this work is as follows:

$$H=\begin{bmatrix} H_{AA} & H_{AA'} & H_{AB} & H_{AB'} \\ H^*_{AA'} & H_{AA} & H^*_{AB'} & H^*_{AB} \\ H^*_{AB} & H_{AB'} & H_{BB} & H_{BB'} \\ H^*_{AB'} & H_{AB} & H^*_{BB'} & H_{BB} \end{bmatrix},$$

$$H_{AA}=a^{000}_{AA}(3)+a^{100}_{AA}[\cos(\xi_x)+2\cos(\tfrac{1}{2}\xi_x)\cos(\tfrac{1}{2}\xi_y)]+a^{002}_{AA}[3\cos(2\xi_z)]\,,$$

$$H_{BB}=a^{000}_{BB}(3)+a^{100}_{BB}[\cos(\xi_x)+2\cos(\tfrac{1}{2}\xi_x)\cos(\tfrac{1}{2}\xi_y)]+a^{002}_{BB}[3\cos(2\xi_z)]\,,$$

$$H_{AB}=a^{0\bar{1}0}_{AB}[e^{-i(1/3)\xi_y}+2\cos(\tfrac{1}{2}\xi_x)e^{i(1/3)\xi_y}]+a^{020}_{AB}[e^{i(2/3)\xi_y}+2\cos(\xi_x)e^{-i(1/3)\xi_y}]$$
$$+a^{120}_{AB}[\cos(\xi_x)e^{i(2/3)\xi_y}+\cos(\tfrac{3}{2}\xi_x)e^{i(1/6)\xi_y}+\cos(\tfrac{1}{2}\xi_x)e^{-i(5/6)\xi_y}]\,,$$

$$H_{AB'}=a^{0\bar{1}1}_{AB'}[e^{i(1/3)\xi_y}+2\cos(\tfrac{1}{2}\xi_x)e^{-i(1/6)\xi_y}]\cos\xi_z\,,$$

$$H_{BB'}=a^{0\bar{1}1}_{BB'}[e^{-i(1/3)\xi_y}+2\cos(\tfrac{1}{2}\xi_x)e^{i(1/6)\xi_y}]\cos\xi_z\,,$$

$$H_{AA'}=a^{001}_{AA'}(3\cos\xi_z)\,,$$

where $\xi_x=ak_x$, $\xi_y=a\sqrt{3}k_y$, $\xi_z=\frac{1}{2}ck_z$, and following the definition in the original article, the notation $a^{ijk}_{\alpha\beta}$ denotes the matrix element between sites α and β in unit cells located relative to each other by $T=i\hat{t}_x+j\hat{t}_y+k\hat{t}_z$. The overbar indicates a negative number. A different coordinate system was used here, accounting for the different notation of some of the parameters.

APPENDIX C: SOME CALCULATION DETAILS

This appendix provides a brief description of some of the specific computational aspects concerning the present work. A more general discussion is found in Sec. III and in Ref. 48.

In the first step of the KKR procedure symmetry is used to simplify the evaluation of the matrix elements

$$V_{lm,l'm'}(r)=\int Y^*_{lm}(\hat{r})V(\vec{r})Y_{l'm'}(\hat{r})\,d^2r,\quad |\vec{r}|=\text{const}$$

which appear in the system:

$$\sum_{l'm'}\left\{\left[\frac{-\hbar^2}{2m}\left[\frac{d^2}{dr^2}-\frac{l'(l'+1)}{r^2}\right]-E\right]\delta_{lm,l'm'}+V_{lml'm'}(r)\right\}P^l_{El'm'}(r)=0\,,$$

where

$$P^l_{Elm}(r)=rR^l_{Elm}(r)$$

and

$$\phi^l_E(\vec{r})=\sum_{lm}R^l_{Elm}(r)Y_{lm}(\hat{r})$$

are the solutions to Schrödinger's equation within a muffin-tin sphere. From symmetry we determine which matrix elements are nonzero, then by expanding products of spherical harmonics into crystal harmonics it is possible to further reduce the total number of integrations and stored integrals.

TABLE VII. Relationship between SWMc parameters and JD parameters.

$\gamma_0=-a^{0\bar{1}0}_{AB}+2a^{020}_{AB}+\frac{1}{2}a^{120}_{AB}$
$\gamma_1=\frac{3}{2}a^{001}_{AA'}$
$\gamma_2=3a^{002}_{BB}$
$\gamma_3=\frac{1}{2}a^{0\bar{1}1}_{BB'}$
$\gamma_4=\frac{1}{2}a^{0\bar{1}1}_{AB'}$
$\gamma_5=3a^{002}_{AA}$
$\Delta=3[a^{000}_{AA}-a^{000}_{BB}-\frac{1}{2}(a^{100}_{AA}-a^{100}_{BB})+a^{002}_{BB}-a^{002}_{AA}]$

For graphite $l=2$ expansion, there are 12 nonzero $V_{lml'm'}(r)$ components and these can be expressed in terms of four crystal harmonics, a substantial reduction from the original 45 integrals:

$$V_{lml'm'}(r)=\sum_{\alpha} I^{\alpha}_{lml'm'} \int Z_{\alpha}(\hat{r})V(\vec{r})d^2r \ ,$$

$$|\vec{r}|=\text{const}$$

where the I coefficients are constant and, where

$$Z_1(\hat{r})=1 \ ,$$

$$Z_2(\hat{r})=(\tfrac{5}{4})^{1/2}(3z^2-1) \ ,$$

$$Z_3(\hat{r})=(\tfrac{35}{8})^{1/2}(3y^2-x^2)x \ ,$$

$$Z_4(\hat{r})=(\tfrac{105}{8})^{1/2}[z^4-\tfrac{6}{7}(\tfrac{5}{4})^{1/2}(3z^2-1)-\tfrac{1}{5}] \ ,$$

are from Ref. 68. These crystal harmonics are orthogonal and invariant under the operations of the group D_{3h}. Because of the symmetry we need only perform the angular integrations over a fraction of the unit sphere which for graphite is $\frac{1}{12}$. For convenience we chose a $\frac{1}{4}$ spherical domain.[69]

The Δ_{NM} [see Eq. (2), Ref. 48] matrix elements were computed in an irreducible section of the interstitial region shown in Fig. 11. The integration algorithm was the 3D Gaussian technique described in Ref. 48. The coordinate system was chosen to most conveniently accommodate this step of the calculation.

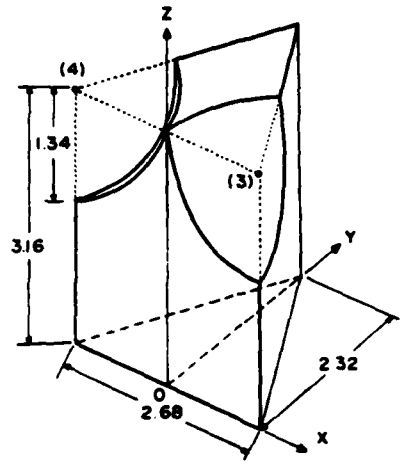

FIG. 11. Interstitial region of irreducible sector. Dimensions are in atomic units.

[1]P. R. Wallace, Phys. Rev. 71, 622 (1947).
[2]C. A. Coulson and R. Taylor, Proc. R. Soc. London Ser. A 65, 815 (1952).
[3]W. M. Lomer, Proc. R. Soc. London Ser. A 277, 330 (1955).
[4]D. F Johnson, Proc. R. Soc. London Ser. A 227, 349 (1955); 237, 48 (1956).
[5]J. C. Slonczewski and P. R. Weiss, Phys. Rev. 109, 272 (1958).
[6]F. Bassani and G. Pastori Parravicini, Nuovo Cimento B 50, 95 (1967).
[7]G. S. Painter and D. E. Ellis, Phys. Rev. B 1, 4747 (1970).
[8]M. Tsukada, K. Nakao, Y. Uemura, and Nagai, J. Phys. Soc. Jpn. 32, 54 (1972).
[9]H. Nagayoshi, M. Tsukada, K. Nakao, and Y. Uemura, J. Phys. Soc. Jpn. 35, 396 (1973).
[10]H. Nagayoshi, K. Nakao, and Y. Uemura, J. Phys. Soc. Jpn. 41, 1480 (1976).
[11]H. Nagayoshi, K. Nakao, and Y. Uemura, Solid State Commun. 10, 225 (1976).
[12]A. Zunger, Phys. Rev. B 17, 626 (1978).
[13]R. Dovesi, C. Pisani, and C. Roetti, Int. J. Quantum Chem. 17, 517 (1980).
[14]P. G. Perkins, A. K. Marwaha, and J. P. Stewart, Theor. Chim. Acta 57 (1980); LCAO (CNDO), self-consistent.
[15]J. W. McClure, Phys. Rev. 108, 612 (1957).
[16]L. G. Johnson and G. Dresselhaus, Phys. Rev. B 7, 2275 (1973).
[17]L. Samuelson, I. P. Batra, and C. Roetti, Solid State Commun. 33, 817 (1980); I. P. Batra and L. Samuelson, Synth. Met. 1, 223 (1979/80).
[18]R. F. Willis, B. Fitton, and G. S. Painter, Phys. Rev. B 9, 1926 (1974).
[19]W. van Haeringen and H. G. Junginger, Solid State Commun. 7, 1723 (1969).
[20]N. A. W. Holzwarth, S. G. Louie, and S. Rabii (unpublished).
[21]C. Mallett, J. Phys. C (GB) 14, L213 (1981).
[22]J. W. McClure, Phys. Rev. 119, 606 (1960).
[23]D. E. Soule, IBM J. Res. Dev. 8, 268 (1964).
[24]S. J. Williamson, S. Foner, and M. S. Dresselhaus, Phys. Rev. 104A, 1429 (1965).
[25]J. A. Woolam, Phys. Rev. B 4, 3393 (1971).
[26]M. S. Dresselhaus and J. G. Mabroides, IBM J. Res. Dev. 8, 262 (1964); Carbon 1, 263 (1964); A. Misu, E. E. Mendez, and M. S. Dresselhaus, J. Phys. Soc. Jpn. 47, 199 (1979).
[27]P. Nozières, Phys. Rev. 109, 1510 (1958).
[28]T. Uda, H. Ushio, and Y. Uemura, J. Phys. Soc. Jpn. 36, 652 (1974).
[29]S. J. Williamson, M. Surma, H. C. Praddaude, R. A. Patten, and J. K. Furdyna, Solid State Commun. 4, 37 (1966).
[30]I. L. Spain, in *Chemistry and Physics of Carbon*, edited

by P. L. Walker and P. A. Thrower (Dekker, New York, 1973), Vol. 8.

[31]I. L. Spain, in *Chemistry and Physics of Carbon*, edited by P. L. Walker, Jr. and P. A. Thrower (Dekker, New York, 1980), Vol. 8.

[32]J. W. McClure, in *Physics of Semimetals and Narrow Bandgap Semiconductors*, edited by D. L. Carter and R. T. Bate (Pergamon, New York, 1971).

[33]R. F. Willis, B. Deuerbacher, and B. Fitton, Phys. Rev. B 4, 2441 (1971).

[34]A. Bianconi, S. B. M. Hagstom, and R. Z. Bachrach, Phys. Rev. B 16, 5543 (1977).

[35]I. T. McGovern, W. Eberhardt, E. W. Plummer, and J. E. Fischer, Physica 99B, 415 (1980).

[36]R. F. Willis and B. Fitton, J. Vac. Sci. Technol. 9, 651 (1972).

[37]J. M. Thomas, E. L. Evans, M. Barber, and P. Swift, Trans. Faraday Soc. 67, 1875 (1971).

[38]J. M. Muller, F. Feser, G. Wiech, and A. Faessler, Phys. Lett. 44A, 263 (1973).

[39]F. R. McFreely, S. P. Kowalczyk, L. Ley, R. G. Cavell, R. R. Pollak, and D. A. Shirley, Phys. Rev. B 9, 5268 (1974).

[40]F. C. Chalkin, Proc. R. Soc. London Ser. A 194, 42 (1948).

[41]E. Tosatti and F. Bassani, Nuovo Cimento 65, 161 (1970).

[42]E. A. Taft and H. R. Philipp, Phys. Rev. 138A, 197 (1965).

[43]S. Ergun, J. B. Yasinsky, and J. R. Townsend, Carbon 5, 403 (1967).

[44]D. L. Greenaway, G. Harbeke, F. Bassani, and E. Tosatti, Phys. Rev. 178, 1340 (1969).

[45]G. Guizetti, L. Nosenzo, E. Reguzzoni, and G. Samoggia, Phys. Rev. Lett. 31, 154 (1973).

[46]W. S. Boyle and P. Nozières, Phys. Rev. 111, 782 (1958).

[47]N. A. W. Holzwarth, S. Rabii, and L. A. Girifalco, Phys. Rev. B 18, 5190 (1978).

[48]D. P. DiVincenzo and S. Rabii, preceding paper, Phys. Rev. B 25, 4110 (1982)

[49]J. D. Bernal, Proc. R. Soc. London Ser. A 106, 749 (1924).

[50]D. Sands, *Introduction to Crystallography* (Benjamin-Cummings, Reading, Mass., 1969).

[51]*International Tables of X-Ray Crystallography*, edited by G. Wycoff (Kynoch, London, 1952).

[52]J. F. Cornwell, *Group Theory and Energy Bands in Solids* (North-Holland, Amsterdam, 1969).

[53]F. Herman and S. Skillman, *Atomic Structure Calculations* (Prentice-Hall, Englewood Cliffs, 1963).

[54]J. C. Slater, *The Self-Consistent Field for Molecules and Solids* (Mc-Graw-Hill, New York, 1974).

[55]K. Schwartz, Phys. Rev. B 5, 2466 (1972).

[56]G. S. Painter, Phys. Rev. B 7, 3520 (1973).

[57]J. Korringa, Physica (Utrecht) 13, 392 91947).

[58]W. Kohn and N. Rostoker, Phys. Rev. 94, 1111 (1954).

[59]J. C. Slater, *Symmetry and Energy Bands In Crystals* (Dover, New York, 1972).

[60]There are various techniques to approximate certain of these integrals. See, for example, D. H. Chadi and M. L. Cohen, Phys. Rev. B 8, 5747 (1973); A. B. Chen, *ibid.* 16, 3291 (1977).

[61]P. R. Bevington, *Data Reduction and Error Analysis for the Physical Sciences* (McGraw-Hill, New York, 1969).

[62]N. A. W. Holzwarth, Phys. Rev. B 21, 3655 (1980).

[63]J. W. McClure, IBM J. Res. Dev. 8, 255 (1964).

[64]K. Nakao, J. Phys. Soc. Jpn. 47, 208 (1979).

[65]W. W. Toy, M. S. Dresselhaus, and G. Dresselhaus, Phys. Rev. B 15, 4077 (1977).

[66]J. Blinowski, N. H. Hau, C. Ragaux, J. P. Vieren, G. Furdin, and J. Melin, J. Phys. (Paris) 41, 47 (1980).

[67]S. A. Saffran and F. J. DiSalvo, Phys. Rev. B 20, 4889 (1979).

[68]D. G. Bell, Rev. Mod. Phys. 26, 311 (1954), reprinted in *Symmetry in the Solid State*, edited by R. S. Knox and A. Gold (Benjamin, New York, 1964), p. 299.

[69]A. M. Stroud, *Approximate Calculation of Multiple Integrals* (Prentice-Hall, Englewood Cliffs, 1971).

[70]E. Mendez, A. Misu, and M. S. Dresselhaus, Phys. Rev. B 21 827 (1980).

[71]R. L. Benbow, Phys. Rev. B 22, 3775 (1980).

Electronic Structure of Third-Stage Lithium Intercalated Graphite

N. A. W. Holzwarth
Corporate Research and Science Laboratories, Exxon Research and Engineering Company, Linden, New Jersey 07036

and

Steven G. Louie
Department of Physics, University of California, Berkeley, California 94720

and

Sohrab Rabii
University of Pennsylvania, Moore School of Electrical Engineering, Philadelphia, Pennsylvania 19104
(Received 24 July 1981)

Self-consistent, first-principles electronic-structure calculations were carried out for LiC_{18}, a model high- (third-) stage graphite intercalation compound. The results illustrate the charge distribution and screening mechanisms in this class of compounds and account for many of their unusual electronic properties. The total charge transferred is found to be well concentrated on the bounding carbon layers, while the conduction-electron contribution is much more delocalized.

PACS numbers: 71.25.Pi, 71.55.Dp

One of the outstanding questions about the electronic structure of graphite intercalation compounds is the distribution of charge among the inequivalent bounding and interior carbon layers in third- and higher-stage compounds. Simple model calculations have suggested that the screening of the intercalant ions by the conduction electrons is much longer range in these π-electron metals than it would be for a two-dimensional free-electron metal.[1,2] Qualitatively, the expectation of long-range screening is due to a phase-space argument and is based on the assumption that the partially filled π bands of the intercalation compound are not appreciably distorted from the corresponding linear dispersion bands of layers of two-dimensional graphite. Within a Thomas-Fermi approximation,[1,2] one can assume that the screening charge is distributed among the layers such that the Fermi energy of each layer is self-consistently adjusted according to the electrostatic potential at that layer. Because a two-dimensional band with linear dispersion can accommodate fewer electrons than the corresponding band with quadratic (free-electron) dispersion for a given Fermi energy, the electrons must be distributed over a larger number of layers. It has been suggested that this long-range screening contributes to the stability of the ordered structures in the high-stage compounds.[2] The charge distribution also has important consequences for the conductivity and other electronic properties of these compounds.[3-6]

There is a delicate balance of several competing factors which determines the charge distribution in addition to the phase-space effect mentioned above. For example, for the donor compounds, the intercalant ions provide a potential which attracts the conduction electrons to the bounding carbon layers. Opposing this effect, the effective attraction is reduced by polarization of valence electrons. In addition, the conduction electrons tend to be delocalized over several layers by their interlayer kinetic energy and by their electron-electron Coulomb repulsions. A realistic evaluation of all of these coupled effects is difficult to treat within a simple model. We have, therefore, carried out a detailed self-consistent electronic-structure calculation for a prototype third-state compound, LiC_{18}. Our results[7] illustrate the unusual properties of these π-electron metals.

Third-state Li-intercalated graphite has been synthesized by a few groups.[8,9] However, its detailed crystal structure is not known and its stoichiometry is perhaps under dispute.[10] It is nevertheless an interesting compound from a theoretical point of view, since it is a third-stage compound for which a detailed band structure can be undertaken with use of present techniques. The structure chosen for this study uses the smallest possible unit cell containing inversion symmetry, yet maintaining a reasonable local geometry for the C and Li atoms: $ABC\gamma CAB\beta BCA\alpha ABC$.[11]

The calculations were carried out self-consis-

tently in the local-density approximation by using a pseudopotential formulation and by representing all the valence-electronic wave functions in terms of a mixed basis set consisting of plane waves and linear combinations of atomic orbitals.[12] The ionic pseudopotentials were generated from all-electron atomic calculations.[13] The exchange-correlation potential was that of Hedin and Lundqvist.[14] To provide bases of comparison, calculations were carried out for graphite and for first-[15] and second-stage lithium-intercalated graphite in addition to the third-stage compound.[7]

For the purpose of quantifying the effects of charge transfer in LiC_{18}, we first considered the electronic structure of graphite itself modified to the LiC_{18} crystal structure (with the Li atoms removed). The band structure near the Fermi level of "modified" graphite is shown in Fig. 1(b) along the M–K–H[16] directions where it is compared with that of graphite in the Bernal structure [Fig. 1(a)].[17] The change in the layer stacking reduces the π-band splitting at the K point to 0.9 eV in modified graphite, compared with 1.5 eV in Bernal graphite, although the intralayer dispersion is similar in the two structures.

In LiC_{18}, the Li atoms arrange themselves in a $\sqrt{3}\times\sqrt{3}$ structure with respect to a graphite layer so that the direction equivalent to that plotted in Fig. 1(b) is M–Γ–A and the corresponding dispersion is plotted in Fig. 1(c). The dispersion due to the M–K bands of modified graphite is readily discernible; the additional bands having larger dispersion are due to zone "folding." The minimum splitting of the π bands due to the interlayer interactions is increased to 1.8 eV in LiC_{18}. The additional 0.9 eV splitting for LiC_{18} relative to that of modified graphite results from the attractive potential of the screened intercalant ions. The uppermost four π bands have amplitudes which are primarily concentrated on the interior layers, while the lower eight π bands are concentrated on the bounding layers.

The total valence charge density of LiC_{18} looks very similar to that of graphite itself because of the large density associated with the C valence electrons. It is more informative to look at the total electronic density difference between LiC_{18} and modified graphite as shown in the contour plot of Fig. 2(a). It is quite evident from Fig. 2(a) that the total density difference is concentrated in the sandwhich region between the C planes surrounding the Li ions. This is not a surprising behavior for a metal. However, it is surprising that the conduction-electron contribution[18] to the density of this π-electron metal [Fig. 2(b)] is much more delocalized than is the total-density difference and is not appreciably distorted from its π-like form. The fact that the conduction states are not distorted by the intercalant ions was noted previously for LiC_6 (Ref. 15) and attributed to the antibonding character of these states. This result (which may contribute to the high conductivity of graphite intercalation compounds) is most likely a general feature. We shall see that the delocalization of the conduction electrons is achieved not only because of the phase-space effect[1,2] but also because of the large polarizability of the valence electrons of graphite.

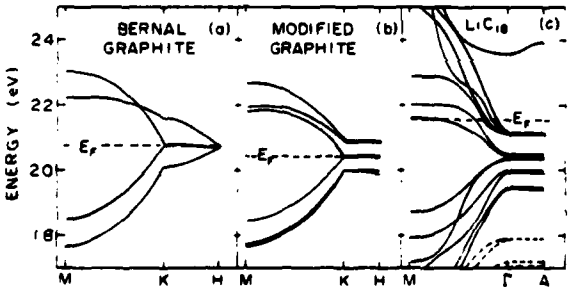

FIG. 1. (a) Energy-band dispersion of the π bands near E_F for graphite in Bernal structure, (b) graphite modified to the structure of LiC_{18}, (c) and for LiC_{18}. The zero of energy has been taken at the bottom of σ bands. In (c), the top of the σ bands (dashed curves) and the bottom of the Li-metal band (top curve) are indicated in the energy range shown.

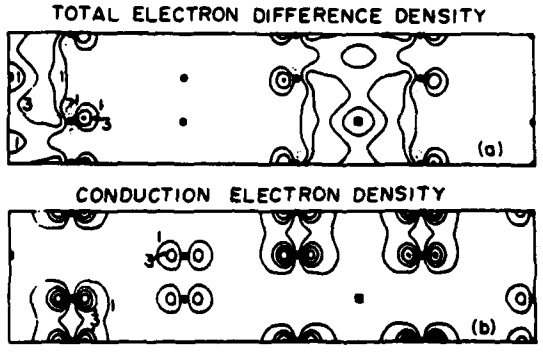

FIG. 2. (a) Contour plot of electronic charge density for LiC_{18} minus that of modified graphite (b) and for the conduction electrons of LiC_{18}. Contour values are given in units of 0.01 electrons/Å^3. Atomic positions are denoted by filled squares for Li and by circles for C. Plane shown contains c axis and passes through Li atoms and C-C bonds.

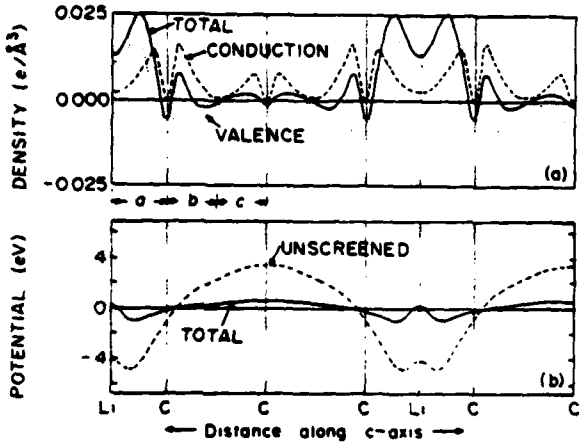

FIG. 3. (a) Electronic charge density (b) and electrostatic potential averaged in layer plane and plotted along the c axis. In (a), the "total" density difference (LiC_{18} minus modified graphite), the "conduction" density (of LiC_{18}), and the "valence" density difference (total minus conduction) are compared. In (b), the zero of the potential is set to be the volume average. The "total" potential difference (LiC_{18} minus modified graphite) is compared with that of the unscreened potential (Li^+ ionic pseudopotentials plus electrostatic potential due to conduction electrons in LiC_{18}).

These points are illustrated more quantitatively in Fig. 3(a), which displays the density along the c axis averaged in the layer planes. In addition to the total density difference and the conduction-electron contribution, the valence density difference[18] is also shown. The polarization of the valence difference density is clearly seen in this plot. A portion of the polarization charge comes from the upper filled π bands. In LiC_{18}, these states are concentrated on bounding layers; whereas in graphite, they are distributed over all layers. But in addition to this transfer of charge within the manifold of π orbitals, there is also a distortion polarization of the graphite valence charge density toward the Li ions.

One can define three distinct regions along the c axis as shown in Fig. 3(a): (a) bounding region, (b) intermediate region, and (c) interior region. The distribution of charge among these volumes is given in Table I. The percentages of charge in the sandwich region (a) are 89% of the total density difference and only 43% of the conduction-electron contribution. The percentages of charge associated with the interior layer (c) are 6% of the total density difference and 19% of the conduction-electron contribution.

The screening effects of these charge distributions are more easily seen in terms of their corresponding electrostatic potentials. In Fig. 3(b) the layer average of the "total" electrostatic potential difference (LiC_{18} minus that of modified graphite) is compared with that of the "unscreened" electrostatic potential (Li^+ pseudopotentials plus electrostatic potential of conduction electrons). We see that the effects of the valence-electron screening are such that averaged total potential is only between $\frac{1}{4}$ and $\frac{1}{8}$ of the averaged unscreened potential throughout the unit cell. The effects of the local-density exchange and correlation contributions are small relative to these electrostatic effects.

Although our detailed calculations[7] have been performed for a specific material, the qualitative conclusions of this study are likely to be generally applicable to graphite intercalation compounds. The results are not inconsistent with known experimental results for third- and higher-stage compounds. For example, measurements of Raman frequencies of intralayer graphite modes of dilute intercalation compounds[19] show a doublet ascribed to bounding- and interior-layer contributions. The interior mode having a frequency nearly equal to that of pure graphite is quite consistent with our qualitative result that the total-density difference is small for the interior layer. On the other hand, transport and Fermi-surface measurements are sensitive only to the conduction-electron distribution and on the basis of the present work, should reflect a more uniform distribution among C layers. Together with the use of models[1-6] to aid in the interpretation of the ex-

TABLE I. Distribution of electronic charge in LiC_{18}. Notation and regions (within half unit cell) as defined for Fig. 3(a).

	Region *a*	Region *b*	Region *c*
Total difference	0.45 electron	0.03	0.03
Conduction electron	0.21	0.19	0.09
Valence difference	0.23	−0.17	−0.07

perimental results for extremal areas of the Fermi surface,[20] magneto-optic spectra, plasma frequencies, densities of states, etc., we hope that the present work will help to establish the distribution of conduction electrons in graphite intercalation compounds.

We would like to thank S. Safran for useful conversations and A. Freeman for pointing out Ref. 17.

A major portion of this work was completed at the University of Pennsylvania and was supported by the National Science Foundation under Materials Research Laboratory Grant No. DMR-79-23647 and by the Army Research Office under Contract No. DAAG-29-77-C400. This work was also supported by National Science Foundation Grant No. DMR-78-22465. One of us (S.G.L.) gratefully acknowledges support from a Sloan Foundation Fellowship.

[1]L. Pietronero, S. Strassler, H. R. Zeller, M. J. Rice, Phys. Rev. Lett. 41, 763 (1978); L. Pietronero, S. Strassler, and H. R. Zeller, Solid State Commun. 30, 305 (1979).

[2]S. A. Safran and D. R. Hamann, Phys. Rev. 22, 606 (1980), and 23, 565 (1981).

[3]J. Blinowski and C. Rigaux, J. Phys. (Paris) 41, 667 (1980).

[4]N. A. W. Holzwarth, Phys. Rev. B 21, 3661 (1980).

[5]L. Pietronero, S. Strassler, H. R. Zeller, and M. H. Rice, Phys. Rev. B 22, 904 (1980).

[6]G. Dresselhaus and S. Y. Leung, Solid State Commun. 35, 819 (1980).

[7]N. A. W. Holzwarth, S. G. Louie, and S. Rabii, Bull. Am. Phys. Soc. 26, 450 (1981).

[8]R. Juza and V. Wehle, Naturwissenschaften 52, 560 (1965).

[9]D. Billaud, E. McRae, and A. Herold, Mater. Res. Bull. 14, 857 (1979).

[10]S. Basu, C. Zeller, P. J. Flanders, C. D. Fuerst, W. D. Johnson, and J. E. Fischer, Mater. Sci. Eng. 38, 275 (1979).

[11]In this notation A,B,C refers to stacking of graphite layers while γ,β,α refers to the stacking of the intercalant layers.

[12]S. G. Louie, K.-M. Ho, and M. L. Cohen, Phys. Rev. B 19, 1774 (1979).

[13]D. R. Hamann, M. Schlüter, and C. Chiang, Phys. Rev. Lett. 43, 1494 (1979).

[14]L. Hedin and B. I. Lundqvist, J. Phys. C 4, 2064 (1971).

[15]N. A. W. Holzwarth, S. Rabii, and L. A. Girifalco, Phys. Rev. B 18, 5190 and 5206 (1978). The differences between the present results for LiC_6 and the earlier calculations can be ascribed to self-consistency and the use of a different exchange-correlation potential.

[16]Notation of C. Herring, J. Franklin Inst. 233, 525 (1942). Pseudo hexagonal symmetry is described with $K-M$ for modified graphite and $\Gamma-M$ for LiC_{18} lying perpendicular to the reflection symmetry plane.

[17]Results for the occupied bands of graphite in the Bernal structure agree well with the overall experimentally determined band features to within ± 0.2 eV. Moreover, the valence charge density of the present results is in quantitative agreement with the experimentally derived valence charge density analyzed by R. Chen, P. Trucano, and R. F. Stewart, Acta Crystallogr., Sect. A 33, 823 (1977).

[18]We have defined the conduction-electron density as that contributed by partially occupied bands in LiC_{18}. The valence density difference is defined as the total density difference minus the conduction-electron contribution.

[19]J. J. Song, D. D. L. Chung, P. C. Eklund, and M. S. Dresselhaus, Solid State Commun. 20, 1111 (1976); R. G. Nemanich, S. A. Solin, and D. Guerard, Phys. Rev. B 16, 2965 (1977).

[20]The analysis of magneto-oscillatory data for graphite intercalation compounds is complicated by the appearance of extra signals and by the difficulty of detecting the high-frequency signals as has been recently pointed out by the detailed study of second-stage AsF_5 intercalated graphite by R. S. Markiewicz, H. R. Hart, Jr., L. V. Interrante, and J. S. Kasper, Synth. Met. 2, 331 (1980); J. E. Fischer, M. H. Moran, J. W. Milliken, and A. Briggs, Solid State Commun. 39, 439 (1981).

PHYSICAL REVIEW B VOLUME 26, NUMBER 10 15 NOVEMBER 1982

X-ray form factors and the electronic structure of graphite

N. A. W. Holzwarth*
Corporate Research-Science Laboratories, Exxon Research and Engineering Company, Linden, New Jersey 07036

Steven G. Louie
Department of Physics, University of California, Berkeley, California 94720

Sohrab Rabii
University of Pennsylvania, Moore School of Electrical Engineering, Philadelphia, Pennsylvania 19104
(Received 23 February 1982)

The bonding and spectroscopic properties of graphite are investigated by carrying out first-principles, self-consistent electronic structure calculations, and by comparing the results with high-resolution data from recent x-ray diffraction and angle-resolved photoemission measurements. The theoretical valence-charge density is in excellent agreement with values derived from experimental x-ray form factors. Unlike other group-IV covalent materials, the bonding charge exhibits a prominent double-humped structure due to the lack of *p* core states. The energy band structure is also in good agreement with experimental measurements and previous calculations.

I. INTRODUCTION

Graphite intercalation compounds and adlayers of atoms on graphite have generated a great deal of theoretical and experimental interest in the past several years. These systems have potentially important technological applications, and they also provide realistic situations for the fundamental study of two-dimensional phenomena. As a consequence, renewed interest in the properties of graphite itself has been stimulated. There is, in fact, a very large literature on the electronic properties of graphite, including electron-density maps derived from x-ray diffraction data[1] and the energy-band measurements derived from high-resolution angle-resolved photoemission techniques.[2] There is also a very large number of theoretical calculations on the electronic structure of graphite. However, some features of the theoretical results are model dependent.

In the present paper we present the results of first-principles self-consistent calculations of the electronic structure of graphite, with the use of density-functional theory[3] in the local-density approximation[4] and mixed-basis pseudopotential techniques.[5] Our motivation is (1) to provide a deeper understanding of the bonding and spectroscopic properties of graphite and (2) to provide a basis of comparison for a study of graphite intercalation compounds using the same theoretical framework and computational techniques. Results for the intercalation compounds are published elsewhere.[6,7] The remainder of the paper is organized as follows. In Sec. II details of the calculation method are presented. In Sec. III the calculated distribution of valence-electron density is presented and compared with that derived from the analysis of x-ray diffraction experiments by Chen, Trucano, and Stewart.[1] The self-consistent valence density is also compared with that of superposed spherical atomic charge densities in order to illustrate aspects of the C−C bonding. In Sec. IV the calculated band structure is presented and compared with various spectroscopic measurements of band energies[2,8−10] and compared with a few of the previous calculations.[11−16] We do not attempt to make a thorough comparison of our band-structure results with the numerous results available in the literature, since this has been done by several other workers.[13−15] We are able, however, to understand how certain band features are sensitive to calculations methods, to self-consistency, and to the choice of the exchange-correlation approximation, as well as to establish our electronic structure of graphite as a credible one. Summary and conclusions are presented in Sec. V.

II. METHODS OF CALCULATION

The self-consistent band-structure calculations were carried out in the local-density approximation

and by representing the electron wave functions in terms of a mixed-basis set consisting of plane waves and linear combinations of atomic orbitals (LCAO's) as developed by Louie, Ho, and Cohen.[5] To take advantage of the numerical efficiency of a Fourier-space evaluation of the matrix elements, the calculations were formulated in terms of pseudopotentials and pseudo-wave-functions. The Hedin-Lundqvist[4] approximation for the exchange-correlation potential was used throughout this work.

A. Pseudopotential

We chose to use the norm-conserving pseudopotentials developed by Hamann, Schlüter, and Chiang.[17] This form of pseudopotential has the following advantages:

(1) the pseudopotential being energy independent over a reasonable energy range,

(2) the pseudo-wave-functions converging to the actual wave functions outside spheres of specified radii about each atom, and

(3) the integrated "pseudocharge" being equal to the integrated actual charge in the core regions.

Within the framework of the norm-conserving pseudopotentials of Hamann *et al.*,[17] there is some leeway in the choice of the functional form of the pseudopotentials in the core regions. For reasons of numerical efficiency, we have chosen a functional form that would ensure (a) that the Fourier transform of the pseudopotentials would have minimal extent as a function of reciprocal-lattice wave vector and (b) that the radial dependence of the nonlocal pseudopotential would have approximately Gaussian form. Since for the elements of interest in the present work, namely, C and Li, only *s*- and *p*-wave interactions are appreciable, we have followed the standard practice of approximating the *d*-wave and higher angular momenta interactions with the *s*-wave pseudopotential. This approximation has been proven to be reasonable for most semiconductors.

The *s*-wave atomic pseudopotentials were generated from the all-electron atomic potentials $V_A(r)$ using the following two-step procedure.[17] First the pseudopotential was set equal to the functional form

$$\Phi_0^{(1)}(r)=V_A(r)\{1-\exp[(-r/r_0')]\}+c_0\exp[-(r/r_0)^2]\ . \tag{1}$$

Here the constant c_0 was chosen so that the pseudopotential $\Phi_0^{(1)}(r)$ had a (nodeless) bound-state wave function $W_0^{(1)}(r)$ at the all-electron valence energy E_0. The pseudopotential radii r_0' and r_0 were chosen so that the pseudopotential would converge to the all-electron potential in the bonding region of the crystal. In the second step the pseudo-wave-function was modified so that it converged to the all-electron wave function for $r>r_l$, using the functional form

$$W_l^{(2)}(r)=\gamma_l W_l^{(1)}(r)+\delta_l r^l\exp[-(r/r_l)^2]\ , \tag{2}$$

where $l=0$ for *s* wave, and γ_l and δ_l are constants. The final atomic pseudopotential is then determined by inverting the Schrödinger equation for the pseudopotential corresponding to the pseudo-wave-function $W_l^{(2)}(r)$

$$\Phi_l^{(2)}(r)=\frac{\left[\frac{\hbar^2}{2m}\left[\frac{1}{r^2}\frac{d}{dr}r^2\frac{d}{dr}-\frac{l(l+1)}{r^2}\right]+E_l\right]W_l^{(2)}(r)}{W_l^{(2)}(r)} \tag{3}$$

The *p*-wave pseudopotential was generated by a similar two-step procedure, except that, for numerical reasons, in order to simplify the nonlocal potential contributions, the first-step *p* pseudopotential was taken to be of the form

$$\Phi_1^{(1)}(r)=\Phi_0^{(2)}(r)+c_1\exp[-(r/r_1)^2]\ . \tag{4}$$

Once the neutral atomic pseudopotentials were obtained, the ionic pseudopotentials $\Phi_0^I(r)$ and $\Phi_1^I(r)$ were determined[17] by subtracting the valence-electron screening potentials due to Hartree and exchange-correlation interactions. The configuration $2s^1p^3$ was used to generate the carbon pseu-

TABLE I. Numerical parameters used in computation.

Pseudopotential parameters		Carbon	Lithium
r_0 $(=r_0')$	[Eq. (1)]	0.7 bohr	1.5 bohr
r_l	[Eq. (4)]	0.55 bohr	1.5 bohr
q_l^2	[Eq. (11)]	2.1 bohr^{-2}	0.35 bohr^{-2}
Basis-set parameters			
Plane waves		$0\le\lvert\vec{k}+\vec{G}\rvert^2\le 3$ bohr^{-2}	
Fourier expansion of localized orbitals		$0\le\lvert\vec{k}+\vec{G}\rvert^2\le 25$ bohr^{-2}	

dopotential, and the configuration $2s^{1/2}2p^{1/2}$ was used to generate the lithium pseudopotential; however, several other atomic configurations yielded virtually the same ionic pseudopotentials. The pseudopotential parameters used in the present work are listed in Table I.

B. Numerical methods of the mixed-basis band-structure calculations

The numerical methods used in the present work are for the most part described in Ref. 5. The orbitals used to construct the LCAO components of the basis set were the valence-electron pseudo-wavefunctions with radial components $W_l^{(2)}(r)$ described above. For both C and Li, LCAO Bloch functions were constructed for each of the s and p valence orbitals. The convergence requirements of the basis set in the present work were determined primarily by the C pseudopotentials. Therefore, it was appropriate to check convergence using the diamond band structure. Using the range of plane waves and the range of reciprocal-space expansion of the LCAO wave functions listed in Table I, eigenvalues were converged to within a maximum error of 0.2 eV.[18] It was necessary to permit this relatively large error in order to keep the computation time within reason for the high-stage intercalation compounds. We found our choice of numerical LCAO functions to be preferable to Gaussian orbitals. In a limited test using the diamond band structure, we found that the use of single Gaussian LCAO's required the inclusion of more plane waves to achieve comparable convergence.

Because the local orbitals $W_l^{(2)}(r)$ extend beyond a single site, the on-site approximation described in Ref. 5 could not be used in the present work. Consequently, the most time consuming part of the calculation was the evaluation of matrix elements of the pseudopotential between LCAO functions. The matrix elements of the local pseudopotentials (s-wave part of ionic pseudopotentials plus Hartree and exchange-correlation contributions of the valence electrons) were evaluated using the fast-Fourier-transform technique. This technique is essentially an efficient trapezoidal-rule integration throughout the unit cell. The integration mesh is determined by the inverse of the maximum reciprocal-space range $Q_{\max}$ of the matrix-element components. The component having the largest reciprocal-space range in the present work is the C s-wave ionic pseudopotential with $Q_{\max} \approx 8$ bohr^{-1}.

The contributions of the nonlocal pseudopotential (p-wave ionic pseudopotential minus s-wave ionic pseudopotential) to the matrix elements were evaluated using a separable-form approximation described below. The matrix element of the nonlocal pseudopotential between two LCAO basis functions, with Fourier components denoted by $W_i(\vec{q})$, is given by

$$\langle i \mid V_{\rm NL} \mid j \rangle = \sum_{\vec{G},\vec{G}'} W_i^*(\vec{k}+\vec{G}) V_{\rm NL}(\vec{k}+\vec{G},\vec{k}+\vec{G}') \times W_j(\vec{k}+\vec{G}') , \tag{5}$$

where $V_{\rm NL}(\vec{k}+\vec{G},\vec{k}+\vec{G}')$ is the plane-wave matrix element of the nonlocal potential. The idea of the separable form is that the plane-wave matrix element is approximated by

$$V_{\rm NL}(\vec{k}+\vec{G},\vec{k}+\vec{G}') \approx \sum_{\mu,\nu=0}^{M} A_{\mu\nu} f_\mu^*(\vec{k}+\vec{G}) f_\nu(\vec{k}+\vec{G}') , \tag{6}$$

where $f_\nu(\vec{k}+\vec{G})$ are specified functions and $A_{\mu\nu}$ are constant coefficients, so that Eq. (5) becomes

$$\langle i \mid V_{\rm NL} \mid j \rangle \approx \sum_{\mu,\nu=0}^{M} A_{\mu\nu} F_\mu^{i*} F_\nu^j , \tag{7}$$

with

$$F_\nu^j \equiv \sum_{\vec{G}'} f_\nu(\vec{k}+\vec{G}') W_j(\vec{k}+\vec{G}') . \tag{8}$$

Provided that the number of significant coefficients $A_{\mu\nu}$ are kept small, Eq. (7) is then more efficient to evaluate than the direct form [Eq. (5)].

The plane-wave matrix element of the nonlocal potential is given by

$$V_{\rm NL}(\vec{k}+\vec{G},\vec{k}+\vec{G}') = \frac{(4\pi)^2}{\Omega} \sum_{\vec{\tau}} e^{-i(\vec{G}-\vec{G}')\cdot\vec{\tau}} \Phi_l^{\vec{\tau}}(\mid \vec{k}+\vec{G} \mid, \mid \vec{k}+\vec{G}' \mid) \sum_M Y_{lM}^*(\hat{k}_G) Y_{lM}(\hat{k}_{G'}) , \tag{9}$$

where

$$\Phi_l^{\vec{\tau}}(\mid \vec{k}+\vec{G} \mid, \mid \vec{k}+\vec{G}' \mid) \equiv \int_0^\infty r^2 dr\, j_l(\mid \vec{k}+\vec{G} \mid r) j_l(\mid \vec{k}+\vec{G}' \mid r) [\Phi_{\vec{\tau}l}^l(r) - \Phi_{\vec{\tau}0}^l(r)] . \tag{10}$$

In Eqs. (9) and (10) Ω is the unit-cell volume, τ represents the atomic site, l represents the angular momentum of the nonlocal potential ($l=1$ in the present work), and $\hat{k}_G \equiv (\vec{k}+\vec{G})/|\vec{k}+\vec{G}|$. It is apparent from Eq. (9) that the separable approximation need only be made to the function $\Phi_l^\tau(q,q')$, since the other factors are already in separable form. The choice of separable functions is not unique. Our choice was

$$\Phi_l^\tau(q,q') \simeq \sum_{n,n'=0}^{N} \mathscr{C}_{nn'}^{\tau l}\{\exp[-(q^2+q'^2)/4q_{\tau l}^2]\}q^{l+2n}(q')^{l+2n'} , \tag{11}$$

where

$$\mathscr{C}_{nn'}^{\tau l} \equiv \sum_{\nu=0}^{n}\sum_{\nu'=0}^{n'} \mathscr{E}_{n-\nu}J_\nu \mathscr{E}_{n'-\nu'}J_{\nu'} \int_0^\infty r^2 dr\, r^{2l+2\nu+2\nu'}[\Phi_{\tau l}^l(r)-\Phi_{\tau 0}^l(r)] ,$$

$$\mathscr{E}_n \equiv [n!(4q_{\tau l}^2)^n]^{-1} \text{ and } J_n = [(-2)^n n!(2l+2n+1)!!]^{-1} .$$

This form of the separable function has one adjustable parameter for each nonlocal potential, the range parameter $q_{\tau l}$. The expansion (11) is absolutely convergence when the radial part of the nonlocal potential takes the Gaussian form $\exp(-q_{\tau l}^2 r^2)$. We found this choice of separable functions using $q_{\tau l} \approx r_{\tau l}^{-1}$ to be adequate for both C and Li, although care had to be exercised for possible divergences at large q. Here $r_{l\tau}$ is the pseudopotential radius defined in Eqs. (1) and (2).

The charge density of the occupied states for each iteration in the self-consistent process was evaluated as described in Ref. 5. Because of the existence of partly filled bands, midpoint sampling algorithms were more appropriate than special point algorithms, since the latter are heavily dependent upon the continuity of the integrand and of its derivatives. For LiC_{12} and LiC_{18}, a 19-point midpoint sampling was used within the irreducible sectors ($\frac{1}{4}$) of the Brillouin zones. Equivalent or better samplings were used for LiC_6 and graphite.

III. VALENCE-ELECTRON-DENSITY DISTRIBUTION

Graphite has the Bernal[19] structure with D_{6h}^4 symmetry and four atoms and two inequivalent types per unit cell. The atoms are arranged in layers of hexagonal lattices with lattice constant $a=2.46$ Å; the separation between layers is $c/2=3.35$ Å. Adjacent layers are shifted in an *ABAB* stacking such that half of the carbon atoms (type *a*) are directly above and below carbon atoms in the adjacent layers, while half (type *b*) are directly above and below centers of carbon hexagons in the adjacent layers.

Graphite is one of the few materials for which a detailed analysis of the x-ray diffraction data has been performed in terms of the valence-electron density.[1] In Fig. 1(a), the results of our self-consistent electronic structure calculations for the valence-electron density is presented in comparison with the density generated by the most refined fit to the x-ray form factors[1] [Fig. 1(b)]. The overall agreement between the two density distributions is excellent: $\pm 0.15 e/\text{Å}^3$ throughout the entire unit cell, close to the experimental accuracy. The experimental density is generally higher than the calculated density. A contributing factor to this trend is the fact that the experimental fitting parameters were not constrained to the total number of electrons. The set of parameters[1] used to generate

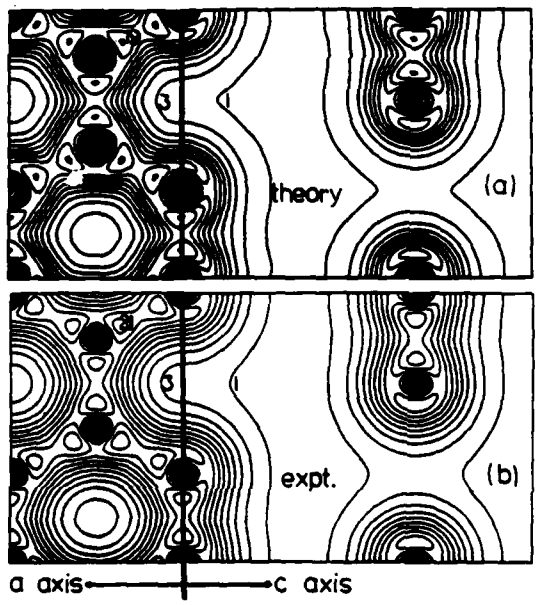

FIG. 1. Contour plots of valence-electronic-charge density for graphite: (a) Present results, and (b) results from analysis of x-ray data by Chen, Trucano, and Stewart (Ref. 1). Contour values are given in units of $0.1 e/\text{Å}^3$. Atomic positions are denoted by filled circles. Two planes are shown—one containing an *a* axis and the other containing the *c* axis and both intersecting at 90° along a C−C bond. In (a) the dashed circle denotes the pesudopotential radius. In (b) the authors quote a standard deviation of $\pm 0.1 e/\text{Å}^3$.

Fig. 1(b) overestimates the total density by $0.034e/\text{Å}^3$. Since ours is a pseudocharge density, the shape of the density within the pseudopotential radius [indicated in Fig. 1(a) by a dashed circle] is not simply related to the real electron density. However, the integral of the real charged within the same region.[17] The experimental determination of the valence charge near the core region is also somewhat less accurate since the core contribution has been assumed to have a particular form and did not enter into the experimental fit. The difference between the two distinct carbon sites is very slight—negligible in the calculated density and smaller than the standard deviation in the experimentally derived density. This indicates that the ground-state density is rather insensitive to the interlayer structure. This insensitivity was also shown by Posternak, Wimmer, and Freeman[20] who reported favorable agreement of their calculated electron density for a single graphite layer with the experimental results of Ref. 1.

Figure 1 illustrates the highly anisotropic structure of the graphite valence density and the large concentration of charge that constitutes the C−C bonds. The density along the bond exhibits a double-humped feature with peak densities of roughly $2.1e/\text{Å}^3$, 10% higher than the density at the bond center. This distinctive feature of the C−C bond has also been seen in diamond[21,22] and is very likely to be due to the competing effects of the *s*- and *p*-wave ionic pseudopotentials. For carbon, the *p*-wave ionic pseudopotential is significantly more attractive than is the *s*-wave ionic pseudopotential. For group IV, materials in the third and higher rows of the Periodic Table, such as Si, Ge, and Sn, the existence of *p*-core states causes the *p* and *s* pseudopotentials to have roughly equal strength and the covalent bonds do not exhibit a double-humped feature.

It is informative to consider the formation of the graphite bonds by comparing the experimental density with that due to the superposed density of spherical carbon atoms as shown in Fig. 2. Even though the atomic configuration has been taken as sp^3 (sp^2 plus p_z), the superposed density is not nearly as concentrated along the bonding directions as is the actual graphite density. The superposed density has a peak of $1.8e/\text{Å}^3$ in a nearly spherical region about each carbon atom in contrast to the higher peak values along bond directions exhibited in the actual graphite density. The maximum density at the midpoint of the C−C bond is 30% smaller for the superposed density than that of graphite.

From the Coulombic and exchange-correlation potentials generated from the superposed atomic valence density of Fig. 2 and the ionic pseudopotentials of the C^{4+} ions, one obtained the first-iteration charge density shown in Fig. 3. From this figure, it is apparent that the first-iteration charge density is close to that of the final-iteration density shown in Fig. 1(a) and within the standard deviation of the experimental density shown in Fig. 1(b). Within this point of view, it is apparent that the ionic potentials are the dominant factor which concentrate charge in the bond region of graphite and that the precise shape of the screening charge plays a secondary role. On a somewhat finer scale, we can compare the first- (Fig. 3) and last- [Fig. 1(a)] iteration charge densities to see that the first-iteration density is overconcentrated in the bond region. The self-consistent density is slightly more extended into the nonbonding regions. This behavior is also reflected in changes in the energy bands as a function of iteration, as will be discussed in Sec. IV.

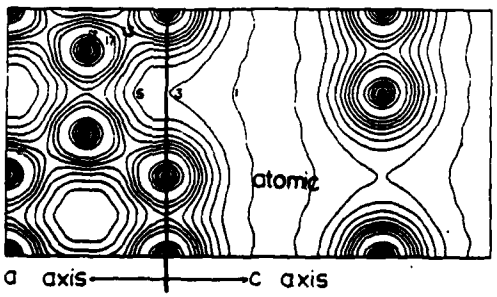

FIG. 2. Contour plot of superposed valence-electron-charge density of sp^3 carbon atoms in the graphite structure. Contour values are given in units of $0.1e/\text{Å}^3$. Atomic positions are denoted by filled circles. The two planes shown are as in Fig. 1.

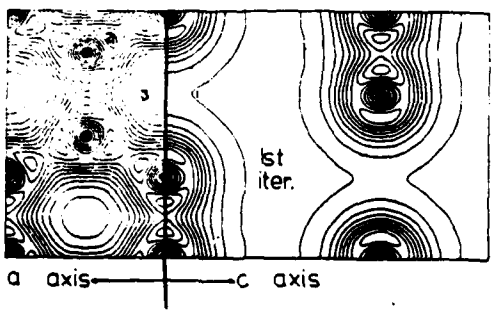

FIG. 3. Contour plot of first-iteration valence-electronic-charged graphite in units of $0.1e/\text{Å}^3$. Atomic positions are denoted by filled circles. The two planes shown are as in Figs. 1 and 2.

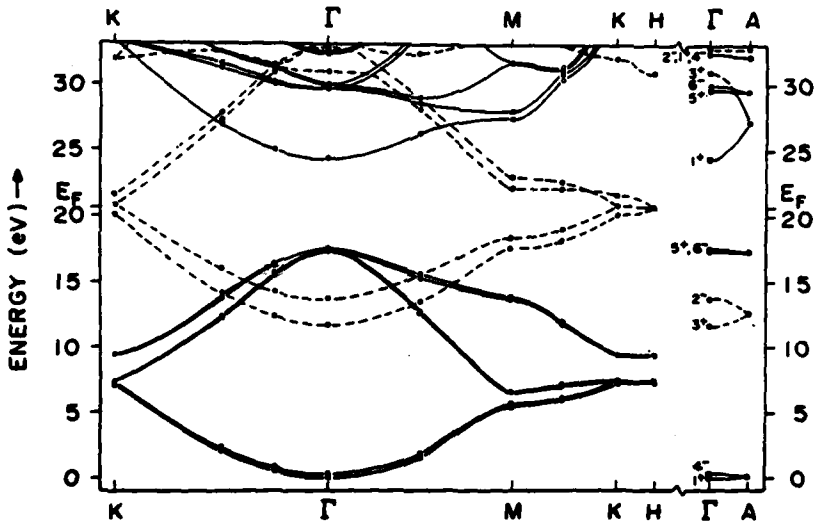

FIG. 4. Self-consistent band structure of graphite (Hedin-Lundqvist exchange-correlation potential). Dashed lines denote π bands, solid lines denote σ bands.

IV. BAND STRUCTURE

The band structure of graphite has been reported by many authors. Within these reported results, there are 1–2-eV variations in the calculated σ- and π-band extrema, and in the splitting of the π bands due to interlayer interactions. It is our opinion that most of the calculated band dispersions are generally consistent with the available experimental data. However, as will be discussed below, we can identify some of the factors which cause these discrepancies.

TABLE II. Band energies (in eV) for graphite.

	Present results Hedin-Lundqvist	Slater	Previous calculations		Experimental
Γ-point states					
bottom σ band[a]	0	0	0[b]	0[c]	0[d]
	0.3	0.2	0.5[b]	0.3[c]	
bottom π band	11.7	12.9	12.5[b]	11.3[c]	12.5[d]
	13.7	14.5	14.2[b]	13.0[c]	13.4[d], 16.8[e]
top σ band	17.4	17.2	16.1[b]	15.2[c]	16.0[d]
	17.5	17.4		15.2[c]	
unoccupied σ bands	24.5	26.9	28.3[b]	26.6[c]	
	29.8	30.1	28.0[b]	26.8[c]	27.5[f]
	30.1	30.4	28.7[b]	26.8[c]	
E_F	20.8	21.5	20.5[b]	19.5[c]	20.6[d], 22.5[e]
π bands near E_F[g]					
$E_2^0-E_3^0$	0.7	0.5	0.44[h]	0.44[c]	0.72[i]
$E_3^0-E_1^0$	0.8	0.6	0.55[h]	0.61[c]	0.84[i]

[a]Lowest σ band chosen as zero of energy; all energies in eV.
[b]Reference 12.
[c]Reference 13.
[d]Angle-resolved photoemission, Ref. 2.
[e]Angle-integrated photoemission, Ref. 10.
[f]Reference 8.
[g]Notation of Slonczewski and Weiss, Ref. 23.
[h]Reference 11.
[i]Reference 9.

The present band-structure results calculated using the Hedin-Lundqvist[4] exchange and correlation potentials are given in Fig. 4. Various features of our results[18] are compared with some previous calculations and experiments in Table II. In general, the present results for the occupied bands are consistent with the previous literature. The splitting of the bands at the K point near the Fermi level is in good agreement with experiment although the detailed 0.01-eV dispersions of the Fermi-level bands along the K-H direction[14,23] are beyond the accuracy of the present calculations. The total valence-band width (20.8 eV), the σ-band width (17.3 eV), and the σ-π band separations [12.7 eV (bottom) and 4.8 eV (top)] are within a few electron volts of previous calculations[11–16] and of angle-resolved photoemission measurements.[2] In fact, the spread in previously calculated results, as well as the uncertainties introduced in the photoemission process in determining these high-binding energy-band features, are also on the order of a few electron volts. We find that the bottom of the π band is split by 2.0 eV due to interlayer interactions, whereas the σ bands (which are highly concentrated near the carbon layers) are being split considerably less. The present value of the π-band splitting is consistent with previous calculations[11–16] but twice that inferred from photoemission.[2] The photoemission value is a lower limit due to the effects of c-axis dispersion which enter for the geometry of the experiment.

The most puzzling feature of the present results is the location of the first unoccupied σ band. This band, which has a band minimum of character Γ_1^+, is of particular importance to the Li intercalation compounds since it would strongly hybridize with the bottom of the Li $2s$ band. In our results, using the Hedin-Lundqvist exchange-correlation approximation, this Γ_1^+ band is 2–4 eV below previously calculated values. However, since this feature is the minimum of a parabolic band, it may not be experimentally detectable. The band contributes a very low density of states and is, therefore, not easily detected in reflectivity measurements.[24,25] Moreover, it would be located below the vacuum level so as not to be accessible to photoemission measurements. An examination of the electron-density distribution for this state shows that it has an extra node near each carbon ion and is highly concentrated in the region between the two carbon planes. In LCAO language, one would be tempted to label this state as the bottom of the carbon $3s$ band. We find that the inclusion of plane waves in the mixed-basis set is essential to the proper description of this state; their omission significantly shifts its energy position. The Γ_1^+ state for an inadequate basis set is forced to have a higher energy than it does in a converged basis expansion such as used in the present work. However, basis-set completeness does not explain the entire discrepancy; a recent Korringa-Kohn-Rostoker calculation, in which muffin-tin corrections were included and all expansions were well converged,[13] showed this state to be 2 eV higher than in the present results. As will be discussed below, the remaining discrepancy can be attributed partly to self-consistency and partly to the use of different exchange-correlation approximations.

The effects of self-consistency on the band energies (at the zone center) are illustrated in Fig. 5. The diagram on the left of the figure illustrates the results for graphite using the Hedin-Lundqvist exchange-correlation approximation.[4] The three diagrams on the right of the figure present the analogous results for three stages of Li-intercalated graphite. The extra bands in the Li-intercalated compounds are caused by zone folding due to the Li superlattice. It is interesting to note that the trends seen in the intercalation compounds are similar to that seen in graphite itself. This can be understood since Li only contributes one electron compared with 24, 48, or 72 carbon electrons, respectively, for stage-1, -2, and -3 Li-intercalated graphite. Thus

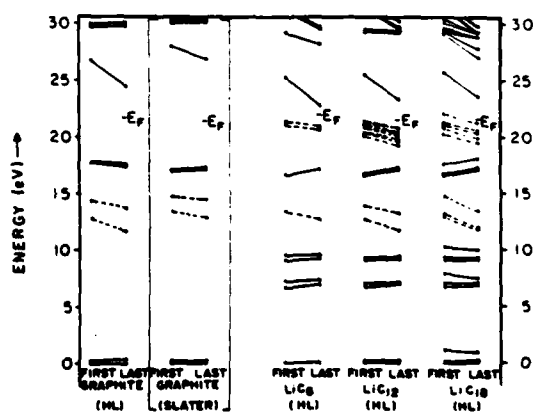

FIG. 5. Energy-level diagram showing the effects of self-consistency on the Γ-point levels for the first-iteration (FIRST) and self-consistent (LAST) potentials. HL denotes Hedin-Lundqvist exchange-correlation approximation, while SLATER denotes Slater's approximation. The last three panels of the figure show the results for three stages of Li-intercalated graphite. Dashed lines denote π bands, solid lines denote σ bands.

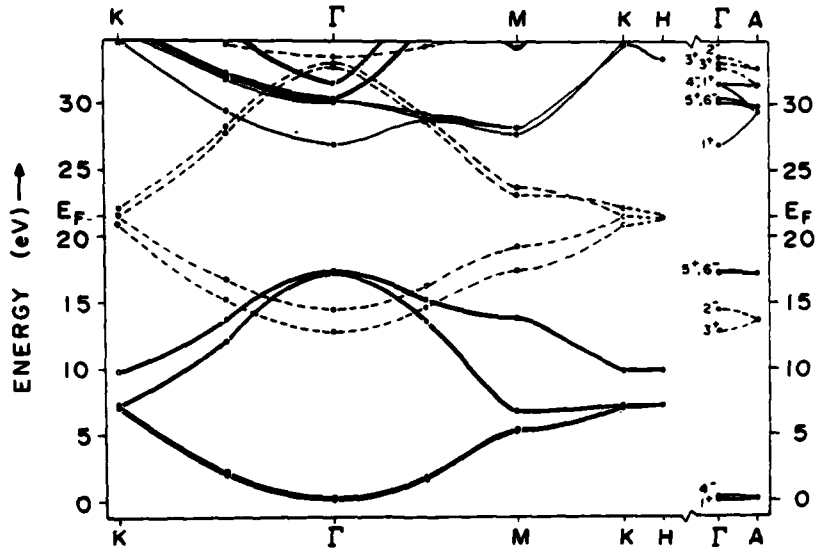

FIG. 6. Self-consistent band structure of graphite for Slater's exchange-correlation approximation. Dashed lines denote π bands, solid lines denote σ bands.

the major changes in the self-consistency process are those for the carbon electrons.

The energy shifts between the non-self-consistent and self-consistent energy-bands result from the charge-density changes shown in Figs. 1–3. Namely, the superposed atomic density (Fig. 2) is too diffuse to self-consistently screen the ionic potential of the crystal. The resulting first-iteration charge density (Fig. 3) is overconcentrated in the bonding regions. (The corresponding energy bands are shown in the far-left portion of Fig. 5.) By the final iteration, the charge [Fig. 1(a)] has relaxed slightly into the nonbonding regions, and the π bands become lowered in energy. The unoccupied Γ_1^+ band is lowered by 3 eV in energy during the self-consistency iteration. The lowering of the energy of the π and Γ_1^+ states, which have appreciable extent in the region between the carbon planes, is affected mainly by the exchange-correlation potential which becomes more attractive with increasing electron density. It is important to have a complete basis set to correctly describe the self-consistent screening charge.

The effects of the exchange-correlation approximations on the bands of graphite were studied by performing a self-consistent calculation using Slater's exchange approximation.[26] The Hedin-Lundqvist exchange-correlation potential is generally less attractive than the Slater exchange potential by a density-dependent factor that varies from $\frac{2}{3}$ (at high density) to 1.2 (at low density). For the densities appropriate to graphite, the factor varies only from 0.7 in the bonding region to 0.9 between carbon planes. As a result, the Slater exchange-correlation potential is systematically more attractive in the bonding region so that the self-consistent density is more concentrated in the bonding regions than is the density derived from the Hedin-Lundqvist form. The resulting zone-center eigenvalues are illustrated in the second panel of Fig. 5 and the complete band structure is given in Fig. 6. The band energies are also listed in the second column of Table II. It is evident that concentration of the wave functions of the occupied states into the bonding region causes the splitting of the bottom of the π band to decrease by 0.5 eV and causes the unoccupied Γ_1^+ band to move up by 2.5 eV in energy. The splitting of the bands near the Fermi level for the Slater approximation is in slightly poorer agreement with experiment than is the splitting for the Hedin-Lundqvist approximation.

V. SUMMARY

This study has demonstrated that self-consistent local-density calculations for graphite are capable of determining electron-charge-density distributions in

quantitative agreement with experiment. Although the Hedin-Lundqvist form of the exchange-correlation function is a more sophisticated approximation than is the Slater function, both results are consistent with the x-ray data, as is the first-iteration (non-self-consistent) charge density. The energy bands are somewhat more sensitive to these factors, and the self-consistent Hedin-Lundqvist bands agree best with experimental determination of the bands near the Fermi level. We have successfully established our results as a reasonable basis of comparison for intercalation compounds of graphite.

ACKNOWLEDGMENTS

We would like to thank R. C. Tatar and J. R. Chelikowsky for helpful discussions, and A. J. Freeman and M. A. Posternak for pointing out Ref. 1. This work was supported by National Science Foundation Materials Research Laboratory Grant No. DMR79-23647, Army Research Office Contract DAAG-29-77-C400, and National Science Foundation Grant No. DMR78-22465. One of us (S.G.L.) would like to acknowledge support from a Sloan Foundation Fellowship.

---

*Present address: Department of Physics, City College of CUNY, Convent Avenue at 138 St., New York, N.Y. 10031.

[1]R. Chen, P. Trucano, and R. F. Stewart, Acta Crystallogr. Sect. A 33, 823 (1977).

[2]W. Eberhardt, I. T. McGovern, E. W. Plummer, and J. E. Fischer, Phys. Rev. Lett. 44, 200 (1980).

[3]P. Hohenberg and W. Kohn, Phys. Rev. 136, B864 (1964); W. Kohn and L. J. Sham, *ibid.* 140, A1133 (1965).

[4]L. Hedin and B. I. Lundqvist, J. Phys. C 4, 2064 (1971).

[5]S. G. Louie, K. M. Ho, and M. L. Cohen, Phys. Rev. B 19, 1774 (1979).

[6]N. A. W. Holzwarth, S. G. Louie, and S. Rabii, Phys. Rev. Lett. 47, 1318 (1981).

[7]N. A. W. Holzwarth, S. G. Louie, and S. Rabii (unpublished).

[8]R. F. Willis, B. Feuerbacher, and B. Fitton, Phys. Rev. B 4, 2441 (1971).

[9]G. Bellodi, A. Borghesi, G. Guizzetti, L. Nosenzo, E. Reguzzoni, and G. Samoggia, Phys. Rev. B 12, 5951 (1975).

[10]A. Bianconi, S. B. M. Hagström, and R. Z. Bachrach, Phys. Rev. B 16, 5543 (1977).

[11]G. S. Painter and D. F. Ellis, Phys. Rev. B 1, 4747 (1970).

[12]R. F. Willis, B. Fitton, and G. S. Painter, Phys. Rev. B 9, 1926 (1974).

[13]R. C. Tatar and S. Rabii, Phys. Rev. B 25, 4126 (1982).

[14]A. Zunger, Phys. Rev. B 17, 626 (1978).

[15]I. L. Spain, in *Chemistry and Physics of Carbon*, edited by P. L. Walker and P. A. Thrower (Dekker, New York, 1973), Vol. 8, p. 1.

[16]H. Nagayoshi, K. Nakao, and Y. Uemura, J. Phys. Soc. Jpn. 41, 1480 (1976).

[17]D. R. Hamann, M. Schlüter, and C. Chiang, Phys. Rev. Lett. 43, 1494 (1979).

[18]The self-consistency of our calculated energy levels and the relative positions among levels were converged to well within 0.05 eV. The absolute position of the levels, on the other hand, were converged to within 0.2 eV. This relatively large error was permitted in order to keep the calculations for the stage-3 intercalation compound within a reasonable computation time.

[19]J. D. Bernal, Proc. R. Soc. London, Ser. A 106, 749 (1924).

[20]M. A. Posternak, E. Wimmer, and A. J. Freeman, Bull. Am. Phys. Soc. 26, 483 (1981).

[21]M. T. Yin and M. L. Cohen, Phys. Rev. B 24, 6121 (1981).

[22]A. Zunger and A. J. Freeman, Phys. Rev. B 15, 5049 (1977).

[23]J. C. Slonczewski and P. R. Weiss, Phys. Rev. 109, 272 (1958); J. W. McClure, *ibid.* 108, 612 (1957).

[24]E. A. Taft and H. R. Philipp, Phys. Rev. 138, A197 (1965).

[25]D. L. Greenway, G. Harbeke, F. Bassani, and E. Tosatti, Phys. Rev. 178, 1340 (1969).

[26]J. C. Slater, Phys. Rev. 81, 385 (1951); 82, 538 (1951).

Effect of In-Plane Density on the Structural and Elastic Properties of Graphite Intercalation Compounds

K. C. Woo
Moore School of Electrical Engineering and Laboratory for Research on the Structure of Matter, University of Pennsylvania, Philadelphia, Pennsylvania 19104

and

W. A. Kamitakahara
Ames Laboratory and Department of Physics, Iowa State University, Ames, Iowa 50011

and

D. P. DiVincenzo
Department of Physics and Laboratory for Research on the Structure of Matter, University of Pennsylvania, Philadelphia, Pennsylvania 19104

and

D. S. Robinson
Department of Physics and Materials Research Laboratory, University of Illinois at Urbana-Champaign, Urbana, Illinois 61801

and

H. Mertwoy, J. W. Milliken,[a] and J. E. Fischer
Moore School of Electrical Engineering and Laboratory for Research on the Structure of Matter, University of Pennsylvania, Philadelphia, Pennsylvania 19104
(Received 21 June 1982)

Dramatic differences in structure, elastic properties, and order-disorder temperatures are observed for stage-2 Li-graphite of different in-plane density, indicating the importance of long-range interactions in cohesive properties. LiC_{12} is three-dimensionally ordered up to ~500 K with $\sqrt{3}\times\sqrt{3}$ Li superlattice and *AA* graphite stacking, whereas LiC_{18} is disordered at 300 K and has *AB* stacking. LO and LA (00*l*) phonon energies are 30% greater in the former, which can be understood in terms of electrostatic effects.

PACS numbers: 63.20.Dj, 61.12.Dw, 62.20.Dc

We report several dramatic differences in vibrational and structural properties between dense and dilute compounds of state-2 Li-graphite. Specifically, we have observed major differences in intercalate ordering, graphite stacking sequences, order-disorder temperatures, and (00*l*) longitudinal phonon energies by means of neutron scattering measurements. The considerable recent interest in the ordering transitions of graphite intercalation compounds[1] (GIC) and the similarity of ordering and/or staging phenomena to those in related systems [e.g., rare gases absorbed on graphite[2] and intercalated transition-metal dichalcogenides[1] (ITMD)] impart a wider relevance to the results reported here.

GIC's generally progress from small to large intercalant density through staging. A stage-*n* compound consists of a sequence of *n* graphite layers and one intercalant layer repeated along the *c* axis. In contrast, most of the ITMD's are stage 1 at all accessible concentrations with continuously variable filling of the van der Waals gap. Several recent results[3,4] imply that stage-2 Li-graphite occurs with two different intercalant densities within the occupied van der Waals gaps, both of which are at least metastable at 300 K. It is the only known graphite system to do so. The unique possibility of exploring crystal structure, phase transitions, and lattice dynamics via neutron scattering in intercalation compounds of different in-plane stoichiometry is provided by our ability to synthesize large samples of Li-graphite. The ITMD's can only be prepared in the form of powder or small crystals and are thus not amenable to lattice dynamics studies by neutron scattering. The present work represents the first such study of an intercalation compound as a function of in-plane density.

 © 1983 The American Physical Society

Stage-2 Li-graphite is prepared in two distinct colors, pink and blue, by immersing Union Carbide highly oriented pyrolytic graphite (HOPG) or Goodrich pyrolytic graphite (PG) in molten Li/Na alloy. We used 99% enriched ^{7}Li. The blue samples[5] are grown in 3.5 mol% Li at 200–300 °C while pink is obtained with 5–6% Li at 400 °C. Other reaction conditions[4] as well as the vapor-phase technique[3] also appear to give two distinct phases. Experiments were carried out on both HOPG and PG samples using a triple-axis spectrometer at the Oak Ridge high-flux isotope reactor with fixed incident neutrons of 14.77 meV or fixed neutron final energy of 13.65 meV. The HOPG and PG samples had about 5° and 12° mosaic spread after intercalation, respectively. The samples were packaged in stainless-steel envelopes.[6] Results were identical for both types of starting materials; most of the inelastic data were obtained from the larger PG samples.

The Drude edges of the pink and blue materials are 2.6 and 1.45 eV, respectively, indicating that the pink samples have higher in-plane Li density.[7] DiCenzo, Basu, and Wertheim[8] conclude from x-ray photoemission core-level intensities that blue samples have a chemical formula $LiC_{18\pm1}$. In this work, we observe a $\sqrt{3}\times\sqrt{3}$ Li superlattice for pink samples, consistent with Guerard's original report on stage-2 Li-graphite of unspecified color[9] and with more recent data of Billaud *et al.*[4] on stage-2 Li-graphite described as blue. We find that the pink color degrades superficially towards blue even in clean argon atmosphere, so that Billaud's blue material can reasonably be considered to be the same as Guerard's stage-2 and our pink compound. The $\sqrt{3}\times\sqrt{3}$ Li superlattice implies an ideal chemical formula LiC_{12}. Using the intensity of Li(100), Li(200), and graphite(100) reflections,[10] we estimate that the pink samples used in this work are $LiC_{13.5\pm1.5}$. Weight-uptake measurements are unreliable because of variable amounts of alloy which occupy gross defects in the starting material.[5] The repeat distances of LiC_{12} and LiC_{18} were found to be 7.024 and 7.055 $\pm$0.005 Å, respectively, consistent with stronger interlayer Li-C Coulomb interaction in the denser phase. Similar effects are observed in overcharged acceptor compounds.[11] Intermediate compositions either do not exist or are much less stable. In samples with overall Li concentrations between LiC_{18} and LiC_{12}, two distinct phonon branches characteristic of the pure phases are detected, suggesting separation into blue and pink phases.

Figure 1 is a schematic representation of the elastic scattering results. For LiC_{12} at 295 K $(h00)$ scans reveal cylindrically averaged (100) and (200) reflections from the $\sqrt{3}\times\sqrt{3}$ Li superlattice, while the $(10l)$ and $(\sqrt{3}0l)$ scans confirm[9,12] the unusual $\alpha AA\alpha AA\cdots$ stacking. In contrast, no Li reflections are found in LiC_{18}, and the $(\sqrt{3}0l)$ scan shows a doubling of the unit cell along $\bar{c}$ indicating $AB/BA/AB\cdots$ stacking. This sequence is locally similar to graphite $(ABAB\cdots)$ but different globally from all other stage-2 alkali GIC's $(AB/BC/CA\cdots)$.[1] The same diffractogram is found for LiC_{18} quickly cooled to 10 K, implying either that the order-disorder transition (if any) occurs below 10 K or that the ordering process takes place very slowly below 300 K. In contrast, LiC_{12} disorders at $T_0\sim500$ K; the corresponding process in stage-1 LiC_6 $(\alpha A\alpha A$ stacking) occurs at[6,12] 715 K. Intensity estimates for various ordered LiC_{18} phases indicate that their reflections would have been observable in the $(h0l)$ scans had they existed. Details of the phase transitions will be presented elsewhere.

The Li-graphite system is unique in that one must invoke attractive interlayer Li-Li interactions, in addition to the repulsive elastic and/or electrostatic interlayer interactions,[13] in order to arrive at an eclipsed intercalant stacking se-

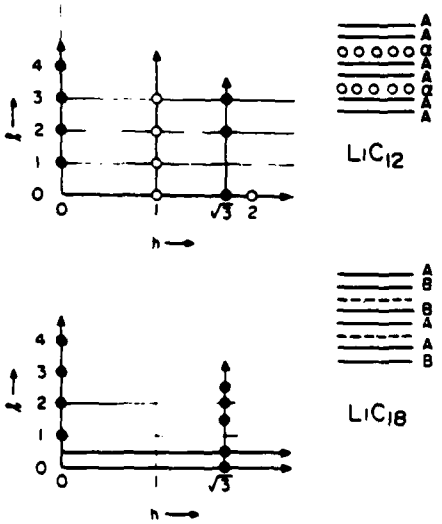

FIG. 1. Schematic reciprocal-space diagram for LiC_{12} at 295 K and LiC_{18} at 10 K, indicating the scans performed (heavy lines) and the reflections observed (filled circles: predominantly graphite reflections; open circles: Li reflections). Indexing is in units of the LiC_{12} cell. Implied structures are shown as insets.

quence in LiC_6. This attractive component must be fairly long range because it is still important in the stage-2 compound LiC_{12}. Since LiC_6 and LiC_{12} have the same in-plane structure and intercalant stacking, the ~200 K difference in T_0's is a rough measure of the difference between the net Li-Li interlayer interaction acting at distances of 3.7 and 7.0 Å. Even at the larger distance, this interaction is apparently strong enough to override the C-C interlayer interaction, forcing the unusual *AA* sequence as long as the Li's are locked to their C neighbor layers. In LiC_{18}, on the other hand, either the lower density or the absence of a commensurability term reduces the Li-C nearest-layer coupling such that the C-C nearest-layer interaction (which favors *AB* stacking) takes over, yielding the usual graphitic sequence. This weak Li-C coupling may be a factor contributing to the lower T_0 of LiC_{18}.

Figure 2 shows the measured (00*l*) phonon dispersion for LiC_{12} and LiC_{18}, along with the fits of a one-dimensional nearest-neighbor force-constant model which we discuss later. The phonon energies are ~30% greater in the denser material. Since the two branches observed are primarily graphitelike,[14] we are directly probing the effect of intercalant density on the host elastic properties transverse to the layers. To the best of our knowledge, this is the first time that such an experiment has been possible. The low-frequency slopes yield sound velocities v_s and compressibilities k_{tot} as follows: 5.56×10^5 cm/sec and 2.69×10^{-12} cm²/dyn for LiC_{12}; 4.07×10^5 cm/sec and 1.42×10^{-12} cm²/dyn for LiC_{18}. These values, along with previous data[15] on MC_{24} (M = K, Rb, Cs), are consistent with a simple model for the elastic energy, in which the contribution of the two adjacent C layers k_c is graphitic and the C-I-C sandwich is represented by an electrostatic term k_i. The composition law gives $k_{tot} = (c_i k_i + c_c k_c)/(c_i + c_c)$, where c_i and c_c are the appropriate layer separations, 3.70 and 3.35 Å, respectively. We estimate the concentration dependence of k_i as follows. The electrostatic energy for the C-*I*-C sandwich has recently been shown to be[16] $E_{es} \propto A_0 \sigma^2 c_i$, where σ is charge/area and A_0 is area per *I* atom. The electrostatic and total energies for the sandwich are related by[17] $\partial E_{es}/\partial c_i = 3c_i\, \partial^2 E_{tot}/\partial c_i^2$. But the sandwich compressibility is defined as $k_i = (A_0/c_i)(\partial^2 E_{tot}/\partial c_i^2)^{-1}$. Combining these equations gives the particularly simple result $k_i \propto \sigma^{-2}$; i.e., k_i decreases with the inverse square of the concentration (assuming unity charge transfer). Interestingly, k_i is independent of sandwich thickness c_i. These results combined with the composition law predict a linear relationship between the experimentally measured quantities plotted in Fig. 3, with an intercept equal to the graphite value. The fact

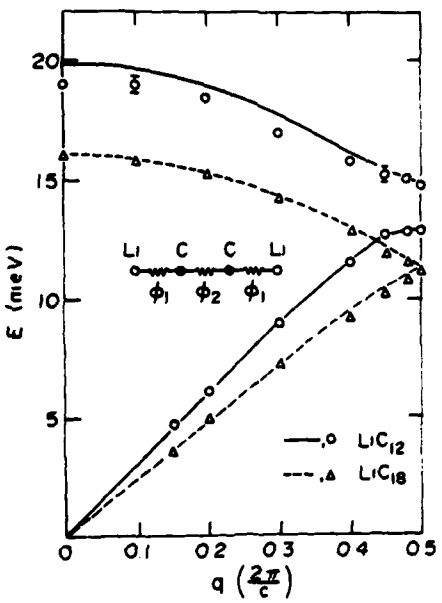

FIG. 2. Experimental (00*l*) phonon dispersion for LiC_{12} (circles) and LiC_{18} (triangles). Solid and dashed curves are the corresponding fits of a nearest-neighbor force-constant model (Ref. 15), shown as an inset.

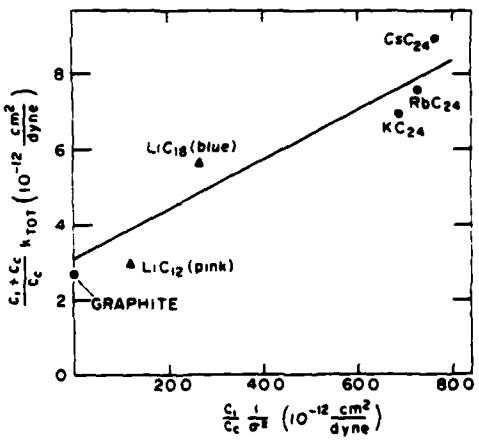

FIG. 3. Scaled compressibilities vs the scaled inverse square of intercalant concentration for stage-2 alkali GIC's. Solid line is the electrostatic model result described in the text and the symbols are from neutron data (present work plus Ref. 15).

that these predictions agree with all the available data[15] to within 10% indicates that the interlayer C-I interaction is indeed primarily electrostatic.

We attempted to analyze the data of Fig. 2 with a nearest-neighbor force-constant model, motivated by its successful application to the lower graphitelike acoustic and optic branches of stage-2 and -3 heavy alkali compounds.[18] The fit to LiC_{18} is good, yielding $\varphi_1 = 5750$ dyn/cm and $\varphi_2 = 3000$ dyn/cm for C-Li and C-C force constants, respectively. In contrast, the LiC_{12} fit is poor for the optic branch (Fig. 2). Further evidence of the failure of this model for LiC_{12} is that $\varphi_2 = 4070$ dyn/cm is unphysically large, whereas the four dilute disordered stage-2 GIC's (LiC_{18}, MC_{24}) give φ_2 values comparable to graphite (as would be expected from a nearest-neighbor model). Zabel and Magerl[15] subsequently found it necessary to use a mixed one-dimensional ion shell/Born–von Karman model to fit the upper alkalilike optic branches of MC_{24} and KC_{36}. While this latter model might also produce a better fit to the lower optic branch of LiC_{12}, it is significant that LiC_{12} is the only stage-($n \geq 2$) compound for which the nearest-neighbor force-constant model does not fit all the graphitelike branches reasonably well. This failure could result from the greater charge density ($\frac{1}{8}e$ per C in LiC_{12} vs $\frac{1}{9}e$ per C and $\frac{1}{12}e$ per C in LiC_{18} and MC_{24}, respectively, assuming M^+ in all cases) or from the long-range interactions implied by the structural data.

The C-Li force constant $\varphi_1 = 10\,040$ dyn/cm for LiC_{12}, twice that found for LiC_{18}. This difference could be partially due to the inadequacy of the nearest-neighbor model, although it is consistent with stronger interlayer interactions as deduced from the structural and T_0 arguments as well as with the greater in-plane density.

The dramatic differences observed in the elastic, structural, and order-disorder behavior of the two stage-2 compounds LiC_{12} and LiC_{18} result from a complex interplay of in-plane density, commensurability, and interlayer interactions beyond nearest neighbors. Similar differences in electronic properties probably exist. Compounds of Li-graphite with stage >2 have been reported[4]; it is not presently known if they too exist with different in-plane densities. Detailed studies of Li-graphite may help to explain why staging dominates in GIC's while variable in-plane density is the rule in ITMD's.

This work was supported by the Army Research Office under Contract No. DAAG29-80-K-0019 and by the Department of Energy under Contract No. W-7405-Eng-82; Oak Ridge National Laboratory is operated by Union Carbide under Department of Energy Contract No. W-7405-Eng-26. Sample preparation was supported by the National Science Foundation–Materials Research Laboratory Program under Contract No. DMR-7923647 and No. DMR-8020250. We are grateful to Dr. H. Zabel for helpful discussions and preprints of Refs. 15 and 18. We also gratefully acknowledge the assistance of Dr. R. M. Nicklow and Dr. N. Wakabayashi and the generosity of Dr. A. W. Moore of Union Carbide in providing the HOPG.

---

[a]Current address: Naval Research Laboratory, Washington, D. C. 20375.

[1]For recent reviews, see Physica (Utrecht) 99B (1979), 105B+C (1981); S. A. Solin, Adv. Chem. Phys. 49, 455 (1982).

[2]*Ordering in Two Dimensions*, edited by S. K. Sinha (North-Holland, Amsterdam, 1980).

[3]P. Pfluger, V. Geiser, S. Stolz, and H. J. Guntherodt, Synth. Met. 3, 27 (1981).

[4]D. Billaud, E. McRae, J. F. Mareche, and A. Herold, Synth. Met. 3, 21 (1981).

[5]S. Basu, C. Zeller, P. Flanders, C. D. Fuerst, W. D. Johnson, and J. E. Fischer, Mater. Sci. Eng. 38, 275 (1979).

[6]D. S. Robinson and M. B. Salamon, Phys. Rev. Lett. 48, 156 (1982).

[7]P. Pfluger, K. P. Ackermann, R. Lapka, E. Schupfer, P. Jeker, H. J. Guntherodt, E. Cartier, and F. Heinrich, Synth. Met. 2, 285 (1980).

[8]S. B. DiCenzo, S. Basu, and G. K. Wertheim, Synth. Met. 3, 139 (1981).

[9]D. Guerard and A. Herold, Carbon 13, 337 (1975).

[10]G. E. Bacon, *Neutron Scattering* (Oxford Univ. Press, London, 1955), p. 89. We assumed the Debye-Waller factor to be $B \sin^2\theta$, where B is inversely proportional to mass and θ is the Bragg angle.

[11]A. Metrot and J. E. Fischer, Synth. Met. 3, 201 (1981).

[12]A. Wiedenmann and J. Rossat-Mignod, unpublished.

[13]S. A. Safran, Synth. Met. 2, 1 (1980).

[14]Preliminary data indicate a dispersionless Li branch at 28 ± 1 meV for both LiC_{12} and LiC_{18}.

[15]H. Zabel and A. Magerl, Phys. Rev. B 25, 2463 (1982).

[16]D. P. DiVincenzo and E. J. Mele, Phys. Rev. B 25, 7822 (1982).

[17]Obtained by differentiating the virial theorem, neglecting exchange and correlation.

[18]A. Magerl and H. Zabel, Phys. Rev. Lett. 46, 444 (1981).

Experimental phase diagram of lithium-intercalated graphite

K. C. Woo, Helen Mertwoy, and J. E. Fischer
Moore School of Electrical Engineering and Laboratory for Research on the Structure of Matter, University of Pennsylvania, Philadelphia, Pennsylvania 19104

W. A. Kamitakahara
Ames Laboratory and Department of Physics, Iowa State University, Ames, Iowa 50011

D. S. Robinson
Department of Physics and Materials Research Laboratory, University of Illinois at Urbana-Champaign, Urbana, Illinois 61801
(Received 11 April 1983)

First-order transitions to dilute stage 1 from stages 2–4 and from mixed stages are observed in Li-graphite compounds in the range 430–1020 K. The resulting (T,x) phase boundary agrees generally with predictions by Safran and others except for a sharp peak of very stable stage-2 compositions around $x \sim 0.4$. The commensurability energy does not contribute to this peak since both low-T and high-T phases are disordered.

A unique feature of intercalated layer crystals is the phenomenon of staging,[1] whereby the foreign atoms occupy a periodic sequence of van der Waals gaps in the host crystal (every nth gap in a stage-n compound). The stability of long-period coherent structures has been attributed to long-range electrostatic or elastic ("coherency strain") repulsion among intercalant layers.[2] Safran[3] pioneered the calculation of (T,x) phase diagrams for layered intercalates (x is the concentration expressed as a fraction of the saturation value). At low T, compositions which do not correspond to pure stages are predicted to macroscopically phase-separate into mixed stages, as observed in graphite compounds at 300 K. Safran's simple two-body model predicts a high-T transition $T_c(x)$ at which any compound with $x < 1$ transforms *at constant* x to a stage-1 sequence by reducing the in-plane density.[3] The existence of the dilute stage-1 phase at high T is insensitive to the details of the Hamiltonian, but the phase boundaries reflect the inclusion of additional interactions, screening, etc.[4,5] We have observed transitions to dilute pure stage 1 in Li-graphite compounds with $0.16 < x < 0.99$, using x-ray and neutron diffraction (the latter performed at the Oak Ridge High Flux Isotope Reactor). These are plotted as the solid dots in Fig. 1, which shows a narrow peak of extremely stable stage-2 compositions ranging from $x \approx 0.3$ to 0.5, a feature which is not accounted for by any of the model calculations.[3–5] The peak appears to be superposed on a weaker x dependence of T_c skewed in favor of dilute compounds, as predicted when elastic guest-host interactions are included.[4] This is the first systematic study of the concentration dependence of T_c and thus provides experimental input to the (T,x) staging phase diagram of a prototyp-

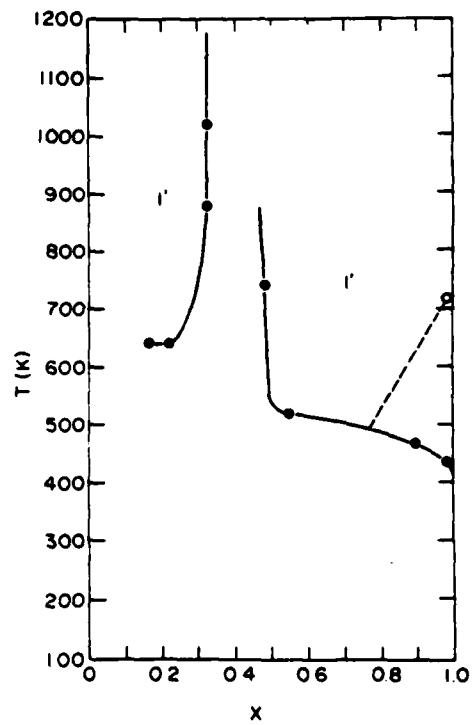

FIG. 1. Experimental upper phase boundary for Li-graphite compounds. Solid dots represent phase-transition temperatures (from x-ray or neutron diffraction) above which only stage 1 is present. Except near $x = 1$ there is a corresponding loss of in-plane order; the $x = 0.99$ sample is three-dimensionally ordered pure stage 1 from 433 to 715 K (open circle from Ref. 11).

 ©1983 The American Physical Society

ical system.[6] We present here an account of how Fig. 1 was obtained, deferring for a longer article a discussion of the phase boundaries of higher stages, detailed analysis of the transitions, etc.

We screened several intercalants by looking for evidence of the stage-2 → stage-1 transition with differential scanning calorimetry. Li-graphite compounds showed such evidence at accessible temperatures whereas KC_{24} and CsC_{24} did not. An advantage of the Li-graphite system is the existence at 300 K of two different stage-2 compositions LiC_{12} and LiC_{18}, which permits the study of in-plane density effects at constant stage.[7] We label these stages 2 and 2′, respectively, where the unprimed integer denotes an ordered commensurate in-plane structure while the primed integer indicates a (generally) less-dense structure with no long-range order. The model calculations do not consider in-plane order or lack thereof, the predicted structures being delineated only by the sequence of occupied gaps. Another advantage is the low Li vapor pressure such that our samples, sealed in thin stainless-steel containers, could be run at high T without deintercalation. (We included excess metal alloy in the containers to maintain equilibrium vapor pressure, a precaution which was probably superfluous—see below.)

Unfortunately Li intercalation compounds transform irreversibly to lithium carbide Li_2C_2 above 750 K (Ref. 8); we turned this to our advantage in some cases. Visible quantities of Li or Li-Na alloy are often incorporated in macroscopic cracks during liquid-phase synthesis,[9] which complicates the determination of x. Thus chemical analyses[9] of stage 2′ samples range from $LiC_{14.5}$ to LiC_{18} while x-ray photoelectron spectroscopy (XPS) core-level intensities[10] give $LiC_{18\pm1}$. We adopt the latter value as being consistent with the blue color, relative to the pink and gold of LiC_{12} and LiC_6, respectively. The presence of alloy in intimate contact with the compound also raises concern that x may vary during a high-T run. We find, however, that the diffracted intensities of the low-T phases are quite reproducible after repeated cycling (except when Li_2C_2 is formed), probably because the time scale of the experiment is short compared to the intercalation time and/or because the compound is in equilibrium with the alloy from which it was grown. Thus we neglect the possible presence of free metal in determining x. Most of our samples were mixed phase at 300 K. The relative amounts of the various phases present in a given sample were estimated from (00l) diffraction intensities in most cases, the exception being mixtures of stages 2 and 2′ which were analyzed via their different carbon-layer stacking sequences.[7] Equivalent homogeneous-phase x values were obtained by assigning $x = 1.0$, 0.5, and 0.33 to pure stages 1, 2, and 2′, respectively. We estimate the error in x to be ± 0.02 via this procedure. Single-phase samples of stages higher than 2 were assumed to follow the dilute LiC_{9n} sequence at 300 K: LiC_{27} stage 3′, LiC_{36} stage 4′, etc. The pale gray colors are consistent with smaller Li content than blue LiC_{18}, etc. From Fig. 1, $T_c(x)$ is either relatively flat or sharply peaked in different regions of x. Thus our approximate x determination is adequate over most of the range while extraordinary efforts would have to be made to resolve different x values near 0.4 corresponding to different T_c's.

The solid dots in Fig. 1 denote the temperatures at which pure stage-1 (00l) diffractograms are first observed upon heating samples of various x. These transitions are all first order, exhibiting ~10-K hysteresis. Above 433 K the $x = 0.99$ sample is pure three-dimensionally ordered stage 1, presumably with Li vacancies because the low-T phase contains 2 vol% stage 2. Upon further heating to 715 K the three-dimensional Li order disappears[11] (open circle), implying the existence of a second boundary between ordered and disordered pure stage-1 phases (dashed line), the former supporting a significant vacancy concentration at high T by analogy to Cs_xC_8.[12] A similar sample transforms to pure stage 1 at $T_c(0.90) = 467$ K, establishing the weak x dependence of the boundary near $x = 1$.

Mixed stage samples near $x = 0.5$ show complex behavior upon heating. Figure 2 shows the normalized T dependence of Li(100) and representative (00l) peak intensities for $x = 0.55$ (stage 2 + 10% stage 1 at 300 K). The stage 2 (004) drops abruptly at 495 K to 40% of its initial strength, levels off, and then disappears between 510 and 520 K. Mirroring this two-step behavior is the growth of stage-1 (002) intensity which is attributed to dilute disordered stage 1′ above 520 K since the Li(100) is gone. Between 495 and 510 K, (10l) neutron scans show stage-1 periodicity so the ordered Li comes from stage 1 while the remaining stage 2 must be disordered. To confirm this, we recorded a ($\sqrt{3}0l$) scan (carbon row) and found a mixture of A-A (stage 1) and

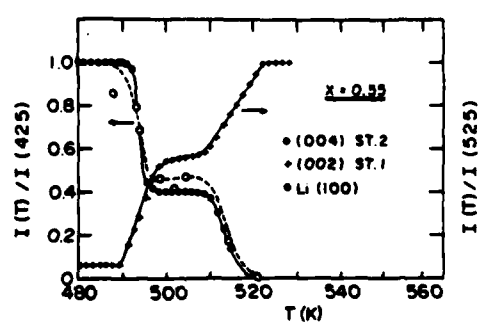

FIG. 2. Staging transitions for a sample with $x = 0.55$. Normalized peak intensity vs T for stage 2 (004), stage 1 (002) from x rays, and in-plane Li(100) from neutrons.

AB/BA (stage 2′) stacking.[7] We take the midpoint of the upper transition as $T_c(0.55) \simeq 515$ K. The data in Fig. 2 were obtained by monitoring a peak after each step change in T, stabilization generally occurring in less than 1 h. Both transitions are fully reversible.[13]

Dramatically different behavior occurs in a slightly different sample, stage 2 with 5% stage 2′ at 300 K whence $x \simeq 0.49$. These coexist until 503 K where the stage 2 begins to disappear and stage 1 emerges. The coexisting $1+2'$ transform at 533 K to $1'+2'$ as the last of the Li(100) disappears. This (third) mixed-phase region continues up to $T_c(0.49) \simeq 733$ K where the 2′ disappears. Holding the sample at 750 K leads to gradual formation of Li_2C_2, leaving behind a lamellar compound with reduced x value. This process increases T_c noticeably, confirming the large negative dT_c/dx through the point (743 K, 0.49).

X-ray studies of three "LiC_{18}" samples showed very different behavior upon heating, suggesting slight differences in x and a steep phase boundary. One such sample transformed completely to Li_2C_2 at 1150 K without showing any staging transitions en route. The other two passed through narrow $1'+2'$ mixed-phase regions and then transformed to pure 1′ at 875 and 1020 K upon first heating. Reversibility was confirmed for the former by working quickly as the Li_2C_2 formed. The attendant reduction in x decreased T_c, indicating a large positive dT_c/dx. We identify the transition as $1'+2' \rightarrow 1'$ since a (10*l*) neutron scan of LiC_{18} at 773 K confirms that the Li is disordered below and above T_c. Thus we can rule out the commensurability energy as a contributing factor to the unusually high stability of stage 2 at $x \simeq 0.33$. The (00*l*) linewidths are the same above and below the phase boundary. Finally, pure stages 3′ and 4′ ($x \simeq 0.22$ and 0.16, respectively) both transform to pure stage 1′ at 640 K so the exact x values are not critical. Neither sample exhibited stage-2′ reflections at any T. These two samples establish the weakly asymmetric "background" which underlies the strong peak in Fig. 1.

The gross features of the experimental phase diagram accord well with Safran's original predictions[3]; only dilute stage 1′ is stable above some concentration-dependent temperature, and the most stable concentration for higher stages is nearer $x \simeq 0.5$ than 0 or 1. An Ising Hamiltonian with two-body interactions[3] thus provides a reasonable basis for treating the statistical mechanics of staging. The upper boundary in Safran's model is symmetric about $x \simeq 0.5$; our data are better reproduced by including an elastic guest-host interaction which breaks the symmetry.[4] The most surprising aspect is the sharp peak between $x \simeq 0.33$ and 0.49; stage 2′ at some x is apparently stable to at least 1150 K. None of the proposed modifications to the theory account for this dramatic effect. The possibility of a second-order transition near the stability limit[3–5] can only be tested on materials with lower T_c.

In Safran's model the T scale depends only on U_0, the in-plane two-body attractive interaction. On this basis one would therefore expect similar T_c's for Li intercalated into different hosts. At 300 K Li_xTiS_2 ($0 < x < 1$) is stage 1′ at all x,[14] a situation which obtains in graphite only above 1150 K if at all. Since the main features of the simple model appear to be borne out by our results, one is tempted to reconcile this discrepancy in the simplest terms possible. For example, an attractive guest-host interaction, stronger for graphite than for TiS_2, could be incorporated into U_0 as an indirect contribution to the Li-Li in-plane attraction.[15] On the other hand, the sharp peak in our phase diagram could be unique to graphite, in which case the T_c scales for Li_xTiS_2 and Li_xC_6 may differ by less than a factor of 2. Similar low-T experiments on Li_xTiS_2 would clearly be of great interest.

ACKNOWLEDGMENTS

This work was supported at the University of Pennsylvania by Army Research Office Contract No. DAAG29-80-K-0019 and at Ames Laboratory by U.S. Department of Energy (DOE) Contract No.W-7405-Eng-82. Oak Ridge is operated by Union Carbide under U.S. DOE contract No. W-7405-Eng-26. Sample preparation was supported by the NSF Materials Research Laboratory Program under Contract No. DMR-7923645 in Pennsylvania and Contract No. DMR-8020250 in Illinois. We gratefully acknowledge stimulating discussions with D. DiVincenzo and S. A. Safran, the assistance of H. Katz, R. M. Nicklow, and N. Wakabayashi and the generosity of A. W. Moore (Union Carbide) in providing the highly oriented pyrolytic graphite. We thank the authors of Refs. 4 and 5 for communicating their results prior to publication.

[1]S. A. Solin, Adv. Chem. Phys. 49, 455 (1982).
[2]S. A. Safran and S. R. Hamann, Phys. Rev. Lett. 42, 1410 (1979).
[3]S. A. Safran, Phys. Rev. Lett. 44, 937 (1980).
[4]J. R. Dahn, D. C. Dahn, and R. R. Haering, Solid State Commun. 42, 179 (1982).
[5]S. E. Millman and G. Kirczenow, Phys. Rev. B 26, 2310 (1982).
[6]Transitions to dilute stage 1 have been reported by R. Clarke, N. Caswell, and S. A. Solin, Phys. Rev. Lett. 42, 61 (1979), and by J. Rossat-Mignod *et al.*, Synth. Met. 2, 143 (1980).
[7]K. C. Woo, W. A. Kamitakahara, D. P. DiVincenzo, D. S. Robinson, H. Mertwoy, J. W. Milliken, and J. E. Fischer, Phys. Rev. Lett. 50, 182 (1933). Stage-2 LiC_{12} has the

same $\sqrt{3} \times \sqrt{3}$ in-plane structure as LiC_6 and $\alpha AA\,\alpha AA$ stacking while LiC_{18} is disordered with AB/BA stacking.

[8]D. Guerard and A. Herold, Carbon 13, 337 (1975).

[9]S. Basu, C. Zeller, P. Flanders, C. D. Fuerst, W. D. Johnson, and J. E. Fischer, Mat. Sci. Eng. 38, 275 (1979).

[10]S. B. DiCenzo, S. Basu, and G. K. Wertheim, Synth. Met. 3, 139 (1981).

[11]D. S. Robinson and M. B. Salamon, Phys. Rev. Lett. 45, 156 (1982); J. Rossat-Mignod *et al.* Solid State Commun. 44, 1339 (1982).

[12]N. Caswell, Phys. Rev. B 22, 6308 (1980).

[13]After 10 cycles T_c is constant to within a few K and x decreased by no more than 0.02.

[14]J. R. Dahn and R. R. Haering, Solid State Commun. 40, 245 (1981).

[15]This would also imply a short-range indirect (host-mediated) interlayer attraction competing with the long-range repulsion which stabilizes pure stages. We suggested an interlayer attraction in Ref. 7 to explain the unusual $\alpha AA\,\alpha AA$ stacking sequence of LiC_{12}.

STAGING TRANSITIONS IN Li-GRAPHITE : PHONON SPECTRA OF DILUTE STAGE 1

K.C. WOO, H. MERTWOY AND J.E. FISCHER
Moore School EE and LRSM, University of Pennsylvania
Philadelphia, PA 19104

W.A. KAMITAKAHARA
Ames Lab and Physics Dept., Iowa State University,
Ames, IA 50011

D.S. ROBINSON
Physics Dept. and Materials Research Lab, University
of Illinois, Urbana, IL 61801

ABSTRACT

First-order transitions to dilute stage one from stages 2,3 and 4 and from mixed stage 1+2 are observed in Li-graphite as predicted by Safran. The upper phase boundary is asymmetric in concentration and is sharply peaked about $x \sim 0.4$. The phonons in the dilute stage 1 have energies between those of LiC_6 and graphite. Unlike the stage 2 compounds, the compressibility does not scale in a simple way with intercalant density.

INTRODUCTION

Staging is one of the most interesting and unique properties of graphite intercalation compounds. Stage *n* is a periodic sequence of *n* layers of graphite and one layer of intercalant. Recently, Safran [1] predicted that only stage 1 is stable above a certain temperature Tm. The transitions from high stages to dilute stage 1 are predicted to be first order except in a limited region near Tm where the transition from stage 2 to dilute stage 1 should be second order. The theory is based on a Hamiltonian including two-body attractive in-plane and replusive interplane interactions and the entropy of a lattice gas at finite temperature. Pure staging at T=0 is a result of interlayer repulsion, the in-plane density being determined (consistent with stoichiometry) by maximizing the total attractive energy. At finite T the entropy of a 2D lattice gas with vacancies overrides the entropy due to "staging defects", such that pure stages (or mixtures thereof) remain stable. Thus staging transitions from high to low stage are expected to occur as a function of increasing T, the transition temperature depending on x, the overall intercalant concentration expressed as a fraction of the maximum value. The upper phase boundary between dilute stage 1 and high stages (or mixtures thereof) is symmetric about x=0.5 in Safran's model, a direct result of the two-body Hamiltonian. In recent extensions of the theory, Dahn et. al. [2] included an elastic guest-host interaction and Millman et. al. [3] accounted for the energy required to separate host layers during intercalation. The latter authors also studied the effect of screening the interlayer repulsion. Either type of modification removes the symmetry about x=0.5 at the expense of introducing more parameters. The high-T transition to dilute stage 1 is a general consequence of the entropy contribution to the free energy and is thus independent of the details of the model Hamiltonian.

We report here an experimental study of staging transitions to dilute stage 1 versus x, and the high-T phonon spectra of the dilute (disordered) stage 1 phase. Li-graphite was chosen for this work because it is the only graphite intercalation system which showed evidence from preliminary differential scanning calorimetry for phase transitions at accessible temperatures [4]. Quantitative DSC will ultimately be useful to fully characterize the transitions reported here. Li-graphite is also the only graphite system that can be prepared in two different stage 2 stoichoimetries, LiC_{12} and LiC_{18} [5], which allows us to explore the effects of in-plane density at constant stage. In a previous study [5] we found that the phonon energies are higher for LiC_{12} ($\sqrt{3} \times \sqrt{3}$ Li superlattice and AA graphite stacking sequence) than for LiC_{18} (AB/BA stacking sequence, "/" denoting disordered Li). Using the data of Zabel and Magerl for other stage 2 alkali-metal graphites [6], we found that the c-axis compressibility decreases with the inverse square of the in-plane intercalant density as expected for a purely ionic model of interlayer bonding [7].

EXPERIMENTAL

The lithium graphite samples were prepared by immersing highly oriented pyrolytic graphite (HOPG) or pyrolytic graphite in Na/Li alloys at high temperature. The samples were sealed in thin stainless steel containers. Both x-ray and neutron diffraction were studied versus T, the latter being particularly important for stage 1 and 2 samples since they permitted both (00ℓ) and (hko) scans to be recorded in reasonable times. For stages 3 and 4 only (00ℓ) x-ray data were obtained. The neutron experiments were performed on a triple-axis spectrometer at the Oak Ridge High Flux Isotope Reactor.

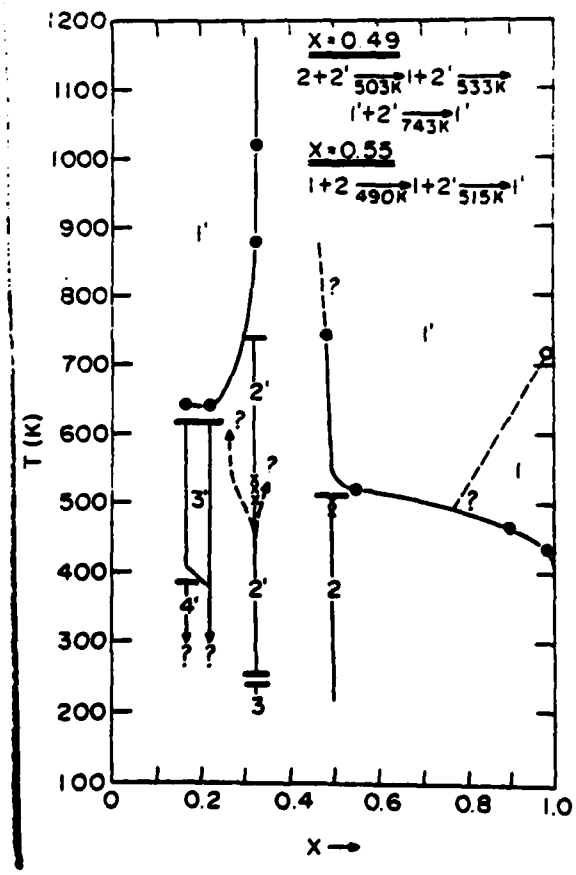

Fig. 1. Experimental phase diagram for Li-graphite. Solid circles represent transitions to dilute stage 1 (ordered) or 1' (disordered) and the open circle (Ref. 8) is the 1→1' transition which implies a boundary between 1' and ordered $LiC_{6+\delta}$ (dashed line-schematic). Crosses are derived from transitions involving macroscopic phase separation. Heavy bars denote upper or lower stability limits for pure stages. Question marks indicate unexplored regions.

RESULTS AND DISCUSSION

Figure 1 shows the (T,x) phase diagram deduced from staging transitions versus T at constant x, observed in Li-graphite samples with x=0.16, 0.22, 0.33 (two samples), 0.49, 0.55, 0.90 and 0.98. The heavy dots represent reversible transitions to dilute stage 1 at $T_c(x)$ and thus define the upper phase boundary. The primes denote disordered Li layers while the unprimed stages all exhibit the $\sqrt{3} \times \sqrt{3}$ in-plane superlattice. The triangular region near x=1 implies a range of T and x in which 3-D ordered $LiC_{6+\delta}$ is the stable phase, the open circle representing the 3-D melting of $\sim LiC_{6.1}$ [8]. Key features of the upper phase boundary are a) T_c is only weakly dependent on x for $x < 0.25$ and $x > 0.5$; and b) a sharp peak centered at $x \sim 0.4$ indicates an unusually stable phase (or phases) with n=2. The existence of the peak was confirmed by briefly holding the x=0.33 and x=0.49 samples above 750K, the temperature at which the intercalation compound LiC_y transforms irreversibly to Li_2C_2. In our case we have $LiC_y \rightarrow ALi_2C_2 + BLiC_{y'}$ where $y' > y$ independent of A and B, i.e., x is reduced. We then remeasured T_c of the remaining intercalation compound, and qualitatively confirmed that dTc/dx is large and positive at $x \sim 0.33$ but large and negative at $\sim x=0.5$. All other samples exhibited fully reversible transitions with small hysteresis; the x=0.55 sample was cycled a total of 10 times in the x-ray and neutron experiments and T_c was constant to within several K. Our results are in good qualitative agreement with Safran's theory; dilute stage 1' is the only stable phase at high T over most of the range of x, and T_c is greater near x=0.5 than at x=0 or 1. In contrast to Safran's prediction, the experimental boundary is markedly asymmetric about x=0.5 both regarding the peak location and the asymptotic values of T_c at large and small x. As pointed out by Safran, this is due to the binary intercalant interactions assumed in his model; inclusion of other interactions i.e., guest-host elastic interaction [2]) will break the symmetry.

The initially mixed stage samples exhibit multiple transitions en route to stage 1' which give information on the stable phase boundaries for stages n and n' > 1. These will be discussed in detail elsewhere. We show in Fig. 2

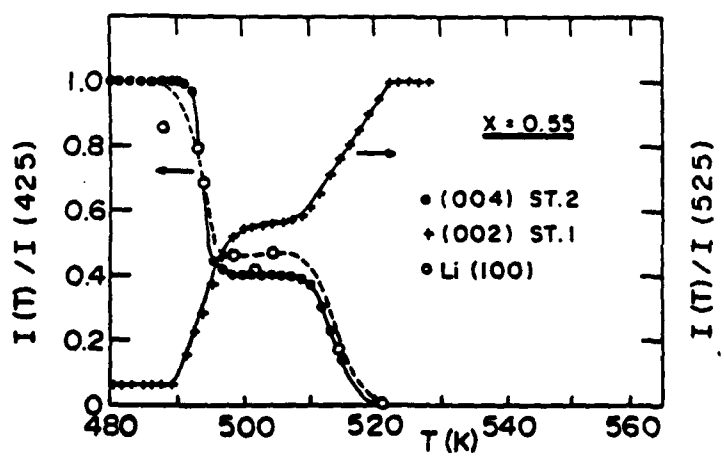

Fig. 2. Temperature dependence of normalized diffraction intensities for x=0.55. (00ℓ)'s from x-ray, Li(100) from neutron diffraction.

an example of the observed behavior. Plotted are the normalized temperature dependences of Li(100) and representative (00ℓ) peak intensities for the x=0.55 sample. At 300K the sample is ~90% LiC_{12} (stage 2) and ~10% LiC_6 (stage 1) as deduced from scanning the Li(100) along c*. The stage 2 (004) drops abruptly at 493K to ~40% of its initial strength, levels off and then disappears between 507 and 515K. Mirroring this two-step behavior is the growth of the stage 1 (002). The transition sequence is summarized in the upper right corner of Fig. 1. The intermediate phase is identified as a mixture of stages 1 and 2' from a c* scan of the Li(100). At both staging transitions we also observe a loss of Li(100) intensity, suggesting that the kinetics of staging transitions are mediated by the Daumas-Herold domain mechanism [9].

An unexpected result is the stability of two distinct stage two phases over a wide temperature range [5]. These are labeled 2' and 2 in Fig. 1. We have no evidence to suggest that they merge at high T, as might be expected from the two-body calculations [1-3]. Clearly some aspect of the 2D Li layer structure is responsible for this behavior; such effects have not been incorporated into the existing models.

It is also apparent that guest-host interactions play an important role in locating the phase boundary on the temperature scale. The Li_xTiS_2 system at 300K exhibits continuously variable x with constant stage 1' during electrochemical intercalation or deintercalation [2], so the upper phase boundary lies below 300K at all x. This is in marked contrast to the present results for the same guest in a graphite host (Fig. 1). Since the general shape of the phase boundary is correctly predicted without explicitly accounting for guest-host interaction [1], a reasonable first-order correction to the two-body Hamiltonian might be to assume that the host mediates the in-plane intercalant attraction, for example by weak hybridization of valence orbitals. Thus the data for Li in graphite and TiS_2 can be reconciled in the framework of Safran's model with a larger effective in-plane Li-Li attraction in the former, attributed to a greater degree of hybridization between Li and C relative to Li and S orbitals. It is also reasonable to expect Li_xTiS_2 to exhibit transitions to higher stages at low T, by analogy to Fig. 1 (although the kinetics might be prohibitively slow).

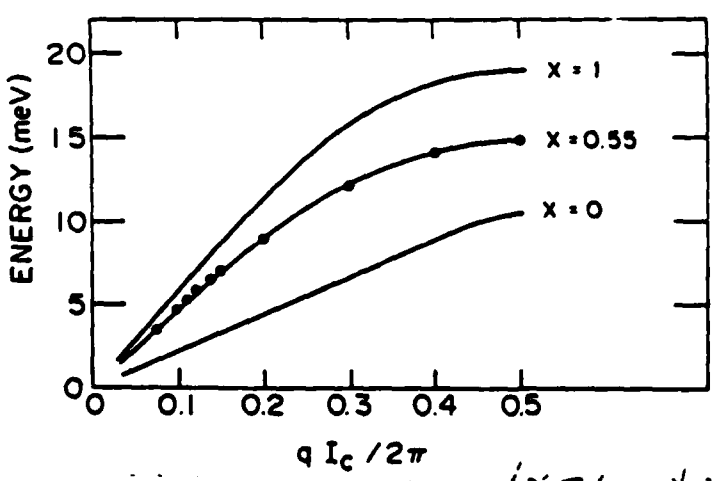

(x=1, top curve)

Fig. 3. (001)L phonons for LiC_6 at 300K, stage 1' with x=0.55 at 550K (middle curve), and graphite at 300K (q) (bottom curve).

In Figure 3 we compare the (001)L phonon dispersion curves for stage 1 (x=1) at 300K [10], stage 1' (x=0.55) at 550K and graphite [11]. Since the Li stage 1 repeat distance is only 10% greater than the C-C interlayer spacing, all three materials can be viewed in zero order as stage 1 compounds with in-plane "coverages" of ~1, 0.55 and 0 respectively. At constant q, the phonon energies increase with coverage, the dilute stage 1' lying between LiC_6 and graphite. This is in qualitative agreement with the trend observed in LiC_{12} and LiC_{18} at 300K, for which the compressibilities scale with in-plane density as would be predicted by a simple coulomb model of interlayer bonding. On the other hand, the nearest neighbor force constant model which predicts a simple relationship between compressibility and intercalant density for stage 2 fails in stage 1. It is also clear that the initial slopes of the acoustic branches are quite different for KC_8, RbC_8 and CsC_8 which have the same in-plane density [6]. The available data suggests that the in-plane density effect at constant stage is much stronger than either the effect of varying the alkali species at constant stage or the stage dependence within a given family of compounds. Data from additional stage 1' samples with different x-values would be useful for quantitative comparison of the several factors which influence the phonon dispersion.

ACKNOWLEDGEMENTS

This work was supported by ARO Grant DAAG29-80-K-0019 (Penn) and DOE Contract W-7405-Eng-82 (Ames). Oak Ridge National Laboratory is operated by Union Carbide under DOE Contract N-7405-Eng-26.

REFERENCES

1. S.A. Safran, Phys. Rev. Lett. 44, 937 (1980).

2. J.R. Dahn, D.C. Dahn and R.R. Haering, Solid State Commun. 42, 179 (1982).

3. S.E. Millman and G. Kirczenow, Phys. Rev. B26, 2810 (1982).

4. We also studied several other donor and acceptor intercalated graphite compounds ranging from stage two to stage seven in x-ray diffraction and failed to observe staging transitions at temperatures below which the compound decomposes or deintercalates.

5. K.C. Woo, W.A. Kamitakahara, D.P. DiVincenzo, D.S. Robinson, H. Mertwoy, J.W. Milliken and J.E. Fischer, to be published.

6. H. Zabel and A. Magerl, Phys. Rev. B25, 2463 (1982).

7. D.P. DiVincenzo and E.J. Mele, Phys. Rev. B25, 7822 (1982).

8. D.S. Robinson and M.B. Salamon, Phys. Rev. Lett. 48, 156 (1982).

9. N. Daumas and A. Herold, C.R. Acad. Sci. Ser. C, 286, 373 (1965).

10. J. Rossat-Mignod, D. Fruchart, M.J. Moran, J.W. Milliken and J.E. Fischer, Synthetic Metals 2, 143 (1980).

11. R. Nicklow, N. Wakabayashi and H.G. Smith, Phys. Rev. B5, 4951 (1972).

Synthetic Metals, 7 (1983) 1 - 12

STAGING TRANSITIONS IN INTERCALATED GRAPHITE

J. E. FISCHER*, C. D. FUERST** and K. C. WOO

Laboratory for Research on the Structure of Matter, University of Pennsylvania, Philadelphia, PA 19104 (U.S.A.)

Summary

Recent experimental results on staging transitions in intercalated graphite are summarized. Transitions to dilute stage 1 at high temperature are observed for Li_xC_6 with $0.16 < x < 0.99$ which give the first experimental information on the upper phase boundary in the (T,x) plane. We observe a transition from dilute disordered stage 2 to ordered stage 3 either at low T or high pressure; the connection between P and T suggests other low-T staging transitions. We also report the first observation of a fractional stage, CMCCM... sequence, as one of the constituents of KC_8 in the pressure range 15 - 19 kbar. Finally, we discuss an unusual ordering transition in "KC_{34}" in which the stage 7 sequence of occupied galleries approaches perfection at low T.

Introduction

An important feature of graphite intercalation compounds is the progression of periodic sequences of filled and empty galleries whose repeat distance decreases as the concentration increases to saturation. These can be viewed as staging transitions *versus* concentration or chemical potential. Statistical mechanics calculations pioneered by Safran [1] provide a framework for understanding staging transitions *versus* temperature and/or concentration. Figure 1 shows the (T,x) staging phase diagram predicted on the basis of a simple 2-body Hamiltonian which neglects the host lattice entirely, except insofar as it defines the lattice gas sites available to intercalant atoms. A general prediction is that dilute stage 1 is the only stable phase at high T regardless of concentration. The physical origin is the dimensionality of the configurational entropy: there are more ways to decorate 2D lattice gas sites than ways to occupy a periodic 1D sequence of galleries. Thus the high-T dilute stage 1 prediction is independent of model refinements; in the simple case, the T scale of the stage 1 phase boundary is set by the in-plane attractive interaction U_0.

*Also Moore School of Electrical Engineering.
**Also Physics Department.

0379-6779/83/$3.00 © Elsevier Sequoia/Printed in The Netherlands

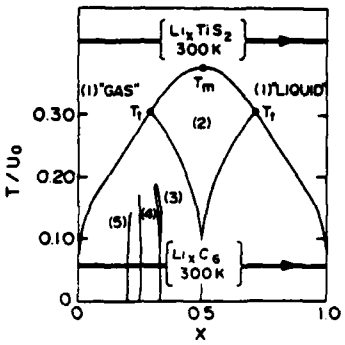

Fig. 1. Theoretical staging phase diagram based on 2-body interactions, after ref. 1. The two heavy lines represent, schematically, the experimental observations for Li intercalated into TiS_2 and graphite, after refs. 2 and 3, respectively. The 2-body model would imply widely different U_0 values for the two systems.

It has been traditional to distinguish GICs, which stage, from intercalated transition metal dichalcogenides (ITMDs), which mostly do not, by invoking the tendency of the former to have commensurate in-plane structures, or at least to have discrete values of reciprocal in-plane density, s, defined as the ratio of C to M atoms per layer of each. We now know that this distinction is only a matter of thermodynamic scale. Shown schematically at the top of Fig. 1 is a horizontal trajectory representing the 300 K electrochemical intercalation of Li into TiS_2, a system which exhibits stage 1 periodicity independent of x [2]. We can therefore deduce that in Safran's model $U_0 < 750$ K for this system. At much lower T/U_0 is a second "trajectory" representing 300 K diffraction measurements on Li_xC_6, for which periodic sequences up to at least stage 5 have been observed [3]. Above 750 K, however, only stage 1 occurs over most of the range of x (see below), and thus for Li–graphite $U_0 > 1500$ K in the 2-body model. The different T scales for the same intercalant in two host crystals underscore the need to account for host dilation, guest–host interaction, etc. [2, 4].

Several types of periodic sequences are predicted to occur in Safran's model and in subsequent modifications [4]. An example is "fractional stages" with more than one M layer per repeat unit, *e.g.*, stage 3/2 with CMCCM as the c-axis repeat. Safran did not discuss these in detail since they had not been seen experimentally, and later theoretical work included efforts to eliminate fractional stages from the equilibrium phase diagram [4]. Not surprisingly, second- and higher neighbor interlayer interactions are needed to stabilize these more complex stages. We present below the first experimental observation of a fractional stage, which occurs only at high pressure [5]. It is not at all obvious how this fits in with our current understanding of the phase diagram.

Prior to the phase diagram calculations, Safran and Hamann [6] showed that long range elastic dipole repulsion between intercalant islands would drive the system to perfect staging. With no constraints on s, single stage

regions could exist over a range of x. If s were "quantized" (*e.g.*, by the tendency to form in-plane commensurate structures), then *either* phase separation into multiple stages would result except at a few special x values, or defects would appear in the staging sequence to accommodate the correct ratio of filled to empty galleries. We have quantified the staging defects in a nominally stage 7 K–GIC; these defects are presumably metastable at 300 K, being due to quenching in a small deviation from the equilibrium stoichiometry of the single stage compound. The defect concentration diminishes markedly at a low-T first-order phase transition [7] which is also observed in c-axis resistivity [8] and static susceptibility [9].

Phase diagram of Li_xC_6

Figure 2 is a simplified schematic version of the experimental phase diagram [10] which ignores the distinction between 3-D ordered and in-plane disordered structures [11]. It is constructed from a number of high- and low-T X-ray, and high-T neutron diffraction results on samples ranging from $x = 0.16$ to $x = 0.99$. The solid dots on the upper phase boundary indicate temperatures above which only stage 1 reflections are observed at particular x values. As predicted, the transition to stage 1 is observed even down to $x = 0.16$ (in-plane disordered stage 4 at 300 K, presumed to be LiC_{36}). Shaded regions denote mixtures of two stages. The unshaded single stage regions for stages 2, 3 and 4 are inferred from intermediate transitions between the ground state and the dilute stage 1 high-T limit; these are discussed in detail elsewhere [10]. Strictly speaking, portions of these regions are mixtures of two distinct phases [11], *e.g.*, the region labelled "stage 2"

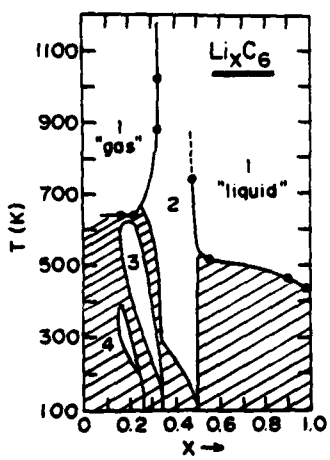

Fig. 2. Experimental staging phase diagram for Li_xC_6 derived from X-ray and neutron diffraction. Except at $x = 0.33$, all compositions transform to dilute stage 1 (●) below the chemical stability limit 750 K. The spike of highly stable stage 2 compositions at $x \gtrsim 0.33$ is not accounted for by existing theories.

includes ordered "pink" LiC_{12} and dilute, disordered "blue" LiC_{18} at some (T,x) values. These coexist up to at least 500 K, but at very low T the only equilibrium stage 2 phase is the ordered one with $x = 0.5$. In general, the high concentration limit of a stage n region corresponds to the close-packed ordered phase with general formula Li_xC_{6n}, consistent with the $\sqrt{3} \times \sqrt{3}$ superlattice. For example, stage 2 cannot exist beyond $x = 0.5$ due to hard core repulsion.

The upper phase boundary in Fig. 2 confirms the overall features predicted by Safran [1], while the asymmetry towards greater stability of higher stages at small x can be attributed to the effects of the graphite host [2, 4]. A major surprise is the strong peak between $x = 0.33$ and $x = 0.49$. The Li–GIC system is known to be stable up to ~750 K, unambiguously establishing the overall shape of the upper phase boundary. For the "superstable" concentrations we were obliged to continue the experiments into a temperature regime in which the GICs slowly tranformed into Li_2C_2, so it is difficult to extract detailed quantitative information about this extremely interesting and unexpected aspect of the phase diagram. We know for certain, however, that three samples of nominally $x = 0.33$ did not exhibit any stage 1 lines up to 870 K, 1020 K and >1150 K. The first two temperatures are indicated by the dots on the steeply rising portion of the phase boundary. Thus there inarguably exists an anomalous sharp spike which is not accounted for in any of the model calculations. The spike separating stage 2 from stage 1 cannot be attributed to commensurability effects since stage 2 does not exhibit long-range in-plane order above 500 K. In our view, the existence of this superstable region presents a major challenge to theories of staging in intercalated systems.

Similar experiments on heavy alkali GICs have been generally unsuccessful. Apparently the T scale of the upper phase boundary is much higher than in Li_xC_6 or Li_xTiS_2. It is tempting to attribute these different limiting temperatures to variations in the elastic energy required to dilate the host crystal [2]. TiS_2 expands negligibly to accommodate Li, while the C–C interlayer spacing increases by 10% in Li_xC_6. For the heavy alkalis the expansion ranges from 61% to 77% from K to Cs in graphite. The increased elastic strain energy appears to correlate with the T scale of the stage n/stage 1 phase boundary.

While the dilute "LiC_{18}" stage 2 with $x = 0.33$ may not transform to stage 1 at high T, it does transform at constant x to a compact ordered stage 3 at low T. Figure 3 shows the time-dependent growth and decay of stages 3 and 2 $(00l)$ reflections, respectively, at a constant 240 K. Scans along Li and C rows show a simple stacking sequence ABAαABAα for the low-T ordered stage 3 phase, which can thus be represented by $LiC_{6\times3}$. The fact that the transition does not go to completion means either (a) the sample contains a small amount of dense stage 2 LiC_{12} at 300 K or (b) the stoichiometry of "blue", dilute stage 2 is actually more Li-rich than LiC_{18}, or (c) 240 K lies in the 2 + 3 coexistence regime. We did not make detailed studies *vs.* T due to the slow kinetics; in Fig. 2 we have provisionally assigned

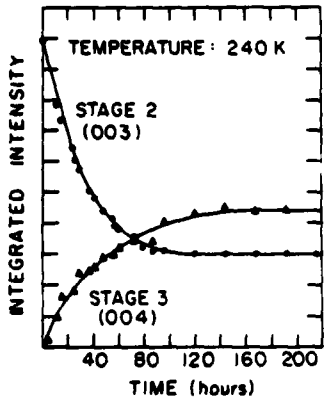

Fig. 3. Dynamics of a partial dilute stage 2 → ordered stage 3 transition in "LiC_{18}" at 240 K. The decay of stage 2 (003) is accompanied by the growth of the stage 3 (004), although the time constants are not the same. Other phases may be present.

240 K as the upper limit of stage 3 at $x = 0.33$. It is reasonable to suppose that no further in-plane condensation occurs at lower T since $LiC_{6\times3}$ is close-packed (but see below for KC_8!). So at $x = 0.33$ the ground state is probably single stage 3, progressing through a slow first-order transition to stage 2 at ~240 K and then to the stage 1 dilute limit at much higher T, perhaps in excess of 1100 K. As noted above, the steepness of the 2/1 boundary at $x \sim 0.33$ is completely unexpected, there being *no obvious* reason why tiny variations in site occupancy of a disordered phase should have such a strong effect on the stability.

Similar transition sequences probably occur at smaller x, as suggested by the tilted stages 3 and 4 single-phase regions. We have not confirmed the analogous low-T transitions to ordered structures having higher stage indices than at 300 K. We have, however, confirmed at $x = 0.16$ the sequence $4 \rightarrow 4 + 3 \rightarrow 3 \rightarrow 3 + 1 \rightarrow 1$ upon heating from 300 K to 640 K [10].

In general, the progression from the ground state with increasing T occurs *via* integral stages of decreasing index, with no evidence for fractional stages. It is not known if the dense, ordered and dilute, disordered stage 2 phases merge at some T. The stability region of stage 2 does not extend below $x = 0.25$ since samples of stages 3 and 4 at 300 K transform to stage 1 with no stage 2 reflections evident in the mixed phase regions.

Dilute stage 2 Li–graphite exhibits a pressure-induced staging/densification transition at 300 K, entirely analogous to what is observed in dilute stage 2 K–graphite [12], KC_{24}. It also appears to be the same transition discussed above, which occurred at ~240 K and atmospheric pressure. The c-axis resistivity of "LiC_{18}" shows a 4-fold increase at 2.9 kbar, the relaxation upon removing the pressure being slow enough to permit X-ray experiments *en route* back to the $P \approx 0$ structure. We initially observe a stage 3 sequence in the $(00l)$'s which relaxes to pure stage 2 in 1 - 4 days. If we

assume that this is the same low-T transition which occurred at 1 bar, as suggested by the similarity of $\rho_c(T)$ and $\rho_c(P)$ anomalies and by the slow kinetics of both effects, then we can construct the 2/3 phase boundary in the (P,T) plane for $x = 0.33$ shown in the lower right-hand corner of Fig. 4. We have chosen 220 K as the critical temperature at $P = 0$, assuming that the incompleteness of the $2 \rightarrow 3$ transition at 240 K (Fig. 3) is due to equilibrium coexistence at that temperature. Since the 2.9 kbar, 300 K transition in "LiC_{18}" is analogous to the 7 kbar, 300 K transition in KC_{24}, it is tempting to use the observed 1 bar, 220 K transition in the former to predict an analogous low-T transition in the latter. This we do in Fig. 4, assuming the same slope, dP/dT, for both compounds. This obviously neglects many factors: the different volume per intercalant, different areal densities at $x = 0.33$, and different degeneracies of the respective ordered structures. Nonetheless, the prediction is that KC_{24} should transform to ordered stage 3 upon cooling through ~120 K, a prediction which has not been borne out by the many low-T experiments on this compound [13]. On the other hand, within the limitations of our extrapolation procedure, it is perhaps more than fortuitous that the $P = 0$ extrapolation corresponds to T_u, the upper anomaly temperature below which the in-plane structure of KC_{24} exhibits a complex pattern of modulation satellites [13]. A possible argument could be that the expected slow kinetics hinders the predicted staging/densification transition, the result being the quenching in of the observed complex in-plane structure. In fact, one plausible interpretation of this structure is a modulation of the K layer by the graphite substrate which drives the K–K near-neighbor separation towards the commensurate 2×2 value, 4.92 Å. The slow kinetics thus frustrates in-plane condensation from the 6 Å nearest-neighbor distance in the disordered high-T phase, which, in turn, would have triggered a stage 2 → stage 3 transition to preserve bulk stoichiometry.

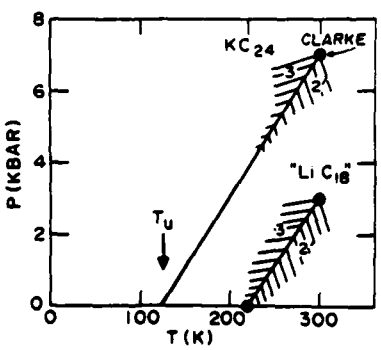

Fig. 4. Schematic of the stage 2/stage 3 phase boundary in the (P,T) plane for $x = 0.33$. "LiC_{18}" boundary derived from observation of the 2/3 transition at (2.9 kbar, 300 K) and at (1 bar, ~200 K). Assuming identical slopes, an extrapolation of Clarke's datum (ref. 12) to $P = 0$ implies a staging/densification transition in KC_{24} at T_u where electronic anomalies and in-plane ordering have been observed (ref. 13).

KC_8 at high pressure

Subsequent to the pressure-dependent X-ray studies of Clarke *et al.*, we measured $\rho_c(P)$ at 300 K for stages 1 - 5 K–GICs up to 25 kbar [14] in order to study the combined effects of stage changes and intercalant areal density on the *c*-axis electronic transport. We were surprised to find a sharp ρ_c anomaly at 15 kbar in KC_8, since all the known structural transitions involved condensation from $s = 12$ to $s = 8$ accompanying the increase in stage index [12], and $s = 8$ was thought to be the high-density, or hard sphere limit for potassium in graphite. A staging transition in KC_8 would imply densification to a smaller discrete value of s, as discussed in the "Introduction". Alternatively, one might expect some stage disordering at high pressure if the K–K nearest neighbor distance were to decrease below the 2×2 commensurate value. Aspects of both phenomena were observed in the (00*l*) neutron diffraction experiments discussed below, and in single crystal, high pressure X-ray studies to be reported elsewhere [15].

Figure 5(a) shows an (00*l*) neutron scan of KC_8 at 15 kbar [5]. In addition to the original stage 1 reflections, we observe five new peaks whose

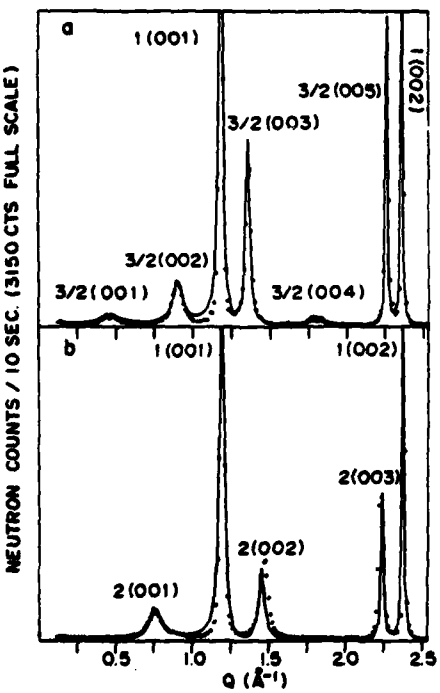

Fig. 5. Neutron (00*l*) scans for KC_8 at (a) 15 kbar and (b) 19 kbar, both at 300 K (ref. 5). Both pressures are in stable, mixed-stage regions. At 15 kbar we observe for the first time a "fractional stage", with layer sequence CMCCM... *i.e.*, stage 3/2. Solid lines calculated from the Hendricks–Teller model (ref. 16) to account for staging defects (see text).

13.61 Å repeat distance is appropriate for the sum of stage 1 and stage 2 packages at this pressure, *i.e.*, CMCCM... staging sequence denoted stage 3/2 (3 carbon and 2 metal layers per repeat). The transition to a stable 2-phase region can be represented as follows: $6KC_{8\times1} \rightarrow 4KC_{6\times1} + K_2C_{8\times3}$, that is, the stage 1 at high pressure has $s = 6$ and a $\sqrt{3} \times \sqrt{3}$ superlattice while the stage 3/2 phase retains the $P = 0$ value $s = 8$.

At 14 kbar, just below the emergence of the stage 3/2 peaks, we observe anomalous broadening of the $(00l)$'s which we attribute to random nucleation of the $s = 8 \rightarrow s = 6$ condensation which leaves behind "anti-islands" of unfilled galleries. By 15 kbar the strain energy associated with the random arrangement of $s = 6$ islands and $s = \infty$ anti-islands is sufficient to drive the system to a well-ordered stage, except that the incomplete $8 \rightarrow 6$ condensation dictates a 2-phase mixture. The new $s = 6$ islands order into macroscopic regions of "superdense" stage 1 KC_6, while the empty galleries combine with the remaining uncondensed $s = 8$ regions to produce stage 3/2. The stage ordering is not perfect even in the stable 2-phase region. The solid curve in Fig. 5(a) is calculated from the Hendricks–Teller model [16] with the stage 1 phase consisting of a random sequence of 96% filled, 4% empty galleries and the stage 3/2 represented by an exactly stoichiometric 1:1 mixture of stages 1 and 2 packages with probability 0.8 that they occur in the proper sequence. The agreement with the experimental points is extremely good; in particular the Q-dependent widths and relative amplitudes within each phase are very well reproduced. Notice that the types of disorder are different for the two phases: stage 1 exhibits "stoichiometry disorder" produced by randomly "doping" a perfect 1-D crystal with graphite package "impurities", while stage 3/2 is extremely well modelled by positional disorder in an exactly stoichiometric phase.

The parameters characterizing the staging disorder change little, if at all, with pressure through the stable 2-phase region 15 - 19 kbar, whereupon the stage 3/2 gives way to stage 2 as shown in Fig. 5(b). The stage 1 reflections are entirely unaffected by this second transition, which we therefore ascribe to $K_2C_{8\times3} \rightarrow 2KC_{6\times2}$, that is, the remaining $s = 8$ regions condense to $s = 6$ making possible the $3/2 \rightarrow 2$ staging transition entirely within this phase of the system. Evidently the additional volume decrease from 15 to 19 kbar provides sufficient driving force for the second step in the $8 \rightarrow 6$ condensation. Staging disorder in the "superdense" stage 2 KC_{12} is again evident from Fig. 5(b) *via* the decreasing linewidth with increasing Q. The existence of the potassium $\sqrt{3} \times \sqrt{3}$ commensurate superlattice at high pressure has been directly confirmed in single crystal X-ray film experiments using the diamond anvil technique [15].

The above results raise a number of important questions. In addition to the structural implications, one expects major electronic consequences associated with a nearest neighbor metal distance less than the atomic core diameter. For example, it would be interesting to extend the pressure-dependent superconductivity experiments [17] into the $s = 6$ regime. Similar effects occur in RbC_8 and CsC_8 at slightly higher pressures. It is also

significant that all previous examples of staging transitions *vs.* T, P or x involve disordered in-plane structures on one or both sides of the phase boundary, in which case the kinetics could be mediated by motion of a 2D fluid through Daumas/Hérold domains [18]. Here the staging transitions take place between two ordered in-plane structures, which, if nothing else, implies slower than usual kinetics. In the neutron diffraction experiments, care was taken to ensure that the structure had stabilized at each pressure but there may exist a very slow component which was undetectable on our time scale of several hours maximum. Finally, the connection between hydrostatic pressure and observation of a fractional stage needs to be clarified. Integral stages of high index require a long-range interaction but only between nearest intercalant layers [1], while stage 3/2 as an equilibrium phase implies second neighbor layer interactions over a relatively short distance [4]. It is significant that we do not observe stage 4/3, $K_3C_{6\times4}$, which is directly accessible from KC_8 without phase separation. Stage 4/3 would require correlations among third neighbor K layers, and is predicted [19] to have a narrower stability region than stage 3/2. The multiplicity of $\rho_c(P)$ anomalies [14] suggests that other fractional stages may occur in higher stage K–GICs.

Stage ordering transition in "KC_{84}"

Figure 6 shows temperature-dependent ρ_c [8] and $\chi_\parallel$ [9] (static susceptibility measured with $\vec{H}\parallel\vec{c}$) for a nominally stage 7 K–GIC. Both parameters are sensitive to the c-axis charge distribution as established by the staging configuration and the nonlinear screening of K layers by the delocalized π charge. Both parameters show first-order anomalies centered at ~230 K with ~10 K hysteresis. The sense of the $\chi_\parallel$ anomaly suggests a reduced stage index in the low T phase relative to the nominal stage, because $\chi_\parallel$ is dominated by orbital paramagnetism and x(orbital) *per gram* increases with decreasing K layer separation in the vicinity of stage 7 [20]. Low-temperature X-ray studies were launched [7] to elucidate the structural origin of the anomalies in Fig. 6. As a prelude, room temperature (00l)'s were recorded up to the 23rd order of stage 7. No rogue peaks were detectable at the 2% level. However, the peak positions exhibited small but regular oscillations about the Bragg positions, as represented by the error bars in Fig. 7(a). The origin of these oscillations is the same 1-D disorder phenomenon [16] which gave rise to the Q-dependent widths in Fig. 5. The open circles in Fig. 7(a) are calculated peak positions for a random sequence of a 3:1 ratio of stage 7 and stage 8 unit cells. The agreement with the experimental data is gratifying. In the model calculation the frequency of the oscillation depends on the difference in package thicknesses, which is why there are zeroes at Q values corresponding to graphite (00l) reflections (these occur near $n = 0$, 8, 15, etc., for stage 7). The phase of the oscillations shifts by π if the minority constituent is assumed to have a smaller rather than a

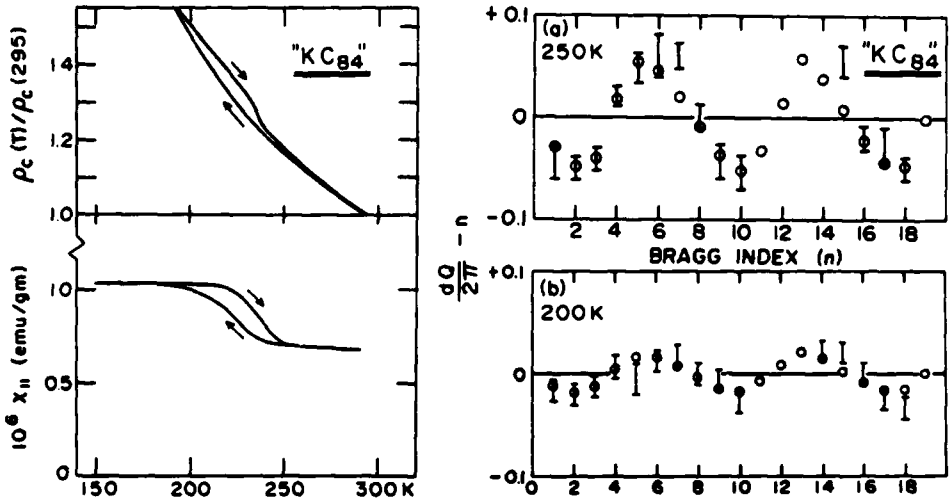

Fig. 6. Electronic anomalies in "KC_{84}", a nominal stage 7 compound. Both c-axis resistivity (ref. 8) and static susceptibility (ref. 9) show first-order anomalies centered at ~ 235 K with ~ 10 K hysteresis.

Fig. 7. The error bars are the measured deviations of (00l) reflection positions from their average (perfect crystal) values for "KC_{84}" at (a) 250 K, (b) 200 K. ○, calculated (ref. 16) assuming random mixtures of stage 7 and 8 units cells with relative abundances 3:1 and 9:1 at 250 K and 200 K, respectively. The improved stage ordering at low T correlates with the electronic anomalies in Fig. 6.

larger thickness than the major component (*i.e.*, for some stage 6 packages in a mostly stage 7 phase). Finally, the amplitude is determined only by the relative abundances if the interpackage correlations are completely random; in the present instance the average structure is stage 7 simply because the 7 packages outnumber the 8's and thus one will find more "regions" of accidentally ordered 7 than ordered 8. Local regions of stage 15 are excluded from the calculation.

In order to study the structural origin of the $\rho_c(T)$ and $\chi(T)$ anomalies, we recorded (00l) diffractograms as a function of increasing T from 200 K up. Several reflections showed discontinuous Q shifts and intensity changes upon warming through 235 K, in excellent agreement with the two warming curves in Fig. 6. The low-T structure is characterized by Fig. 7(b) which shows that the amplitude of the oscillation in the peak position is greatly reduced relative to room temperature. Comparison with model calculations (open circles) shows that the stage ordering has improved, the sample now being well-represented by a random 9:1 mixture of stages 7 and 8 packages. The kinetics of this transition are surprisingly fast; only 10 minutes were required to stabilize the change in (00l)'s after 5 K temperature increments. It is not known whether the K layers order or not below 235 K.

The staging disorder at 300 K is most likely a metastable situation quenched in from the growth condition. As such, one would expect sizeable variations from sample to sample since the stability regions for pure, high stages are very narrow. Furthermore, the transition should not be discussed in terms of the equilibrium phase diagram in which the stage number increases with decreasing temperature (in this case the "average" stage number has the opposite T-dependence). The improved stage ordering at low T is, of course, in the correct sense for an entropy-driven order–disorder transition. Situations like that depicted in Fig. 7(a) would presumably relax toward a perfect stage 7 or to a mixture of two adjacent perfect stages, depending on the concentration width of the stage 7 region at 300 K. Hastening the process by annealing may be problematic; since there is so little potassium in the compound, it would be very difficult to maintain and verify constant x.

The analysis of this unusual stage-ordering transition is in terms of a temperature-dependent "stoichiometry disorder", where the term "stoichiometry" refers only to the overall numbers of filled and empty galleries. The reversibility of the transition can be taken as evidence that no potassium enters or leaves the compound. Therefore, if fewer galleries are empty at low T (as implied by the reduction in the fraction of stage 8 cells), then the filled galleries must, on average, have a greater in-plane density in the low-T phase. It would therefore be quite interesting to determine the in-plane structure, the implication being that if the K layers order, there should be a sample-dependent incommensurability which derives from the quenched-in stoichiometry disorder. Another possibility is that in-plane condensation/ordering associated with the stage ordering transition could lead to interesting modulated in-plane structures [13] with variable in-plane density.

The 30% anomaly in $\chi_{\parallel}(T)$ (Fig. 6) underscores the extreme sensitivity of the orbital susceptibility to the screening charge distribution [20]. The higher positive χ at low T means that there are (on average) fewer graphite interior layers which contribute a huge diamagnetic term, since they contain little or no excess charge. The sense of the $\rho_c(T)$ anomaly is incompatible with a defect scattering interpretation because the resistivity is greater in the "ordered" state. This isn't too surprising since the c-axis mean free path may, in fact, be less than the lattice constant (~25 Å), the latter being, in addition, the length scale of the disorder; at 240 K ρ_c for "KC_{84}" is slightly *greater* than that of HOPG [8]. The sense of the ρ_c anomaly may be connected to the unusual stage dependence of $\rho_c(T)$ reported previously [8].

Conclusion

Stage ordering and staging transitions in GICs continue to provide challenges to theory and experiment. The interplay of competing interactions provides a rich variety of stable structures as a function of T, P and x;

more novel phases surely remain to be discovered. Advances in understanding GICs should stimulate new work in ITMDs, from which one can hope to achieve a global understanding of phase equilibria in quasi-2D guest–host systems.

Acknowledgement

This paper summarizes the results of several fruitful and enjoyable collaborations, principally with J. D. Axe, F. J. DiSalvo, J. B. Hastings, W. A. Kamitakahara and D. B. McWhan. Major support was provided by the NSF MRL Program DMR 82-16718 and by ARO Contract DAAG29-80-K0019.

References

1 S. A. Safran, *Synth. Met.*, *2* (1980) 1.
2 J. R. Dahn, D. C. Dahn and R. R. Haering, *Solid State Commun.*, *42* (1982) 179.
3 D. Billaud, E. McRae, J. F. Marêché and A. Hérold, *Synth. Met.*, *3* (1981) 21.
4 S. E. Millman and G. Kirczenow, *Phys. Rev. B*, *26* (1982) 2810.
5 C. D. Fuerst, J. E. Fischer, J. D. Axe, J. B. Hastings and D. B. McWhan, *Phys. Rev. Lett.*, *50* (1983) 357.
6 S. A. Safran and D. R. Hamann, *Phys. Rev. B*, *22* (1980) 606.
7 C. D. Fuerst, T. C. Koch, J. E. Fischer, J. D. Axe, J. B. Hastings and D. B. McWhan, in M. S., and G. Dresselhaus, J. E. Fischer and M. J. Moran (eds.), *Intercalated Graphite*, Materials Research Society Symp. Proc., Vol. 20, North-Holland, New York, 1983, p. 39.
8 K. Phan, C. D. Fuerst and J. E. Fischer, *Solid State Commun.*, *44* (1982) 1351.
9 F. J. DiSalvo, J. V. Waszczak and J. E. Fischer, Ext. Abstr., *15th Bien. Conf. on Carbon*, Philadelphia, PA, 1981, p. 38.
10 K. C. Woo, H. Mertwoy, J. E. Fischer, W. A. Kamitakahara and D. S. Robinson, *Phys. Rev. B*, *27* (1983) 7831.
11 K. C. Woo, W. A. Kamitakahara, D. P. DiVincenzo, D. G. Robinson, J. W. Milliken, H. Mertwoy and J. E. Fischer, *Phys. Rev. Lett.*, *50* (1983) 182.
12 R. Clarke, N. Wada and S. A. Solin, *Phys. Rev. Lett.*, *44* (1980) 1616.
13 For a review see J. B. Hastings, in L. Pietronero and E. Tosatti (eds.), *Physics of Intercalation Compounds*, Springer, New York, 1981, p. 206.
14 C. D. Fuerst, D. Moses and J. E. Fischer, *Phys. Rev. B*, *24* (1981) 7471.
15 J. M. Bloch, V. Cajipe, D. Moses, H. Katz and J. E. Fischer, to be published.
16 S. Hendricks and E. Teller, *J. Chem. Phys.*, *10* (1942) 147.
17 L. E. DeLong, V. Yeh, V. Tondiglia, P. C. Eklund, S. E. Lambert and M. B. Maple, in M. S., and G. Dresselhaus, J. E. Fischer and M. J. Moran (eds.), *Intercalated Graphite*, Materials Research Society Symp. Proc. Vol. 20, North Holland, New York, 1983, p. 195.
18 N. Daumas and A. Hérold, *C.R. Acad. Sci.*, *268* (1969) 373.
19 P. Bak and R. Bruinsma, *Phys. Rev. Lett.*, *49* (1982) 249.
20 S. A. Safran and F. J. DiSalvo, *Phys. Rev. B*, *20* (1979) 4889.

INTERNATIONAL JOURNAL OF QUANTUM CHEMISTRY, VOL. XXIII, 1223-1230 (1983)

Energy-band Structure and Charge Distribution for BaC_6 †

N. A. W. HOLZWARTH

Corporate Research-Science Laboratories, Exxon Research and Engineering Company, Linden, New Jersey 07035, U.S.A.

D. P. DiVINCENZO, R. C. TATAR, AND S. RABII

Moore School of Electrical Engineering, University of Pennsylvania, Philadelphia, Pennsylvania 19104, U.S.A.

Abstract

An *ab initio* self-consistent calculation has been carried out for the electronic properties of BaC_6. Energy bands and charge densities are presented for BaC_6 and compared with those of LiC_6. The results show that the band originating from Ba states has a mixture of *s* and *d* character and the *d* component hybridizes appreciably with the π bands of graphite. The Fermi level intersects this band as well as the graphite π bands, giving rise to a complicated Fermi surface with several types of carriers. Depending on the type of volumetric partitioning, the charge transfer from Ba to graphite layers is determined to be between 0.7 and 1.0 electron per Ba atom. The calculated results are consistent with available transport and optical measurements.

1. Introduction

BaC_6 is one of the members of a family of layered materials known as the graphite intercalation compounds [1], where layers of foreign atoms such as Li,K,Ba, . . . or molecules such as AsF_5,$SbCl_5$, . . . are inserted between the graphite layers. In all cases the foreign species (intercalants) and the graphite planes form a well ordered sequence, where *n* layers of carbon atoms are positioned between every two intercalant layers. This phenomenon is referred to as staging, and *n* denotes the stage of the compound. BaC_6 is a stage one compound, i.e., having the highest possible concentration of the intercalant. In the compounds formed by insertion of the alkali or alkaline earth metals into graphite, the intercalant atoms are also ordered within their layers up to temperatures somewhat above room temperature. To first approximation, the process of intercalation leads to transfer of charge between the intercalant layer and the host, causing an increase in carrier concentration over that of pure graphite, resulting in metallic behavior [2]. However, at a more detailed level, the changes in the graphite band structure due to intercalation go beyond this rigid band model and an *ab initio* approach to this problem is required. Energy band structure calculations for the first stage alkali metal intercalation compounds have been carried out for LiC_6 and KC_8

† Partially supported by NSF-MRL Program under Grant No. DMR-79-23647, and by ARO Contract No. DAAG-29-77-C400.

© 1983 John Wiley & Sons, Inc. CCC 0020-7608/83/041223-08$01.80

AD-A146 148 FUNDAMENTAL ELECTRONIC PROPERTIES OF DONOR-TYPE GRAPHITE INTERCALATED COM..(U) MOORE SCHOOL OF ELECTRICAL ENGINEERING PHILADELPHIA PA S RABII ET AL. 2/2

UNCLASSIFIED 01 AUG 84 ARO-17299.18-PH DAAG29-80-K-0019 F/G 11/2 NL

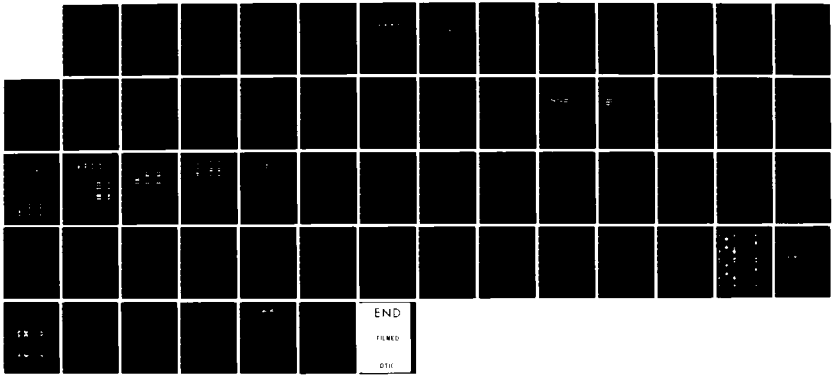

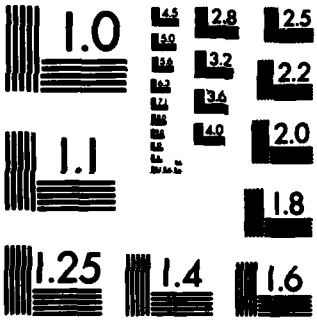

MICROCOPY RESOLUTION TEST CHART
NATIONAL BUREAU OF STANDARDS-1963-A

[3–6]. In this work we present the results of a first-principles calculation of the energy band structure and the charge densities for BaC_6.

BaC_6 is one of the less studied members of the graphite intercalation compounds. Other than synthesis and structural studies [7] only its optical properties have been reported [8]. No theoretical studies of this material have been performed. However, on the basis of a rigid band model, one may expect it to exhibit higher electrical conductivity than the well studied alkali metal intercalation compounds, since Ba has two valence electrons to donate to the graphite layers. The larger interlayer separation of graphite sheets in BaC_6 also points to the possibility of a highly two dimensional Fermi surface.

In this work we present the results of first-principles calculations of the energy band structure and charge densities of BaC_6 carried out to test the above speculations as well as to provide a model for the interpretation of the experimental studies that will increasingly become available.

2. Formalism

The calculations were carried out self-consistently, using density functional theory [9] in the local density approximation [10], with the Schrödinger equation for valence electrons given as

$$[T + V(\mathbf{r})^{\text{ion}} + V^{\text{val}}(\rho)]\psi_i(r) = E_i\psi_i(r),$$

where $\rho = \Sigma_i|\psi_i(r)|^2$ and i runs over the occupied valence states. $V^{\text{val}}(\rho)$ contains the electron–electron repulsive term plus the exchange-correlation contribution. The ionic part of the potential is treated using the nonlocal norm-conserving pseudopotentials as developed by Hamann et al. [11] and Kerker [12]. These pseudopotentials are chosen such that the pseudo-wave-functions converge to the actual all electron wave functions outside a specified core sphere about each atom and the integral of the pseudocharge within this sphere is equal to that of the actual charge. These pseudopotentials have the advantage of being independent of energy over a reasonable energy range. For C we have used the Hamann et al. [11] form including s and p pseudopotentials. For Ba we employ the Kerker form [12] and the extension of these pseudopotentials to included relativistic effects other than spin–orbit interaction [13]. Figure 1 shows the pseudopotentials for C and Ba. In addition to s and p we have also included d pseudopotentials since the $5d$ atomic levels of Ba are only 1.2 eV above the $6s$ states.

The valence wave functions were represented in a mixed basis of plane waves and LCAO Bloch states following the approach of Louie et al. [14]

$$\psi_i(\mathbf{r}) = \sum_{\mathbf{G}} C^i_G e^{i(\mathbf{k}+\mathbf{G})\cdot\mathbf{r}} + \sum_j C^i_j\phi_j(\mathbf{k},\mathbf{r}),$$

where $\mathbf{G}$ is a reciprocal lattice vector. The LCAO set $\phi_j(\mathbf{k},\mathbf{r})$ includes s and p-type atomic functions at carbon sites, while the set on the Ba site contains only d functions. It is expected that Ba s electrons are adequately represented by the plane wave ex-

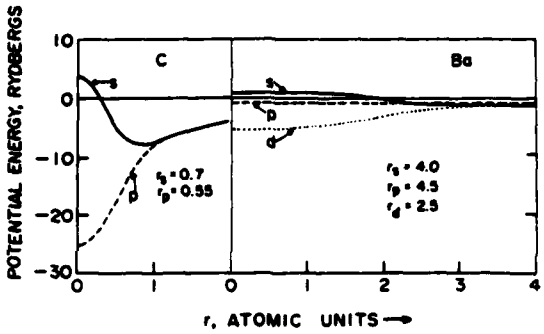

Figure 1. Ionic pseudopotentials for C and Ba.

pansion. In the actual calculation, the localized functions are also expanded in terms of plane waves and the necessary matrix elements are evaluated numerically using Fourier space techniques.

3. Crystal Structure

In pristine graphite, the hexagonal carbon sheets are arranged such that half the carbon atoms in each layer are directly above the atoms in the layer below (site *a*), while the other half are located above the center of the hexagons in the layer underneath (site *b*). This is referred to as *AB* stacking. In contrast, the carbon layers in all first stage intercalation compounds of graphite are positioned such that all the carbon atoms in one layer are directly above those in the layer below, leading to *AA* stacking.

The crystal structure for BaC_6 has been determined by Guerard et al. [12]. The space group is $P6_3/mmc$, the same as for graphite. The Ba atoms within the intercalant layer occupy positions above the center of every third carbon hexagon. The in-plane lattice parameter is measured to be 4.302 ± 0.006 Å, $\sqrt{3}$ times the carbon–carbon second nearest neighbor distance, while the distance between nearest neighbor C planes is 5.25 ± 0.02 Å. The carbon bond in BaC_6 is 10% dilated over that of pure graphite. The intercalant layers are arranged such that the Ba in adjacent layers occupy two of the three possible positions α and β, leading to $A\alpha A\beta A\alpha \ldots$ stacking [Fig. 2(a)]. In order to make the calculations more tractable, we chose an alternate crystal structure for this study, i.e., $A\alpha A\beta A\gamma A\alpha \ldots$ stacking, where the Ba atoms in adjacent layers occupy all the three α, β, and γ positions [Fig. 2(b)]. This choice leads to a smaller unit cell, in the form of a slanted hexagonal prism containing six carbon and one Ba atoms.

In order to see the details of charge transfer between the intercalant and carbon layers, we have also carried out these calculations for the same structure with the Ba atoms removed. We refer to this as C_6. For the purpose of comparison we also present the results for LiC_6 with the same structure.

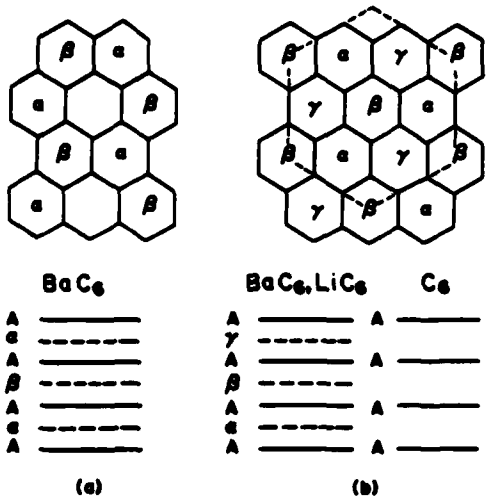

Figure 2. (a) In-plane structure and stacking sequence for BaC_6; (b) In-plane structure and the stacking sequence used in this calculation for BaC_6 as well as for LiC_6 and C_6.

4. Results

The Brillouin zone for BaC_6 structure used in this calculation is a slanted hexagonal prism with the base making an angle of 25.4° with the k_xk_y plane (Fig. 3). Figure 4 shows the energy bands in the vicinity of the Fermi level for the three systems studied. The zero of energy is taken to be the bottom of the graphite σ bands. The C_6 bands are essentially those of graphite, folded in the smaller Brillouin zone of the present structure, with a reduction of the k_z dispersion of the bands brought about by the larger

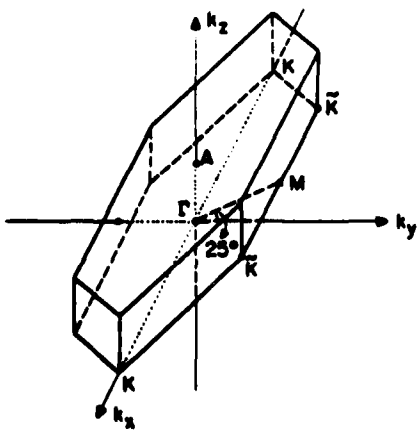

Figure 3. Brillouin zone for the assumed structure, labeling the high symmetry points and directions.

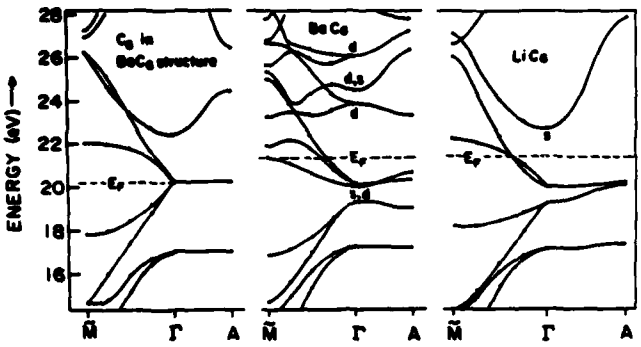

Figure 4. Energy band structure for C_6, LiC_6, and BaC_6 in the vicinity of the Fermi level for two high symmetry directions. Bands of metal *s* and *d* character are indicated.

c-axis parameter. The bands coming together at 20.2 eV at Γ are the π bands of graphite, while those originating at 17 and 22.5 eV correspond to the bonding and antibonding σ bands respectively. For LiC_6, the free-electron-like band with the minimum at 22.7 eV is due to Li 2*s* levels hybridized with the graphite antibonding σ bands. This band is entirely above the Fermi level, indicating a charge transfer of one electron per intercalant atom to the carbon layers. The remainder of the bands can be identified with those of C_6. Furthermore, hybridization with Li s states has resulted in a splitting of 0.72 eV in the σ bands at Γ. This is, however, not a gap in the density of states since the bands overlap in the Γ–*A* direction.

In the case of BaC_6, the minimum of the lowest metal band is located well below the Fermi level, indicating a partial charge transfer. This band has a mixture of *s* and *d* characters. By integrating the charge within a specified volume of BaC_6 and subtracting that of C_6 from it, we can estimate the total charge transfer. First we considered a slab geometry, assigning a slab of thickness of 3.35 Å to the C plane, and a slab of thickness 1.90 Å to the Ba plane. The charge redistribution per unit cell was found to be one electron in the C slab and one electron in the Ba slab. Second we studied a spherical geometry, placing a sphere of radius 2.2 Å (half the Ba–Ba nearest neighbor distance) around the Ba atoms. The charge transfer within this sphere was found to be 1.3 electrons. Of this charge, 0.2 electrons have s character while 1.1 electrons have *d* character. By comparison, for a ground state Ba atom, the total $6s^2$ charge in a sphere of the same radius is 0.8 electrons. The unoccupied 5*d* atomic orbitals are much more contracted than are the 6*s* orbitals, and could accomodate twice as much charge within this sphere.

In discussing the charge distribution, we shall refer to the charge residing in the filled σ and π bands of C_6 below the pure graphite Fermi level as the valence charge, and the charge in the remaining bands as conduction charge. For both LiC_6 and BaC_6, the valence charge has the same definition as in C_6, however, the conduction charge in BaC_6 also includes the electrons occupying the metal bands. Since small amounts of charge transfer will not be clearly seen in contour plots for total charge, we will present the difference densities between BaC_6 or LiC_6 and C_6. Figure 5 presents

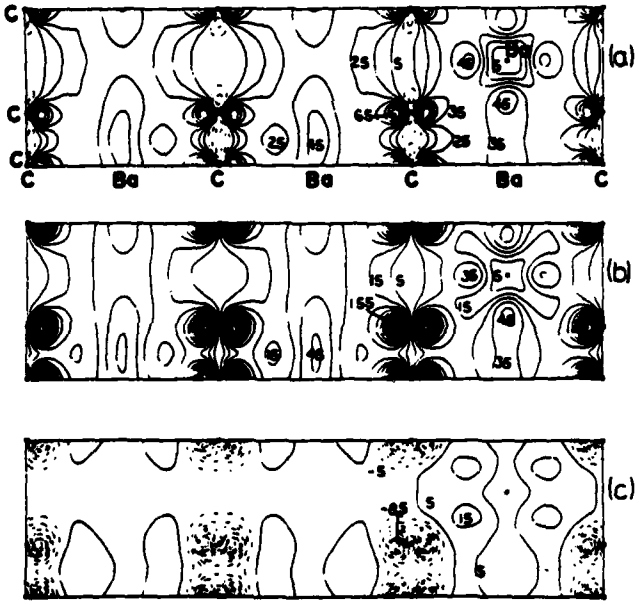

Figure 5. Difference charge density contours for BaC_6 along the c direction in units of $0.001e/Å^3$. (a) Total difference density. (b) Conduction density. (c) Valence difference density.

separate plots for total difference density, conduction density, and the valence difference density for BaC_6 along the c axis (perpendicular to the graphite planes). If there were no hybridization between the metal and graphite states, Figures 5(a) and 5(b) would be identical, however, such hybridization does exist and Figure 5(c) shows the polarization of the graphite valence charge in response to the presence of Ba. We can further see from Figure 5(b) that the conduction charge around the carbon atoms has the expected π nature since these charges reside in the π bands of graphite, while the charge around the Ba atoms is primarily d-like.

In Figure 6 we compare the difference densities for BaC_6 and LiC_6, and in addition give the contours in the carbon and also the intercalant planes. We can see that in the case of LiC_6, very little charge lies in the Li plane and whatever exists is s-type. However, there is appreciable charge in the Ba plane and the d nature of these electrons is easily observed. It should be emphasized that the total difference density is very close to the conduction density, and the latter is not shown here.

We can thus conclude that the rigid band model is particularly inappropriate for the first stage Ba intercalation compound BaC_6. The Fermi surface is quite complicated, having three sheets. Two of the sheets derive from the electrons in the graphite π bands, while the third results from the metal band. We find substantial hybridization among these bands, which is consistent with the low conductivity which is reported [8] for BaC_6. Preliminary optical reflectivity measurements [8] indicate that the intraband plasma frequency ω_p of BaC_6 is higher by (30–40%) than that of the alkali

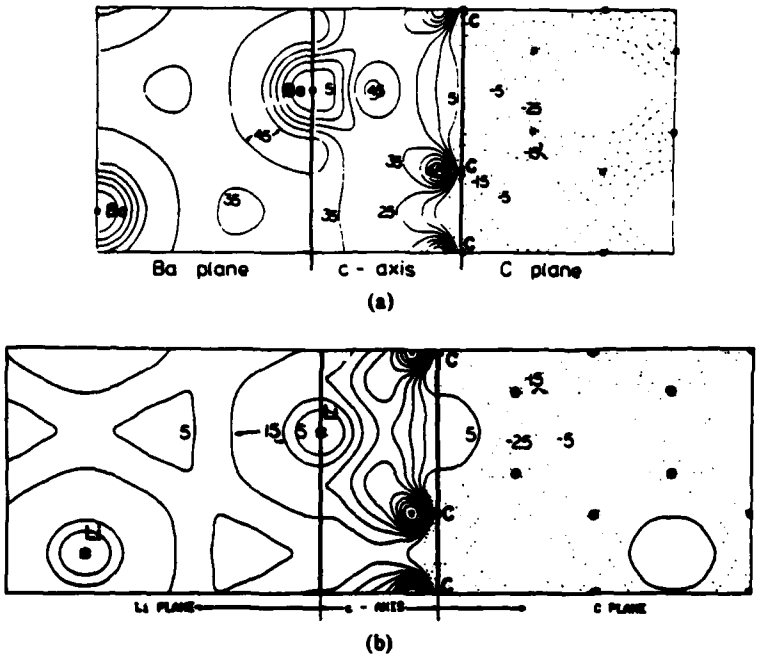

Figure 6. (a) Total difference charge density for BaC_6 in Ba plane, c direction, and in the graphite plane; (b) corresponding total difference densities for LiC_6 in units of $0.001e/Å^3$.

metal intercalation compound LiC_6. This shift of the plasma frequency is influenced by various factors. The presence of an extra conduction electron in the alkali earth compound favors an increase in ω_p, but the larger c-axis lattice constant of BaC_6 as compared with LiC_6 works against it. So, while the experimental result is roughly consistent with the present work, further calculation would be required to carry the comparison of theory and experiment further.

Acknowledgment

We acknowledge many helpful discussions with other members of the graphite group at Penn.

Bibliography

[1] *Proceedings of the Franco-American Conference on Intercalated Compounds of Graphite*, F. L. Vogel and A. Herold, Eds. (Elsevier, Lausanne, 1977); *Proceedings of the International Conference on Layered Materials and Intercalates*, C. F. van Brugen, C. Haas, and H. W. Myron, Eds. (North-Holland, Amsterdam, 1980); *Proceedings of the Second Conference on Intercalation Compounds of Graphite*, F. L. Vogel, Ed. (Elsevier, Lausanne, 1980).

[2] J. E. Fischer, Mater. Sci. Eng. 31, 211 (1977).

[3] N. A. W. Holzwarth, S. Rabii, and L. A. Girifalco, Phys. Rev. B **18**, 5190 (1978); N. A. W. Holzwarth, L. A. Girifalco, and S. Rabii, ibid. 5206 (1978).
[4] T. Inoshita, K. Nakao, and H. Kamimura, J. Phys. Soc. Jpn. **43**, 1237 (1977); **45**, 689 (1978).
[5] T. Ohno, K. Nakao, and H. Kamimura, J. Phys. Soc. Jpn. **47**, 1125 (1979).
[6] D. P. DiVincenzo and S. Rabii, Phys. Rev. B **25**, 4110 (1982).
[7] D. Guèrard, M. Cheabouni, P. Lagrange, M. El Makrini, and A. Herold, Carbon **18**, 257 (1980).
[8] K. C. Woo, P. J. Flanders, and J. E. Fischer, Bull. Am. Phys. Soc. **27**, 272 (1982).
[9] P. Hohenberg and W. Kohn, Phys. Rev. **136**, B864 (1964); W. Kohn and L. J. Sham, Phys. Rev. **140**, A1133 (1965).
[10] L. Hedin and B. I. Lundqvist, J. Phys. C **4**, 2064 (1971).
[11] D. R. Hamann, M. Schlüter, and C. Chiang, Phys. Rev. Lett. **43**, 1949 (1979).
[12] G. P. Kerker, J. Phys. C **13**, L189 (1980).
[13] L. Kleinman, Phys. Rev. B **21**, 2630 (1980); G. B. Bachelet, D. R. Hamann, and M. Schlüter, Bull. Am. Phys. Soc. **27**, 407 (1982).
[14] S. G. Louie, K. Ho, and M. L. Cohen, Phys. Rev. B **19**, 1774 (1979).

Synthetic Metals, 8 (1983) 197 - 203

CALCULATION OF THE OPTICAL SPECTRA FOR GRAPHITE

N. X. CHEN and S. RABII

University of Pennsylvania, Moore School of Electrical Engineering & Laboratory for Research on the Structure of Matter, Philadelphia, PA 19104 (U.S.A.)

N. A. W. HOLZWARTH

City College of the City University of New York, Department of Physics, New York, NY 10031 (U.S.A.)

Summary

The optical spectra of graphite is calculated over a range of 40 eV. The calculations are based on the *ab initio* self-consistent field energy band structure of graphite using norm-conserving pseudopotentials. The calculated $\epsilon(\omega)$ is in excellent agreement with the results from reflectivity and electron energy loss measurements.

1. Introduction

The electronic energy band structure of graphite has been the subject of numerous theoretical investigations (see refs. 1 and 2 for review of previous works). The explanation of the optical spectra over a large energy range is a critical test for any proposed band structure model.

Previous theoretical studies of the optical spectra of graphite have been of two types. Most calculations which cover a large energy range have used 2-dimensional energy bands and constant velocity matrix elements [2 - 4]. They could not incorporate the in-plane band splittings of ~1 eV caused by interlayer interactions. Furthermore, they did not obtain the optical spectra with the radiation polarized along the *c*-axis. Meanwhile, in only one case has the full dielectric tensor $\epsilon_{\mu\nu}(\omega)$ been calculated by using the 3-dimensional Slonczewski–Weiss model of graphite bands [5]. However, the results only cover a range of 7 eV and are limited to π bands.

In the present work we report the results of a totally *ab initio* calculation of $\epsilon(\omega)$ covering a range of more than 40 eV. The calculated results are compared with the reflectivity and electron energy-loss measurements.

2. Energy band structure calculation

We have extended the previous calculation of the energy band structure of graphite [6] to cover a range of 60 eV. The technique used is the *ab initio*

0379-6779/83/$3.00 © Elsevier Sequoia/Printed in The Netherlands

norm-conserving pseudopotential theory [7] with the wave-functions expanded in a mix-basis of plane waves and localized orbitals [8]. The energy bands are initially calculated at 20 points in 1/24 of the Brillouin Zone. For calculation of the momentum matrix elements, the pseudo-wave functions are completely expanded in a plane wave representation,

$$|j, \vec{k}> = \sum_m a_m^j(\vec{k}) \exp[i(\vec{K}_m + \vec{k})\vec{r}]$$

where j is the band index and $\vec{K}_m$ is the reciprocal lattice vector. If we neglect the nonlocality of the pseudopotential, the momentum matrix element between states i and j at the same k is simply given by,

$$< i, \vec{k}|p|j, \vec{k} > = \sum_m a_m^{i*}(\vec{k})\ a_m^j(\vec{k})(\vec{K}_m + \vec{k})$$

According to our estimate, the average nonlocal contribution to the momentum matrix elements is less than 10%.

Subsequently, the $\vec{k} \cdot \vec{p}$ interpolation procedure was used to obtain the energy bands and momentum matrix elements at a mesh of 9216 points in the entire Brillouin Zone. In order to guarantee the accuracy of the $\vec{k} \cdot \vec{p}$ interpolated transition energies and momentum matrix elements over a range of 40 eV, the *ab initio* band structure calculation had to be performed over a range of 62 eV at each of the 20 points in the irreducible zone. Figure 1 shows partial energy band structure with important transitions labeled for later discussion.

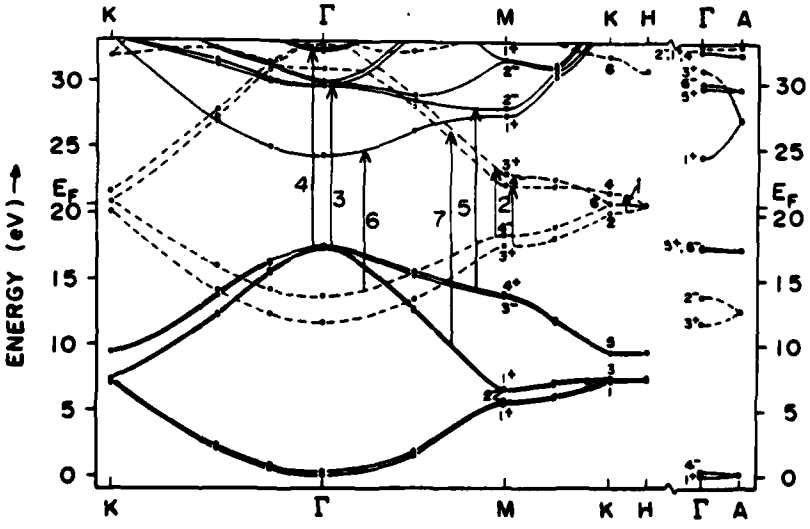

Fig. 1. The partial energy band structure of graphite with some of the major optical transitions indicated by arrows and labeled from 1 to 7.

3. Complex dielectric tensor

The interband contribution to the dielectric tensor is given within the relaxation time approximation [9], and at zero temperature, by,

$$\epsilon_{\mu\nu}(\omega) = \delta_{\mu\nu} - \frac{e^2}{\pi^2 m^2 \omega} \sum_{ij}' \int \frac{d^3k}{\hbar\omega_{ij}(\vec{k})} \left[\frac{P_{ij}{}^{\mu}(\vec{k}) P_{ji}{}^{\nu}(\vec{k})}{-\tilde{\omega} + \omega_{ij}(\vec{k})} - \frac{P_{ij}{}^{\nu}(\vec{k}) P_{ji}{}^{\mu}(\vec{k})}{\tilde{\omega} + \omega_{ij}(\vec{k})} \right]$$

where $\tilde{\omega} = \omega + i/\tau$, and $\hbar\omega_{ij}(k) = E_j(k) - E_i(k)$. The primed summation is taken over states such that $E_i < E_F < E_j$, where E_F is the Fermi energy.

The relaxation time τ is generally energy and k-dependent, although it is usually assumed to be a constant and its primary effect is the broadening of the structure in the spectra. Johnson and Dresselhaus [5] have used a value of 2×10^{-14} s for τ in the energy range up to 7 eV. We have calculated the dielectric function for a range of τ between 10^{-15} and 2×10^{-14} s, with the final results given for the value of 10^{-15} s, in order to obtain reasonably smooth curves using only one value of τ for the entire energy range. However, we believe that it is better to set τ at a higher value and try to achieve the smoothness by using more points in the summation mesh in the reciprocal space.

The space group for graphite, G_s, is $P6_3/mmc$ with the point factor group, $P = G_s/T$, which is isomorphic to D_{6h}. Thus the dielectric tensor is diagonal and has only two independent components $\epsilon_\perp$ and $\epsilon_\parallel$, corresponding to the electric field perpendicular and parallel to the c-axis, respectively.

The intraband contribution to $\epsilon(\omega)$ was calculated using the Drude model

$$\epsilon_\alpha \text{ intra} = \frac{-\omega_{p\alpha}{}^2}{\omega(\omega + i/\tau')}$$

where the $\omega_{p\perp}$ and $\omega_{p\parallel}$ are the plasma frequencies, chosen as 0.95 eV and 0.1 eV, respectively. τ' is the relaxation time for intraband transition, chosen as 0.5×10^{-13} s.

4. Results and discussion

Taft and Phillip (TP) have carried out reflectivity measurements in graphite up to 26 eV with polarization perpendicular to the c-axis and have obtained $\epsilon_{1\perp}$ and $\epsilon_{2\perp}$ through Kramers–Kronig analysis of the data [10]. The electron energy loss spectra have been measured by Zeppenfeld [11] from 6 to 30 eV. Greenaway *et al.* [12] have measured the reflectivity of graphite in the visible and ultraviolet regions for both parallel and perpendicular polarizations from 2 to 5 eV. Subsequently Tosatti and Bassani (TB) combined the experimental results of Zeppenfeld and Greenaway *et al.* and obtained $\epsilon_{1\perp}(\omega)$, $\epsilon_{2\perp}(\omega)$, $\epsilon_{1\parallel}(\omega)$, and $\epsilon_{2\parallel}(\omega)$ by Kramers–Kronig analysis [13].

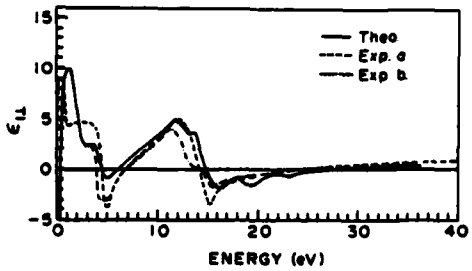

Fig. 2. The real part of the in-plane component of the dielectric tensor as a function of frequency. The experimental curves a and b refer to refs. 10 and 13, respectively.

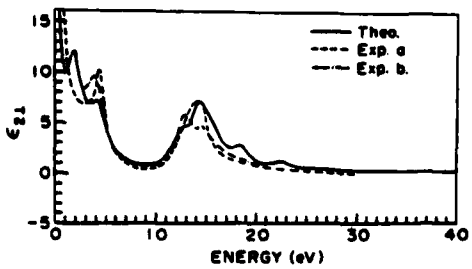

Fig. 3. The imaginary part of the in-plane component of the dielectric tensor as a function of frequency. The experimental curves a and b refer to refs. 10 and 13, respectively.

Figures 2 and 3 show the calculated $\epsilon_{1\perp}$ and $\epsilon_{2\perp}$ along with the results of (TP) and (TB). The overall agreement between theory and experiments is excellent and calculated plasma frequencies, occurring at $\epsilon_{\perp}(\omega) = 0$, have values of 6.1 eV and 27 eV, in good agreement with the measured values of 7 eV and 25 - 27 eV.

The main structure in $\epsilon_{2\perp}(\omega)$ is primarily due to the σ–σ transitions labeled "5" and "4" in Fig. 1, while its low energy shoulder is attributed to the σ–σ transition "3". One of the experimental curves also shows the double peak for this structure at the same photon energy as given by the calculation. The 4.7 eV peak is due to the saddle point transition "2" at M [13]. The peak at 2 eV in the calculated spectra does not have a corresponding structure in the experimental results.

Figure 4 shows the calculated and experimental sum rule

$$n^{eff}(\omega) = \left(\frac{m}{4\pi e^2 N}\right)\frac{2}{\pi}\int_0^{\omega} \omega' \epsilon_2(\omega')\, d\omega'$$

giving the effective number of valence electrons per carbon atom that have contributed to the photon absorption in the perpendicular polarization. The first step in both the calculated and experimental curves is due to the main π–π transition (M,K), while the second step is the result of σ–σ as well as the remainder of the π–π transitions. The shape of the calculated

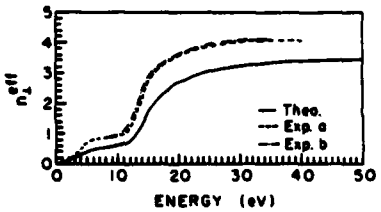

Fig. 4. The sum rule for the effective number of valence electrons per atom obtained from $\epsilon_{2\perp}$. The experimental curves a and b refer to refs. 10 and 13, respectively.

curve is in excellent agreement with the experiments. Even though, at saturation, the calculated sum rule for $\epsilon_{2\perp}$ only accounts for 80% of the valence electrons, this is considered to be in very good agreement considering the total *ab initio* nature of the calculation [14].

Figures 4 and 5 show the corresponding results for $\epsilon_{1\parallel}(\omega)$. According to the experiment, there are two plasma frequencies at 14 and 18.2 eV, while the calculated result in Fig. 4 only shows one, at 19 eV. The calculated $\epsilon_{1\parallel}(0)$ is 2.5 - 2.8, which is close to the experimental value of 2.35 [12]. In Fig. 5, the main structure near 11 eV comes from the π–σ transition labeled "6" in Fig. 1. This structure receives contributions from a large region of the Brillouin Zone surrounding the Γ–M direction. This identification is quite important since it helps to pin-point the minimum of the first unoccupied σ band at the center of the zone. This band is unusual and significant in the sense that it has a large dispersion along the c-axis: the precise location of its minimum has been a subject of disagreement between different calculations, and it hybridizes very strongly with the alkaline s-levels in the graphite intercalation compounds [6, 15 - 17]. The 11 eV structure was originally attributed to the σ–π transition "7" by (TB). However, the energy was off by over 3 eV from all the band structure calculations.

Figure 6 shows the sum rule for $\epsilon_{2\parallel}$. The disappearance of the saturation step at low energy is attributed to the fact that the major π–σ transitions start at ~11 eV, as shown in Figs. 1 and 5. The theoretical result also

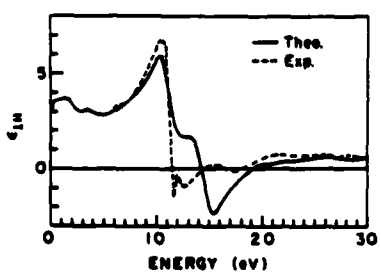

Fig. 5. The real part for the c-axis component of the dielectric tensor as a function of frequency. The experimental curve refers to ref. 13.

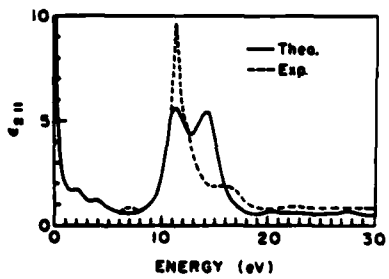

Fig. 6. The imaginary part for the c-axis component of the dielectric tensor as a function of frequency. The experimental curve refers to ref. 13.

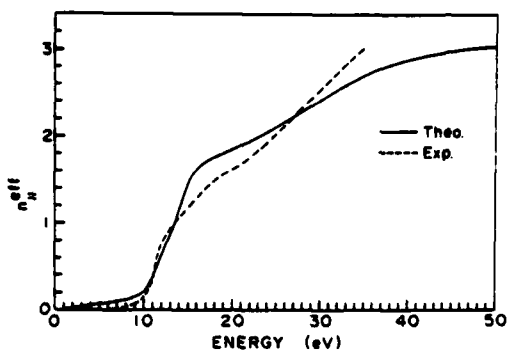

Fig. 7. The sum rule for $\epsilon_{2\parallel}$. The experimental curve is after ref. 13.

indicates that $n_{\parallel}^{eff}$ reaches saturation only at energies beyond 50 eV, well above the range of the present experimental measurements.

The reflectivity at high frequencies, *i.e.*, after the significant oscillation strengths are exhausted, must fall off at ω^{-4}. This requirement is excellently satisfied by our results. The high frequency behavior of the calculated reflectivity indicates that the necessary range of the experimental measurements has to be extended to 40 eV and 55 eV, respectively, for the electric field perpendicular and parallel to the c-axis.

We can thus conclude that our *ab initio* self-consistent energy band structure of graphite has successfully explained its optical spectra and, furthermore, we may expect similar success in our calculation for the alkali-graphite intercalation compounds, which are now in progress.

Acknowledgements

We gratefully acknowledge the many helpful discussions with J. E. Fischer and R. C. Tatar, and the resources provided by the Moore School Computing Facility. This work was supported by National Science

Foundation Materials Research Laboratory Grant No. DMR-79-23647, and Army Research Office Contract DAAG-29-77-C400.

References

1 R. C. Tatar and S. Rabii, *Phys. Rev. B, 25* (1982) 4126.
2 A. Zunger, *Phys. Rev. B, 17* (1978) 626.
3 F. Bassani and G. Parravicini, *Nuovo Cimento, 50* (1967) 95.
4 G. S. Painter and D. E. Ellis, *Phys. Rev., 81* (1970) 4747.
5 L. G. Johnson and G. Dresselhaus, *Phys. Rev., 87* (1974) 2275.
6 N. A. W. Holzwarth, S. G. Louie and S. Rabii, *Phys. Rev. B, 26* (1982) 5382.
7 D. R. Hamann, M. Schluter and C. Chiang, *Phys. Rev. Lett., 43* (1979) 1494.
8 S. G. Louie, K. M. Ho and M. L. Cohen, *Phys. Rev. B, 19* (1979) 1774.
9 H. Ehrenreich and M. H. Cohen, *Phys. Rev., 115* (1959) 786.
10 E. A. Taft and H. R. Phillip, *Phys. Rev., 138* (1965) A197.
11 K. Zeppenfeld, *Z. Phys., 211* (1968) 391.
12 D. L. Greenaway, G. Harbeke, F. Bassani and E. Tosatti, *Phys. Rev., 178* (1969) 1340.
13 E. Tosatti and F. Bassani, *Nuovo Cimento, 65B* (1970) 161.
14 F. Wooten, *Optical Properties of Solids*, Academic Press, New York, 1972.
15 N. A. W. Holzwarth, S. Rabii and L. A. Girifalco, *Phys. Rev. B, 18* (1978) 5190.
16 N. A. W. Holzwarth, S. G. Louie and S. Rabii, *Phys. Rev. Lett., 47* (1981) 1318.
17 N. A. W. Holzwarth, S. G. Louie and S. Rabii, *Phys. Rev. B, 28* (1983) 1013.

ELECTRONIC STRUCTURE OF GRAPHITE INTERCALATION COMPOUNDS

N.A.W.HOLZWARTH*, Corporate Research-Science Laboratory, Exxon Res. and Eng. Co., Linden, N.J. 07036

S.G. LOUIE, Dept. of Physics, University of California, Berkeley, CA. 94720

and

SOHRAB RABII, Moore School of Electrical Engineering, University of Pennsylvania, Philadelphia, PA. 19104

ABSTRACT

In this paper we present a brief survey of previous work as well as some new preliminary results for graphite fluoride compounds.

INTRODUCTION

Many aspects of the electronic structure of graphite intercalation compounds are now well understood. In this paper, we review some of the qualitative features of these results. Because of shortness of space, we cannot be complete, and we apologize for our omissions.

Four topics are considered. First, the use of rigid bands models to describe properties involving states near the Fermi level are discussed. These models are non-trivial and explain many of the unusual transport properties of graphite intercalation compounds. Secondly, results of detailed first principles calculations are discussed. The notion of an ideal intercalation compound is introduced, with LiC_6 being the example, BaC_6 being the counter example, and KC_8 being somewhere in between. The third section deals with model high stage compounds. The distribution of charge among inequivalent C layers, and the contributions to the screening of the intercalant ions due to graphite states throughout the valence bands compared with those due to graphite states near the Fermi level is discussed. It is seen that the total charge density screens the intercalant ions nearly completely within the region between the two graphite planes surrounding an intercalant layer. The conduction electron screening is more extended. Finally, the charge distribution and energy bands for a model of CF are presented.

SIMPLE MODELS

A theoretical idea which has guided much of the research on graphite intercalation compounds is that upon intercalation by a donor material, the unoccupied π bands of graphite are partially

*Present address: Dept. of Physics, City College of CUNY, New York, N.Y. 10031

filled. Similarly, upon intercalation by an acceptor material, the occupied π bands of graphite are partially emptied. Various rigid band models for a general intercalation compound have been developed [1-7] with the assumptions that the intralayer and interlayer interactions (the latter in modified form) of the graphite π orbitals are preserved upon intercalation. In these models, the intercalant states need not be directly considered, except in terms of providing the mechanism for charge transfer. Such models have used to describe a variety of electronic properties of graphite intercalation compounds which depend upon states near the Fermi level. The results of these model calculations demonstrate some of the unusual electronic behavior of these materials, largely due to the unusual intralayer dispersion of the graphite π bands near E_F. In Table I, we summarize the dependence on Fermi energy of various properies of 2 dimensional rigid band graphite compared with that of a 2 dimensional rigid band metal having parabolic dispersion.

TABLE I.
Fermi energy dependence of various properties
for rigid band models of 2-dimensional metals

Notation: K = energy independent constant
E = Fermi energy measured from band extremum

	Parabolic dispersion	Graphite dispersion
Density of states	K	KE (for small E)
Number of states	KE	KE^2 (for small E)
D. C. conductivity	KE	KE (for small E)
Low field magnetoresistance	0	>0
Low field Hall coefficient	KE	KE x (strong function of E)
Orbital magnetization	<0	>0 (for $E > E_c$)

Generally the results derived from rigid band-type models are consistent with experiments that deal with states near the Fermi energy. For example, the positive orbital magnetization of low and high stage donor compounds was successfully explained by Safran et. al. [2]. An explanation of the unusually small low field Hall coefficient was offered by the calculation of Holzwarth [4]. However, detailed comparisons are difficult because some parameters in the models are not well known.

Rigid band type of models have been extended to 3rd and higher stage materials by several authors [3,5-7]. For these materials, the distribution of charge among inequivalent carbon

layers depends upon several competing effects. The electrostatic potentials resulting from charge transfer between the intercalant and graphite π bands tend to localize the transferred charge near the intercalant layer. Counteracting this effect are interlayer hopping and intralayer Coulomb repulsions of the excess graphite charge, as well as screening of the Coulomb interactions by polarization of the graphite valence electrons. Since these effects are so very delicately balanced, results of model calculations tend to be sensitive to parameters that are not well known. Therefore, it is worthwhile to perform first principles calculations for some representative high stage as well as low stage compounds in order to establish some qualitative trends.

DETAILED CALCULATIONS FOR FIRST STAGE DONOR COMPOUNDS

From first principles band structure calculations on graphite intercalation compounds, one can develop a more detailed picture of the electronic states and charge density throughout the 30 eV range of valence and low-lying conduction bands. In addition to the general picture, one can also address the more specific issue of the validity of the rigid band model for the states near the Fermi level of these compounds. Specifically, one would like to know where the intercalant states lie in relation to the Fermi level of the compound, and to what extent they perturb the graphite π bands in the vicinity of E_F.

The first of such calculations were carried out for KC_8 [8]. In this work it was found that the K ions were only 60% ionized and that some of the states near E_F contained appreciable K character, which seemed to be consistent with a number of experimental results. Other calculations for KC_8 have been performed, some of which agree and others which disagree [9] with the original result. Recent electron loss and photoemisson measure measurements [10] lend support for the view [9] that the K band is fully ionized and that the Fermi level bands of KC_8 are largely of graphite π character. For this compound as well as for the related compounds RbC_8 and CsC_8, the 2 x 2 superlattice structure as well as the relatively large intralayer density of the intercalant cause the bottom of the intercalant band to come very close to E_F so that calculated results are very sensitive to the details of the calculation.

By contrast, the situation for LiC_6 is much more straightforward. Early calculations [11] indicated the Li to be completely ionized and the Fermi level bands to be appreciably unperturbed graphite π states, the bottom of the intercalant band lying a few eV above E_F. This result was consistent with a number of experiments and other calculations [12-14]. One of the most direct comparisons between theory and experiment is obtained from angle resolved photoemission. In Fig. 1, the experimental results of Eberhardt et al.[13] are reproduced in comparison with recent calculated bands for LiC_6 obtained using self-consistent local density theory and mixed basis pseudopotential techniques [15,16]. In this figure, the experimental results include distributions for electrons in occupied bands emitted normal to the c-axis ($k_z = 0$) as well as photoyield results for excitation from the Li 1s level to probe the unoccupied bands having appreciable Li character.

Thus, theoretical and experimental evidence suggests that, with respect to the rigid band model, LiC_6 is an ideal intercalation compound. One reason for this behavior is that the graphite π states near E_F contain considerable antibonding character. These states, having rapid spatial variation within a layer plane, cannot effectively hybridize with the slowly-varying donor s orbitals.

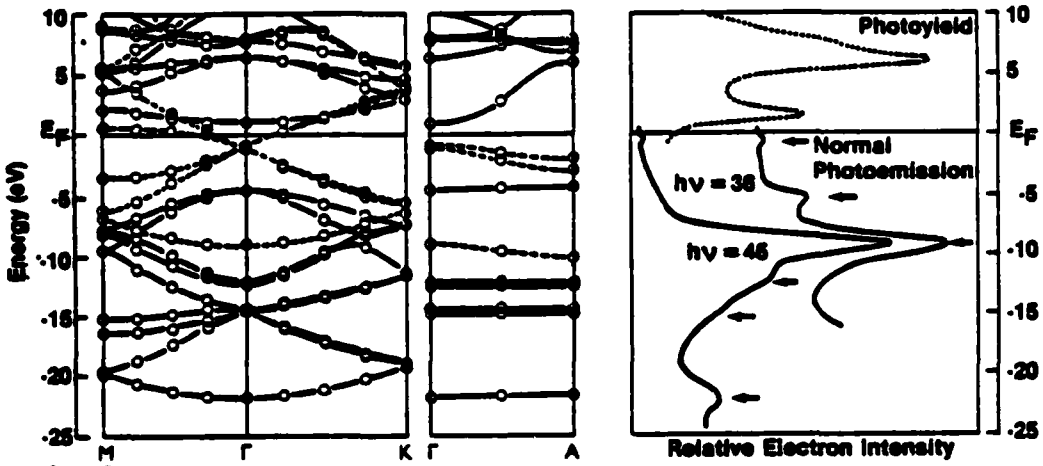

1. Calculated self-consistent energy bands for LiC_6 (Ref. 15) in the AαAαAα stacking structure compared with experimental photoemission and photoyield results of Eberhardt et al. (Ref. 13). The calculated π band are designated with dashed lines while the σ bands are designated with full lines. In this figure the zero of energy is taken at the Fermi level.

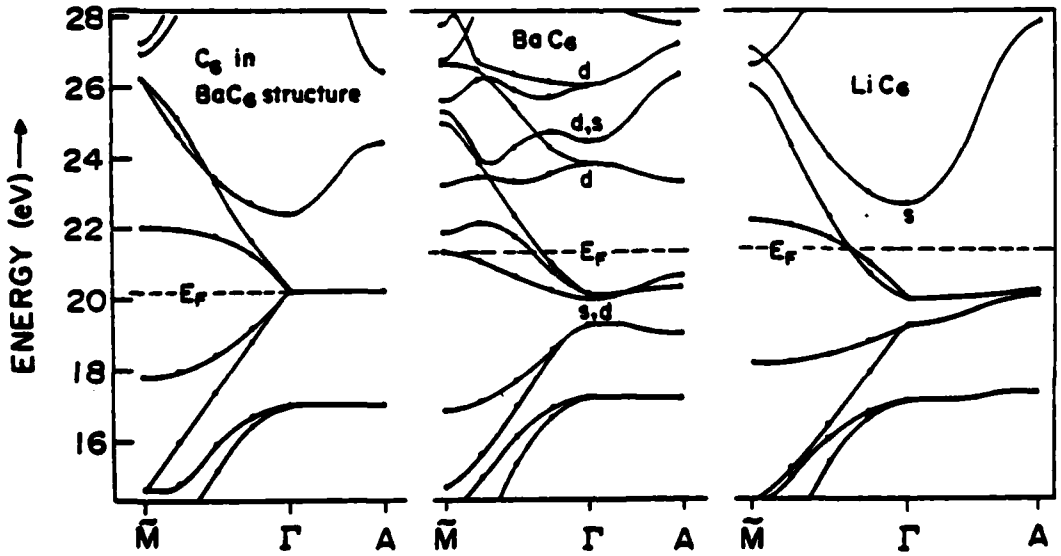

2. Comparison of the energy bands of BaC_6 (central panel) with its reference graphite compound (left panel) and LiC_6 (right panel). For BaC_6 and LiC_6, the stacking sequence was taken to be AαAβAγA. The labels s and d denote the orbital character of the intercalant contribution to the indicated bands. The zero of energy in this figure, as well as in Figs. 3 and 4, is taken at the bottom of the lowest graphite σ band.

At the other extreme, BaC_6 is a non-ideal intercalation compound. Since Ba is an alkaline earth metal, it has the possibility of transferring 2 electrons per intercalant atom. However, self-consistent calculations [17] indicate that due to the strong electronegativity of the second electron as well as hybridization of the graphite π bands with the low-lying 5d states of Ba, the occupied bands of BaC_6 include appreciable Ba character accounting for roughly 1 electron per intercalant. In Fig. 2, the self-consistent band structures for BaC_6 are compared with those of a reference graphite material (BaC_6 with the Ba atoms removed) and with LiC_6.

In order to get a more quantitative picture of the hybridization of the intercalant states with those of graphite, we have plotted the densities of states (DOS) and partial densities of states (PDOS) for LiC_6 and for BaC_6, compared with their respective reference graphite compounds. To construct the DOS and PDOS, we approximated the integration over the Brillouin zone by a mid point sampling, using the derivative of a Fermi function to smooth over unphysical structure introduced by the sampling.

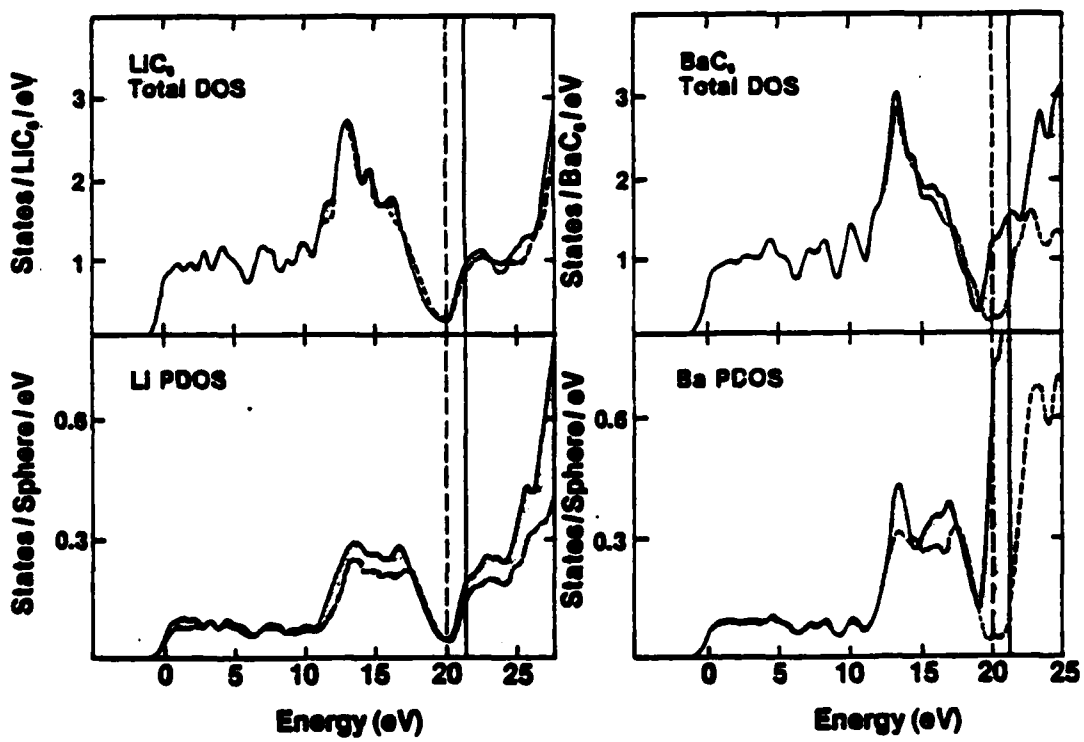

3. Total density of states (DOS) and partial densities of states (PDOS) for LiC_6 ($A\alpha A\alpha A\alpha$) and BaC_6 ($A\alpha A\beta A\gamma$). In each panel, the DOS or PDOS for the intercalation compound (full curve) is compared with that of the reference graphite compound (dashed curve), with shading used to emphasize the regions of positive difference. The sphere radii used for the Li and Ba PDOS's were 3.1 bohr and 4.3 bohr respectively.

The shaded regions of the PDOS curves indicate which of the states in the intercation compound contribute to the charge near the intercalant site. It is not surprizing that there is a large contribution in the energy range 13-17 eV corresponding to the polarization of bonding π bands of graphite by the intercalant ions. The σ electrons are also polarized, but due to their small spatial extent they hardly contribute to the intercalant PDOS shown in Fig. 3. The polarization of σ electrons by the intercalant ions is more clearly demonstrated in contour plots of the total difference density of LiC_6 or BaC_6 in a C plane [15,17], where it is shown to create a deficit of charge (with respect to the reference graphite compound) from the C-C bonds. For LiC_6, in the vicinity of E_F the shape of the DOS and PDOS curves are nearly identical to those of the reference graphite compound. Peaks in the PDOS curve above E_F correspond to the unoccupied Li - like states. For BaC_6, there is an additional large density of Ba states near E_F.

FIRST PRINCIPLES CALCULATIONS FOR HIGH STAGE DONOR COMPOUNDS

From first principles calculations for model high stage compounds one can estimate some of the effects which determine the distribution of charge amoung inequivalent C layers. Many of these effects can be adequately modeled by representing the interactions of the intercalant ions in terms of their planar average. The electronic structure for such a model was determined self-consistently by T. Ohno [18]. He found that the valence electrons of graphite are very effective for screening the electrostatic potentials introduced by intercalation such that for a model representing a third stage compound of stoichiometry XC_{36} (X = K, Rb, or Cs), 99% of the total transferred charge (as determined from Mulliken populations) was associated with the bounding layers. It was found that the graphite σ electrons play a large role in the screening of the intercalant ions.

First principles calculations for forms of 2nd and 3rd stage Li intercalated graphite -- LiC_{12} and LiC_{18} -- were performed by the present authors [15,19]. In this work the intercalant ions were treated explicitly. The energy bands for 1st, 2nd, and 3rd stage Li intercalated graphite are compared with their corresponding reference graphite compounds in Fig. 4 for the Γ point (k = 0) states of the $\sqrt{3} \times \sqrt{3}$ superlattice Brillouin zone. This figure shows the non rigid shifts of the various bands with respect to their reference graphite compounds. In general, the σ states are shifted to higher energy while the π states are shifted to lower energy. The bottom of the unoccupied intercalant band closely follows the Γ_1^+ band of graphite and moves to higher energy with higher stage. For the third stage compound, states having eigenfunctions that are mainly localized on the interior layers are shifted to higher energy with respect to the corresponding states localized on the bounding layers, by roughly 1 eV. The splitting of the π bands due to interlayer hopping is of comparable magnitude.

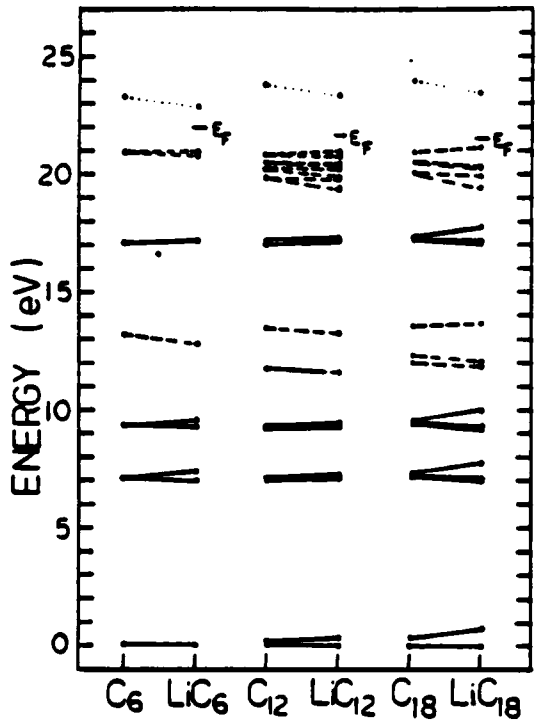

4. Calculated self-consistent Γ point energies for LiC_6 ($A\alpha A\alpha A\alpha$), LiC_{12} ($AB\alpha BC\beta CA\gamma$), and LiC_{18} ($ABC\alpha CAB\beta BCA\gamma$) compared with those of their reference graphite compounds. Full lines denote σ bands, dashed lines denote π bands, and dotted lines denote the unoccupied Γ_1^+ band which strongly hybridizes with the bottom of the intercalant s band.

The polarization of charge due to the intercalant ions is similar for stages 2 and 3. The total transferred charge in the sandwich region, as defined by the integrated charge between 2 graphite planes surrounding an intercalant layer minus that of the reference graphite compound, was found to be 90%. On the other hand, the conduction electron contribution, as defined by charge contributed by electrons in partly filled bands was found to be 40%. The behavior of the 2 types of densities relates to the analogous behavior discussed above for stage 1 compounds and can be exhibited by different types of experiments. For example, the total difference density is probed by C 1s spectroscopy. The conduction electron density is related to the density probed by transport measurements.

ELECTRONIC STRUCTURE OF GRAPHITE FLUORIDE COMPOUNDS -- PRELIMINARY RESULTS

There has been some recent interest in graphite fluoride compounds as possible intercalation compounds (at low F concentration) [20,21] as well as for modeling possible defects which limit the conductivity of graphite MF_6^- compounds [2]. The structure of C_4F used in the present work was that proposed by Rudorff [23] in which the fluorines form two 2 x 2 superlattices above and below the graphite planes in such a way that there is a center of inversion at the mid point of 1/4th of the C hexagons. The F's were assumed to be located over C atoms at a distance of 1.4Å. There is no detailed structural data to confirm this structure, and in fact Mallouk and Bartlett [21] as well as Ebert [24] have found indirect evidence that the Rudorff structure is not correct. Nevertheless, the detailed electronic structure of C_4F in the

Rudorff structure is useful starting point for a study of low concentration fluoride compounds of graphite. The self-consistent band structure together with the partial densities of states are shown in Fig. 5. The F σ band is split off from the bottom of the C σ band by 11 eV. The F p bands span a 10 eV range below the Fermi level, interacting with the lower π and upper σ bands of graphite, the lowest F p state having primarily π character. Since the unfluorinated carbons in this structure form isolated rings, a band gap is introduced near the Fermi level. Our calculations show that C_4F in the Rudorff structure 2 eV band gap semiconductor.

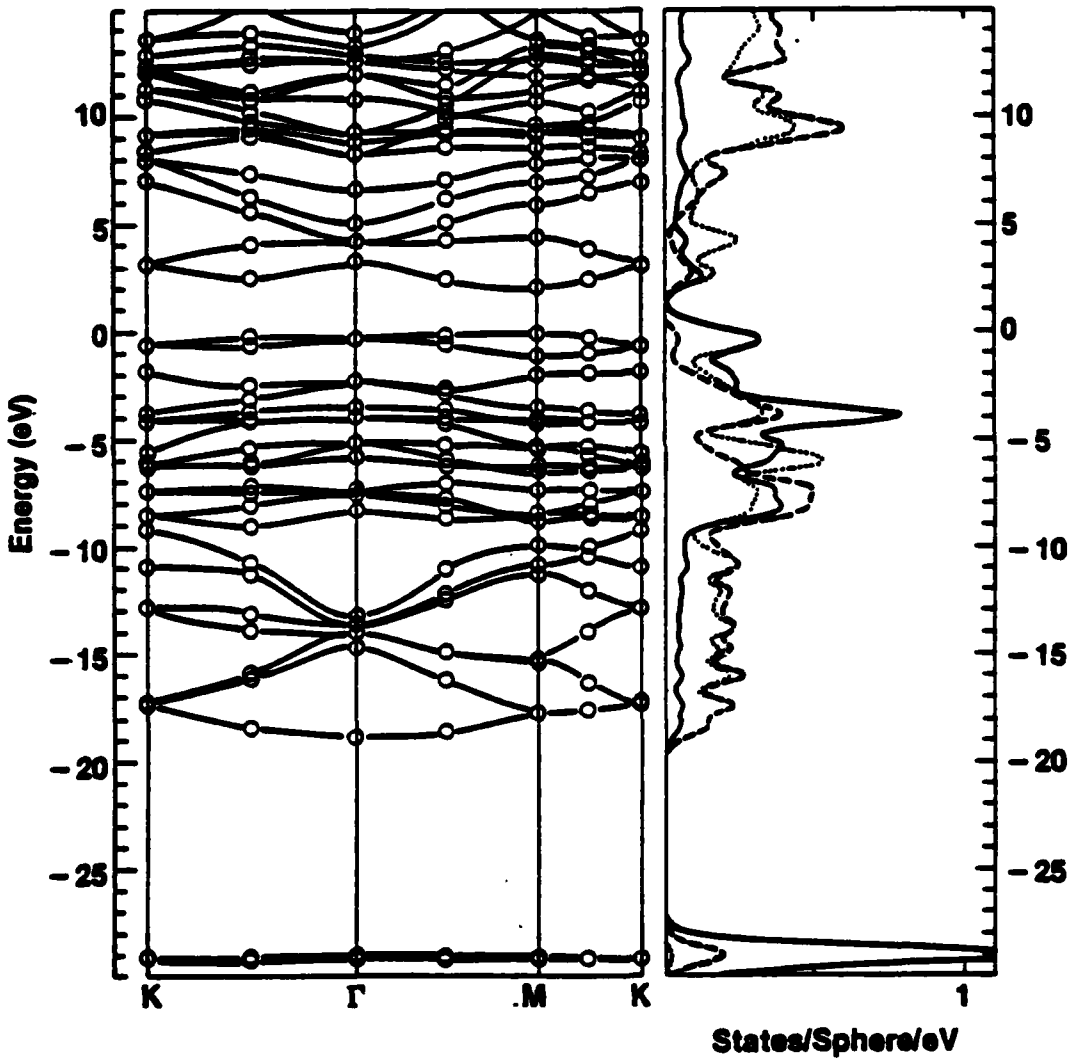

5. Calculated self consistent band structure and partial densities of states for C_4F in the Rudorff structure (Ref. 22). The partial densities of states for F (full curve), for C with a nearest neighbor F (dashed curve), and for C with no nearest neighbor F (dotted curve)calculated using sphere radii of 1.3 bohr for both F and C.

The valence charge density is shown in Fig. 6. It is seen that the fluorinated carbons have slightly more charge than the unfluorinated carbons. In Fig. 7, the difference density (the valence density of C_4F minus that of its reference graphite compound) is shown. In this figure, it is seen that the excess charge density induced by F has σ character at the expense of some loss of graphite π density. This result is consistent with the band structure results of Fig. 5, where it is seen that the weakly antibonding component of the graphite π bands have been moved to bands above the Fermi level.

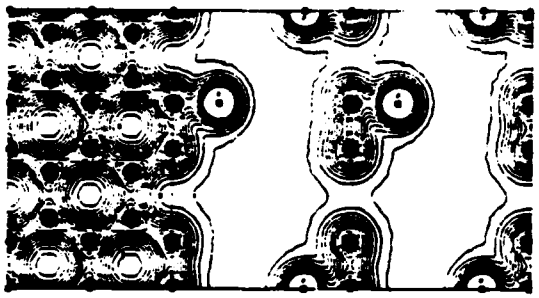

6. Contour plot of total valence density of C_4F in Rudorff structure, showing C plane (left panel) and adjoining perpendicular plane along c-axis (right panel). Contour levels are given in units of 0.1 electrons/Å^3. Peak density near F atoms is omitted. Atomic locations are denoted by filled squares.

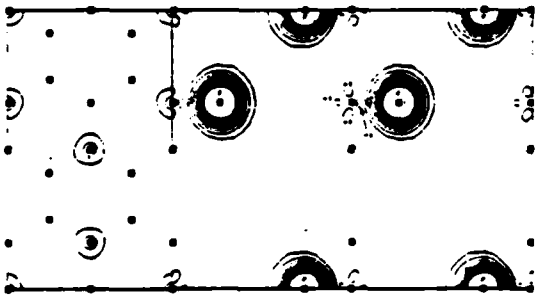

7. Contour plot of total difference density of C_4F (Fig. 6) minus that of reference graphite compound, shown in same planes as in Fig. 6. Positive contours (full curves) and negative contours (dashed curves) are given in units of 0.1 e/Å^3.

ACKNOWLEDGEMENTS

We would like to thank L. Ebert, T. Mallouk, N. Bartlett, and J.E. Fischer for very helpful suggestions concerning the graphite fluoride calculations. In addition, we would like to thank J.E. Fischer, S. Saffran, D. DiVincenzo, and R. Tatar for helpful discussions throughout the course of this work.

A portion of this work was carried out at the University of Pennsylvania and supported by National Sciece Foundation MRL Grant No. DMR79-23647, ARO Contract DAAG-29-77-C400, and National Science Foundation Grant. No. DMR78-22465. SGL would like to also acknowledge support from a Sloan Foundation Fellowship.

REFERENCES

1. E. G. Mele and J. J. Ritsko, Phys. Rev. Lett. 43, 68 (1979)

2. S. A. Safran and F. J. DiSalvo, Phys. Rev. B 20, 4889 (1979)

3. J. Blinowski, N. H. Hau, C. Rigaux, J. P. Vieren, R. Le Toullec, G. Furdin, A. Herold, and J. Melin, J. Physique 41, 47 (1980), J. Blinowski and C. Rigaux, J. Physique 41, 667 (1980)

4. N. A. W. Holzwarth, Phys, Rev. B 21, 3665 (1980)

5. S. Shimamura and A. Morita, J. Phys. Soc. Japan 51, 502 (1980)

6. S. A. Safran and D. R. Hamann, Phys. Rev. B 23, 565 (1981)

7. S. Y. Leung and G. Dresselhaus, Phys. Rev. B 24, 3490 (1981)

8. T. Ohno, K. Nakao, and H. Kamimura, J. Phys. Soc. Japan 47, 1125 (1979), T. Inoshita, K. Nakao and H. Kamimura, J. Phys. Soc. Japan 43, 1237 (1977)

9. D. P. DiVincenzo and S. Rabii, Phys. Rev. B 25, 4110 (1982)

10. J. J. Ritsko and C. F. Brucker, to be published.

11. N. A. W. Holzwarth, S. Rabii, and L. A. Girifalco, Phys. Rev. B 18, 5190 (1978)

12. G. K. Wertheim. P. M. Th. M. Van Attekum, and S. Basu, Solid State Comm. 33, 1127 (1980)

13. W. Eberhardt, I. T. McGovern, E. W. Plummer, and J. E. Fischer, Phys. Rev. Lett. 44, 200 (1980)

14. I.P. Batra and L. Samuelson, Syn. Met. 1, 233 (1979/80)

15. N. A. W. Holzwarth, S. G. Louie, and S. Rabii, to be published.

16. S. G. Louie, K. M. Ho, and M. L. Cohen, Phys. Rev. B 19, 1774 (1979)

17. N. A. W. Holzwarth, D. P. DiVincenzo, R. C. Tatar, and S. Rabii, Proc. of of 4th International Congress on Quantum Chemistry, Sweden, Jun 14-19 (1982)

18. T. Ohno, Ph.D. Thesis, Department of Physics, Faculty of Science, University of Tokyo, 1981.

19. N. A. W. Holzwarth, S. G. Louie, S. Rabii, Phys. Rev. Lett. 47, 1318 (1981)

20. L. B. Ebert, Ann. Rev. of Mat. Sci. 6, 181 (1976)

21. T. E. Mallouk and N. Bartlett, 184th ACS National Meeting, Kansas City, Missouri, Sept. 12-17, 1982. (paper # 145 of Inorganic Section)

22. J. E. Fischer, private communication.

23. W. Rudorff, Adv. Inorg. Chem. Radiochem. 1, 233 (1959), W. Rudorff and G. Rudorff, Chem. Ber. 80, 417 (1947)

24. L. Ebert, private communication.

Lithium-intercalated graphite: Self-consistent electronic structure for stages one, two, and three

N. A. W. Holzwarth*
Corporate Research—Sciences Laboratory, Exxon Research and Engineering Company, P. O. Box 45, Linden, New Jersey 07036

Steven G. Louie
Department of Physics, University of California, Berkeley, California 94720

Sohrab Rabii
Moore School of Electrical Engineering, University of Pennsylvania, Philadelphia, Pennsylvania 19104
(Received 23 February 1983)

First-principles electronic structure calculations were carried out for LiC_6, LiC_{12}, and LiC_{18} representing first-, second-, and third-stage model graphite intercalation compounds. By comparing the charge density of these compounds to that of reference graphite compounds, we could define a "total difference density" in order to quantify charge transfer and polarization in these materials. The total difference density is found to be highly concentrated near the intercalant ions. However, the conduction electrons (those in partially occupied bands) are found to have the distribution of virtually undistorted π wave functions and have a much more delocalized distribution than that of the total difference density. These two types of charge distributions account for many of the unusual electronic properties of graphite intercalation compounds.

I. INTRODUCTION

In a recent short paper[1] we presented the results for the electronic structure of a model third-stage graphite intercalation compound: LiC_{18}. The present paper is a more detailed presentation of this work in comparison with results for the two lower-stage compounds, LiC_6 and LiC_{12}. Results for graphite itself and for diamond were presented in separate papers.[2]

The calculational methods are described in Ref. 2. Briefly, the calculations were carried out self-consistently in the local-density approximation using a pseudopotential formulation and by representing the electronic wave functions in terms of a mixed-basis set consisting of plane waves and linear combinations of atomic orbitals as developed by Louie, Ho, and Cohen.[3] The ionic pseudopotentials were generated from all-electron atomic calculations using the formulation of Hamann, Schlüter, and Chiang.[4] The exchange-correlation potential was that of Hedin and Lundqvist.[5] These calculational methods were particularly successful in determining a valence charge density of graphite which is in excellent agreement with that determined from experimental x-ray form factors.[6]

The outline of the paper is as follows. In Sec. II, the crystal structures chosen for this study are discussed. In Sec. III, the results of the charge-density distributions and local densities of states are presented. In Sec. IV, the energy bands and Fermi-surface properties are discussed. Discussion and conclusions are presented in Sec. V.

II. STRUCTURAL CONSIDERATIONS

Despite the fact that from a theoretical point of view the Li-intercalated graphite compounds are the most simple of the intercalation compounds,[7] they are apparently somewhat difficult to prepare and to characterize. Staged compounds of Li-intercalated graphite as high as stage five have been reported,[8] but the structure and stoichiometries of even the low-stage compounds are only recently being determined. In general, the Li atoms are inserted between two layers of graphite, causing the two layers to change their registry from *AB* stacking to *AA* stacking and causing a 10% increase in the interlayer separation from 3.35 to 3.70 Å.[9] The Li atoms are arranged directly between carbon hexagons in a triangular lattice having a $\sqrt{3}\times\sqrt{3}$ registry with respect to the hexagonal lattice of graphite. The intralayer lattice constant of the hexagonal graphite lattice constant a is also slightly dilated with respect to that of graphite. For the first-stage compounds, the intralayer dilation is 1% and $a=2.485$ Å.[9] For higher-stage compound the dilation is somewhat less. For simplicity we chose to study the idealized stoichiometries and structures shown in Fig. 1 and detailed in Table I. Some of the reasoning behind these choices is given below.

The first-stage compound is agreed to have the stoichiometry LiC_6. Several authors[9–11] have suggested the structure of LiC_6 to be D^1_{6h} symmetry with layer stacking $A\alpha A\alpha A\alpha$.[12] On the basis of electron diffraction, Kambe *et al.*[13] determined the low-temperature (< 220 K) form of LiC_6 to have a layer stacking of $A\alpha A\beta A\gamma$. This structure is apparently in disagreement with neutron-diffraction results.[11] For the present study, we chose to use the simpler D^1_{6h} structure, shown in Fig. 1 (first panel), in order to compare with our previous non-self-consistent calculations using modified Korringa-Kohn-Rostoker (KKR) techniques.[14,15]

The second-stage compound apparently has two metastable stoichiometries at room temperature: LiC_{12} and LiC_{18}.[8–11,16–18] Guérard and Hérold[9] suggested the structure to have the stacking sequence $AA\alpha AA\alpha AA\alpha AA\alpha$ which is in agreement with recent neutron-diffraction results for the LiC_{12} form of second-stage Li-intercalated

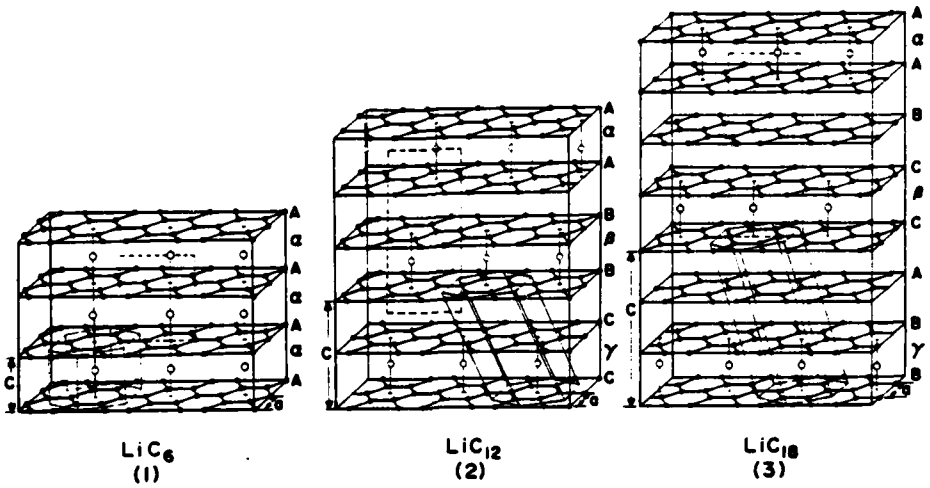

FIG. 1. Structures of Li-intercalated graphite compounds LiC_6 (stage 1), LiC_{12} (stage 2), and LiC_{18} (stage 3) assumed in present study. Carbon atoms are denoted by filled circles connected along nearest-neighbor bonds. Li atoms are denoted by unfilled circles. Primitive unit cells are indicated for each structure. Dashed rectangle in each structure denotes the plane used in contour plots shown in Figs. 2–7.

TABLE I. Lattice parameters for Li-intercalated graphite compounds.

LiC_6 (structure based on Ref. 9)

Primitive lattice vectors:

$\vec{T}_1 = a\sqrt{3}[(\sqrt{3}/2)\hat{x} + \frac{1}{2}\hat{y}]$,

$\vec{T}_2 = a\sqrt{3}[-(\sqrt{3}/2)\hat{x} + \frac{1}{2}\hat{y}]$,

$\vec{T}_3 = c_1\hat{z}$, $a = 2.485$ Å, $c_1 = 3.706$ Å

Atomic locations within unit cell:

C atoms: $\pm[\frac{1}{3}(\vec{T}_1+\vec{T}_2)+\frac{1}{2}\vec{T}_3]$

$\pm[\frac{1}{3}\vec{T}_1+\frac{1}{2}\vec{T}_3]$

$\pm[\frac{1}{3}\vec{T}_2+\frac{1}{2}\vec{T}_3]$

Li atom: 0

Symmetry directions:

$\Gamma \le k \le A$ $\quad \vec{k} = x\vec{G}_3$ $\quad 0 \le x \le \frac{1}{2}$

$\Gamma \le k \le M$ $\quad \vec{k} = x(\vec{G}_1 - \vec{G}_2)$ $\quad 0 \le x \le \frac{1}{2}$

$\Gamma \le k \le K$ $\quad \vec{k} = x(\vec{G}_1 + \vec{G}_2)$ $\quad 0 \le x \le \frac{1}{3}$

LiC_{12} and LiC_{18} (assumed structures)

Primitive lattice vectors:

$\vec{T}_1 = a\sqrt{3}[(\sqrt{3}/2)\hat{x} + \frac{1}{2}\hat{y}]$, $\vec{T}_2 = a\sqrt{3}[-(\sqrt{3}/2)\hat{x} + \frac{1}{2}\hat{y}]$,

$\vec{T}_3 = (2a/\sqrt{3})\hat{y} + c_n\hat{z}$, $a = 2.485$ Å,

$c_2 = 7.056$ Å(LiC_{12}), $c_3 \equiv 10.406$ Å(LiC_{18})

LiC_{12} and LiC_{18} (assumed structures *continued*)

Atomic locations within unit cells:

C atoms: $\pm\left[\left[\frac{1-2p_n}{3}\right](\vec{T}_1+\vec{T}_2)+p_n\vec{T}_3\right]$

$\pm\left[\left[\frac{1-2p_n}{3}\right]\vec{T}_1-\frac{2p_n}{3}\vec{T}_2+p_n\vec{T}_3\right]$

$\pm\left[\frac{-2p_n}{3}\vec{T}_1-\left[\frac{1+2p_n}{3}\right]\vec{T}_2+p_n\vec{T}_3\right]$

$\pm\left[-\left[\frac{1+2p_n}{3}\right](\vec{T}_1+\vec{T}_2)+p_n\vec{T}_3\right]$

$\pm\left[-\left[\frac{1+2p_n}{3}\right]\vec{T}_1-\frac{2p_n}{3}\vec{T}_2+p_n\vec{T}_3\right]$

$\pm\left[\frac{-2p_n}{3}\vec{T}_1+\left[\frac{1-2p_n}{3}\right]\vec{T}_2+p_n\vec{T}_3\right]$

$p_n \equiv \frac{c_1}{2c_n}$ where $n=2$ for LiC_{12} and 3 for LiC_{18}

Additional C atoms in LiC_{18}: $\pm[-\frac{1}{3}(\vec{T}_1+\vec{T}_2)+\frac{1}{2}\vec{T}_3]$

$\pm[-\frac{1}{3}\vec{T}_1+\frac{1}{2}\vec{T}_3]$

$\pm[+\frac{1}{3}\vec{T}_2+\frac{1}{2}\vec{T}_3]$

Li atom: 0

Symmetry directions:

$\Gamma \le k \le A$ $\quad \vec{k} = x\vec{G}_3$ $\quad 0 \le x \le \frac{1}{2}$

$\Gamma \le k \le M$ $\quad \vec{k} = x(\vec{G}_1 - \vec{G}_2)$ $\quad 0 \le x \le \frac{1}{2}$

$\Gamma \le k \le \bar{K}$ $\quad \vec{k} = x(\vec{G}_1 + \vec{G}_2)$ $\quad 0 \le x \le \frac{1}{3}$

graphite.[11,18] Recently, Woo *et al.*[18] have determined the second-stage LiC_{18} to have the stacking sequence *AB-BA-AB* with no in-plane order of the Li layers. For simplicity, we chose to study second-stage LiC_{12} in the hypothetical structure shown in Fig. 1 (second panel), having a stacking sequence $A\alpha AB\beta BC\gamma CA\alpha A$. Such a stacking sequence for the graphite layers has been observed in second-stage graphite nitrate[19] and in second-stage potassium graphite.[20] The stacking sequence for the Li layers was chosen in order to have a unit cell of only 13 atoms with an inversion center.

To our knowledge, the structure of the third-stage compound has not been reported. We assumed the stoichiometry LiC_{18} and chose the structure $A\alpha ABC\beta CAB\gamma BCA\alpha ABC\beta$ as shown in the third panel of Fig. 1 in order to have a unit cell of only 19 atoms with an inversion center and to maintain a reasonable local geometry for the C and Li atoms. The stacking sequence for the graphite layers is not what is commonly found for other third-stage compounds,[10,20] where the adjacent graphite layers order as *ABA* and *ACA*. The *ABC* stacking is that found in the less common form of graphite—rhombohedral graphite.[21,22] The structural difference between Bernal[23] and rhombohedral graphite has a large effect on the Fermi-surface properties of the two forms of graphite.[21,22] However, for LiC_{18}, the Fermi energy is much larger and subtle structural differences are not as important. One of the factors which establishes the charge distribution in LiC_{18} is the tendency of electrons to delocalize along the *c* axis, which depends upon the average number of nearest-neighbor atoms in adjacent layers and which is the same for the *ABC* and *ABA* stackings.

III. RESULT FOR ELECTRONIC DENSITY DISTRIBUTIONS

In Ref. 2 we showed that the present calculational methods yield a valence electronic charge density for graphite and diamond which are in excellent agreement with that inferred from x-ray-intensity measurements.[6] Since we have used the pseudopotential approximation, the density in the core region does not have exactly correct shape, but because of the norm-conserving aspect of the pseudopotential,[4] the integrated charge within the pseudopotential radius is equal to the actual charge within the same volume.

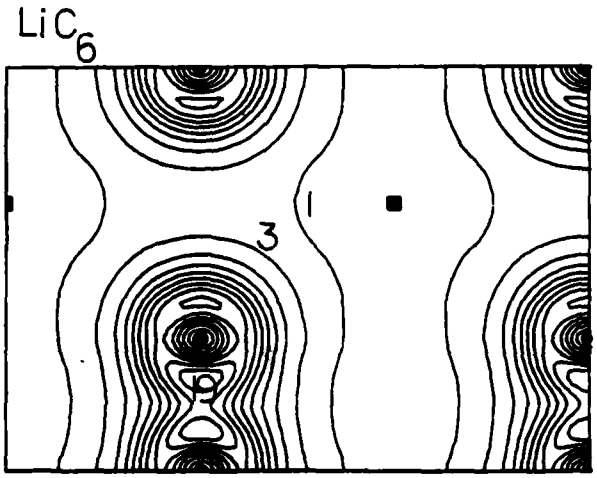

FIG. 2. Contour plot of total valence-electron charge density of LiC_6. Contour values are given in units of 0.1 electrons/Å^3. Atomic positions are denoted by filled squares for Li and circles for carbon. Plane shown contains *c* axis and passes through Li atoms and C—C bonds as shown by the dashed rectangle in Fig. 1 (first panel).

Results for the valence electronic charge density for LiC_6, LiC_{12}, and LiC_{18} are shown in Figs. 2—4, respectively. From these figures it is seen that the density distributions for the Li-intercalated graphite compounds are very similar to each other and to graphite itself. The 1% dilation of the intralayer lattice constant in the intercalation compounds results in a slightly lower peak density along a C—C bond than in graphite. Close examination of the density for LiC_6 in comparison to graphite itself reveals a slightly higher density in the π-orbital region. This excess π density is a direct consequence of the charge transfer from the Li intercalant ions. In LiC_{12} and near the bounding layer of LiC_{18}, this excess π density is seen to be asymmetric with higher density on the side facing another C layer than on the side facing a Li layer. This result seems counterintuitive since one expects the Li ions to polarize the graphite electrons toward the Li planes. However, the distance between C planes in the "sandwich region" on either side of a Li plane is 10% larger than the distance between adjacent C planes. This expansion tends to de-

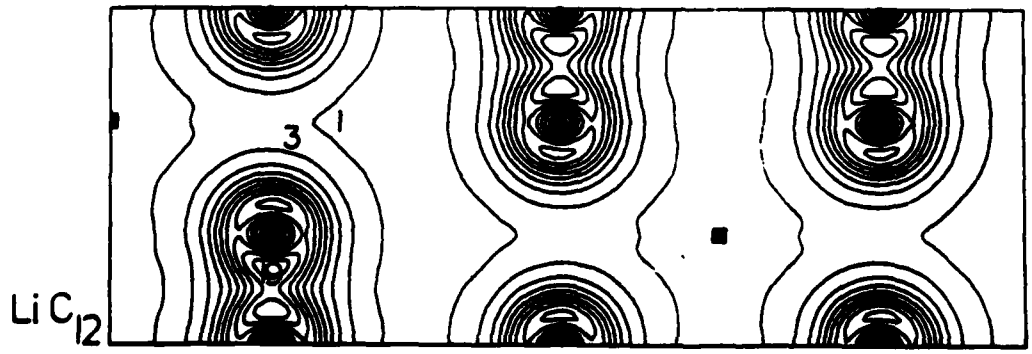

FIG. 3. Contour plot of total valence-electron charge density of LiC_{12}. Contour values are given in units of 0.1 electrons/Å^3. Atomic positions are denoted by filled squares for Li and circles for carbon. Plane shown contains *c* axis and passes through Li atoms and C—C bonds as shown by the dashed rectangle in Fig. 1 (second panel).

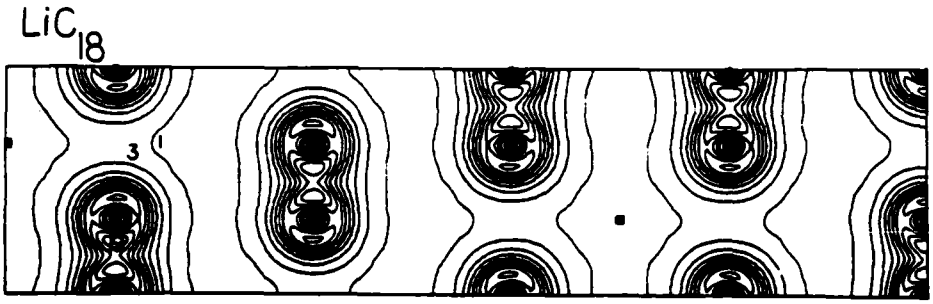

FIG. 4. Contour plot of total valence-electron charge density of LiC_{18}. Contour values are given in units of 0.1 electrons/Å^3. Atomic positions are denoted by filled squares for Li and circles for carbon. Plane shown contains c axis and passes through Li atoms and C—C bonds as shown by the dashed rectangle in Fig. 1 (third panel).

crease the valence-electron density between C planes on either side of a Li plane with respect to the density between adjacent C planes. The expansion effect masks the polarization effect, and the net result is the asymmetric distribution seen in Figs. 3 and 4.

In order to factor out the effects of c-axis expansion from the more interesting effects of charge transfer and polarization, we compared the density of each of the intercalation compounds with that of graphite modified to the same structures. For future reference, we will call these fictious modified graphite materials C_6,C_{12}, and C_{18} for the first-, second- and third-stage forms. The total-electron-difference density for LiC_6 is shown in Fig. 5(a). The peak density is located in π-like contours on each C site. These contours are distorted in the direction of the Li ions in evidence of the polarization effects. In order to better understand the origin of this structure, the total-electron-difference density was considered as a sum of two parts: the conduction-electron-difference contribution [Fig. 5(b)] and the valence-electron-difference contribution [Fig. 5(c)]. The conduction-electron-difference contribution was defined as that derived from the partially filled bands. This density represents states located in energy above E_F of pure graphite and corresponds to states receiving the transferred charge. These states determine the Fermi-surface properties of LiC_6. The valence-electron-difference contribution was defined as the difference between the total-difference density and the conduction-electron-difference contributions. It can be directly associated with the polarization of the graphite charge density. The total-difference density and the conduction-electron-difference density both integrate to a single electron per unit cell while the valence-electron-difference density integrates to no net charge per unit cell.

From Fig. 5(b), it is apparent that the conduction-electron-difference contribution retains its π-like form with very slight polarization effects. This result had been noted previously on the basis of non-self-consistent calculations.[15] By the argument to follow, the effect is expected to be a general property of graphite intercalation compounds due to the nature of the conduction states, especially their partially antibonding character.[15] From perturbation theory, the distortion polarizability of a graphite state depends largely on virtual excitations to the lowest unoccupied state of the compound. The wave function for this state is a smooth function in the layer plane and its matrix element with a wave function having oscillatory

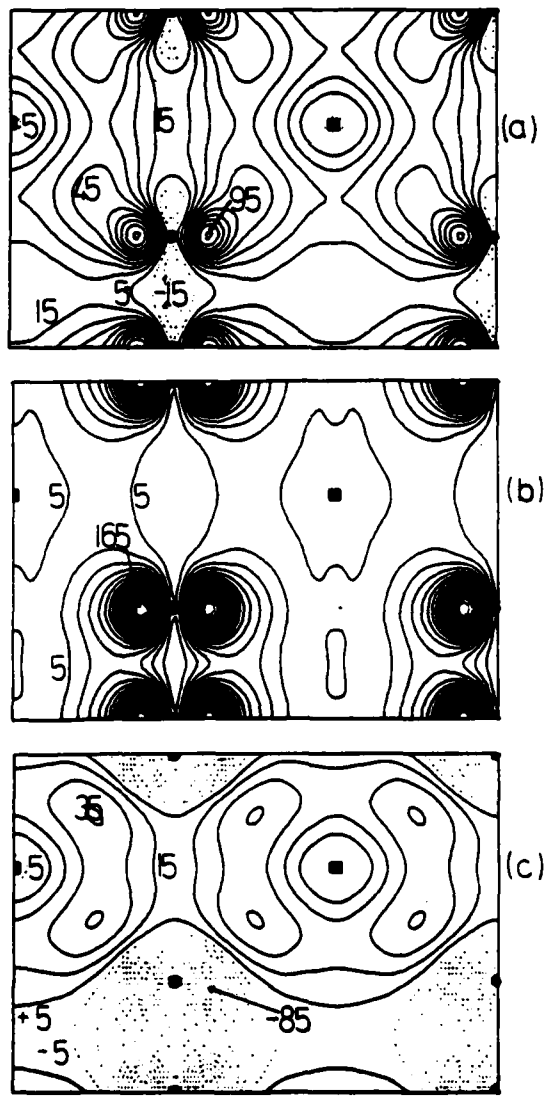

FIG. 5. Contour plots of electronic charge density for LiC_6: (a) total-difference density, (b) conduction-electron contribution, and (c) valence-electron contribution. Contour values are given in units of 0.001 electrons/Å^3. Atomic positions are denoted by filled squares for Li and circles for carbon. Plane shown is the same as in Fig. 2.

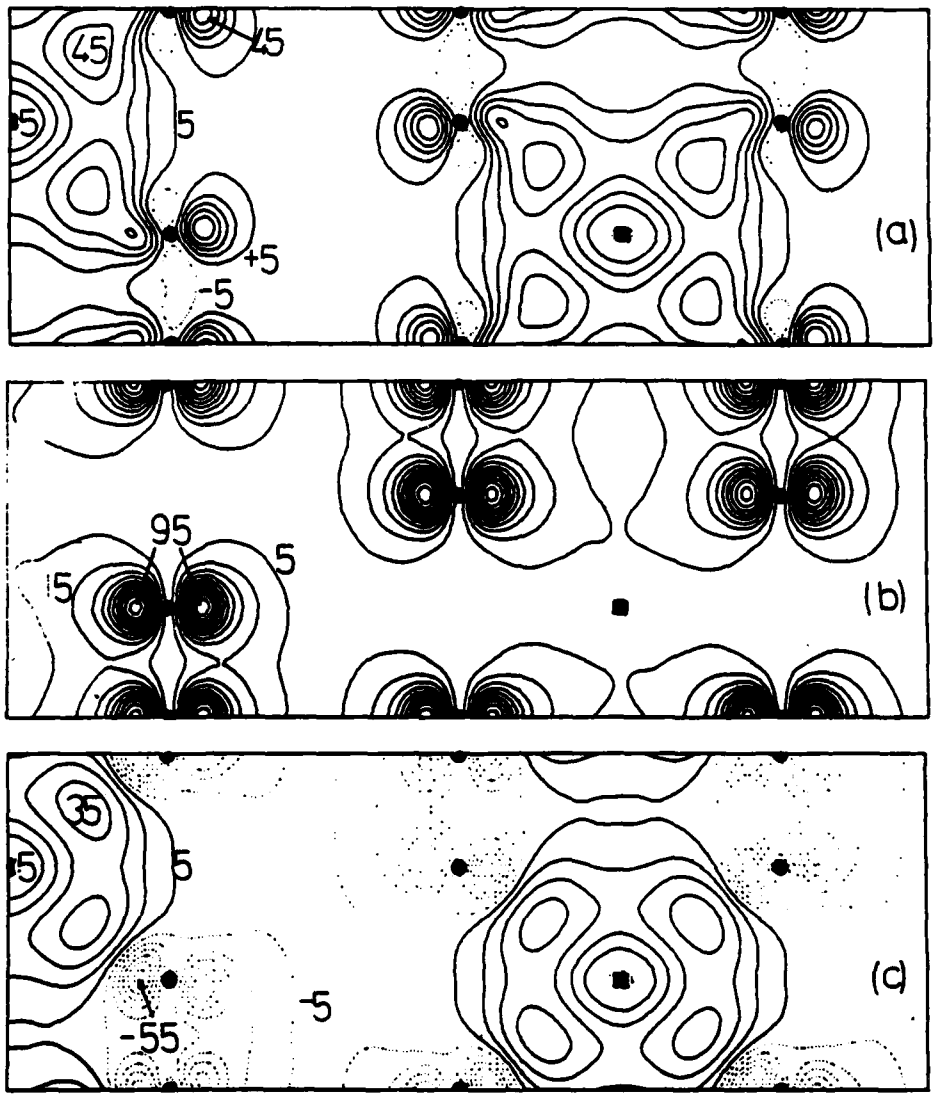

FIG. 6. Contour plots of electronic charge density of LiC_{12}: (a) total-difference density, (b) conduction-electron contribution, and (c) valence-electron contribution. Contour values are given in units of 0.001 electrons/Å^3. Atomic positions are denoted by filled squares for Li and circles for carbon. Plane shown is the same as in Fig. 3.

character in a layer plane, such as a partially antibonding graphite π state, is much smaller than the matrix element with a smooth wave function such as a bonding graphite π state. Hence, the conduction states of graphite are less polarizable than the valence states near the bottom of the π band. The valence-electron-difference density in Fig. 5(c), on the other hand, shows strong polarization effects; there exists a deficit of charge near the C planes and an excess of charge near the Li ions. From an analysis of the local density of states given below, we shall see that the valence-state polarization is not due only to states at the bottom of the π band, but also due to states spreading over a wide energy range.

The results of a similar charge-density analysis for LiC_{12} are shown in Fig. 6. Because of the reduced intercalant concentration and hence reduced charge transfer per carbon atom, the peak densities displayed in these plots for the second-stage compound are smaller than those for LiC_6 by roughly a factor of $\frac{1}{2}$. The polarization effects are exemplified by the asymmetry in the difference densities about each C site. As for the first-stage compound, the polarization effects on the conduction electrons [Fig. 6(b)] are very slight in comparison with that of the total- and valence-electron-difference densities.

The results for LiC_{18} are shown in Fig. 7. Near the bounding C layer and the Li plane, the total-electron-difference density [Fig. 7(a)] is strikingly similar to that of the second-stage compound shown in Fig. 6(a). Note that the difference density near the interior layer is small. However, the conduction-electron-difference contribution shown in Fig. 7(b) is much more delocalized. The valence-electron-difference density shown in Fig. 7(c) is also very similar in the region near the Li planes to that of the lower-stage compounds although the deficit region for

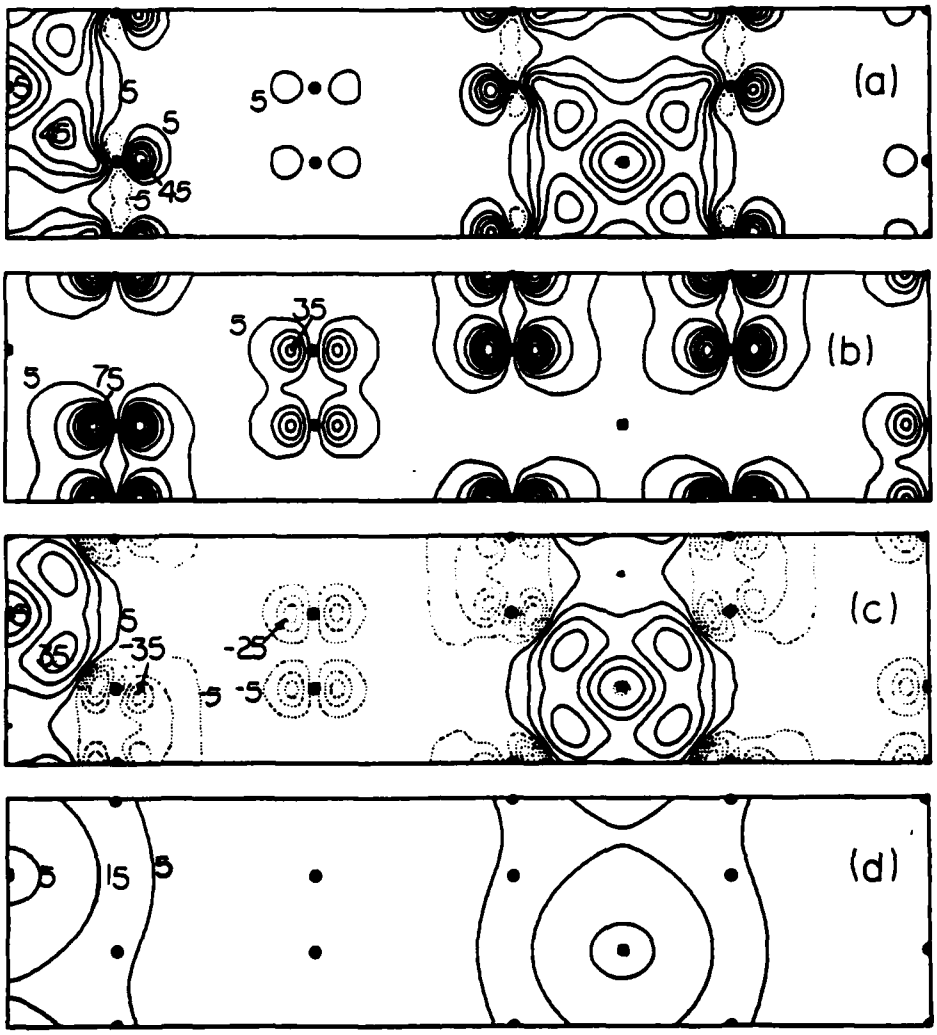

FIG. 7. Contour plots of electronic charge density for LiC_{18}: (a) total-difference density, (b) conduction-electron contribution, and (c) valence-electron contribution. Part (d) is a contour plot of superposed atomic charge density of Li 2s in the LiC_{18} structure. Contour values are given in units of 0.001 electrons/Å^3. Atomic positions are denoted by filled squares for Li and circles for carbon. Plane shown is the same as in Fig. 4.

LiC_{18} is more delocalized. In order to compare the polarization charge and that of a Li 2s bound-state density, the superposed density for atomic Li 2s states in the LiC_{18} structure is shown in Fig. 7(d). The polarization charge [Fig. 7(c)] retains some of its C character and therefore has more structure than that of the superposed atomic Li density. However, the similarity in the shapes of the two densities in Figs. 7(c) and 7(d) near the Li plane is apparent. In general the polarization charge is more localized near the Li ions than is the superposed charge, having a higher peak density in the Li plane at about 1 Å from each Li site and a lower density at the midpoint of the Li-Li separation.

An additional feature of the total-electron-difference density contour plots is the appearance of a deficit of charge in the region of the C—C bonds. In order to see the details of this effect, it is interesting to see the total-electron-difference density in some of the planes perpendicular to the planes presented in Figs. 5—7. Contour plots of the difference density in the Li plane and the bounding C-layer plane are shown in Fig. 8. The plot is for LiC_6, but the plots for the higher-stage compounds are very similar. The main difference is that, due to the reduced charge transfer per carbon atom, the contour levels in the bounding C-layer plane are lower in the higher-stage compounds by a factor of roughly $\frac{1}{2}$. The contour plot for the difference density in the Li-layer plane shown in the left-most panel of Fig. 8 is relatively structureless showing a saddle point in the difference density along a Li-Li nearest-neighbor distance—not indicative of a bond in the usual sense. The difference density in the C-layer plane shown in the right-most panel of Fig. 8 shows the withdrawal of electrons from the C—C bonds. There are two types of C—C bonds. The C—C bonds (type 1) in C hexagons with their center directly above or below a Li site suffer the greatest deficit while C—C bonds (type 2)

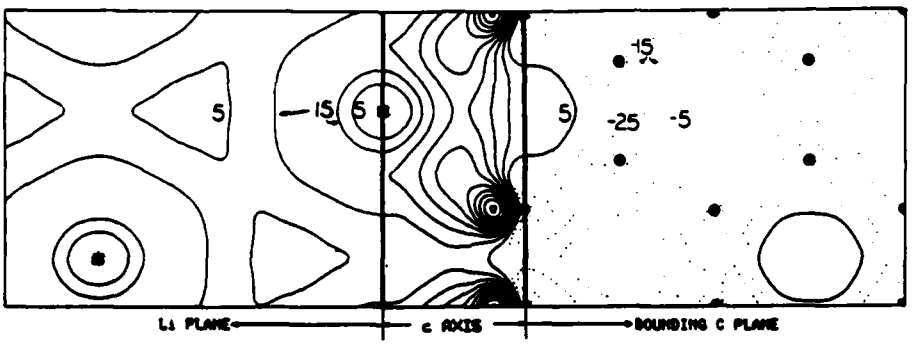

FIG. 8. Contour plot of total-difference density for LiC_6 shown in Li plane (left panel), plane of Fig. 5 (center panel), and in ("bounding") carbon-layer plane (right panel). The three planes intersect at 90° angles at the edges indicated by thick lines. Contour values are given in units of 0.001 electrons/Å^3. Atomic positions are denoted by filled squares for Li and circles for carbon.

which are further from the Li sites are affected less. This demonstrates the localized nature of the polarization. The withdrawal of charge from the C–C bond is quantified in Table II in terms of the integrated charge within a sphere centered on the various types of C–C bonds. For a sphere $\frac{1}{8}$th of the radius of the bond length, the charge with drawn from the type-1 bond is twice that withdrawn from the type-2 bond and 6 times that withdrawn from a bond in the interior layer of LiC_{18}. The percentages for LiC_{12} and the bounding layer of LiC_{18} are identical. The amount of charge withdrawal is small—a maximum of ~1% of the total, but this magnitude is large enough to affect the force constants and bond length of the C–C bond, for example. Our calculations were performed with an ideal structure—all C–C bonds having equal length. Although total energies and lattice relaxation were not included in the calculation, the results suggest that a structure with a slight dilation of the type-1 bonds relative to the type-2 bonds might have lower energy than the ideal structure. Such a structural effect of a distorted hexagonal structure within each bounding C plane could perhaps explain why the *AAαAA* stacking sequence (rather than *ABαBC* or *ABαBA*) occurs for LiC_{12}. That is, if registry of C atoms along the *c* axis is energetically more favorable for LiC_{12} in the presence of hexagonal distortion, only the *AAαAA* structure enables such registry.

TABLE II. Bond-charge changes. Percentage charge in carbon–carbon bonds of LiC_{6n} minus that of C_{6n} in sphere of radii $\frac{1}{4}$ and $\frac{1}{8}$ of the carbon–carbon bond length.

	$\frac{1}{4}$	$\frac{1}{8}$
LiC_6		
Bond 1[a]	−0.9%	−1.2%
Bond 2[b]	−0.5%	−0.6%
LiC_{12}		
Bond 1[a]	−0.4%	−0.6%
Bond 2[b]	−0.3%	−0.3%
LiC_{18}		
Bond 1[a]	−0.4%	−0.6%
Bond 2[b]	−0.3%	−0.3%
Bond 3[c]	−0.1%	−0.1%

[a]C–C bond in bounding layer in a C hexagon directly above or below a Li site.
[b]C–C bond in bounding layer in a C hexagon not directly above or below a Li site.
[c]C–C bond in interior layer.

In order to address the issue of charge transfer more quantitatively, it is helpful to look at the charge averaged in a layer plane and plotted along the *c* axis as shown in Figs. 9–11 for LiC_6, LiC_{12}, and LiC_{18}, respectively. The results of the linear plots follow the same trends shown in the contour plots as discussed above. Further, we can define regions *a*, *b*, and *c* as shown in these figures to compare the total integrated charge of the sandwich region, intermediate region, and interior region, respectively. The integrated charges for the three regions are listed in Table III. There are several interesting features of these results. First, the total-difference density in the sandwich region *a* is essentially the same in LiC_{12} and LiC_{18}, roughly 90% of the total excess charge. Secondly, the conduction-electron charge in regions *a* and *b* is nearly identical for both LiC_{12} and LiC_{18} indicating that the distortion polarization of the conduction states is small in contrast to that of the total-difference density. Thirdly, for LiC_{18}, roughly 20% of the conduction-electron charge is located in the interior layer, more than 3 times the charge of the total-difference density in this region.

One of the interesting questions remaining is to determine the origin of the charge density shown in the above results. This we can address by examining the local density of states of LiC_{18}. For this purpose, we have divided the crystal into the five regions *A*–*E* shown in Fig. 12(a). Region *A* is near the Li plane and is similar to region *D* if it were not for the Li atoms. Regions *B* and *C* are associated with the bounding carbon layer while region E is associated with the interior carbon layer. Comparing the local density of states for LiC_{18} in all of these regions (full line) with that of pure graphite in the LiC_{18} structure "C_{18}" (dashed line), for each region there is a strong similarity in the shape of the two curves. However, in each region there is an energy shift characteristic of an approximately two-dimensional electronic band structure modulated by the electrostatic potential in that region created by the charge transfer. The two curves have been aligned so that the bottom of the lowest-energy σ band is taken to be the zero of energy.

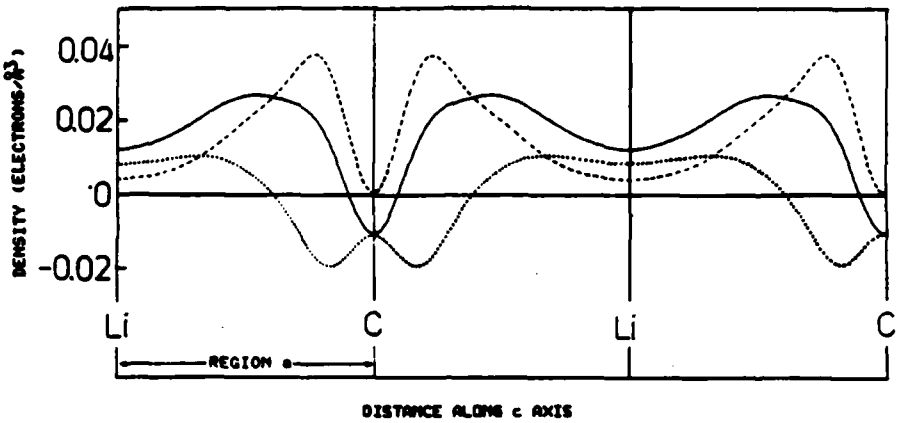

FIG. 9. Electronic charge densities for LiC_6 averaged in layer planes and plotted along c axis: total-difference density (full lines), conduction-electron contribution (dashed line), and valence-difference density (dotted line). Region definitions are those used in Table III.

The first interesting question is what is the origin of the charge near the Li plane? We can address this question by looking at the local density of states for region A in comparison to that for region D. Since these two regions are located between carbon planes, the main contribution to the occupied density in these regions is due to the π electrons whose band minimum is at roughly 12 eV. In region A the electrostatic potential for LiC_{18} shifts the energy levels to lower energies by approximately 0.5 eV. In region D the electrostatic potential of LiC_{18} shifts the energy levels to higher energies by approximately 0.5 eV. In addition to these rigid shifts there are some intensity differences between the graphite and LiC_{18} local-density-of-states curves. In region D, these differences are very small fluctuations throughout the region of occupied states, while in A systematic differences are apparent. Namely, the local density of states for LiC_{18} in region A for the occupied states is systematically higher than that of graphite especially for the bonding π bands in the region 12–18 eV. The density near the Li atoms is thus largely derived from the combined effects of the distortion of states in a 6-eV range of energy from the bottom of the π bands of graphite. The σ electrons also contribute to the polarization charge as evidenced by the bond-charge deficit shown in Fig. 8. However, because of their small extent into region A, their contribution is hardly visible in Fig. 12(a). A second interesting point illustrated in Figs. 12(a) and 12(b) is that states within roughly 1 eV on either side of the Fermi level of LiC_{18} have a local density of states whose shape is essentially identical to that of C_{18}. This result corroborates the arguments made above that the Fermi-level states are essentially unpolarizable.

A third point illustrated in Fig. 12(b) is the magnitude and sign of the electrostatic potential shifts associated with the bounding and interior carbon layers. To a first approximation, the local density of states (LDOS) of the interior layers (full curve E) is rigidly shifted by about 1 eV above the LDOS of the bounding layer (full curves B and C). In the region of the Fermi level, the electrostatic shift has been successfully modeled by several authors[25–28] who considered the effects of intercalation on the π bands of graphite alone.

Finally, the contribution of unoccupied Li $2s$ states is illustrated in Fig. 12(a) as enhancement in the local density of states of region A in the vicinity of 25 eV, several eV above E_F.

IV. RESULTS FOR BAND STRUCTURES

The band structure of LiC_6 is shown in Fig. 13 and is compared with previous calculations and experiment in Table IV. In general, the differences between the present

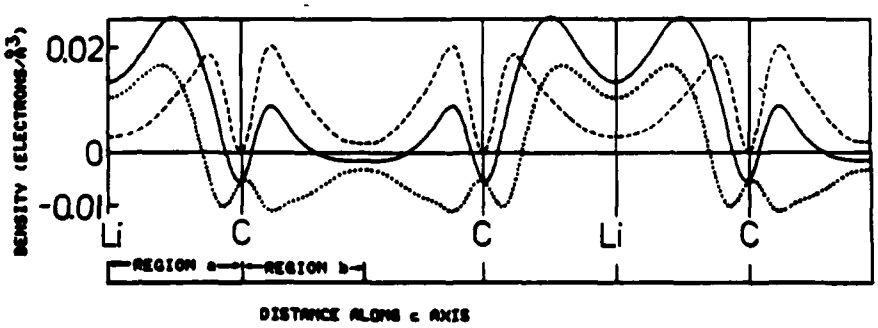

FIG. 10. Electronic charge densities for LiC_{12} averaged in layer planes and plotted along c axis: total-difference density (full lines), conduction-electron contribution (dashed line), and valence-difference density (dotted line). Region definitions are those used in Table III.

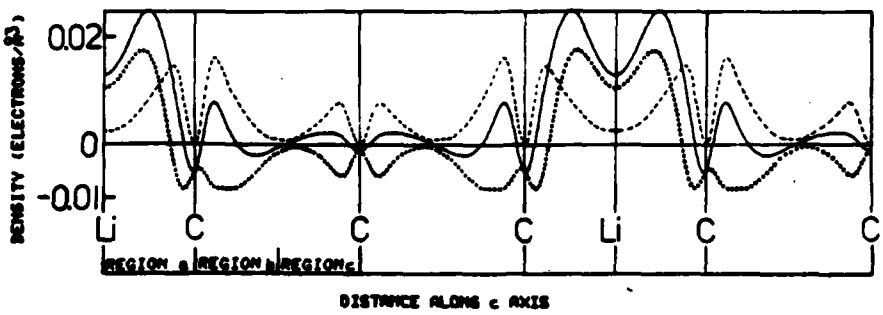

FIG. 11. Electronic charge densities for LiC_{18} averaged in layer planes and plotted along c axis: total-difference density (full lines), conduction-electron contribution (dashed line), and valence-difference density (dotted line). Region definitions are those used in Table III.

self-consistent band-structure results and the previous non-self-consistent results[14] follow the similar comparison for graphite itself.[2] The lower valence bands are in good agreement with the photoemission measurements.[24] The photoemission peak at 0.5 eV below the Fermi energy due to the "back-folded" π bands is perhaps related to the calculated bands at Γ; the corresponding states at A lie 1 eV or more lower in energy.

The band structures of LiC_{12} and LiC_{18} are shown in Figs. 14 and 15, respectively, along the symmetry directions defined in Table I. The general features of the bands are quite similar to those in LiC_6 except that there are 2 times as many and 3 times as many graphite bands for LiC_{12} and LiC_{18}, respectively, corresponding to the larger unit cells. By looking at the eigenfunctions one can distinguish states which are primarily localized on the bounding layers or on the interior layers for LiC_{18}. One finds that the interior-layer bands are raised in energy with respect to the corresponding levels of the bounding layers by roughly 1 eV. The magnitude of this electrostatic effect is comparable to the interlayer interaction of the π states as evidenced by the fact that the π-band splittings are only a few tenths of an eV larger for LiC_{18} than for LiC_{12}.

V. SUMMARY AND DISCUSSION

In summary, as a result of our study, we have learned about a number of properties of the model graphite intercalation compounds which we expect are generally applicable to this class of compounds.

(1) The total charge density of the intercalation compound screens the intercalant ion on a relatively short length scale. This is particularly evident in Table III where it is shown that 90% of the total-difference density of the second- and third-stage compounds is located in the sandwich region between two graphite layers surrounding a Li layer. This is also evidenced in Fig. 8 and Table II in terms of greater charge deficit from the C—C bond (type 1) closer to a Li ion. This total-charge-density distribution affects a number of ground-state properties such as the interlayer bond lengths[29] and force constants.[7,30] Evidence for the fact that the total-difference density is localized

TABLE III. Distribution of electronic charge in LiC_{6n}. Definitions of charge components and of regions are as defined for Figs. 9–11.

	Region a	Region b	Region c
LiC_6			
Total	0.50		
Conduction	0.50		
Valence	0		
LiC_{12}			
Total	0.45	0.05	
Conduction	0.26	0.24	
Valence	0.19	−0.19	
LiC_{18}			
Total	0.45	0.03	0.03
Conduction	0.21	0.19	0.09
Valence	0.23	−0.17	−0.07
Li 2s			
Superposed atomic densities	0.40	0.09	0.01

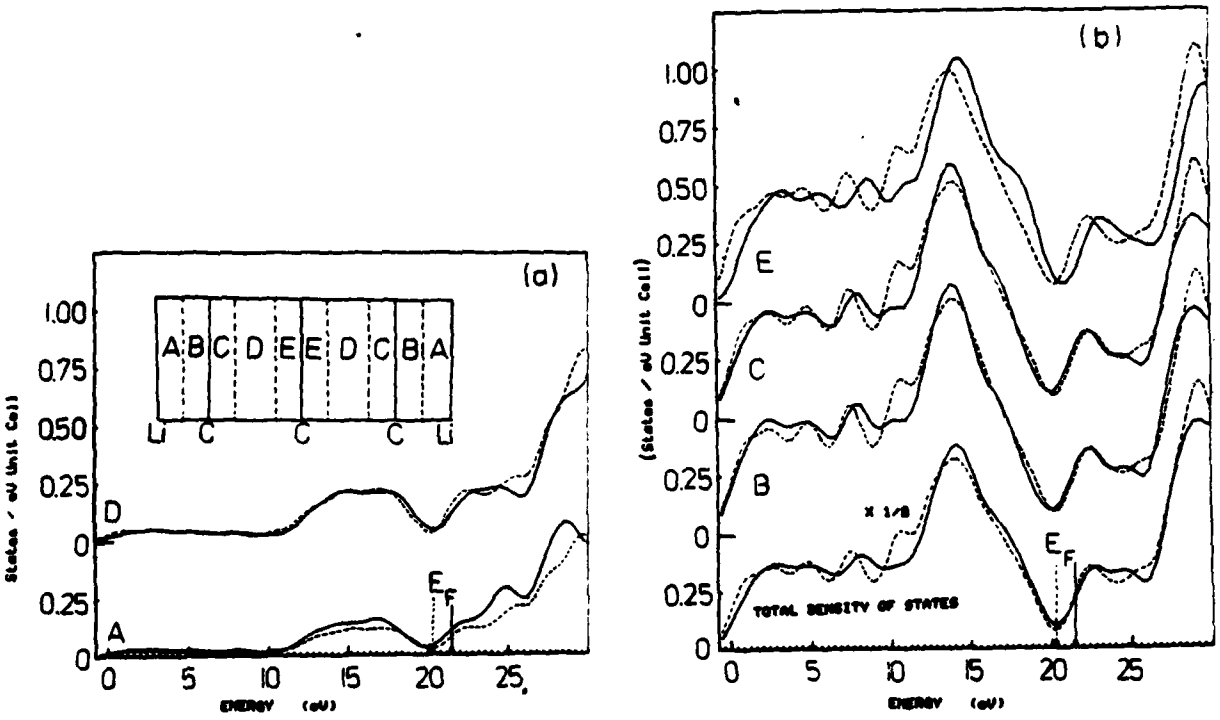

FIG. 12. Local density of states for LiC_{18} (full lines) and C_{18} (dashed lines). In (a) the inset is a diagram of the unit cell showing the division of regions $A-E$. Note that the volumes of $A-C$ and E are equal while D has a 60% larger volume. Sum of volumes $A+B+C+D+E$ is half that of a unit cell. In (a) the local density of states (LDOS) for region A (a bounding region between C planes near a Li plane) is compared with that of region D (an interior region between C planes). In (b) the LDOS for regions B and C (near a bounding C layer) and E (near an interior C layer) are compared with the total densities of states. Densities of states were obtained using histograms 0.4 eV wide smoothed with a Gaussian convolution function having a decay width of 1 eV.

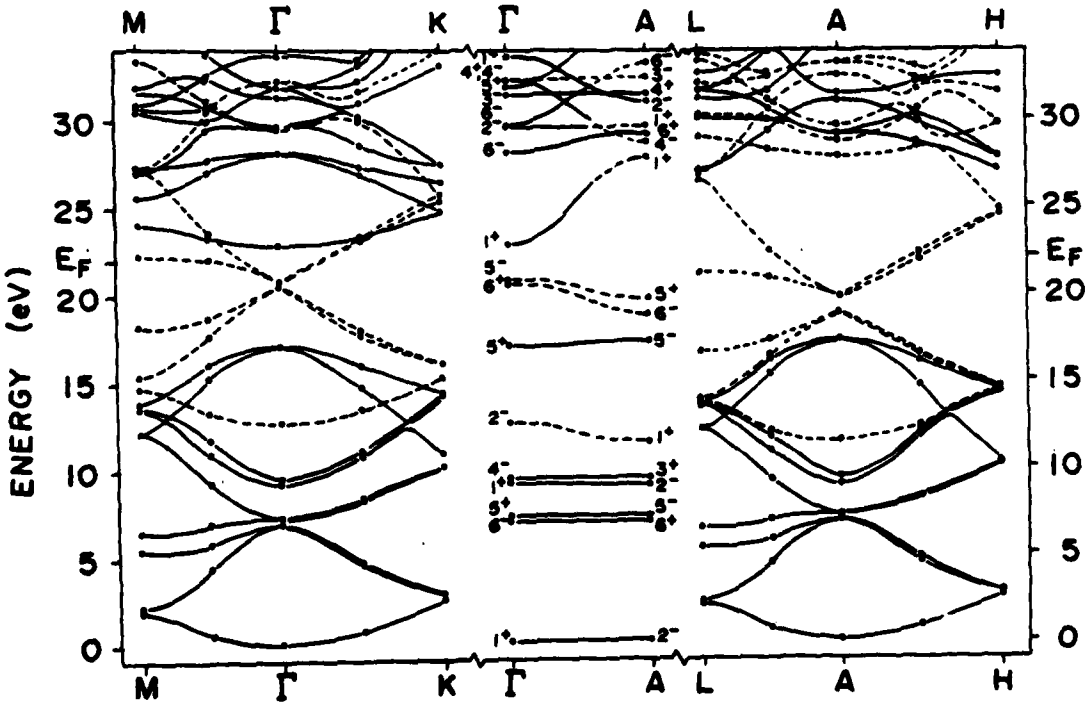

FIG. 13. Band structure of LiC_6. Dashed lines denote π bands; full lines denote σ bands. Energies calculated at points indicated by circles. Zero of energy taken at bottom of σ band. Notation for Brillouin zone and symmetry labels are the same as in Ref. 14. Brillouin-zone labels are also defined in Table I.

TABLE IV. Energy bands for LiC_6 in eV.

	Present results		Previous results[a]		Experiment[b]
	Γ	A	Γ	A	$\Gamma-A$
Bottom σ band[c]	0	0.2	0	−0.3	0
Back-folded σ bands	6.9	7.0	6.3	6.4	7.3
	7.3	7.3	6.8	6.7	
	9.2	9.1	8.4	8.0	9.5
	9.5	9.5	8.4	8.5	
Bottom π band	12.7	11.6	12.4	12.0	13.2
Top σ band	17.1	17.3	15.8	15.8	17.0
Back-folded π bands	20.6	18.8	20.1	19.4	22.0
	20.9	19.9	20.3	19.5	
E_F	21.6		21.8		22.5
"Metal" band	22.9	27.9	23.4	27.6	≈24.0[d]

[a]Reference 14.
[b]Reference 24. Experimental error quoted as ≤ 0.5 eV with respect to Fermi level.
[c]Bottom of σ band at Γ taken as zero of energy.
[d]From photoyield; level not necessarily at Γ.

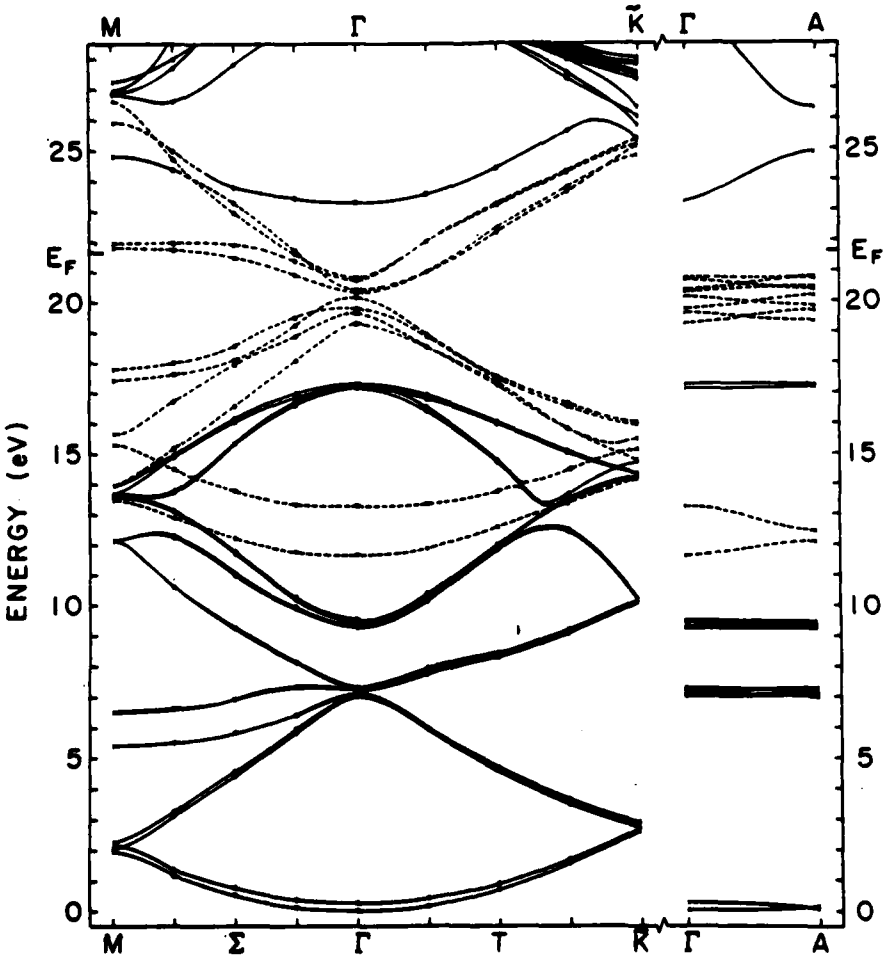

FIG. 14. Band structure of LiC_{12}. Dashed lines denote π band; full lines denote σ bands. Energies calculated at points indicated by circles. Zero of energy taken at bottom of σ band. Brillouin-zone labels are defined in Table I.

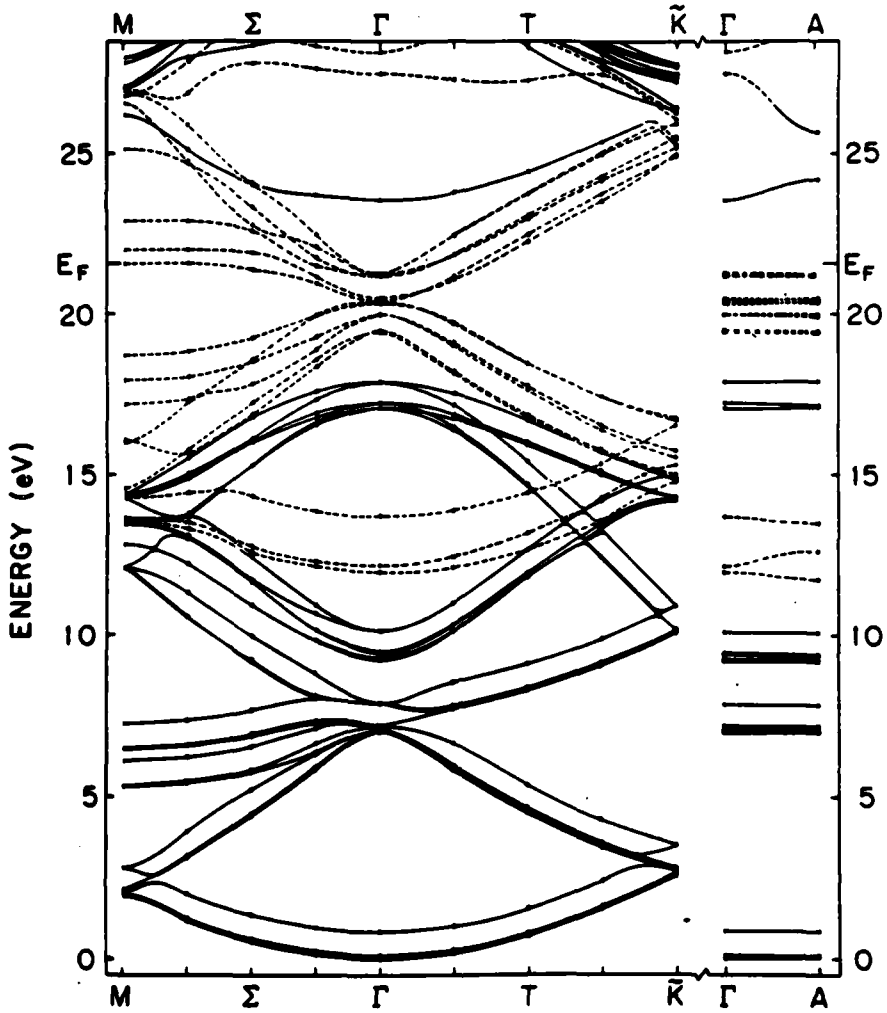

FIG. 15. Band structure of LiC_{18}. Dashed lines denote π bands; full lines denote σ bands. Energies calculated at points indicated by circles. Zero of energy taken at bottom of σ band. Brillouin-zone labels are defined in Table I.

near the Li ion has been suggested by the analysis of x-ray-photoemission measurements of the C 1s binding energies in a second-stage Li-intercalated graphite compound of presumed composition LiC_{18}.[31] The argument of the localized charge is based on the analysis of the linewidth to be consistent with four distinct C sites. If the difference density were more delocalized about the Li ion, there would be fewer distinct sites and a smaller linewidth. From the local density of states, we have, moreover, seen that the polarization charge is derived from the combined effects of a distortion of all the low-lying valence states of graphite. We have argued that this charge redistribution might result in a small lattice relaxation, lengthening the bonds closest to the Li ions and have cited the existence of the *AAαAA* stacking sequence for LiC_{12} as indirect evidence of this distortion effect.

(2) The conduction-electron contribution to the charge density is much more delocalized than the total-difference density and is virtually undistorted from a graphite π-like form. This is evidenced in Figs. 5(b), 6(b), and 7(b) as well as in Table III and in the form of the local density of states near the Fermi level as shown in Fig. 12. This behavior is due to the partly antibonding character of the states and has direct consequences in the transport[8,10] and Fermi-surface properties of graphite intercalation compounds. At the present time there is no direct evidence of the extent of the conduction-electron distribution. The most promising experimental tools for measuring this effect are the de Haas–van Alphen or Shubnikov–de Haas effects.[7] However, at the moment the results seem to be too sample dependent to be reliable.[32] The nondistortability of the π electrons near the Fermi level has been assumed in several successful model calculations[25–28] and is likely to be one of the major contributing factors to the high conductivity of the graphite intercalation compounds.

(3) Much of the physics of the electronic structure of the graphite intercalation compounds involves the manifold of the π states of graphite as shown by Safran and Hamann.[27] These authors were able to model the effects

of the σ electrons by a uniform dielectric constant. In fact, a comparison of the charge distribution predicted by such a model with that of the present results for the conduction electrons was quite reasonable.[33] However, not all of the effects of intercalation can be explained by such a model. The distribution of the total-difference density, the effects on the C—C bond, and the contribution to the polarization charge from the bonding π orbitals requires a more detailed treatment. The present results should help in the formulation of more sophisticated model calculations for more dilute intercalation compounds.

ACKNOWLEDGMENTS

We would like to thank J. E. Fischer, S. Safran, D. P. DiVincenzo, and R. C. Tatar for their helpful suggestions and stimulating discussions. A portion of this work was completed at the University of Pennsylvania supported by the National Science Foundation—Materials Research Laboratories program under Grant No. DMR-79-23647 and U.S. Army Research Office Contract No. DAAG-29-77-C400. One of us (S.G.L.) would like to acknowledge support from an Alfred P. Sloan Foundation Fellowship and National Science Foundation Grant No. DMR-78-22465.

*Present address: Department of Physics, City College of the City University of New York, Convent Avenue at 138th Street, New York, New York, 10031.

[1]N. A. W. Holzwarth, S. G. Louie, and S. Rabii, Phys. Rev. Lett. 47, 1318 (1982).

[2]N. A. W. Holzwarth, S. G. Louie, and S. Rabii, Phys. Rev. B 26, 5382 (1982); in Proceedings of the Symposium on the Local Density Approximations in Quantum Chemistry and Solid State Theory, Copenhagen, Denmark, June 11—12, 1982, edited by J. Avery and J. P. Dahl (in press).

[3]S. G. Louie, K.-M. Ho, and M. L. Cohen, Phys. Rev. B 19, 1774 (1979).

[4]D. R. Hamann, M. Schlüter, and C. Chiang, Phys. Rev. Lett. 43, 1494 (1979).

[5]L. Hedin and B. I. Lundqvist, J. Phys. C 4, 2064 (1971).

[6]R. Chen, P. Trucano, and R. F. Stewart, Acta Crystallogr. A 33, 823 (1977).

[7]For a comprehensive review, see, for example, M. S. Dresselhaus and G. Dresselhaus, Adv. Phys. 30, 139 (1981).

[8]D. Billaud, B. McRae, J. F. Mareche, and A. Hérold, Synth. Metals 3, 21 (1981).

[9]D. Guérard and A. Hérold, Carbon 13, 337 (1975).

[10]R. Juza and V. Wehle, Naturwissenschaften 52, 560 (1965).

[11]J. Rossat-Mignod, D. Fruchart, M. J. Moran, J. W. Milliken, and J. E. Fischer, Synth. Metals 2, 143 (1980).

[12]Capital letters denote graphite planes and Greek letters denote Li planes.

[13]N. Kambe, M. S. Dresselhaus, G. Dresselhaus, S. Basu, A. R. McGhie, and J. E. Fischer, Mater. Sci. Eng. 40, 1 (1979).

[14]N. A. W. Holzwarth, S. Rabii, and L. A. Girifalco, Phys. Rev. B 18, 5190 (1978).

[15]N. A. W. Holzwarth, L. A. Girifalco, and S. Rabii, Phys. Rev. B 18, 5206 (1978).

[16]S. Basu, C. Zeller, P. J. Flanders, C. D. Fuerst, W. D. Johnson, and J. E. Fischer, Mater. Sci. Eng. 38, 275 (1979).

[17]D. Billaud, E. McRae, and A. Herold, Mater. Res. Bull. 14, 857 (1979).

[18]J. E. Fischer, private communication; K. C. Woo, W. A. Kamitakahara, D. P. DiVincenzo, D. S. Robinson, H. Mertwoy, J. W. Milliken, and J. E. Fischer, Phys. Rev. Lett. 50, 182 (1983).

[19]D. E. Nixon, G. S. Parry, and A. R. Ubbelohde, Proc. R. Soc. London Ser. A 291, 324 (1966).

[20]D. E. Nixon and G. S. Pairy, Brit. J. Appl. Phys. (J. Phys. D) 1, 291 (1968).

[21]R. R. Haering, Can. J. Phys. 36, 352 (1958).

[22]J. W. McClure, Carbon 7, 425 (1969).

[23]J. D. Bernal, Proc. R. Soc. London Ser. A 106, 749 (1924).

[24]W. Eberhardt, I. T. McGovern, E. W. Plummer, and J. E. Fischer, Phys. Rev. Lett. 44, 200 (1980).

[25]L. Pietronero, S. Strässler, H. R. Zeller, and M. J. Rice, Phys. Rev. Lett. 41, 763 (1978); L. Pietronero, S. Strässler, and H. R. Zeller, Solid State Commun. 30, 305 (1979).

[26]S. A. Safran and D. R. Hamann, Phys. Rev. B 22, 606 (1980).

[27]S. A. Safran and D. R. Hamann, Phys. Rev. B 23, 565 (1981).

[28]J. Blinowsky and C. Rigaux, J. Phys. (Paris) 41, 667 (1980).

[29]L. Pietronero and S. Strässler, Phys. Rev. Lett. 47, 593 (1981).

[30]G. Dresselhaus and S. Y. Leung, Solid State Commun. 35, 819 (1980).

[31]S. B. DiCenzo, S. Basu and G. K. Wertheim, Synth. Metals 3, 139 (1981).

[32]The analysis of magneto-oscillatory data for graphite intercalation compounds is complicated by the appearance of extra signals and by the difficulty of detecting the high-frequency signal as has been recently pointed out by the detailed study of second-stage AsF_5-intercalated graphite by R. S. Markiewicz, H. R. Hart, Jr., L. V. Interrante, and J. S. Kasper, [Synth. Metals 2, 331 (1980)]; J. E. Fischer, M. J. Moran, J. W. Milliken, and A. Briggs, [Solid State Commun. 39, 439 (1981)].

[33]S. A. Safran, N. A. W. Holzwarth, and D. R. Hamann, in *Physics of Intercalation Compounds: Proceedings*, Vol. 38 of *Springer Series in Solid State Sciences, July, 1981, Trieste, Italy*, edited by L. Pietronero and E. Tosatti (Springer, New York, 1982).

Ab Initio Calculation of the Optical Spectra of LiC_6 and the Origins of its Plasmons

Nan-Xian Chen and Sohrab Rabii
Moore School of Electrical Engineering & Laboratory for Research on the Structure of Matter, University of Pennsylvania Philadelphia, Pennsylvania 19104
(Received 27 February 1984)

We present the results of the first *ab initio* calculation of the optical spectra of LiC_6 up to 40 eV. The results are in excellent agreement with experiment and are used to identify the structures seen in the optical spectra of this compound, and are also used to clarify the origins of the observed and calculated plasmons. Some of the results appear to be common to all alkali-graphite intercalation compounds.

PACS numbers: 78.20.Dj, 78.40.Kc

There have been a number of recent measurements of the optical spectra of the alkali-graphite intercalation compounds.[1-4] The availability of our accurate *ab initio* self-consistent energy band structure of graphite and its intercalculation compounds[5,6] has enabled us to calculate their dielectric functions over a large range of energy. We report the first such calculation for graphite intercalation compounds. Furthermore, we show that if there are significant contributions to $\epsilon(\omega)$, in the same energy range, from both intraband and interband transitions, care must be taken in assignment of the origins of the measured plasmons.

The calculation is carried out within the relaxation-time approximation with dielectric function given as

$$\epsilon_{\alpha\beta}(\omega)=\delta_{\alpha\beta}+\Delta_{\alpha\beta}^{\text{inter}}(\omega)+\Delta\epsilon_{\alpha\beta}^{\text{intra}}(\omega). \tag{1}$$

The interband contribution is given by

$$\Delta_{\alpha\beta}^{\text{inter}}(\omega)=-\frac{e^2}{\pi^2m^2\omega}\sum_{ij}{}'\int\frac{d^3k}{\hbar\omega_{ij}(\vec{k})}\left[\frac{p_{ij}^{\alpha}(\vec{k})p_{ij}^{\beta}(\vec{k})}{-\tilde{\omega}+\omega_{ij}(\vec{k})}-\frac{p_{ij}^{\beta}p_{ij}^{\alpha}(\vec{k})}{\tilde{\omega}+\omega_{ij}(\vec{k})}\right], \tag{2}$$

where $\tilde{\omega}=\omega+i\hbar/\tau$, and $\hbar\omega_{ij}(\vec{k})=E_j(\vec{k})-E_i(\vec{k})$. The primed summation is taken over states such that $E_i<E_F<E_j$, where E_F is the Fermi energy.

The Drude model with a single scattering time is used for the intraband contribution

$$\Delta_{\alpha\beta}^{\text{intra}}(\omega)=\frac{-\omega_p^2\delta_{\alpha\beta}}{\omega(\omega+i\hbar/\tau')}. \tag{3}$$

We have used an initial mesh of 30 000 points in 1/24 of the Brillouin zone in conjunction with a modified Gilat-Raubenheimer interpolation scheme.[7] In the case of graphite, we have compared the optical spectra using the present modified Gilat-Raubenheimer scheme based on 20 k points in the subzone, with a $\vec{k}\cdot\vec{p}$ interpolation for energy levels and momentum matrix elements generating 480 points in the same subzone. The results of these two approaches agreed well with each other, and in fact the former was in better agreement with experimental results and involved less computational effort.

Since there are no independent measures of the relaxation times for LiC_6, we estimated the intraband τ from the dc conductivity to be 0.5×10^{-13} sec. For the interband τ, the value of 2×10^{-14} sec was chosen by Johnson and Dresselhaus[7] for graphite π bands. Since our calculations cover a much larger energy range we chose the constant value of 0.2×10^{-14} sec for the entire 40-eV range. The interband plasma[5] frequency, ω_p, was taken from the calculated Fermi surface of Holzwarth, Louie, and Rabii as 6.7 eV for the in-plane component and 2.2 eV for the c-axis part.

Even though the energy-band calculations were carried out using a nonlocal pseudopotential, the oscillator strength for interband transition was taken to be the matrix element of momentum between the initial and final states. However, the neglect of the nonlocal contribution to the matrix elements was estimated to result in errors of less than 10%.

Figures 1 and 2 show the comparison of the experiment[1] and the present calculation for the $\epsilon_{1\perp}$ and $\epsilon_{2\perp}$, the real and imaginary components of dielectric function with the polarization perpendicular to the c axis of the crystal. The calculated values are absolute and have been checked by sum rule, accounting for 18 of the 25 electrons (four contributed by each of the six carbon atoms and one by the lithium atom) over a range of 0–34.3 eV. This

 © 1984 The American Physical Society

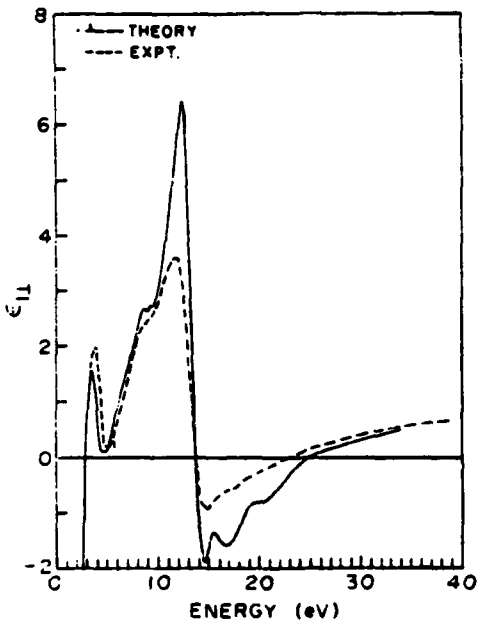

FIG. 1. The real part of in-plane component of the dielectric tensor of LiC_6 as a function of frequency. The experimental results are from Ref. 1.

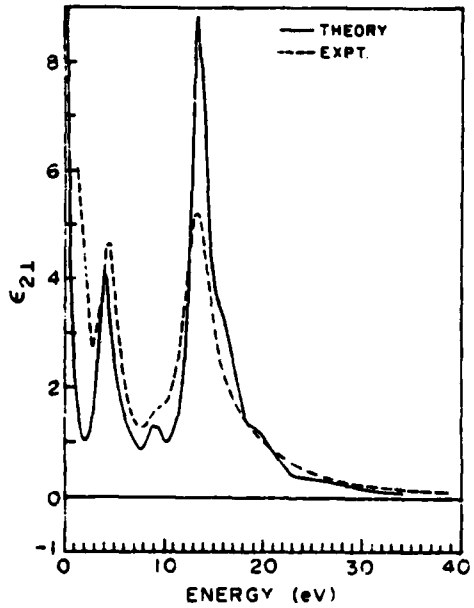

FIG. 2. The imaginary part of in-plane component of the dielectric tensor of LiC_6 as a function of frequency. The experimental data are from Ref. 1.

is generally considered an achievement in view of the *ab initio* nature of the calculation and the fact that transitions above 34 eV are not included. It is seen that the agreement between theory and experiment is excellent. Figure 2 shows major peaks for $\epsilon_{2\perp}$ at 4.0 and 13 eV which are similar to those measured and calculated for graphite.[8-11] These structures correspond to transitions that are also allowed in graphite; however, due to the back folding they correspond to contributions from a different region in LiC_6 Brillouin zone. The small structures near 9 eV are absent in graphite and become allowed in LiC_6 due to the upward shift of the Fermi level and become more complex due to the Brillouin zone folding. There is indication that these structures are also directly observed with reflectivity measurements on LiC_6.[12]

The interpretation of $\epsilon_{1\perp}$ is more complicated. We observe plasmons ω_{p1}, ω_{p2}, ω_{p3} occurring at 2.85, 6.3, and 25 eV. In order to clarify the origin of these plasmons we show the interband and intraband contributions to $\epsilon_{1\perp}$ spectra, respectively, in Fig. 3. The scattering time for the interband component is taken as 2×10^{-14} sec, in contrast to the value of 0.2×10^{-14} sec in the final results in order to produce a zero crossing in $\epsilon_{1\perp}$ spectra, and to make the discussion of the different contributions clearer. The intraband component was obtained by using the parameters of the Fermi surface from the early calculation of energy band structure of LiC_6 by Holzwarth, Rabii, and Girifalco.[13] There are two types of carriers at the center of the zone with plasma frequencies of $\omega_{p\ \mathrm{upper}} = 5.5$ eV and $\omega_{p\ \mathrm{lower}} = 4.7$ eV. Assuming the same relaxation time τ' for both carriers, we arrive at an effective intraband plasma frequency $\omega_p = (\omega_{p\ \mathrm{upper}}^2 + \omega_{p\ \mathrm{lower}}^2)^{1/2} = 6.7$ eV. We notice that the observed plasmon ω_{pl} at 2.85 eV corresponds to oscillation of these carriers, screened by the large positive component of the interband ϵ_1 in this frequency range. This unusual behavior of

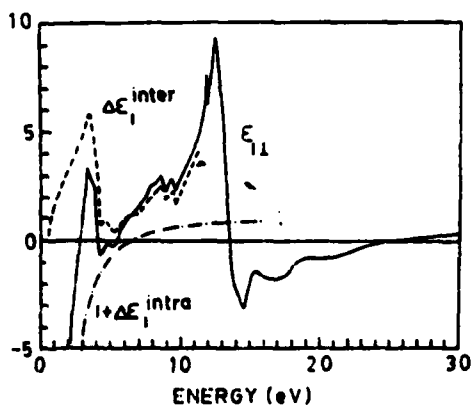

FIG. 3. The interband and intraband contributions to the real part of the calculated dielectric tensor.

LiC_6 also occurs for KC_8 in which the intraband plasmon observed[2] at 2.38 eV corresponds to the unscreened effective plasma frequency of 4.5 eV.[14] This situation is in fact a general characteristic of the spectra of the alkali-graphite intercalation compounds since in all cases the energy of the π-π^* transition occurs in the range where the intraband effects are significant. A related phenomenon is observed in silver with the difference that, there, the intraband oscillations of s electrons are screened by the interband transitions involving the d electrons.[15] This effect is absent when ω_p, which appears in Eq. (3), is much less than ω_{p2} as is the case in graphite. Since, because of the raising of the Fermi level in LiC_6, the π-π^* transitions lose strength, the large intraband contribution is necessary in LiC_6 to lead to an effective plasmon at this frequency. This is sometimes referred to as an interband plasmon in literature. The plasmon ω_{p3}, occurring at 25 eV, is totally due to interband transition since the free-carrier effects have disappeared at this energy. The same interband plasmon is also observed in graphite. The structures near 15.5 and 19.5 eV in the $\epsilon_{1\perp}$ spectra, which appear in both experimental and theoretical results, stem from a number of σ-σ^* transitions with significant oscillator strength distributed in almost all the Brillouin zone. There are also two peaks at 15 and 19.5 eV in the joint density of states of LiC_6.

Figure 4 shows the measured and calculated energy-loss spectra and again the agreement between theory and experiment is excellent. According to this calculation the three large plasmons as well as the two small structures around 9 eV correspond exactly to those in the $\epsilon_{1\perp}$ spectra. This is an important check on the accuracy of the results imposed by the Kramers-Kronig relation between the real and imaginary parts of the conjugate pairs, such as ϵ_1 and ϵ_2. There is, however, a 3-eV difference between the main peak in the measured electron-energy-loss spectra and the ϵ_1 spectra obtained from it by Kramers-Kronig analysis. This is the result of uncertainty in the extrapolation of the quantities that have to be integrated in the Kramers-Kronig analysis and also due to the fact that the variations of ϵ_1 and ϵ_2 in the energy range around ω_{p3} are rather weak, but critical in determining the position of the peak in the electron-energy-loss spectra.

We have also calculated the c-axis component of the optical properties such as $\epsilon_{\parallel}$, $-\mathrm{Im}(1/\epsilon_{\parallel})$, and so on. However, no experimental results are available for this polarization.

In conclusion, we have successfully calculated the optical spectra of LiC_6 from first principles, and shown that not only is it in excellent agreement with experiment, but it also plays a crucial role in the correct identification of origins of the measured plasmons.

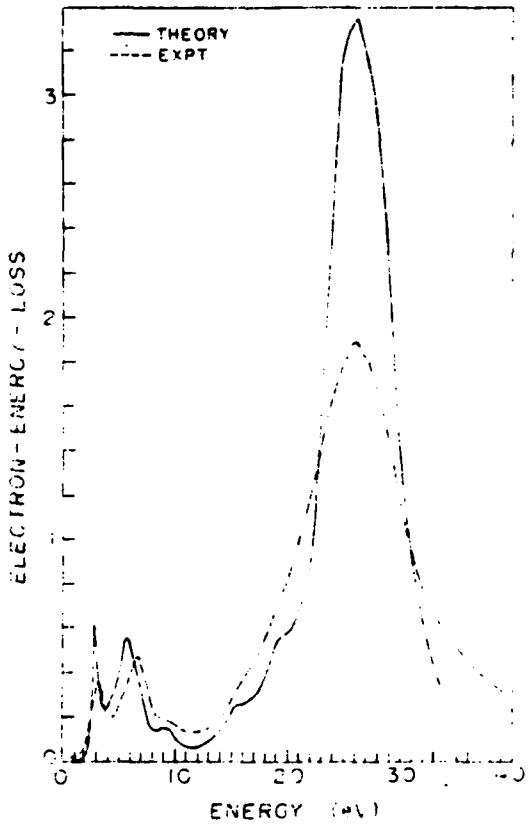

FIG. 4. The electron-energy-loss spectra in a-a plane for LiC_6

The authors gratefully acknowledge the discussions with N. A. W. Holzwarth, R. C. Tatar, J. E. Fischer, E. J. Mele, and M. E. Preil, and the resources provided by the Moore School Computing Facility. This work was supported by National Science Foundation Materials Research Laboratory Grant No. DMR-8216718, and Army Research Office Contract No. DAAG-29-77-C400.

[1]L. A. Grunes, I. P. Gates, J. J. Ritsko, E. J. Mele, D. P. DiVincenzo, M. E. Preil, and J. E. Fischer, Phys. Rev. B 28 6681 (1983).

[2]J. J. Ritsko, E. J. Mele, and I. P. Gates, Phys. Rev. B 24, 6114 (1981).

[3]M. Zanini, S. Basu, and J. E. Fischer, Carbon 16, 211 (1978).

[4]L. A. Grunes and J. J. Ritsko, Phys. Rev. B 28, 3439 983).
[5]N. A. W. Holzwarth, S. G. Louie, and S. Rabii, Phys. v. B 26, 5382 (1982).
[6]N. A. W. Holzwarth, S. G. Louie, and S. Rabii, Phys. v. B 28, 1013 (1983).
[7]L. G. Johnson and G. Dresselhaus, Phys. Rev. 87, 75 (1974).
[8]E. A. Taft and H. R. Phillip, Phys. Rev. 138, A197 965).
[9]D. L. Greenaway, G. Harbeke, F. Bassani, and E. Toti, Phys. Rev. 178, 1340 (1969).
[10]E. Tossati and F. Bassani, Nuovo Cimento 65B, 161 (1970).
[11]N. X. Chen, S. Rabii, and N. A. W. Holzwarth, Synth. Metals 8, 197 (1983).
[12]C. C. Shieh, private communication, 1983.
[13]N. A. W. Holzwarth, S. Rabii, and L. A. Girifalco, Phys. Rev. B 18, 5190 (1978).
[14]D. P. DiVincenzo and S. Rabii, Phys. Rev. B 25, 4110 (1982).
[15]H. Ehrenreich and H. R. Phillipp, Phys. Rev. 128, 1622 (1962).

To appear in Local Density Approximations in Quantum Chemistry and Solid State Physics, Editors: J.P. Dahl and J. Avery. Plenum Press.

Theoretical Valence Charge Densities for Graphite, Diamond, and LiC_6

N.A.W. Holzwarth
Corporate Research-Science Laboratories
Exxon Research and Engineering Company
Linden, New Jersey 07036

Steven G. Louie
Department of Physics
University of California
Berkeley, California 94720

and

Sohrab Rabii
Moore School of Electrical Engineering
University of Pennsylvania
Philadelphia, Pennsylvania 19104

ABSTRACT

The valence charge density of graphite was determined from first-principles, self-consistent electronic structure calculations and found to be in excellent agreement with values derived from experimental X-ray form factors. Similar calculations were carried out for the valence charge densities of diamond and of a first stage intercalation compound, LiC_6.

1. INTRODUCTION

Recent advances in numerical techniques have made it possible to carry out first principles calculations of the ground state properties of solids within density functional theory in the local density approximation [1]. The numerical accuracy of these techniques have now enabled workers to address the question of the accuracy of the local density approximation itself. One of the immedicate outputs of these calculations is the variationally determined valence charge density.

In the present paper, we discuss some recent results for the calculated valence charge density of graphite [2] and diamond and their comparisons with experimental charge densities derived from the analysis of high resolution X-ray diffraction data [3,4]. For purposes of comparisons, we also discuss results for an intercalation compound, LiC_6.

2. METHOD OF CALCULATION

The first-principles band structure calculations were carried out within density functional theory in the local density approximation using several well-established numerical techniques and approximations, suitably modified to treat the relatively strong electron-core interactions of carbon [2].

In order to take advantage of the numerical efficiency of a Fourier space evaluation of the matrix elements, the calculations were formulated in terms of pseudopotnetials and pseudo-wavefunctions. The electron-ion interactions were represented by norm-conserving pseudopotentials as developed by Hamann, Schlüter, and Chiang [5]. This form of pseudopotential has several advantages. The pseudo-wavefunctions and pseudo-charge converge to the actual wavefunction and actual charge outside spheres of specified

radii about each atom and the integrated pseudo-charge is equal to the integrated actual charge inside the core regions. Because of these normalization contraints, the pseudopotentials are energy independent over a reasonable energy range. The electron-electron interactions were represented self-consistently in the local density approximation, using the Hedin-Lundqvist[6] form for the exchange-correlation contribution.

The electronic wave functions were presented in terms of a mixed basis set consisting of plane waves and linear combinations of atomic orbitals (LCAO's) as developed by Louie, Ho, and Cohen [7]. The atomic functions were taken to be the numerical s- and p- wave atomic pseudo-wavefunctions. A sufficient number of plane waves was included in the basis set in order to converge the eigenvalues to within 0.2eV. This relatively large error was permitted in order to be able to treat higher stage graphite intercalation compounds. The self-consistency and the relative positions among levels were converged to well within 0.05eV The matrix elements between LCAO's and the local part of the pseudo-potential were evaluated using the fast Fourier transform technique suggested by Louie, et. al. [7]. The matrix elements between LCAO's and the non-local part of the pseudopotential were evaluated using a separable form approximation [2].

3. VALENCE ELECTRON DISTRIBUTION IN GRAPHITE

Graphite has the Bernal [8] structure with D_{6h}^4 symmetry and 4 atoms, 2 very slightly inequivalent types, per unit cell. The atoms are arranged in layers of hexagonal lattices with lattice constant $a = 2.46$ Å; the separation between layers is $c/2 = 3.35$ Å. Adjacent

layers are shifted in an ABAB stacking such that half of the carbon atoms (type "a") are directly above and below carbon atoms in the adjacent layers, while half (type "b") are directly above and below centers of carbon hexagons in the adjacent layers.

The calculated valence charge density for graphite is shown in Fig. 1a. Contours for two different planes are shown, a carbon plane and a plane containing the c axis. The edge at which the two planes meet is shown with a thick line. This figure illustrates the highly anisotropic structure of the graphite valence density and the large concentration of charge that constitutes the C-C bonds. The density along the bond exhibits a double-humped feature. The peak density is $2.1e/\mathring{A}^3$, 10% higher than the density at the bond center. By contrast, the charge density between carbon planes, drops to less than $0.1e/\mathring{A}^3$.

For comparison, the valence charge density generated by the most refined fit to the X-ray form factors by Chen, Trucano, and Stewart [3], is shown in Fig. 1b. The overall agreement between the two density distributions is exceblent. The experimental standard deviation is quoted to be $\pm\ 0.1e/\mathring{A}^3$. In addition, the set of parameters used to generate Fig. 1b overestimates the total density by $0.034e/\mathring{A}^3$. Therefore, the agreement of the two distributions to within $\pm\ 0.15e/\mathring{A}^3$ throughout the valence region is an encouraging result. Since ours is a pseudo-charge density, the shape of the density within the pseudopotential radius (indicated in Fig. 1a by a dashed circle) is not simply related to the real electron density. However, the integrated pseudo-charge within the pseudopotential sphere is equal to the integral of

the real charge within the same region.

4. VALENCE ELECTRON DISTRIBUTION IN DIAMOND

Diamond is on average a more dense form of carbon, although the nearest neighbor distance is 10% larger. It has the O_h^7 space group and two equivalent atoms per unit cell with cubic lattice constant a=3.57Å . Fig. 2a shows the calculated valence density distribution in a plane containing C-C bonds. The distinctive double humped feature of the bond charge is also exhibited for diamond. Comparing the bond charge of diamond with that of graphite, we see that the peak density for diamond is reduced by 10% of the peak density of graphite. The charge at the bond center in diamond is roughly 75% of its peak density.

The calculated density shown in Fig. 2a agrees well with that calculated by several previous workers [9-11].

Stewart [4] analyzed that valence density of diamond using powder X-ray diffraction data and the equivalent of only 60% of the reflection information used for the analysis of graphite. The results of his analysis are shown in Fig. 2b. In general the experimentally fit densities are more contracted than the calculated densities. The differences between theory and experiment are greater for diamond than for the case of graphite. This is partially due to the fact that the diamond X-ray data is of slightly lower quality than that of graphite. However, the important qualitative features, namely, the double hump of the density along a C-C bond, and the decrease in bond charge relative to that of graphite are well represented by both the experiment and the calculation.

5. VALENCE ELECTRON DISTRIBUTION IN LiC_6

First stage LiC_6 has been reported to have the D_{6h}' space group, having 6 carbon atoms and 1 Li per unit cell [12]. The carbon layers

are in AA registry with respect to each other and the Li atoms align themselves between the layers in the center of one third of the carbon hexagons. The hexagonal unit cell parameters are $\sqrt{3}$ a, where a=2.485Å and c=3.706Å. This represents a 1% dilation of the C-C bond length with respect to that of graphite and a 10% increase in the distance between carbon layers. The calculated density for LiC_6 [13] is shown in Fig. 3 in a plane containing the c-axis and a C-C bond. On the scale shown in the figure, the contours for LiC_6 are barely distinguishable from that of graphite itself, shown in Fig. 1a. In order to consider the effects of charge transfer, therefore, it is useful to define a difference density. We have defined a total difference density as the self-consistent valence density of LiC_6 (Fig. 3) minus the self-consistent valence density of graphite modified to the LiC_6 structure. This total difference density is presented in Fig. 4. By means of this difference density we are able to see the build up of π -like charge near the carbon planes, as well as polarization effects due to the Li ions. Negative contours in the regions of the C-C bonds are indicative of bond weakening due to intercalation.

6. DISCUSSION AND CONCLUSIONS

The successful comparison of calculated and experimental valence densities for graphite presented in Fig. 1 is an encouraging result which establishes a high degree of confidence in the calculation methods. The results for diamond presented in Fig. 2 are also encouraging.

The opportunity to make a detailed comparisons of calculated valence densities with the experimental valence densities derived from X-ray data is relatively rare because there are relatively few experimentally determined valence electron density maps available. Part of the experimental

problem (such as in the case of diamond) is the availability of high quality single crystals. For heavier materials, such as Si, the core contributions to the X-ray scattering becomes more important and the analysis of the valence electron density becomes less accurate.

The charge density itself is important for determining the ground state properties of the materials. The contour plots of the charge density contain important qualitative information about the bonding in these materials. In particular, the double-humped shape of the C-C bond is a distinctive feature that is not exhibited for other Group IV materials such as Si, Ge, and Sn. It is very likely that the double humped feature can be explained in terms of the relative spatial extents of the s- and p- components of the valence wave fucntion. For carbon, the p- wave component is strongly attracted to the C core, while the s-wave component is attracted less strongly as exhibited by the relative strengths of the ionic pseudopotentials. For the heavier materials, the existence of p core states decreases the p- wave attraction to the core, so that the p- wave components of the wave function are able to have larger extent into the bonding region.

Having established credible results for graphite and diamond, we can then address more detailed questions such as charge transfer in graphite intercalation compounds. From our detailed calculations for LiC_6 we find the effects to be on the order of 5% of the peak density in graphite. However, by defining the difference density shown in Fig. 4, the charging and relaxation effects are clearly seen.

ACKNOWLEDGEMENTS

We would like to thank Professor R.F. Stewart and Dr. J.R. Chelikowsky for helpful discussions.

This work was partly supported by National Science Foundation MRL Grant No. DMR79-23647, ARO Contract DAAG-29-77-C400, and National Science Foundation Grant No. DMR78-22465. S.G. Louie would like to acknowledge support from a Sloan Foundation Fellowship.

FIGURE CAPTIONS

1. Contour plots of valence electronic charge density for graphite: (a) present results and (b) results from analysis of x-ray data by Chen, Trucano, and Stewart (Ref. 3). Contour values are given in units of 0.1e /$\mathring{A}^3$. Atomic positions are denoted by filled circles. Two planes are shown -- one containing an a-axis and the other containing the c-axis and both intersecting at 90° along a C-C bond. In (a), the dashed circle denotes the pseudopotential radius. In (b), the authors quote a standard deviation of ± 0.1e/$\mathring{A}^3$.

2. Contour plots of valence electronic charge density for diamond: (a) present results and (b) results from analysis of X-ray data by Stewart (Ref. 4). Contour values are given in units of 0.1e/$\mathring{A}^3$. Atomic positions are denoted by filled squares. The plane shown contains a C-C bond. In (a), the dashed circle denotes the pseudopotential radius.

3. Contour plot of total valence electron charge density of LiC_6. Contour values are given in units of 0.1 electrons/$\mathring{A}^3$. Atomic positions are denoted by filled squares for Li and circles for C. Plane shown contains c-axis and passes through Li atoms and C-C bonds.

4. Contour plots of the total difference density for LiC_6. Contour values are given in units of 0.001e/$\mathring{A}^3$. Atomic positions are denoted by filled squares for Li and circles for C. Plane shown is the same as for Fig. 3.

REFERENCES

1. P. Hohenberg and W. Kohn, Phys. Rev. 136, B864 (1964); W. Kohn and L.J. Sham, Phys. Rev. 140, A1133 (1965).

2. N.A.W. Holzwarth, S.G. Louie, and S. Rabii, to be published.

3. R. Chen, P. Trucano, and R.F. Stewart, Acta Crystallogr. Sec. A 33, 823 (1977).

4. R.F. Stewart, J. Chem. Phys. 58, 4430 (1973).

5. D.R. Hamann, M. Schlüter, and C. Chiang, Phys. Rev. Lett. 43, 1494 (1979).

6. L. Hedin and B.I. Lundqvist, J. Phys. C 4, 2064 (1971).

7. S.G. Louie, K.M. Ho, and M.L. Cohen, Phys. Rev. B19, 1774 (1979).

8. J.D. Bernal, Proc. Roy. Soc. London, Ser. A 106, 749 (1924).

9. M.T. Yin and M.L. Cohen, Phys. Rev. B24, 6121 (1981).

10. G.B. Bachelet, H.S. Greenside, G.A. Baraff, and M. Schluter, Phys. Rev. B24, 4745 (1981).

11. A. Zunger and A.J. Freeman, Phys. Rev. B15, 4716 (1977).

12. D. Guerard and A. Herold, Carbon 13, 337 (1975).

13. N.A.W. Holzwarth, S.G. Louie, and S. Rabii, Phys. Rev. Lett. 47, 1318 (1981) and also to be published.

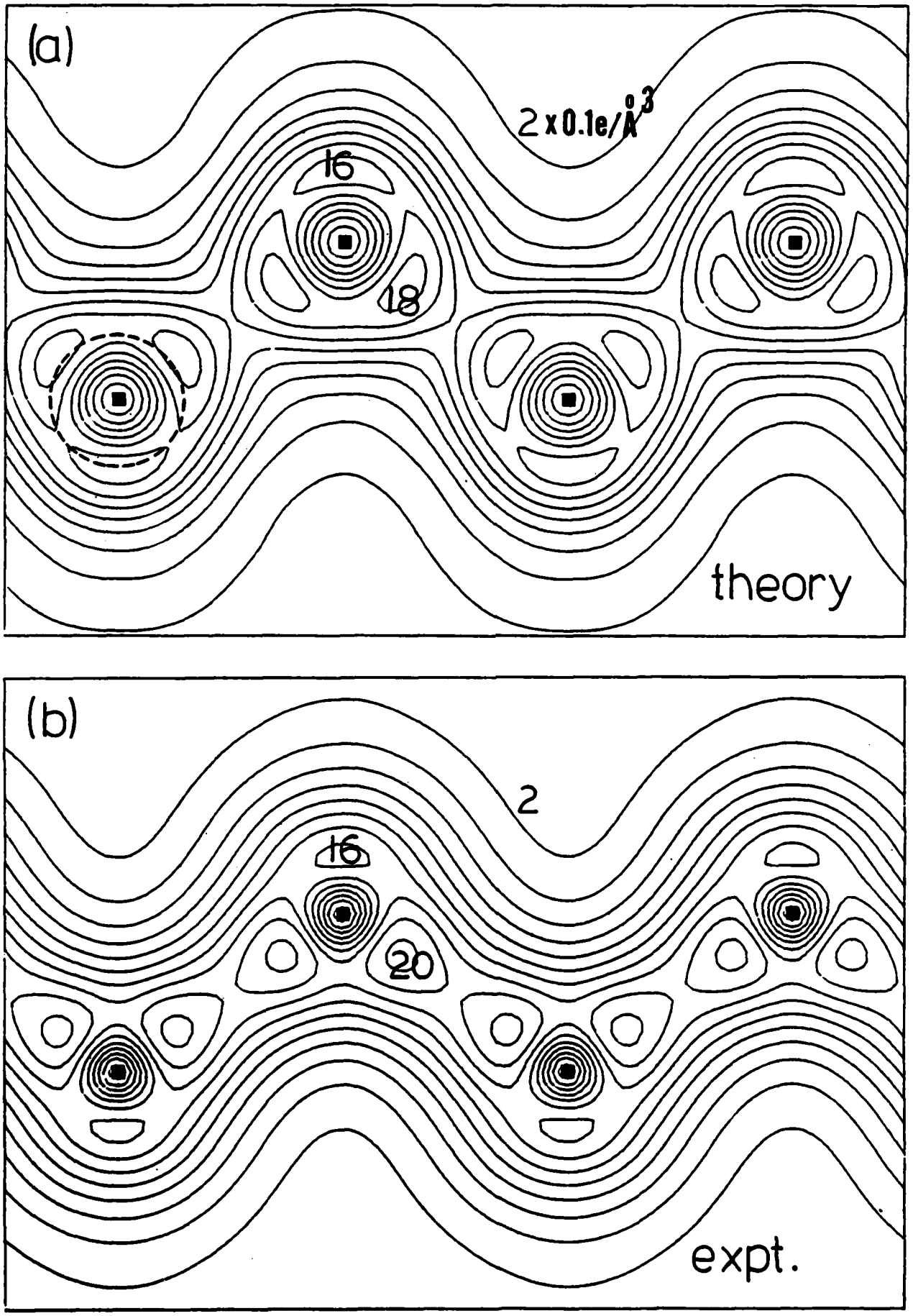

VALENCE CHARGE DENSITY OF DIAMOND

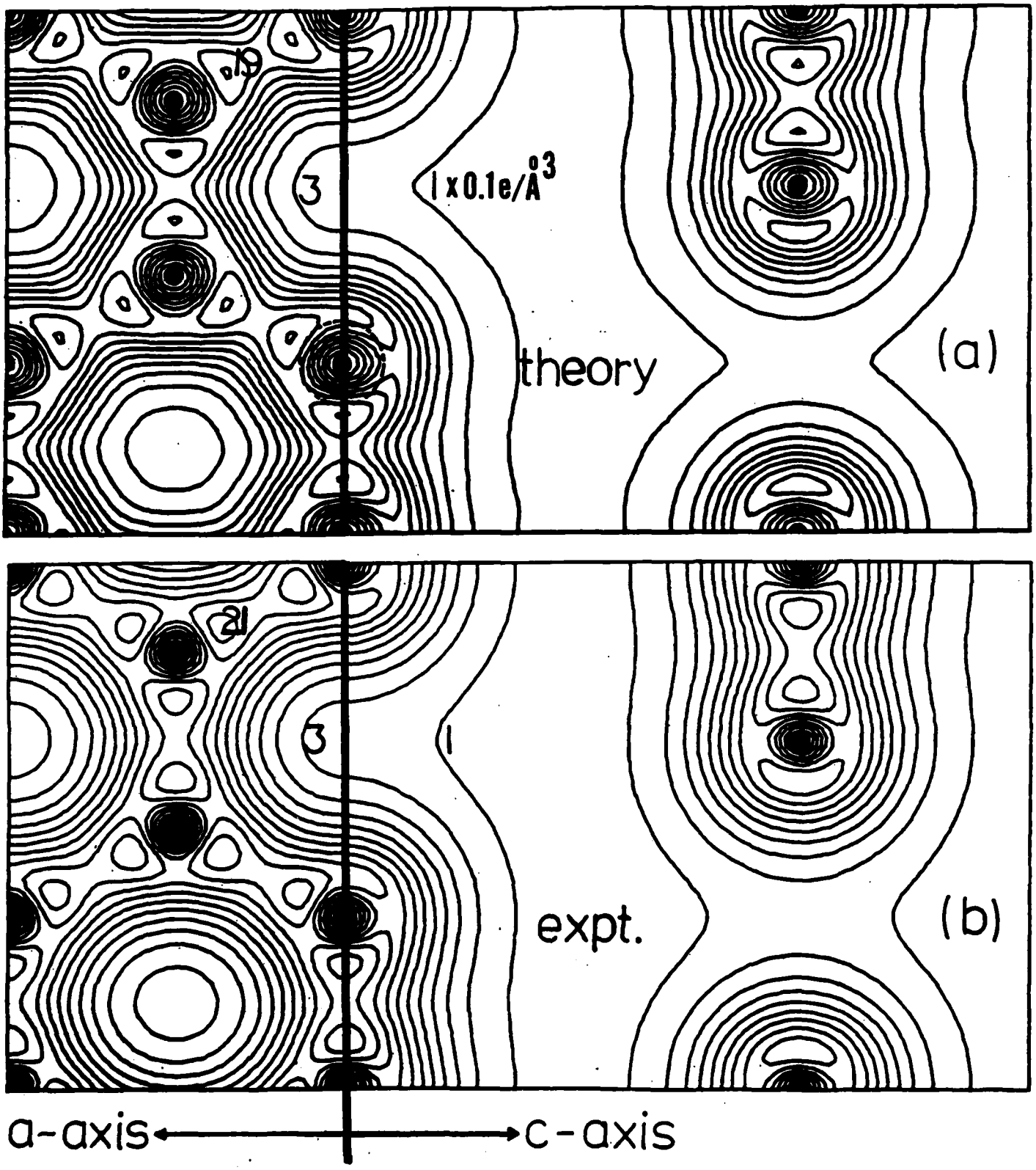

VALENCE CHARGE DENSITY OF GRAPHITE

LiC_6 VALENCE CHARGE DENSITY ($0.1e/Å^3$)

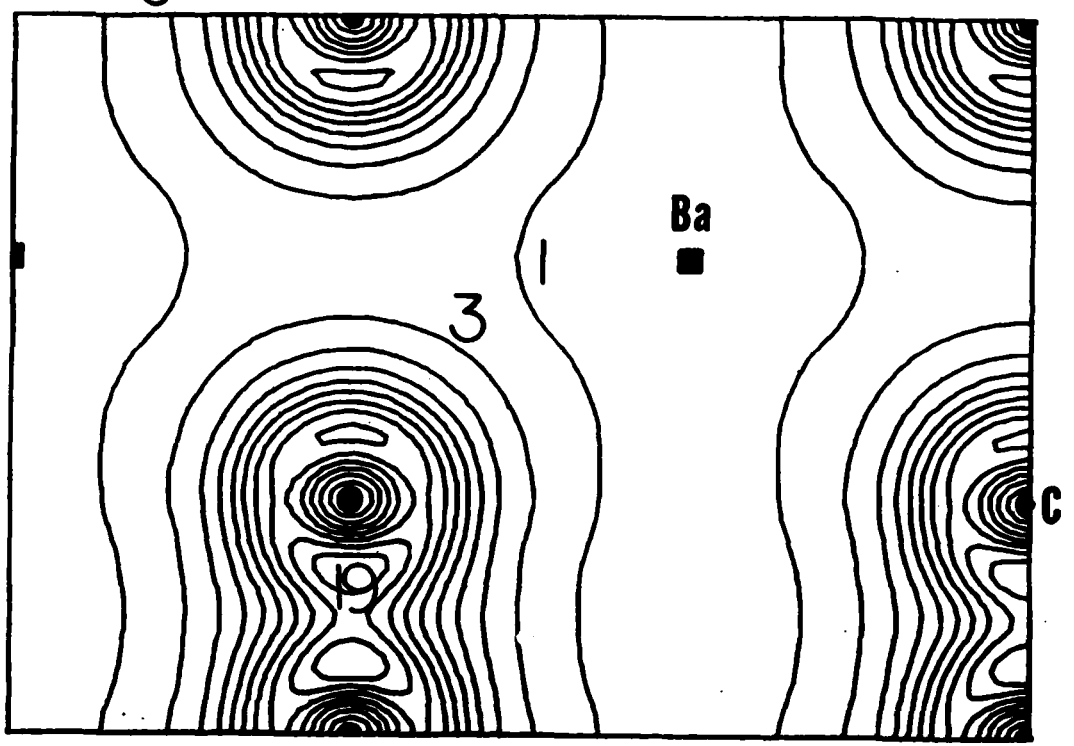

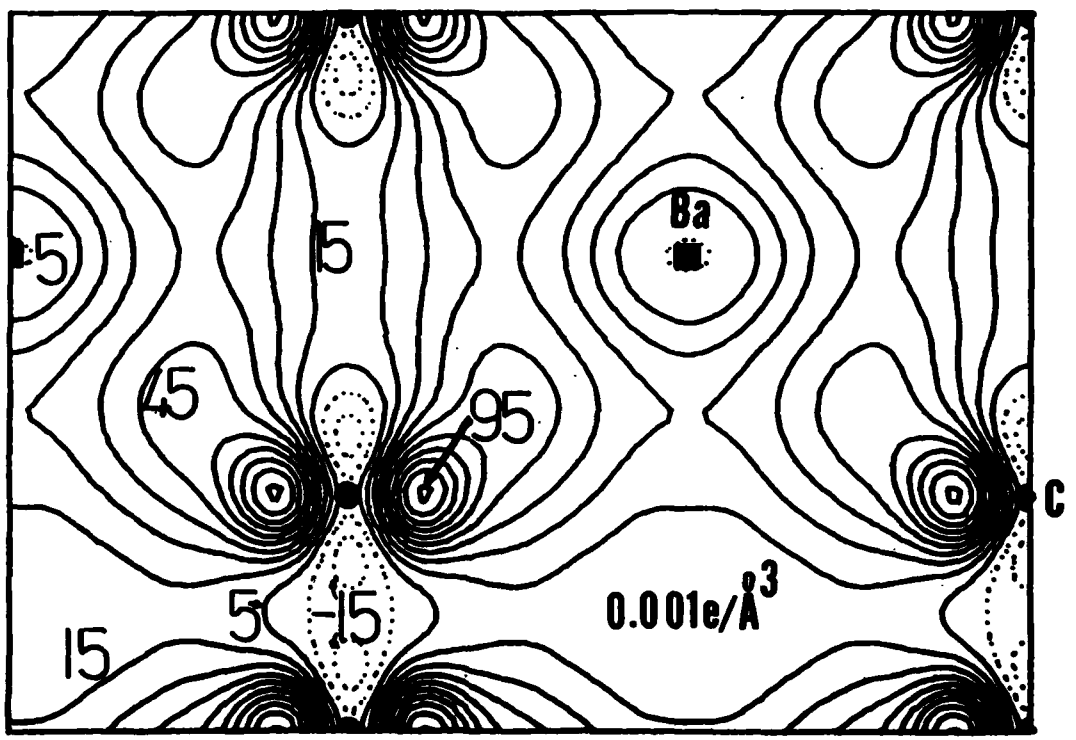

TOTAL DIFFERENCE CHARGE DENSITY FOR LiC_6

ACKNOWLEDGEMENTS

We would like to thank Professor R.F. Stewart and Dr. J.R. Chelikowsky for helpful discussions.

This work was partly supported by National Science Foundation MRL Grant No. DMR79-23647, ARO Contract DAAG-29-77-C400, and National Science Foundation Grant No. DMR78-22465. S.G. Louie would like to acknowledge support from a Sloan Foundation Fellowship.

PHYSICAL REVIEW B VOLUME 30, NUMBER 4 15 AUGUST 1984

Interlayer states in graphite and in alkali-metal–graphite intercalation compounds

N. A. W. Holzwarth
Department of Physics, Wake Forest University, Winston-Salem, North Carolina 27109

Steven G. Louie
Department of Physics, University of California, Berkeley, California 94720

Sohrab Rabii
Moore School of Electrical Engineering, University of Pennsylvania, Philadelphia, Pennsylvania 19104

(Received 23 February 1984)

The character of the first unoccupied band in the graphite intercalation compound LiC_6 is examined. Based on a framework of interacting nonorthogonal states, an analysis of previous band-structure results shows that this band can be interpreted as a hybrid of Li 2*s* and graphite interlayer states.

BPJ246 1983 PACS number 71.25.Pi

In a recent Letter[1] and in several recent conference publications,[2] Posternak and co-workers (PBFWW) have discussed the role of "interlayer states" in graphite and in graphite intercalation compounds. These interlayer states comprise the first unoccupied σ band in both graphite and in LiC_6, having an energy minimum at $\vec{k}=\vec{0}$ with Γ_1^+ symmetry. The existence of the interlayer bands, their approximate energies with respect to the Fermi levels, and their dispersion with respect to $\vec{k}$ have been independently corroborated by several calculations[1-8] as well as by several experiments.[9,10]

The issue addressed by PBFWW concerns the qualitative description of the interlayer band in LiC_6. Specifically, PBFWW stress that the interlayer band in LiC_6 is best described as arising from the interlayer band in pure graphite orthogonalized to the Li 1*s* core states. They take the position that "the occurrence of this band is not correlated to the presence of the Li atoms."[1]

By contrast, in several previous papers,[3,4,7,8] including our work on the electronic structure of LiC_6,[3,4] the same band has been associated with the unoccupied Li 2*s* states and termed a Li *s*-like or "metal" band. This point of view is a logical consequence of the notion[11] that the formation of alkali-metal–graphite intercalation compounds involves the charge transfer of the metal valence electrons to the graphite π bands. In a simple one-electron description of this mechanism, since they are unoccupied, the valence alkali-metal states in the intercalation compound must be energetically located above the Fermi level of the compound. Furthermore, from a consideration of the energetics of the charge-transfer process[12] such as the ionization potential of the alkali-metal atoms modified by the presence of a graphite lattice, one would expect the valance alkali-metal state in the intercalation compound to be located not more than a few electron volts above the Fermi level of the compound. These simple arguments are consistent with the results of detailed calculations of the electronic structure of LiC_6, if one associates the unoccupied "interlayer" band in LiC_6 with significant contributions from the valence alkali-metal states. In modified Korringa-Kohn-Rostoker (KKR) calculations[3] as well as in self-consistent mixed basis pseudopotential calculations,[4] such an identification was suggested by the fact that the eigenvectors for this band, especially near $\vec{k}=0$, have substantial amplitude multiplying the Li 2*s* basis functions. However, even in the early descriptions[3] of this band, it was known to be strongly hybridized with the unoccupied graphite σ band (i.e., the graphite interlayer band). If one accepts the hybrid point of view, the issue then becomes a quantitative question of the degree of hybridization.

Unfortunately, because of the spatially extended nature of both the Li 2*s* states and the pure graphite interlayer states and especially because of their large overlap with each other, it is very difficult to assess the degree of hybridization. However, despite the ill-defined nature of this issue, it is possible to discuss some reasonable measures of the degree of hybridization and to relate them to the analysis of some experimental results reported in the literature as well as the analysis of our own calculational results for the band structure of LiC_6.

Firstly, the photoyield experiments of Eberhardt, McGovern, Plummer, and Fischer[9] measured the absorption of photons due to transitions from a Li 1*s* initial state to unoccupied final states. Because the initial state is localized on the Li sites, the matrix element tends to weight the absorption yield toward transitions with final states having reasonable amplitudes on Li sites. Furthermore, the atomic portion of the selection rules for the dipole absorption process tend to favor final states of Li 2*p* character. Since the Li 2*p* states usually lie higher in energy than the Li 2*s* states, the absorption yield peak found near 2 eV above E_F indicates an upper limit for the experimental "location" of states having Li 2*s* character.

Secondly, Fauster, Himpsel, Fischer, and Plummer[10] have recently measured the unoccupied interlayer bands in both graphite and LiC_6 by means of inverse photoemission experiments, determining the positions of these bands with respect to their corresponding Fermi levels. Their results for LiC_6 are compatible with the photoyield results mentioned above. By comparing the results for graphite and LiC_6 and from a knowledge of the raising of the Fermi level in LiC_6 due to charge transfer, Fauster *et al.*[10] inferred that

the interlayer band in LiC_6 is shifted by approximately 1 eV to lower energy with respect to that of graphite. This 1-eV shift is interpreted as an indication of hybridization. Within the experimental error these results are consistent with our self-consistent mixed basis pseudopotential calculations for graphite[5] and LiC_6 (Ref. 4) which determine the shift to be 1.6 eV.

Thirdly, we have analyzed the results of our calculations[4] in terms of a volumetric measure of the degree of hybridization.[13] We evaluated partial densities of states (PDOS) for LiC_6 and for a reference graphite compound (LiC_6 with the Li atoms removed) by weighting each state by its charge within spheres of radius 3.1 bohr about each Li site. This is shown in comparison with the total DOS in Fig. 1. We find a significant contribution to the total and partial Li DOS in the region of the interlayer state at approximately 23 eV about the bottom of the lowest σ band. Of course, in addition to contributing to the interlayer state, Li contributions are found throughout the spectrum.

Finally, we have analyzed our calculations[4] in terms of an orbital measure of the degree of hybridization. First consider a highly simplified model which exhibits an idealized physical situation. The most simple model would correspond to representing the wave function of the LiC_6 interlayer state as a sum of a Li 2s linear combination of atomic orbitals (LCAO) wave function (ϕ_s) and a graphite interlayer state wave function (ϕ_g):

$$\Psi(\vec{k},\vec{r}) = A(\vec{k})\phi_s(\vec{k},\vec{r}) + B(\vec{k})\phi_g(\vec{k},\vec{r}) \quad (1)$$

The secular equation for the coefficients A and B can be represented as

$$\begin{bmatrix} \epsilon_s & -V \\ -V & \epsilon_g \end{bmatrix}\begin{bmatrix} A \\ B \end{bmatrix} = E\begin{bmatrix} 1 & S \\ S & 1 \end{bmatrix}\begin{bmatrix} A \\ B \end{bmatrix} . \quad (2)$$

Here $\epsilon_g(\vec{k})$, $\epsilon_g(\vec{k})$, $V(\vec{k})$, and $S(\vec{k})$ denote, respectively, the Li 2s LCAO band energy, the graphite interlayer band energy, the interaction matrix element, and the overlap matrix element. The quantity of interest is a measure of the Li 2s character in an eigenfunction Ψ, which we can take as the Mulliken population.[14]

$$Q_s = \langle A(\vec{k})\phi_s(\vec{k},\vec{r}) | \Psi(\vec{k},\vec{r}) \rangle . \quad (3)$$

While this Mulliken population is not unique—depending both on the Li 2s LCAO function $\phi_s(\vec{k},\vec{r})$ as well as on the other members of the nonorthogonal basis set—we believe that it can provide a reasonable qualitative measure of the hybridization of Li 2s wave functions in the eigenstates of LiC_6 for this very simple model as well as for the realistic band structure which we will discuss in a moment.

If the overlap matrix element $S(\vec{k})$ of Eq. (2) *were* zero, the hybridized spectrum of the intercalation compound $E(\vec{k})$ would be given by

$$E_\pm = \frac{\epsilon_s + \epsilon_g}{2} \pm \left[\left(\frac{\epsilon_s - \epsilon_g}{2}\right)^2 + V^2\right]^{1/2} \quad [\text{for } S(\vec{k}) = 0] . \quad (4)$$

In this case, the spectrum of the compound would consist of two energy levels symmetrically located with respect to the mean of ϵ_s and ϵ_g. The experimental evidence[10] suggests that $\epsilon_g - E_- \approx 1$ eV. The upper hybrid level E_+ has not been experimentally identified, but the data[9,10] suggest that $E_+ - E_- > 7$ eV. These experimental results are consistent with the simplified model (4) only if $\epsilon_s - \epsilon_g > 5$ eV (which is an unphysically large value), and the corresponding Li 2s Mulliken population would be relatively small: $Q_s \leq 14\%$.

On the other hand ϕ_s and ϕ_g are known to overlap appreciably. From our mixed basis pseudopotential calculation results,[4,5] we have evaluated $S(\vec{k})$ and have found $S(\vec{k}) \approx 0.6$ throughout most of the Brillouin zone. Therefore, it is important to consider the spectrum of the full generalized eigenvalue problem (2):

$$E_\pm = \frac{\epsilon_s + \epsilon_g + 2VS}{2(1-S^2)} \pm \left[\left(\frac{\epsilon_s + \epsilon_g + 2VS}{2(1-S^2)}\right)^2 + \frac{V^2 - \epsilon_s\epsilon_g}{1-S^2}\right]^{1/2} . \quad (5)$$

In this case, the spectrum of the compound consists of two energy levels which are highly skewed with respect to the mean of ϵ_s and ϵ_g. Analysis of the experimental results,[9,10] $\epsilon_g - E_- \approx 1$ eV and $E_+ - E_- \approx 7$ eV, leads to the conclusion that $\epsilon_s - \epsilon_g \approx 1$ eV and that $Q_s^- \approx 40\%$. These values are more consistent with the physical arguments[11,12] discussed above.

With slight generalization we can use this orbital partition to analyze the full wave functions $\Psi_i(\vec{k},\vec{r})$ of the ith band of our self-consistent calculations.[4] For this purpose, it is necessary to add to the terms of Eq. (1) a residual function

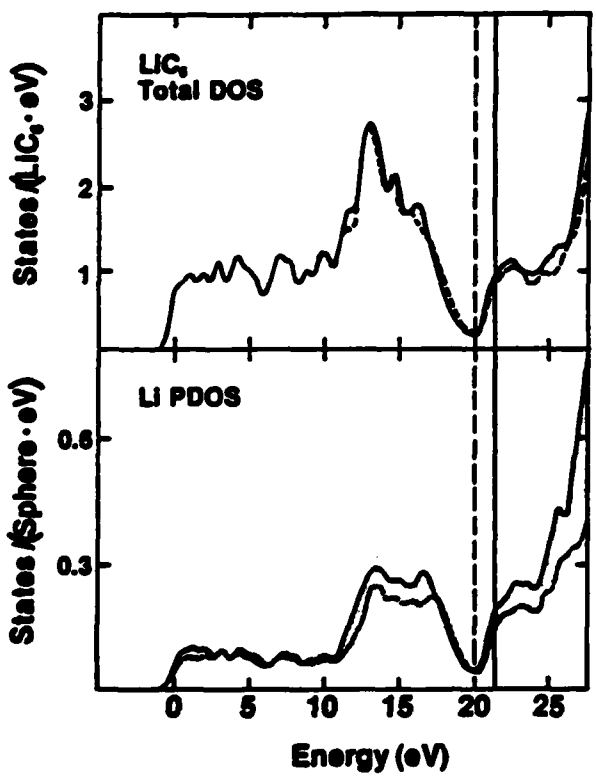

FIG. 1. Total density of states (top) and partial density of states (bottom) for LiC_6 (full curve) and a reference graphite compound—LiC_6 with Li atoms removed—(dashed curve). Shading highlights the positive difference between the LiC_6 and reference curves. The PDOS was determined by weighting each state by its charge within spheres of radius 3.1 bohr about each Li site. The zero of energy was taken at bottom of lowest σ band. Vertical lines denote locations of Fermi levels.

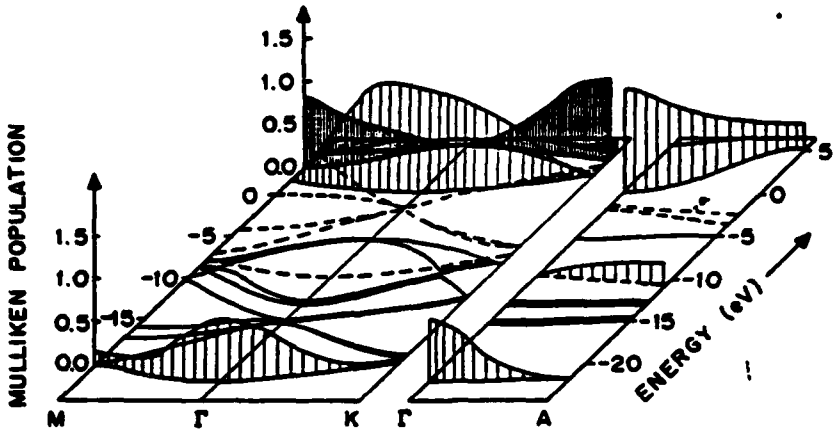

FIG. 2. Three-dimensional representation of the Mulliken population Q_s^i of the Li 2s LCAO functions (vertical direction) along various symmetry directions in the band structure of LiC_6. Zero of energy is taken as E_F. Bands are denoted with dashed lines for π bands and full lines for σ bands.

$R_i(\vec{k}, \vec{r})$, since ϕ_s and ϕ_g do not form a complete set:

$$\Psi_i(\vec{k}, \vec{r}) = A_i(\vec{k})\phi_s(\vec{k},\vec{r}) + B_i(\vec{k})\phi_g(\vec{k},\vec{r}) + R_i(\vec{k}, \vec{r}) \ . \tag{6}$$

In our calculation the Li 2s LCAO function $\phi_s(\vec{k},\vec{r})$ was included in our actual basis set, so that the coefficient $A_i(\vec{k})$ was determined variationally. The graphite interlayer wave function $\phi_g(\vec{k},\vec{r})$ was not explicitly included in the basis set so that we have no direct information about the coefficient $B_i(\vec{k})$ or about the contribution of the residual function $R_i(\vec{k}, \vec{r})$. Nevertheless, the Li 2s Mulliken popularion can be evaluated according to Eq. (3). Due to the normalization of the wave function Ψ_i, information regarding the sum of the graphite and residual contributions can be obtained from the sum rule:

$$Q_s^i + Q_g^i + Q_k^i = 1 \ , \tag{7}$$

where

$$Q_g^i = \langle B_i(\vec{k})\phi_g(\vec{k},\vec{r}) | \Psi_i(\vec{k}, \vec{r}) \rangle$$

and

$$Q_k^i = \langle R_i(\vec{k}, \vec{r}) | \Psi_i(\vec{k}, \vec{r}) \rangle \ .$$

We have reanalyzed our results[4] for the band structure of LiC_6 in order to evaluate $Q_s^i(k)$ throughout the spectrum as shown in Fig. 2. These results indicate that for the interlayer band of LiC_6, Q_s^i has a value of 1.2 at $\vec{k}=0$ (Γ point), decreases to 0 at the band edges in the $\vec{k}=0$ plane due to interaction with higher energy σ bands, and decreases to 0.3 at the A point. We again see that Li contributions are significant throughout the spectrum of LiC_6. In particular, Q_s^i takes a value of 0.7 at the Γ point for the lowest-energy σ band and a value of 0.3 at the A point for the lowest-energy π band. A Mulliken population greater than unity can occur for highly overlapping systems such as in the present case. Consequently, the exact value of Q_s^i is less significant than the fact that it is large for the interlayer band in comparison with its value for different bands i at the same wave vector $\vec{k}$.

In conclusion, we have shown both in terms of a volumetric PDOS analysis and an orbital Mulliken population analysis that the interlayer state of LiC_6 does contain an appreciable amount of Li 2s character. Upon closer examination, within the framework of these analyses, we find evidence of Li 2s character throughout the spectrum of LiC_6. Thus, the description of the interlayer state of LiC_6 as a hybrid of Li 2s and graphite interlayer state contributions is necessarily a simplification of a more highly coupled set of states. However, within this simplification, if one examines the simple model of Eqs. (2) and (5) representing the physics of interacting nonorthogonal states, the hybrid nature of the LiC_6 interlayer band is entirely compatible with the theoretical and experiment results for this system and, in particular, with the "preexistence" of the analogous interlayer band in pure graphite. Because the Li 2s LCAO and the graphite interlayer state are so similar in their spatial extent, other interpretations[1] are possible. However, we feel that the point of view that the occurrence of the LiC_6 interlayer band is not correlated to the presence of Li atoms[1] is misleading. On the other hand, previous[3,4,7,8] shorthand terminology of this band as a "metal band" is perhaps an overstatement on the other extreme.

ACKNOWLEDGMENTS

We would like to thank Corporate Research Science Laboratories of Exxon Research and Engineering Company for the use of their computer in performing the Mulliken population calculations. S.G.L. would like to acknowledge support from the Alfred P. Sloan Foundation and National Science Foundation Grant No. DMR-83-19024. S.R. would like to acknowledge support from the National Science Foundation–Materials Research Laboratories Program under Grant No. DMR-82-16718 and U.S. Army Research Office Contract No. DAAG-29-77-C400.

[1]M. Posternak, A. Baldereschi, A. J. Freeman, E. Wimmer, and M. Weinert, Phys. Rev. Lett. 50, 761 (1983).
[2]M. Posternak, A. Baldereschi, A. J. Freeman, and E. Wimmer, Bull. Am. Phys. Soc. 28, 347 (1983); M. Posternak, A. Baldereschi, A. J. Freeman, E. Wimmer, and M. Weinert, in *Intercalated Graphite*, Material Research Society Symposia Proceedings, Vol. 20 (North-Holland, Amsterdam, 1983), p. 117.
[3]N. A. W. Holzwarth, S. Rabii, and L. A. Girifalco, Phys. Rev. B 18, 5190 (1978).
[4]N. A. W. Holzwarth, S. G. Louie, and S. Rabii, Phys. Rev. B 28, 1013 (1983).
[5]N. A. W. Holzwarth, S. G. Louie, and S. Rabii, Phys. Rev. B 26, 5382 (1982).
[6]R. C. Tatar and S. Rabii, Phys. Rev. B 25, 4126 (1982).
[7]T. Ohno, J. Phys. Soc. Jpn. 49 (Suppl. A), 899 (1980).
[8]R. V. Kasowski, Phys. Rev. B 25, 4189 (1982).
[9]W. Eberhardt, I. T. McGovern, E. W. Plummer, and J. E. Fischer, Phys. Rev. Lett. 44, 200 (1980).
[10]Th. Fauster, R. J. Himpsel, J. E. Fischer, and E. W. Plummer, Phys. Rev. Lett. 51, 430 (1983).
[11]F. R. M. McDonnell, R. C. Pink, and A. R. Ubbelohbe, J. Chem. Soc. London 1951, 191 (1951).
[12]F. J. Salzano and S. Aronson, J. Chem. Phys. 44, 4320 (1966).
[13]N. A. W. Holzwarth, S. G. Louie, and S. Rabii, in *Intercalated Graphite*, Ref. 2, p. 107.
[14]R. S. Mulliken, J. Chem. Phys. 23, 1833 (1955).

END

FILMED

10-84

DTIC